Fracture Processes and Toughening Mechanisms in Solid-State Electrolytes

Johann Perera

Oriel College

University of Oxford

Submitted for the degree of *Doctor of Philosophy*

Michaelmas 2024

Declaration of Originality

I, Johann Perera, declare that this thesis is my own work and has not been submitted to another institution for any other degree or qualification. All contributions from collaborators have been appropriately referenced throughout the work.

This thesis is approximately 38,533 words in length, and so complies with the Materials Science Departmental word limit for a doctoral thesis.

Johann Perera

Michaelmas 2024

Acknowledgements

My first and foremost thanks must go to Professor David Armstrong. Thank you for the opportunity to pursue academic research at a forefront of technology development at the best university in the world. Your support and mentorship both within the lab and outside of it have been invaluable and helped fully enjoy these last four years. Thanks must also go to Dr Ed Darnbrough for his continuous support and answering of last minute questions, in particular helping me to get the full use out of the TESCAN.

I would like to thank the OMG group for all their advice and review; in particular those resident in 21BR 18.02 & Dr Anna Kareer. The productive chats about research and matlab helped me progress so much; as well as the office cricket, Taylor's lunches and other stimulating antics which helped me enjoy my time these four years. In particular Bradley Young, from meeting you that first day in September 2016 who would have guessed we would complete eight years of Materials side by side, as well as multiple Blues and the best ever OUHC record. Genuinely would not be here without you! I would also like to thank the members of the Bruce group for their support and collaboration over the years in all things electrochemical; special mention must go to Dr Dominic Spencer Jolly and Dr Dominic Melvin for their guidance as well.

The members of OUHC and the Vincent's Club who have made these the best four years I've lived. The fun times we had were phenomenal, too many to count and none of them to be matched. The year we won 5 trophies I still look back on fondly. My hockey progressed beyond belief, no one would have believed that I would play Premier League hockey and The Club truly is the college that chose me. Special mention must go to Livi, Kev, Grackle, Mwillo, the TurboLads, the Mullion XI, the Old Men and the cross-country golfers – I hope for many many

more good times to come. To my wonderful housemates Rachel and Tiph, your counsel, guidance and wisdom is unmatched as are the good times had at Asties.

To Samuel Edward Greenbank, having picked me up and supported me for the first six years of my time at Oxford. My fellow hockey badger, DPhil navigator and the best flatmate I've ever had. Living you with was half the reason I wanted to stay, lots of lover for you and the fond memories I have!

To Maranga Mokaya, the strength and speed of our friendship truly shows how much we are brothers. Endless chats about sport, DPhil, faith, relationships and life have helped me truly grow and enjoy life. Warm weather training camps in South Africa, sauna time, road trips to Leeds, embracing the elite athlete life and fully backing myself to play the highest level I can are but a few things you have helped me experience and enjoy. Nothing but love my brother.

My love Stephanie, you have brought no end of joy to my life. If I had to go through this DPhil to find you then the years spent in Oxford have been more than worth it. I am beyond excited for what is in store for us!

Finally, to my parents Ranil & Romie and my little brother Christopher, thank you for the opportunity to always peruse my dreams and enjoyment in life. I love you all so so much and am beyond lucky that you are my family. Words are not enough to say how grateful I am for you, how much I appreciate you and how much love and care I have for you all.

Most of all I thank my heavenly Father for continuing to bless and care for me, all the days of my life.

Abstract

Climate change is a worldwide problem and has made clean energy a global priority. As the shift to clean energy progresses, the demands for improved energy storage continue to grow. The current energy storage solution of choice is the Li-ion battery; however, to meet the energy storage demands of the future, the All-Solid-State-Battery is the most promising next generation technology. The ASSB contains a solid electrolyte which enables the use of lithium metal anodes to achieve greater performance. Unfortunately, this has generated several as of yet unsolved and poorly understood issues all stemming from fracture in the solid electrolyte. Principally, cell failure due to lithium dendrites which grow through and crack the solid electrolyte. This thesis utilises a mechanics based approach to understand the fracture behaviour of solid electrolytes which has until now been poorly characterised.

As the most electrochemically promising solid electrolytes are highly air-sensitive, work is initially carried out to develop novel testing techniques to enable mechanical characterisation of these solid electrolytes; providing the first look at their experimentally determined properties. Firstly, an investigation was carried out into the effect of density on both the mechanical and electrochemical properties of these solid electrolytes. This highlighted that more highly densified solid electrolytes achieved better performance and identified Li_6PS_5Cl as the choice solid electrolyte. Densified Li_6PS_5Cl electrolyte was mechanically tested to determine the dendrite initiation model using local fracture strength, and the dendrite propagation model using fracture toughness. To improve fracture toughness, the effect on mechanical performance of a Li_6PS_5Cl composite using metastabilised zirconia particles was also investigated. To replicate the effect of repeated cycling and mechanical fatigue on two solid electrolytes, Li_6PS_5Cl and $Li_{6.4}La_3Zr_{1.4}Ta_{0.6}O_{12}$, is investigated by a novel micro cantilever fatigue test; this demonstrated that crack growth can occur below the single cycle failure stress.

List of Publications

1. Perera, J; Spencer Jolly, D; Pu, SD; Melvin, DLR; Adamson, P; Bruce, PG. High critical currents for dendrite penetration and voiding in potassium metal anode solid-state batteries. *Journal of Solid State Electrochemistry,* **26,** 1961-1968 (2022).
2. El-Shinawi, H; Darnbrough, E; Perera, J; McClelland, I; Armstrong, DEJ; Cussen, EJ; Cussen, SA. Liquid-phase approach to glass-microfiber-reinforced sulfide solid electrolytes for all-solid-state batteries. *ACS Applied Materials & Interfaces*, **15,** 36512-36518 (2023).
3. Ning, Z; Li, G; Melvin, DLR; Chen, Y; Bu, J; Spencer-Jolly, D; Liu, J; Hu, B; Gao, X; Perera, J; Gong, C; Pu, SD; Zhang, S; Liu, B; Hartley, GO; Bodey, AJ; Todd, RI; Grant, PS; Armstrong, DEJ; Marrow, TJ; Monroe, CW; & Bruce, PG. Dendrite initiation and propagation in lithium metal solid-state batteries. *Nature*, **618**, 287–293 (2023).
4. Gao, X; Liu, B; Hu, B; Ning, Z; Spencer Jolly, D; Zhang, S; Perera, J; Bu, J; Liu, J; Doerrer, C; Darnbrough, E; Grant, PS; Armstrong, DEJ; & Bruce, PG. Solid-state lithium battery cathodes operating at low pressures. *Joule*, **6**, 636-646 (2022).
5. Hu, B; Zhang, S; Ning, Z; Spencer-Jolly, D; Melvin, DLR; Gao, X; Perera, J; Pu, SD; Rees, GJ; Wang, L; Yang, L; Gao, H; Marathe, S; Burca, G; Marrow, TJ; & Bruce, PG. Deflecting lithium dendritic cracks in multi-layered solid electrolytes. *Joule*, **8**, 2623-2638 (2022).

Table of Contents

1. Fundamentals of Batteries

1.1 Broader Perspective

The concept of storing electrochemical energy to be utilised at a later date goes back several centuries, with the voltaic pile invented by Alessandro Volta in the late 18th century the first device able to provide a continuous electrical current from a stored energy, this is widely accepted to be the first battery.[1] The lead-acid battery followed in the mid-19th century developed by Gaston Planté and demonstrated the first type of rechargeable battery.[2] Nickel-cadmium and nickel-metal hydride batteries followed in the early 20th century, enabling advancements in portable technologies.[3]

The greatest advancement came in the late 20th century with the introduction of lithium-ion batteries. Their lightweight design and high energy density led to a portable digital revolution, bringing in a new technological age.[4] Fast-forward to the present day, the need for electrical energy storage has vastly expanded; renewable energy generation driven by formidable environmental concerns demands greater storage capabilities.[5] Developments and enhancements are being made to the existing small-scale portable lithium-ion batteries to provide large-scale energy storage. One such example is the combination of multiple lithium-ion cells, once optimised for portable phones, to form a battery pack suitable to power an electric vehicle.[6,7] Despite the advances, lithium-ion technology is still insufficient to meet the current electrical energy storage needs therefore we need technologies beyond lithium-ion which utilise lithium-metal anodes to form solid-state cells that are hailed as next generation of

battery. However, there are still many challenges that face the solid-state battery which must be overcome through research before this technology can be fully and commercially realised.[6]

1.2 Route to Solid-State Batteries

1.2.1 Lithium-ion Battery

The lithium-ion battery (LIB) is the most commercialised solution for rechargeable and electrochemical energy storage. Development of LIBs has greatly driven the development of microelectronics due to the higher volumetric and gravimetric energy densities than other rechargeable systems, as shown in figure 1.1.[8] LIBs are also popular due to their high-power density, long life and environmentally friendly applications.[9]

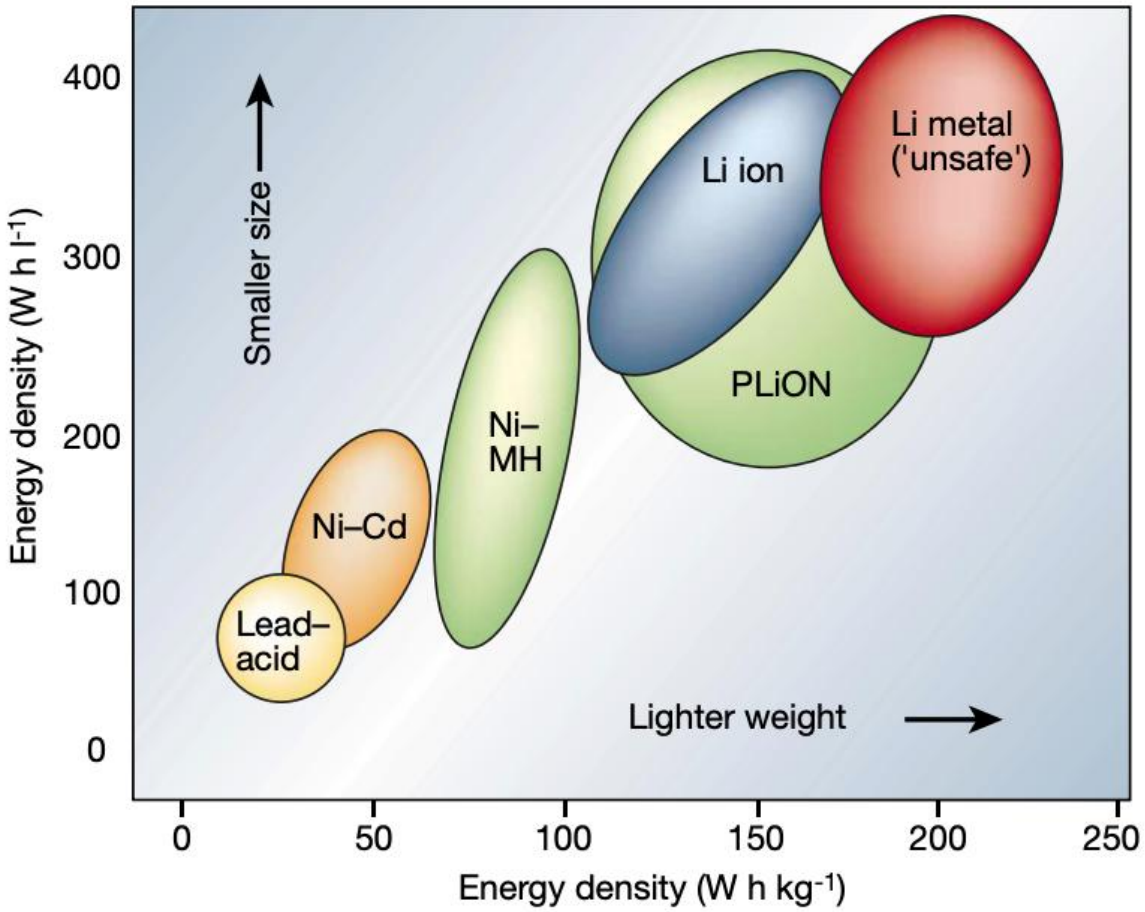

Figure 1.1: Volumetric and gravimetric comparison of the different battery technologies (lead-acid, nickel-cadmium, nickel-metal hydride, lithium-ion, polymer-lithium ion, lithium metal) in terms energy density.[4]

LIBs consist of an arrangement of galvanic (voltaic) cells, each cell is made from four key components, the cathode, anode, separator and liquid electrolyte.[10] During operation of the cell, oxidation and reduction reactions occur at spatially separated electrodes, immersed in the ionically conductive and electronically insulating liquid electrolyte.[11] During cell discharge an oxidation reaction occurs at the (typically graphite) anode creating Li^+ ions and electrons. The liquid electrolyte allows for migration of the Li^+ ions between the electrodes, anode to cathode, whilst preventing the flow of electrons.[12] To maintain charge neutrality between the electrodes, an electron flows from the anode through an external circuit, performing useful work before it

enters the cathode.[12,13] During charging the process is reversed, an external current is applied to the LIB, resulting in oxidation occurring at the cathode to produce Li^+ ions, which are then driven from cathode to anode through the electrolyte.[13,14] A physical separator is also required, to prevent a short-circuit as a result of contact between the electrodes.[15] A schematic diagram of the existing LIB can be seen in figure 1.2.

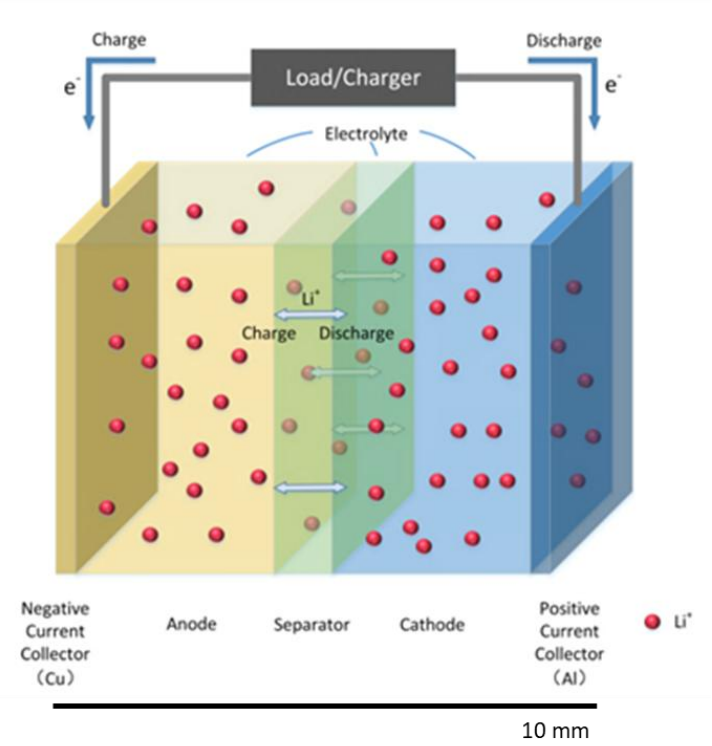

Figure 1.2: Schematic of the lithium-ion battery[16].

Despite their many positives LIBs do have a few safety concerns as well as limits on their potential performance:

- **Interface reactivity and degradation.** A reaction occurs at the interface between the graphite anode and liquid electrolyte which forms an inactive resistive layer more commonly known as the sold electrolyte interphase (SEI).[17,18] The formation of an SEI layer causes a cell capacity fade, due to the loss in active lithium.[19] At the cathode interface, degradation can occur, especially when the cathode active material is under

high charging rates and at elevated temperatures.[20,21] Cathode degradation can also further promote formation of a passivating SEI layer.

- **Unwanted lithium metal plating.** Fast-charging LIBs are highly sought after, particularly for use in electric vehicles to compete with the time taken to re-fuel traditional fossil fuel vehicles. However, due to the resistive SEI layer limiting the diffusion of lithium, fast-charging conditions can lead to lithium metal plating at the anode, also known as a lithium dendrite. This could lead to a cell short-circuit which in turn could cause thermal runaway and an explosion.[22]
- **Safety concerns.** LIBs use an organic liquid electrolyte which is highly flammable and produces toxic fumes if ignited,[23] which poses a major safety concern. Thermal runaway is the most dangerous failure of the LIB and leads to the combustion of the organic liquid electrolyte.[23] Thermal runaway starts with the overheating of the battery system which can be a result of overcharging, exposure to excessive temperatures, or a short circuit. As the internal temperature rises, exothermic chemical reactions occur which causes further dramatic increases in temperature, culminating in catastrophic failure.[24]
- **Limited energy density.** Although the development of LIBs has progressed greatly, there is a theoretical physiochemical limit on its energy density as demonstrated in figure 1.3.[25] Existing LIBs use graphite as the preferred anode as it is electrochemically stable with common liquid electrolytes and the intercalation mechanism is easily reversible.[26] Therefore, LIBs with graphite anodes have an energy density limit of 350 – 400 $Whkg^{-1}$, the main limiting factor being the low specific capacity of graphite, 372 $mAhg^{-1}$.[14,27] The key to overcome this energy density limit and look beyond the current lithium-ion technology is the incorporation lithium metal anodes.

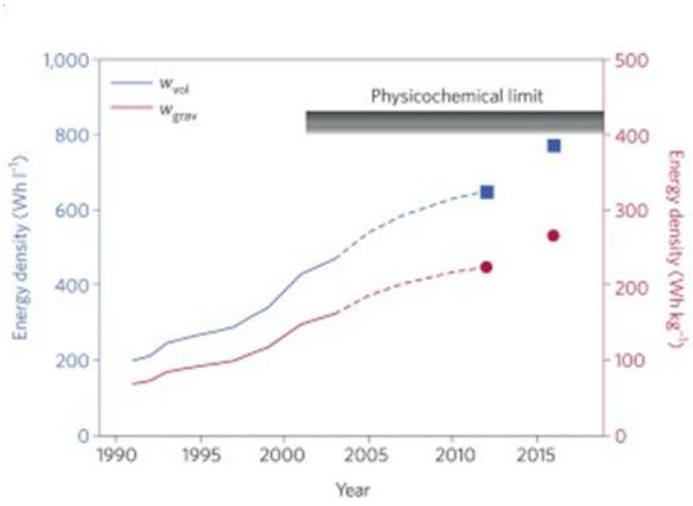

Figure 1.3: Trend of increasing volumetric and gravimetric energy density of LIBs[25].

1.2.2 Lithium metal anodes

Lithium metal anodes have been viewed as the next big breakthrough in battery technology due to their large specific capacity 3860 $mAhg^{-1}$, over ten times larger than that of graphite, its high electro-positivity (-3.04 V vs standard hydrogen electrode), and it being the lightest density of any metal.[26,28] Use of lithium metal anodes has been previously demonstrated in the production of single use (non-rechargeable) cells, in applications such as calculators and watches.[29] Previous attempts to make a rechargeable lithium metal battery have been unsuccessful thus far, due to numerous issues arising during the combination of lithium anodes with organic liquid electrolytes. The two key unresolved issues are:

- **Continuous SEI formation.** Similarly to the graphite anode in the LIB, a passivating SEI layer forms at the interface between the liquid electrolyte and lithium metal, again leading to a loss of lithium, resulting in capacity fade. However, during cycling inhomogeneous stripping/plating and large volume changes in the SEI can cause the layer to fracture, exposing fresh lithium metal. This enables the passivation to occur

again, resulting in further lithium loss and continuous formation of an SEI layer which severely damages the cell, reducing its ability to be recharged.[30,31]

- **Short circuit failure.** Inhomogeneous plating of lithium can easily occur during cycling due to the rougher lithium metal anodes. This can lead to the growth of lithium dendrites which can form through the organic liquid electrolyte, crossing the cell and causing and electrical short circuit. This can lead to catastrophic failure and thermal runaway which could risk an explosion.[32,33]

To unlock the use of lithium anodes the flammable liquid electrolyte must be replaced, to which we look toward the all-solid-state-battery.[34]

1.2.3 All-Solid-State-Battery

All-solid-state-batteries (ASSBs) gain their name due to use of a solid electrolyte (SE); the recent discoveries of new fast Li^+ conducting materials has propelled the ASSB as the most viable option for use of lithium metal anodes. The use of a solid electrolyte could pave the way for safe yet high energy density rechargeable lithium batteries; in particular use of SEs would provide the following clear advantages:

- **Improved safety.** A solid electrolyte offers improved safety over its (typically) organic liquid electrolyte equivalent, which are both highly flammable and toxic.[25]
- **Mitigate continuous SEI formation.** An appropriately selected solid electrolyte can form a stable interface with lithium metal anodes, therefore minimising (and in some cases preventing) degradation at the interface.[35,36] The physical presence of the solid electrolyte blocks SEI formation of fresh unreacted Li metal, thereby significantly reducing any capacity fade at the interface.[37,38]

- **Mechanical dendrite suppression.** Dendritic growth of lithium metal is possible through a liquid electrolyte and can lead to a short circuit. A dense solid electrolyte provides a physical barrier and is hoped that it can mechanically suppress dendrite formation, therefore inhibiting short circuit failure as demonstrated in figure 1.4.[37]

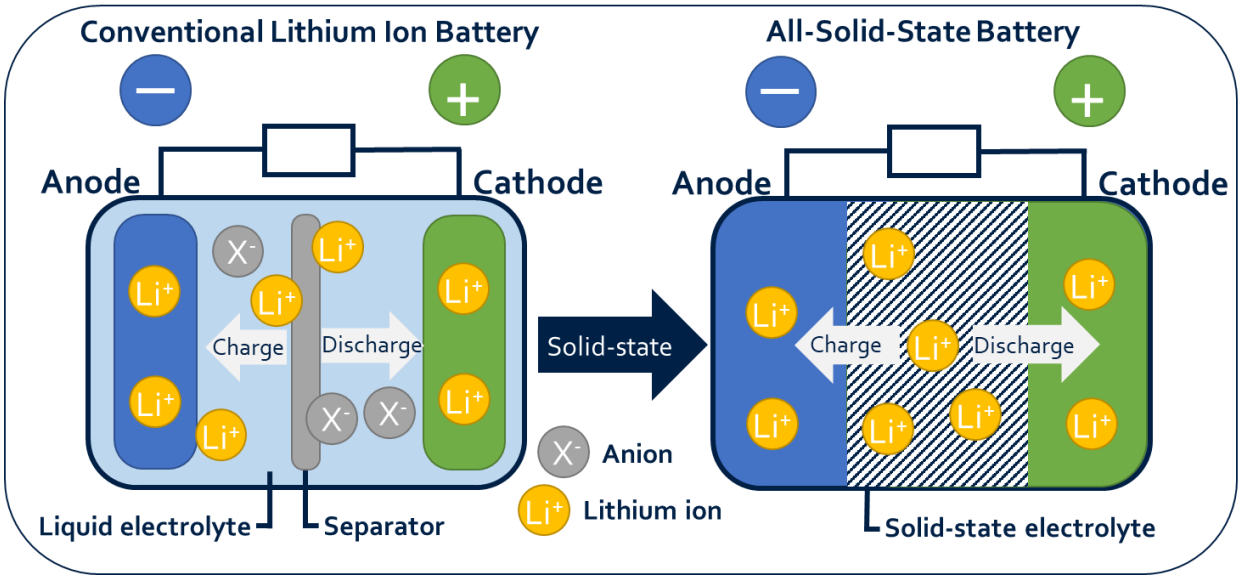

Figure 1.4: A schematic comparing and contrasting the different configuration of the existing LIB and the Li metal ASSB.

Despite all its potential advantages the ASSB has not yet surpassed the performance of the LIB even at the laboratory scale. Some shortcomings are:

- Liquid electrolyte ionic conductivity is significantly higher, of the order 10^{-2} Scm^{-1}, whereas the majority of solid electrolytes have inherently tortuous ionic pathways, and as such cannot reach this level of conductivity, typically 10^{-4}-10^{-3} Scm^{-1}.[39]
- Between most common anodes and cathodes there is a wide voltage window which can lead to poor electrochemical stability of solid electrolytes across the potential difference.
- Higher costs of manufacture due to increased costs when processing ceramics such as high sintering temperatures, isostatic pressing, rolling to thin films etc.

- Poor physical interfacial contact at the Li/solid electrolyte interface, primarily due to the brittle and rigid nature of solid electrolytes, necessitating applied stack pressure for successful cycling.[40] Through better mechanical design of the solid electrolyte, which this thesis aims to address, this issue can be significantly reduced if not completely mitigated.
- Dendrite formation has been observed to still grow even through a solid electrolyte. It was theorised that the physical presence of a solid electrolyte would prevent lithium traversing from anode to cathode and therefore preventing failure by short circuit. However, when operating at high current densities lithium dendrites can penetrate the solid electrolyte; improving the mechanical properties of the solid electrolyte will greatly aid in dendrite resistance and therefore significantly improve the performance of the ASBB.[41]

1.3 Solid Electrolytes

There are two main types of solid electrolyte, inorganic (ceramic) and organic (polymer), in this electrochemical review only inorganic electrolytes are evaluated.

1.3.1 An overview on ceramic solid electrolytes

Solid-state ionic conduction dates back to the 19th century when Michael Faraday observed the conduction of ions through silver sulphide (Ag_2S) and lead (II) fluoride (PbF_2), demonstrating the possibility of ion transport through solid materials.[42] The next big development came in the mid-20th century with the discovery of sodium beta-alumina. Its high ionic conductivity enabled the development and production of the first commercial ASSB, namely the Na-S (sodium/sulphur) cell.[43,44] Whilst Na-S batteries have been widely used in stationary energy storage, other solid-state batteries struggled to compete across other sectors. Lithium-ion

batteries with liquid electrolytes became the choice method for electronic energy storage, and Li-based batteries being the dominant leaders for power and energy density.[45] Only recently has the discovery of materials with high lithium ion conductivity enabled advancements in solid-state battery design, bringing solid electrolytes to forefront of electrochemical energy storage.

1.3.2 Solid Electrolyte Properties: Requirements and Classes

The criteria a solid electrolyte is required to meet are laid out below. Subsequently three of the most common classes of solid electrolytes are explored in more detail.

1.3.2.1 Solid Electrolyte Requirements

To be considered as candidate solid electrolyte for use in high performance solid-state batteries, the ideal material must fulfil the following requirements:

- **High ionic conductivity at room temperature.** Common liquid electrolytes have ionic conductivities of ~10^{-2} Scm^{-1}, however their low transference number means this typically corresponds to a Li^+ ion conductivity of a few mS cm^{-1}.[46] Therefore, it is suggested that solid electrolytes require ionic conductivities ideally >10^{-3} Scm^{-1} at room-temperature.[47]
- **Negligible electronic conductivity**. Low electronic conductivity is essential to function of the battery to prevent any unwanted discharge. It is also necessary to help prevent lithium plating within the solid electrolyte and mitigate dendrite growth.[48] An ideal material will have an electronic conductivity six orders of magnitude lower than its ionic conductivity (<10^{-9} Scm^{-1}).
- **Chemically and electrochemically stable against the electrodes.** Chemical and electrochemical stability will prevent degradation at the interface, which will help

mitigate the effects of capacity fade. Of the current high Li^+ ion conductors, few are stable across the entire voltage window, therefore any resultant passivating (SEI) layers must themselves be either very thin or have enough ionic conductivity to ensure low resistance across the interface.[38,49]

- **Good interfacial contact between electrolyte and electrodes.** Good interfacial contact is key to ensure there is a large contact surface area between the electrolyte and electrode through which ionic conduction can occur. Reduction in this contact area can increase the resistance across the interface and effectively increase the local current density.[50,51]
- **Low cost.** In order for the ASSB to be commercially viable and compete with the LIB, not only does processability of the material need to be low cost, but so do the material raw and production costs. Therefore, solid electrolyte compounds with particularly rare earth (high cost) elements should be avoided where possible.[25]
- **High critical current densities.** Lithium dendrite penetration can occur when a cell is operated above a critical current density, which can lead to short circuit failure. To enable charging of lithium metal anodes and practical rates that are competitive with LIB's, solid electrolytes must have critical current densities ideally >5 $mAcm^{-2}$.[52,53]

This thesis goes on to explore, dendrite prevention is directly linked to the mechanical properties of the electrolyte.[54] As the existing LIB model operates in a liquid phase little mechanical investigation has been carried out into batteries; as energy storage field looks towards the ASSB as the next generation battery the existing lack of understanding behind the mechanical processes occurring within the solid electrolyte necessitates the investigation carried out in this thesis.

1.3.2.2 Oxide SEs

Several oxides with fast lithium ion conducting properties have been produced in the past such as LISICONs, Li-NASICONs and perovskites. However, their instability against lithium metal resulted in them not being selected as viable options for an SE.[55] A new garnet-type ceramic solid electrolyte was shown to exhibit even faster lithium ion conduction as well as stability with lithium; these SEs have the general formula $Li_7La_3Zr_2O_{12}$, or commonly referred to as LLZO.[56,57] The stability against lithium implies that degradation at the anode/SE interface should be reduced and a thick SEI mitigated, however in practice there is still evidence of a resistive layer being formed.[58–60] One advantage that oxides hold over their halide and sulphide counterparts is their far superior stability when exposed to air; this would significantly lower the industrial processability cost when handling the SE on a large scale. However, this is offset by the high sintering temperatures required to produce a dense oxide with the required Li^+ ion conductivity. Overall oxides are an important class of solid electrolytes that have breathed new life into the ASSB field, their suitability as the choice SE remains to be determined.[61]

1.3.2.3 Halide SEs

Halide solid electrolytes have recently emerged as a strong alternative to existing oxide and sulphide materials. Lithium halide electrolytes take the general chemical structure of $Li_3M^{3+}Cl_6$, some examples include Li_3InCl_6 and Li_3ScCl_6.[62–64] Halides have garnered interest due to their fast Li^+ ion conductivity and wide electrochemical stability windows, reducing the formation of a resistive degradation layer at the interface.[65] However, two significant challenges face halide solid electrolytes. The first being the high reactivity against lithium metal anodes to form a mixed ionic and electronic conductor (MIEC) interphase layer at the interface, this significantly increases the internal resistance as well as provides an electronic pathway for electric current to escape.[66] The second being very poor stability in the presence of moisture,

meaning that very costly processes would be required to commercially produce halide SEs.[67] Despite halide solid electrolytes not being the perfect candidate for the ASSB, their promising properties are of use in the field and their potential as a composite is explored in this thesis.

1.3.2.4 Sulphide SEs

Sulphide solid electrolytes have been shown to have the fastest Li^+ ion conductivity of all recently discovered electrolytes. They are typically found either as glasses with general structure Li_2S-P_2S_5, or as either thio-LISICON or argyrodite crystalline materials with their general structures being $Li_{10}GeP_2S_{12}$ or Li_6PS_5Cl, respectively.[68–70] Sulphide solid electrolytes demonstrate a sufficiently wide stability window but their biggest advantage is their apparent reasonable mechanical properties. Excellent interfacial contact has been observed at the anode/electrolyte interface allowing fast ion conduction with little/no increased resistance as cycling progresses.[71] Despite this observation of favourable mechanical properties, very little is known about their mechanical properties due to their highly air and moisture sensitive nature. This thesis provides for the first time experimentally determined mechanical properties of these highly air sensitive sulphides. The degradation of sulphides upon exposure to moisture makes processability difficult, however it has been shown that it can be done on a large scale in a commercially viable manner through the use of dry rooms.[72]

When in contact with lithium metal there is evidence to suggest that the sulphides react and form passivating interphase layers (SEIs), however these have been shown to form exceptionally thin passivating layers such that significant capacity fade is avoided.[73] Sulphide SEs have also demonstrated excellent performance against popular composited cathodes, making them the leading electrolyte class for use in an ASSB. The Li_6PS_5Cl electrolyte, (also

referred to as argyrodite), has been shown to be the best candidate for a solid electrolyte and is explored in more detail in the following section.

1.3.2.5 Li_6PS_5Cl Solid Electrolyte

Li_6PS_5Cl is also referred to as argyrodite as it shares the crystal structure of silver germanium sulphide (Ag_8GeS_6) which is more commonly known as argyrodite.[74] The high mobility of Ag^+ ions in Ag_8GeS_6 prompted Deiseroth et al. to synthesise lithium variants, formula Li_6PS_5X (X: Cl, Br, I).[70] The crystal structure of Li_6PS_5X is shown in figure 1.5, the Li-argyrodite takes the unit cell of a cubic polymorph with the X^- anion forming a face-centred cubic (FCC) structure and the tetrahedral and octahedral voids occupied by S^{2-} ions and PS_4^{3-} units respectively.[75]

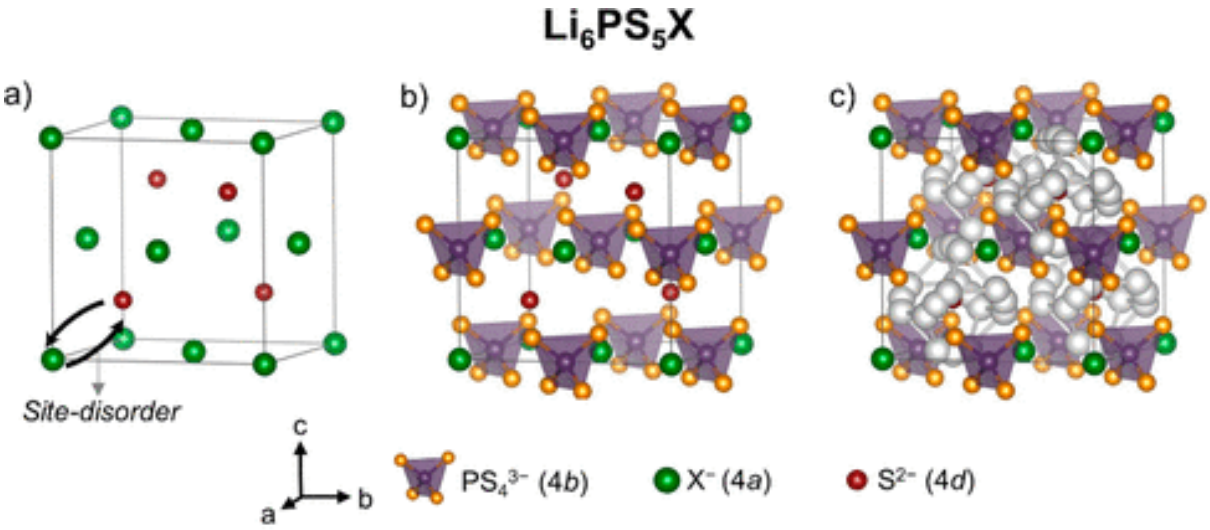

Figure 1.5: Unit cell of the Li_6PS_5X (X = Cl, Br, I) cubic polymorph. In the ordered configuration, a) X^- anions form an fcc structure with S^{2-} ions in half the tetrahedral voids, b) PS_4^{3-} units in the octahedral voids. c) Within this anionic framework, Li^+ sites form cage like structures around the free sulphide positions.[75]

Li_6PS_5Cl is the Li-argyrodite compound of choice because it can be economically mass produced by ball-milling at room temperature and showed high Li^+ ionic conductivity of 10^{-3} Scm^{-1} at room-temperature.[76,77] Li_6PS_5Cl has negligible electronic conductivity of 10^{-9} Scm^{-1},[78] and good electrochemical stability has been reported of up to 7 V vs lithium when using high-

rate cyclic voltammetry (HRCV).[70] However, HRCV is not the best method of measuring stability window principally due to kinetic limitations of the rate of electron transfer and mass transport, as well as the overpotential effects, both symptoms of high scan rates. Other methods such as open circuit cell potential measurements (OCP) reports a stability window value closer to 3 V.[49,79] Li_6PS_5Cl itself is not chemically stable with Li metal; the electrolyte is reduced, forming a thin Li_2S passivating interphase layer, no more than a few tens of nanometres thick, at the interface.[73,80] The Li_2S compounds have been shown to be ionically conducting, meaning a chemically and kinetically stable interface is created, and any further degradation is inhibited.[50] It has been suggested that Li_6PS_5Cl is less brittle than other highly conducting sulphides which would be advantageous, however characterisation is derived from theoretical modelling and the first experimentally measured values are in this thesis.[81] It should be noted that Li_6PS_5Cl is highly air-sensitive, therefore must be processed in an inert atmosphere.[82]

1.4 The Lithium Metal Anode/Solid Electrolyte Interface

The challenges that occur at the anode/electrolyte interface limit the use of lithium metal anodes in solid-state cells, and an exact method by which they arise is yet to be revealed. A better understanding of the mechanisms going on at the interface, specifically concerning Li dendrites and problems due to poor interfacial contact (voiding), is needed to design a successful ASSB. The mechanical properties and processes are pivotal to fully explain the mechanisms, but first the electrochemical side of the challenges occurring at the interface are explored.

1.4.1 Formation of Dendrites

The lithium/solid electrolyte interface is far from ideal: surface flaws on the SE, contaminants in the Li and porosity found in both anode and electrolyte can lead to inhomogeneous plating of lithium and morphological deterioration.[83] This in turn can lead to plating/ingress of lithium into the solid electrolyte, also known as Li dendrite formation, which can lead to short circuit failure. It had been hoped that a physical solid electrolyte would inhibit dendrite formation by mechanical suppression, therefore allowing use of lithium metal anodes. Unfortunately, dendrites have be observed penetrating through a ceramic solid electrolyte when a critical current density (CCD) has been exceeded.[25,84] The Monroe and Newman model, suggested that a solid electrolyte with sufficiently high enough shear modulus, i.e. 2-fold greater than that of Li (4.2 GPa at 298K), would be able to mechanically suppress dendrite formation.[85] However, it has since been shown by multiple groups that Li dendrites are able to penetrate very high shear modulus ceramic solid electrolytes and cause short circuit failure.[25,50,86–93] For example, dendrite formation is seen in LLZO which has a shear modulus of 60 GPa, that far exceeds the estimated ~8.5 GPa limit.[94,95] Several efforts at creating composite solid electrolytes in an attempt to supress dendrite formation have been made; either through doping solid electrolytes or by adding buffer/interlayers between the electrode and electrolyte, however only partial success/improvements have been achieved.[96–99] Other methods include using thin LiPON films to create a flat and amorphous layer on the Li anode to create a uniform Li^+ flux, however this only successful at higher cycling temperatures of > 50ºC.[100]

A key issue is that the method of dendrite initiation and propagation at this point in time is unknown. There are several proposed mechanisms for dendrite formation in the literature, but no consensus as to which is correct, however it is widely accepted that higher current densities

promote dendrite formation.[50] Consequently the prevention of dendrites causing short circuit failure is still the foremost challenge facing realisation of a practical ASSB; this thesis hopes to find its solution by conducting a fundamental materials science investigation.

1.4.1.1 Dry Crack Propagation

A popular mechanism proposes that the growth of a lithium dendrite is due to propagation of a dry crack ahead of dendrite, driven by pressure of a lithium metal flow, through the solid electrolyte. Even 99% dense solid electrolytes will contain defects such as pores and surface cracks and during plating at the interface, some Li will ingress at the defects. This is also known as electrodeposition-induced plastic flow of the electrode metal, the result is lithium metal plating into the pre-existing flaws as shown in figure 1.6.[101] Plating into the solid electrolyte occurs initially at defects found at the anode/solid electrolyte interface because the energy barrier is low, with only the interfacial and surface energies needing to be overcome.[93,102] An enhanced lithium metal flux is experienced at the defects, as they also act as points of uneven interfacial current. Once the flaw is full of lithium, any further Li plated will produce a mechanical response in the form of crack-tip stress. The stress build up at the flaw sites will trigger a stress release mechanism which could take the form of dry crack propagation and/or metal plastic flow, as shown in figure 1.7. If a dry crack penetrates through the solid electrolyte reaching the other electrode, this can provide a path for a lithium dendrite to travel and create a short circuit.

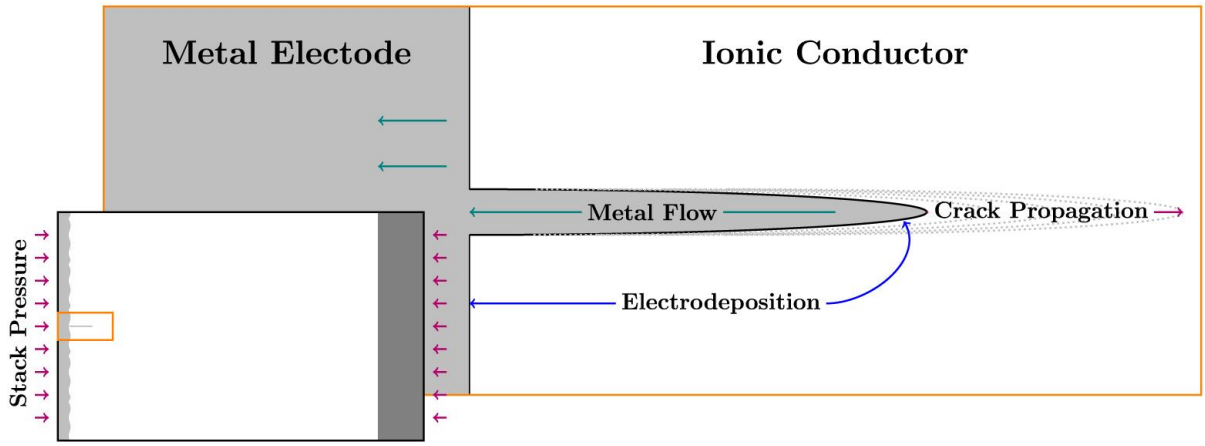

Figure 1.6: Electrodeposition generates local stress, which induces plastic flow of the electrode metal, resulting in lithium metal plating into the pre-existing flaw.[101]

This suggests that dendrite formation depends on the surface morphology of the solid electrolyte, in particular the defect density and size.[93,103] However, for these dry cracks to initiate at the surface very sharp, needle-like surface flaws would be required, these types of defects have not been commonly observed at the SE surface.

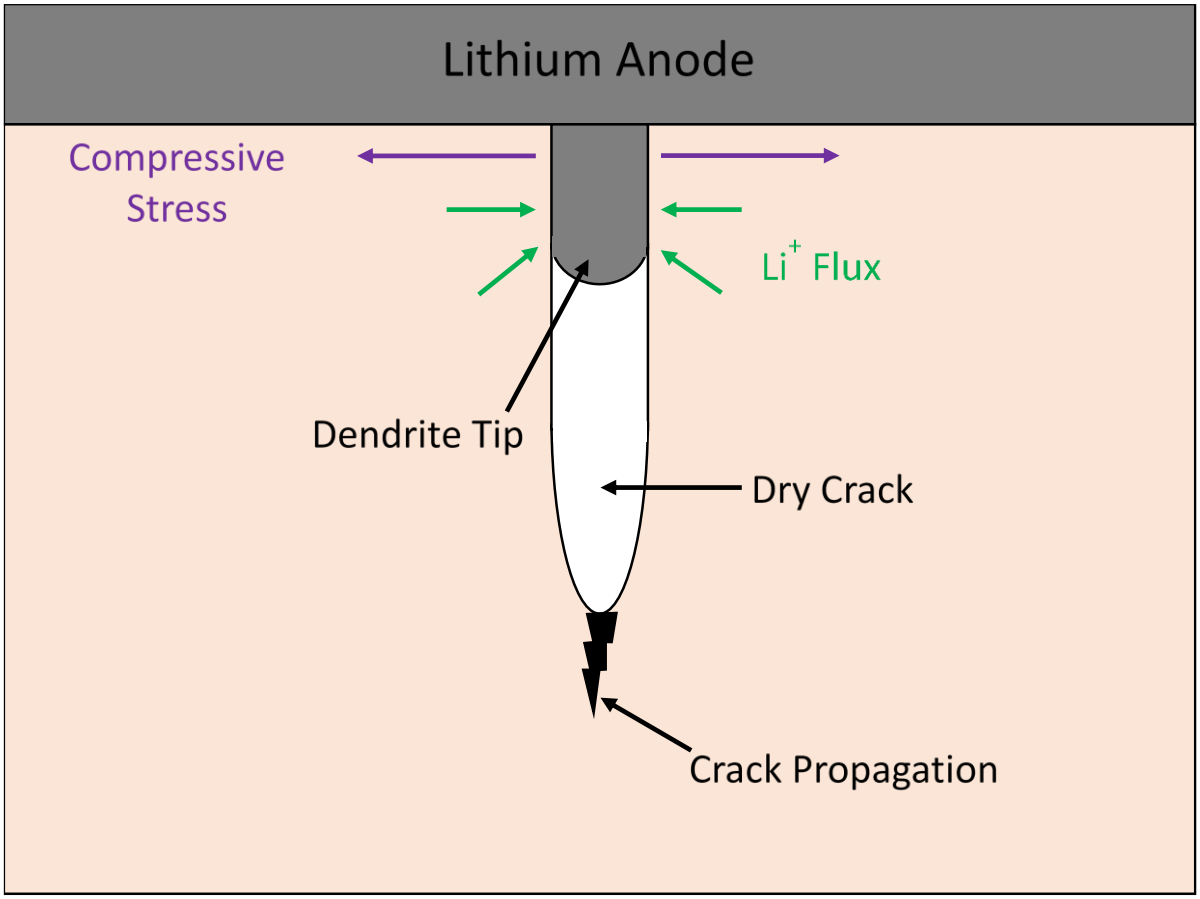

Figure 1.7: Li metal filling a pre-existing flaw, causing a build-up of pressure, driving crack propagation.

1.4.1.2 Grain boundary deposition

Another mechanism is that in a polycrystalline solid (as most solid electrolytes are) lithium preferentially deposits along the grain boundary, creating a lithium filament which results in a short circuit. Work done by E. Cheng et al. showed direct evidence that Li plated intergranularly through the LLZO solid electrolyte, along the grain boundaries. [95] This Li deposition can cause increased stress concentrations at the grain boundaries which can lead to transgranular fracture of the grains, as shown in figure 1.8. Work by M. Nagao et al also showed using *in situ* SEM plated lithium grew along the grain boundaries inside Li_2S-P_2S and then locally generated several cracks.[91] Y. Ren et al. have also shown evidence of lithium penetrating LLZO along grain boundaries and interconnected pores resulting in a short circuit.[104] These results are also supported by the theory of pore interconnectivity proposed by F. Shen et al. Using X-ray

tomography, evidence was found that even though solid electrolyte porosity decreased with increasing temperature, the interconnectivity of the pores increased.[105] Fine porosity is typically found between grain interfaces, i.e. on the grain boundary. High interconnectivity of pores means that it is easier for lithium to ingress into the solid electrolyte along the grain boundaries.[106] This suggests that that lithium dendrite formation depends on the grain boundary density and the interconnected pathway between pores.

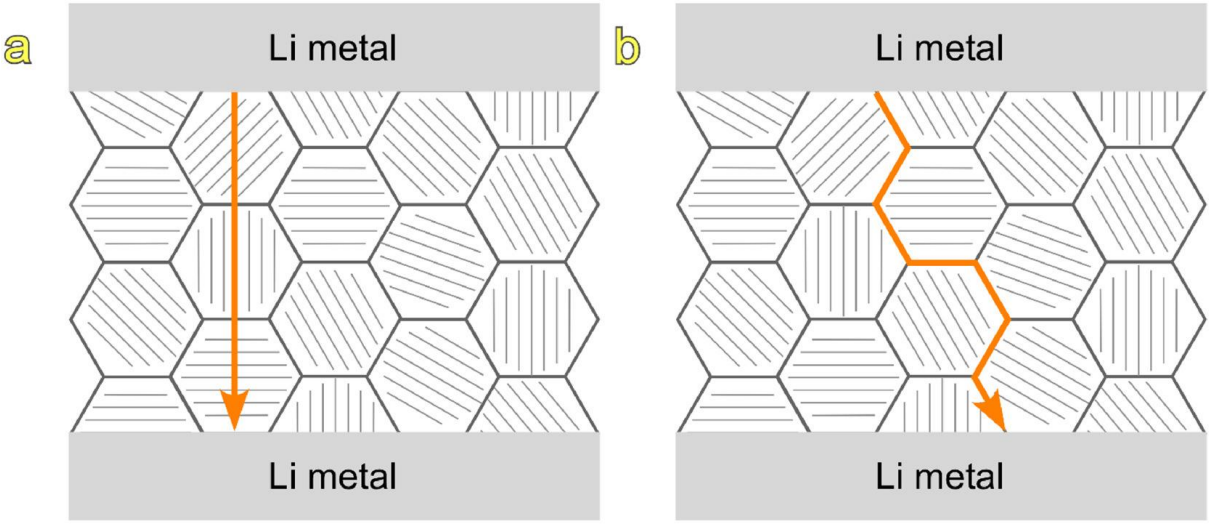

Figure 1.8: Demonstrates the different routes by which Li metal could plate through LLZO solid electrolyte a) transgranular, b) intergranular.[107]

1.4.1.3 Electron Conductivity Tunnelling

A third mechanism suggests that the electronic conductivity of the solid electrolyte allows the formation of dendrites within the electrolyte. Work done by F. Han et al. compared the density, shear modulus, and ionic conductivity of LLZO with LiPON. These properties indicated that LLZO should have a similar if not higher suppression of dendrites than LiPON, however short circuit by dendrite formation still occurred in LLZO at lower current densities. The electronic conductivities were then compared and LLZO has a 3-5 orders of magnitude higher electronic conductivity than LiPON.[48] This mechanism proposes that electrons from the anode material can tunnel into the solid electrolyte, and during plating Li^+ ions are reduced to deposit lithium

metal directly inside the electrolyte, ultimately forming Li dendrites. This suggests that to prevent dendrites, solid electrolyte materials with very low electronic conductivities must be used.

Another study suggests again suggests conduction of electrons results in direct lithium deposition along the grain boundaries. Work by X. Liu et al. suggests that narrow/reduced energy bandgaps of the grain boundaries enables dendrite formation. The research suggests that when the local grain boundary potential exceeds the narrow bandgaps, resistance to electron flow is weakened.[108] Therefore, if leakage current occurs, the grain boundaries act as the electron source resulting in some Li^+ ions receiving electrons at grain boundaries. This then forms isolated lithium deposits inside the grain boundary shown in figure 1.9.

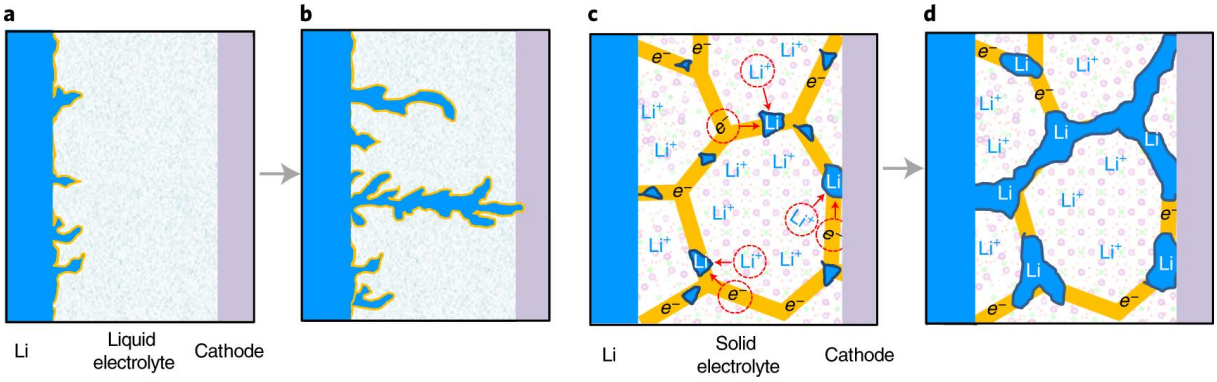

Figure 1.9: a,b) Shows the conventional formation of dendrites and growth through liquid electrolyte. c,d) Shows how dendrite formation inside the SE could be possible through the mechanism of electron tunnelling.[108]

However, given the electronic conductivities of common solid electrolytes, electrons would only be able to tunnel over nm length scales. The current evidence identifies Li deposition at distances greater than is feasible through electron tunnelling, therefore this suggests that electronic conductivity is not the primary mechanism for lithium dendrite formation.

1.4.2 Problem of Voiding

Although the exact mechanism of dendrite growth is unknown, there is a consensus that factors leading to higher current densities at the Li metal anode/solid electrolyte interface, promotes the formation of dendrites. A significant factor that has been shown to increase local current density is poor interfacial contact, leading to a loss of contact surface area. Contact surface area loss can occur due to two reasons: 1) formation of voids at the Li/solid electrolyte interface,[50,109–114] 2) as the battery is cycled, Li^+ ions are moving across the interface, causing a volume change in the electrode.[115] The repeated expansion/contraction makes it difficult to maintain good interfacial contact between two solids.[116]

It has been shown by J. Kasemchainan et al. that there are two critical currents densities to consider that can cause failure in the all-solid-state battery; the critical current density for plating (CCP) and the critical current density for stripping (CCS). By using 3-electrode cells it is possible to separately investigate the processes of plating and stripping, at the metal anode/solid electrolyte interface.[50] Plating is the process that occurs during cell charge, the flux of lithium moves towards the interface. Stripping occurs during discharge of the cell and lithium is removed from the interface.

CCP is the current density at which lithium plated at the interface will ingress into the solid electrolyte, it also known as the critical current density for dendrite formation. If CCP is exceeded, Li filaments will grow through the solid electrolyte, creating a short circuit and failure will occur almost instantaneously.[50] However, there is evidence of failure by dendritic short circuit, occurring even when the cell is cycled below CCP.[51] By considering CCS, this effect can be explained. CCS is defined as “The current density above which the Li is stripped

faster than it is replenished at the Li/solid electrolyte interface",[50] when CCS is exceeded voiding occurs. Void formation occurs when the flux of lithium away from the interface, during stripping is greater than the flux towards it during plating. During stripping a lithium atom from the anode at the interface is ionised, the resulting Li^+ ion flows into the solid electrolyte, leaving behind an electron and a vacant site in the anode. The vacancies in the interface are transported via diffusion away from the interface, and the site is replaced with a new lithium atom. If the flux of Li^+ ions into the SE exceeds the rate at which interfacial vacancies in the lithium metal anode are removed, then voiding occurs. Voiding decreases the interfacial surface area of Li/solid electrolyte (figure 1.10), and increases local current density.

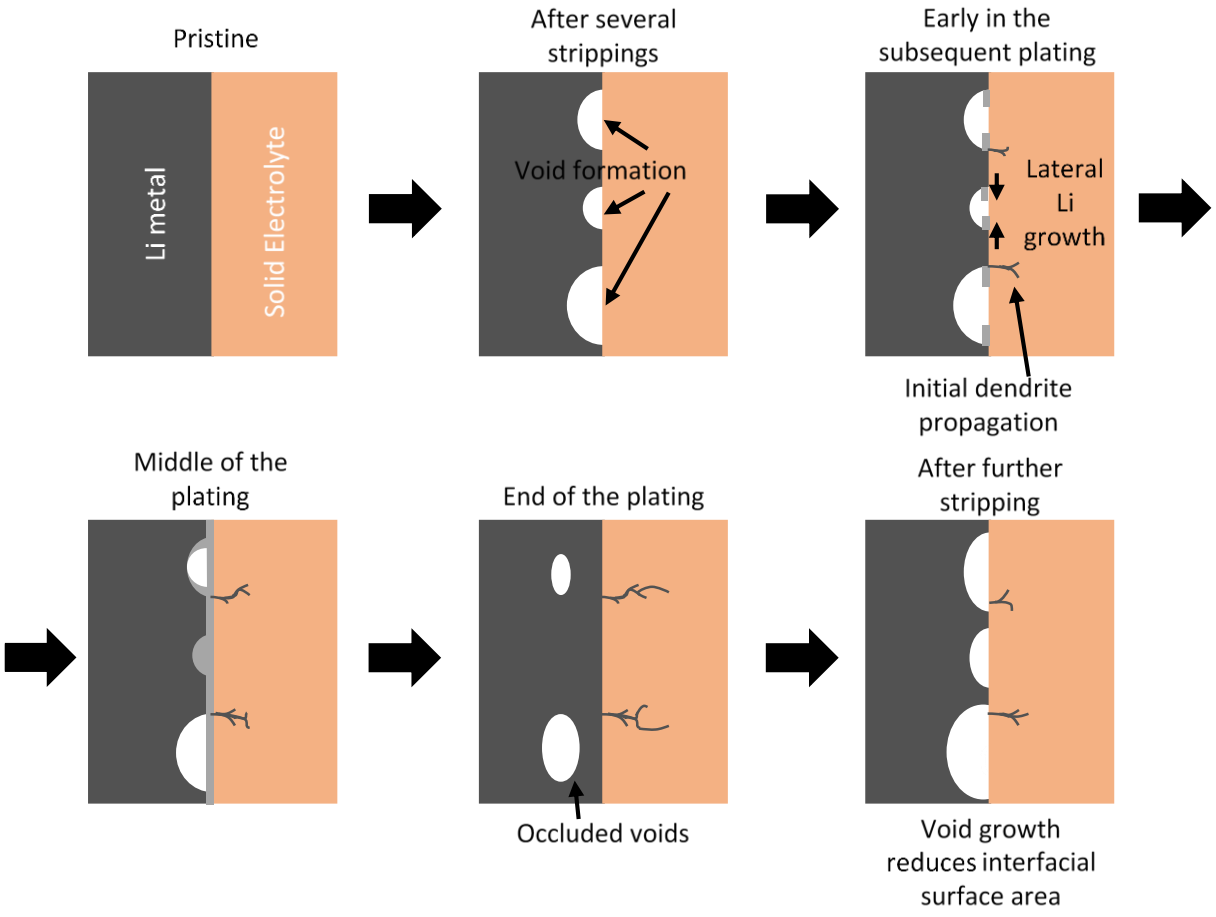

Figure 1.10: stripping and voiding causes a reduction in surface area, ultimately resulting in dendrite formation, when being cycled above CCS adapted from J. Kasemchainan et al.[50]

Below equation 1.1 which links current (*I*), current density (*J*) and surface area (*S.A.*) is shown. This equation shows that for a constant applied current, a decrease in surface area will cause an increase in the local current density:

$$I = S.A. \times J \quad (eqn\ 1.1)$$

The formation of voids causes the current flow through the remaining interfacial contact area to increase, therefore local current density increases. If the local current density exceeds CCP then Li will ingress into the solid electrolyte through the remaining interfacial contact areas causing the formation of dendrites, and therefore failure by short circuit. Therefore, if cycling occurs above CCS, voids will form which leads to failure even though the overall cell is cycled below CCP.

1.5 Mechanics of Batteries

Whilst much has been investigated concerning the electrochemical properties of solid electrolytes, little is known about their mechanical properties. With the LIB battery, the electrolyte was a liquid phase meaning mechanical characterisation was not necessary. The development of the ASSB requires in depth mechanical investigation that as yet has been neglected by the wider energy storage field. A key contributing factor is the highly air-sensitive nature of SEs, which makes mechanical testing of SEs very difficult, and as such the mechanical properties of batteries are not well understood. There has been some more recent progress to unearth the mechanical properties of these material as testing procedures continue to develop. However, there has been no work done on the mechanics-related issues that face the ASSB, specifically surrounding the dendrite formation mechanism. As mentioned previously Li dendrites poses the most serious consequences to failure of the ASSB, is investigated in this thesis. Other mechanically driven failures to consider are cracking and debonding both of which

are affected by the individual mechanical properties of the ASSB components. It is then interesting to consider which mechanical properties of the SEs can be investigated and which will improve our understanding of the ASSB, helping progress its development:

- **Elastic modulus** is an intrinsic material property in general terms it is the material's elastic response (deformation) to an applied external the force.[117] It is usually defined in terms of stress and strain and the specific elastic modulus reported is dependent on how stress and strain are measured; such as Young's modulus, bulk modulus, shear modulus or indentation modulus which is the most commonly referred to modulus in this thesis.
- **Hardness** is a measure of a material's resistance to localised plastic deformation.
- **Fracture toughness** is the ability of a material to resist crack propagation.
- **Fracture stress** is the point on a stress-strain curve where the material physically separates and fractures.
- **Flexural strength** is the maximum stress developed when bending a material just before it breaks or cracks in a bend test.
- **Grain boundary strength** is the fracture strength of the material where the grain boundary is known to be the crack initiating defect.
- **Tensile strength** is the ultimate strength of a material subjected to tensile loading. It is the maximum stress developed in a material in a tensile test.
- **Compressive strength** is the maximum stress a material can sustain when loading under compression. Compressive strength is calculated by dividing the maximum load by the original cross-sectional area of a specimen in a compression test.[118]
- **Fatigue Limit** is maximum level of cyclic applied stress a material can withstand for an infinite number of loading cycles without experience fatigue failure.

1.5.1 Fundamental Solid Electrolyte Mechanical Properties

The major difference between ASSBs and LIBs is the presence of a solid electrolyte. Solid electrolytes are classified as either organic (polymer) and inorganic electrolytes. Within inorganic electrolytes there are several subcategories of SE with the most common being sulphide, oxide and halide SEs.[119] Table 1.1 shows a list of experimentally measured mechanical properties of several SEs. The mechanical measurement was carried out using various types of indentation, however all of these measurements encountered some air exposure, with some being carried out at atmospheric conditions which leads to degradation of the SE and not a true reflection of its mechanical properties.

SE Materials	Modulus (GPa)	Hardness (GPa)	Kc (MPa $m^{1/2}$)
$Li_{1.2}Zr_{1.9}Sr_{0.1}(PO4)_3$ (LZSP)	41	2.2	0.37
$Li_{0.33}La_{0.57}TiO_3$ (LLTO)	200	9.2	~1
$Li_7La_3Zr_2O_{12}$ (LLZO)	150	9.1	0.97–2.37
Al.LLZO	145.6	8.5	1.19
$Li_{1.3}Al_{0.3}Ti_{1.7}(PO_4)_3$ (LATP)	115	7.1	1.10
$Li_2S–P_2S_5$	18.5	1.9	0.23
$Li_{2.9}PO_{3.3}N_{0.5}$ (LIPON)	77	3.9	

Table 1.1: Experimentally determined mechanical properties of SEs.[119]

Table 1.2 shows a list of theoretically calculated mechanical properties of several SEs, including the popular Li_6PS_5Cl solid electrolyte.

SE Materials	Modulus (GPa)
Li_2S-XS (X = Si,Ge)	27.1–31.0
$Li_2S–P_2S_5–P_2O_5$	22.0–27.0
$Li_2O–Li_2S–P_2S_5$	23.3–23.8
$Li_{10}GeP_2S_{12}$ (LGPS)	37.2
Li_6PS_5X (X = Cl, Br, I)	22.1–30.0
Li_3N	150.1–341.3

Table 1.2: Theoretically calculated mechanical properties of SEs.[119]

The data shown in tables 1.1 and 1.2 are the only mechanical properties of SEs found in existing literature; this highlights the need for accurate, experimentally characterised mechanical properties of SEs, using air-sensitive procedures. This thesis provides some much-needed answers and information for this field as well as demonstrating techniques enabling air-sensitive mechanical characterisation.

As mentioned above elastic modulus is a fundamental mechanical property of any given material and a key parameter in materials design and development. It is most generally defined in terms of stress and strain as shown in equation 1.2

$$E = \frac{\sigma}{\varepsilon} \ (eqn\ 1.2)$$

Where E is elastic modulus, σ is stress and ε is strain. Indentation and bulk modulus are defined and calculated specifically for the SEs investigated in this thesis; further detail is given in section 2.6.2. Typically, the modulus is calculated through either tensile tests or indentation (nano/Vickers) tests.[120,121] A theoretical modulus can be calculated from first principles.[122] In table 1.1 the modulus of the oxide SEs has been calculated by using physical indentation tests,

this is possible because oxide SEs are typically more air stable, meaning that they can be tested using conventional techniques without fear of the mechanical properties completely degrading. Although degradation of the oxides is low, reactant surface layers will form as a result of exposure to air, so these results should be viewed with an element of caution and take into consideration the rate of mechanical degradation. The organic SEs are also typically air-stable so can be tested in air. They also are much easier to process than inorganic SEs and as such can easily be made into tension bars, and the modulus can be calculated by undergoing tensile testing.

Sulphide and halide SEs are highly air-sensitive and if exposed to air can react with moisture even at room temperature, causing both mechanical and electrochemical degradation of the material properties. As a result, the mechanical properties of sulphide and halide SEs are relatively unknown and mostly theoretically calculated using first principle law. However, McGrogan et al. developed a method to physically test the sulphide SE, Li_2S-P_2S, by Vickers indentation under inert conditions. The method used is displayed in figure 1.11, it utilises a specialised fluid cell that submerges both the SE and Vickers indenter in mineral oil and the whole indentation test is performed in the oil.[40] Mineral oil is used as it is a fluid medium known to be non-reactive with sulphide SEs. This setup in theory enables the testing of highly air-sensitive materials, however, there are still associated issues such as the presence of the mineral oil will fill the porosity in the SE and will contribute to its elastic response, acting as a compliant medium, effectively reducing the SE stiffness. Therefore, this result should be viewed with a degree of caution and more as an educated estimate rather than an intrinsic material property.

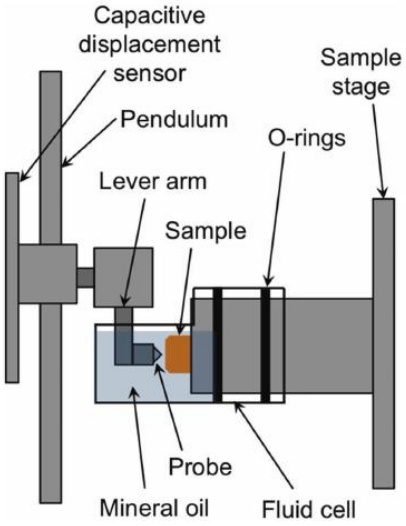

Figure 1.11: Schematic of liquid cell used to immerse the sulphide sample in mineral oil during indentation.[40]

Comparing the elastic moduli of these SEs, the oxides have by far the highest modulus value implying they are the most rigid. This is beneficial for the overall strength of the ASSB but is detrimental for its overall cycling capability. The high stiffness nature of oxide SEs, which can lead to poor interfacial contact and through the issue of voiding (discussed in section 1.4.2) can lead to short circuit failure. Organic SEs have very low elastic moduli which shows they are much more suitable for flexible ASSBs and are likely to form a much more mechanically stable interface. However, its electrochemical properties, in particular its comparatively low ionic conductivity, mean it is not suitable for high energy density applications. Sulphide SEs are a relatively recent development of inorganics SEs and are very promising candidates for the ASSB. Sulphides have been shown to have fast ionic conductivities, even reaching levels of ~10^{-2} Scm^{-1}, and have a moderate stiffness which should result in good interfacial contact.[123]

The two other parameters in table 1.1, Hardness and Fracture Toughness, are material properties relating to the deformation of the SE, therefore physical testing is required. Hardness is a measure of plastic deformation and is typically defined as in equation 1.3.

$$H = \frac{P}{A} \ (eqn\ 1.3)$$

Where H is hardness, P is load and A is deformation area. Fracture toughness describes a materials resistance to fracture and is calculated using the observed crack length after indentation testing. It can be used to directly calculate the stress required for cracks to propagate through the SE. As discussed previously the electrodes can undergo shape or volume changes during cycling that can cause a build-up of stress at the SE interface which can lead to damage/fracture of the SE, the brittle nature of oxide SEs means low crack resistance therefore susceptible to fracture occurring at lower stresses. The soft and ductile nature of organic SEs mean that traditional fracture mechanics are not possible and therefore their fracture properties have not been widely reported. Other ceramic SEs such as sulphides and halides have such high sensitivity to air exposure that it had not previously been possible to measure their fracture properties with existing testing techniques. This thesis demonstrates a novel testing procedure that allows investigation into the fracture mechanics of these solid electrolytes for the first time.

1.5.2 Factors altering the mechanical properties of SEs

There are three main factors that can affect the mechanical performance of inorganic SEs.

1.5.2.1 Microstructure

Many popular inorganic ceramic SEs have a crystalline structure, the mechanical properties of the material can be affected the highly ordered arrangement of atoms, for example the lattice parameter can be used to influence the stiffness of SEs. A smaller lattice parameter usually indicates a higher stiffness, for example Nonemacher et al. showed that doping LLZO with increasing amounts of Ta introduced stronger interatomic bonds, resulting in a reduced overall lattice parameter and an increased elastic modulus.[124,125] Dopant additives are generally touted to improve the mechanical properties and therefore improve electrochemical performance.

However, in the same study by Nonemacher et al. it was shown that the addition of Al to LLZO reduced both the lattice parameter and the modulus. It is thought that the presence of Al reduced the ratio of tetragonal phase by formation of a cubic phase, therefore decreasing stiffness.[125]

The grain size of a material has a significant effect on the plastic deformation properties of SEs, especially for oxides. It has been shown that by hot-pressing LLZO at higher temperatures the grain size can be increased, and the hardness decreased (non-linearly) from 9.9 to 6.3 GPa.[126] Fracture toughness of LLZO is constant for grain sizes above 40 μm, however, as the grain size decreased below this critical value the fracture toughness increased. This is likely because smaller particles have increased grain boundary area therefore increased crack deflection. Grain size can also be altered by introducing a second phase into the SE, e.g. the presence of MgO in LLZTO-MgO increased the homogeneity of the grains, inhibited grain growth thereby reducing grain size which resulted in a higher fracture toughness material.[127] This effect was investigated for sulphides by Singh et al. by varying the particle size in cold pressed Li_6PS_5Cl electrolytes and observing the presence/growth of lithium dendrites.[128] The study showed that there was better surface homogeneity and improved crack deflection was observed, however the porosity of the electrolyte was still very high which as subsequently discussed poses its own challenges.

1.5.2.2 Effect of porosity and other defects

Limiting defects, in particular porosity, can go a long way to mitigating dendrite formation. As discussed previously porosity can act as a defect providing a lower energy barrier for lithium ingress into the SE. Swamy et al. carried out a study using single crystal LLZO (garnet, Ta doped) to investigate its effect on dendrite resistance.[87] A single crystal is considered to be fully dense, free from both internal voids and defects such as grain boundaries. Whilst some improvement in dendrite resistance was observed, it was ultimately limited by the presence of

surface flaws and no notable CCD improvement demonstrated. A different attempt to reduce porosity and defects is the production of glassy electrolytes. Porz et al. developed highly dense glassy LPS, which showed improved resistance to lithium dendrite formation.[93] Later work by Diallo et al. demonstrated that high single plating currents can be achieved in glassy LPS with no lithium dendrite formation.[129] However, this dendrite resistance could not be repeated for cell cycling.[130,131] Another factor to consider is the inherently brittle nature of glasses which makes them much for susceptible cracking and complete brittle failure, as well as increased difficulty during manufacture.[40]

It is also important to consider how the mechanical properties of SEs are affected by porosity. As all inorganic SEs have pores they are never fully densified, therefore theoretical calculations of mechanical properties are likely to be an overestimate of the actual SEs mechanical properties. Cho et al. compared the mechanical properties of LLZO prepared by a sol-gel process and by a solid-state process. Respectively the relative porosities were 5.3% and 1.9%. The solid-state sample had higher modulus and marco hardness (200 GPa, 119 HRB) compared to the sol-gel sample (186 GPa, 93 HRB). However, the trend varied in the opposite way for fracture toughness (1.01 MPa $m^{0.5}$ sol-gel vs 0.72 MPa $m^{0.5}$ solid-state).[132] This is expected as the higher porosity in the sol-gel sample will provide more barriers for crack propagation therefore more crack deflection occurs resulting in more energy absorbed.

1.5.2.3 Composite SEs

A way to improve the SE mechanical properties is to form composite structures. This can be done through many different methods ranging from simply adding inorganic particles to incorporating a fibre matrix.[133–135] It has been shown that incorporating inert inorganic particles into polymer SEs can improve both mechanical and electrochemical performance. F. Croce et

al. use inert particles to create a nanocomposite polymer electrolyte with improved electrochemical performance.[136] The composite SE showed improved ionic conductivity, as despite the non-conductive nature of the inert particles, their addition reduced the SE's crystallinity. Adding inert particles can also improve SE mechanical properties as shown by W. Krawiec et al. The addition of alumina particles to polyethylene oxide (PEO) resulted in increased mechanical stability of the composite SE.[137] The addition of active inorganic particles can make polymer SEs a more viable option by considerably increasing their conductivity. Addition of nanoscale LGPS and LLZO particles can increase the conductivity of PEO by one or or two orders of magnitude.[34,138]

The use of well-dispersed secondary phase particles to improve the mechanical properties of Na-β-alumina by transformation toughening is well documented.[139–144] This was achieved by creating a composite with a dispersion of very fine partially stabilised zirconia particles within the microstructure. The partially stabilised zirconia undergoes a phase transformation under the applied stress of a propagating crack tip which provides a toughening mechanism for the composite. The use of partially stabilised zirconia to provide transformation toughening has become standard practice in ceramic material development, its use to improve the mechanical properties of solid electrolytes are explored in this thesis with and Li_6PS_5Cl composite.

The incorporation of fibre matrix has been shown to significantly increase the mechanical strength of a SE, through toughening mechanisms such as crack deflection and crack-bridging. A composite SE created by electrospinning cellulose/PEO fibres with added GELPEO fibres had improved Elastic modulus than the original PEO SE.[145] Work done by Li et al. shows that a 3D fibre-network of LATP/PAN reinforces a composite PEO SE and again increases its elastic modulus.[146] Using the measurement techniques developed in this thesis, it has been

shown that introducing a glass-microfiber matrix significantly improves the mechanical properties of the sulphide solid electrolyte, β-Li_3PS_4 (LPS).[134]

1.5.3 Electrode Mechanical Properties

Electrode materials can be divided into anode and cathode materials. The role of the anode is to release electrons to the external circuit and positive ions through the electrolyte during discharge. The cathode compliments the anode by receiving the electrons from the external circuit and is reduced by the arriving positive ions. Table 1.3 below shows the mechanical properties of some common electrode materials.

Material	E (GPa)	H (GPa)	Kc (MPa $m^{1/2}$)
$LiCoO_2$	178–191	8.3	0.94
NMC	198	11	
$LiFePO_4$	120.41		
$LiMn_2O_4$	93	8.9	
Si	113	16.6	
Li	4.9	0.6	
In	12.6	1.2	
graphite	6–15	1	0.04–0.05
LiTiO4	181		

Table 1.3: Mechanical properties of electrode materials.[147]

1.5.3.1 Anode Mechanical Properties

As discussed in section 1.2.3 a key aim of the ASSB is to allow the use of lithium metal as the anode material due to its far higher energy density than the existing graphite anodes. As outlined in table 1.3 the elastic modulus of lithium is approximately 1-2 orders of magnitude lower than that of the SEs. This is due to weak interatomic bonding within the lithium which leads to: low modulus, low melting temperature and low activation energy for self-diffusion, which in turn means that Li is highly susceptible to creep at room temperature.[148] A study carried out by Masias et al. showed time-dependent deformation of lithium when under applied pressure, again suggesting the main lithium deformation mechanism is creep.[149] Deformation of lithium

metal can lead to the formation of lithium dendrites (discussed in section 1.4.1) and ultimately the short-circuit of the battery.

1.5.3.2 Cathode Mechanical Properties

Due to the poor interfacial contact between cathode and SEs it is common to find composite cathodes used in ASSBs.[150] Usually a composite cathode will be comprised of active material cathode particles that have a SE coating to increase the contacted surface area between cathode and SE. The mechanical data displayed in table 1.3 is for the pure cathode material and shows that the elastic modulus is greater than most sulphide electrolytes and of the same order of magnitude as most oxide electrolytes. There is little in the literature about how the difference in elastic modulus between the two components affects the elastic modulus of the composite. However, there is consensus that smaller active material particles in the composite cathode is preferred. Smaller active particles increase the total contact area therefore increasing total battery current, they also increase capacity by shortening ion diffusion and charge transportation pathways.[147] They can also help homogenise the distribution of lithium ions and any stress build up due to the associated volume change, therefore helping reduce mechanics related material damage to cathode.[151]

1.5.4 Proposed Solid Electrolyte Failure Mechanisms

Solid electrolyte and the solid electrolyte/electrode interface suffer many different forms of mechanical failure, and the penetration of lithium dendrites the critical limiting factor to production of a successful. In this section several proposed mechanisms for dendrite formation, mitigation and solid electrolyte mechanics are evaluated.

1.5.4.1 Modelling of Lithium Dendrite Mechanics

Lithium dendrites are known to be one of the most severe failure mechanisms in LIBs.[152] The use of SEs in ASSBs cannot completely supress dendrite formation as was previously hoped.[147] Similarly to LIBs, lithium dendrites reduce coulombic efficiency in ASSBs by trapping Li-ions or by causing a short-circuit and catastrophic failure.[153,154] As previously discussed the inhomogeneity of lithium plating at the interface and the associated uneven interfacial currents, cause lithium pile-ups at the interface which results in a local build-up of mechanical stress. Many past models developed to describe the formation of dendrites in LIBs approached the problem from an electrochemical standpoint, overlooking the mechanical effects at the interface. The first model to include a mechanical factor was developed by Barton et al. which considered the surface tension of the anode.[155,156] However, to fully understand the formation of dendrites in ASSBs, the mechanical factors/properties of the SEs and the Li metal must be considered.

A model developed by Monroe et al. predicts the current density stability of deformable interfaces by considering the local strain and interfacial volume changes.[157,158] The model suggests that compressible SEs promote better interfacial stability and SEs with higher Poisson's ratios and elastic modulus have improved dendrite suppression.[147] Natsiavas et al. developed a model that considered pressure assisted diffusion of lithium ions as well as the volume expansion of the intercalated SE.[158] This model confirmed that compressibility of the SE was favourable for good interfacial stability and also showed that dendrite growth can be suppressed, and interfaces stabilised if the SE interface is exposed to a transverse prestress.

Taking a different approach Porz et al. developed an electro-chemo-mechanical model that considered the stress at the tip of a defect and the lithium deposition overpotential, schematic

shown in figure 1.12.[36] When this model is combined with crack propagation fracture law it is possible to relate the defect size and material fracture toughness to the growth of lithium dendrites.

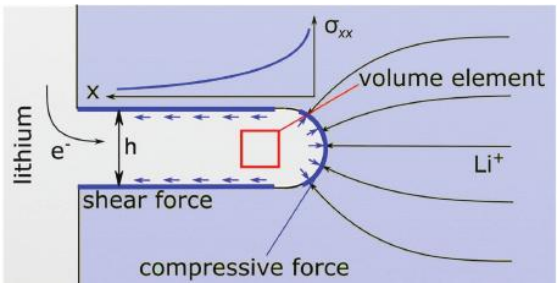

Figure 1.12: Simplified schematic of a Li filament in a SE. The model predicts a maximal stress at the filament tip that decays along the length of the filament from the tip backwards.[36]

A similar model developed by Bucci et al. looks at the effect of surface defects on deposition in consideration with the volume expansion coefficient.[159] The result showed that as crack length increased so did the driving force at the crack tip for lithium plating, and that as hydrostatic pressure increases in the crack the rate of plating decreases.

1.5.4.2 Microstructural Mitigation of Li Dendrites

The above models by Porz et al. and Bucci et al. suggest that primary cause for fracture of the solid electrolyte is presence of defects in the microstructure, particularly at the surface. As discussed previously surface defects provide a lower energy barrier that the lithium dendrite needs to overcome to ingress into the solid electrolyte. Therefore, removal or reduction of microstructural defects in the SE material will aid the suppression of lithium dendrites. It has been shown that failure by short circuit tends to occur earlier in more porous SEs than compared to denser ones.[104] As discussed earlier, porosity and surface defects can lead to the effect of voiding, which is when areas of increased local current density, due to the poor interfacial contact, can initiate lithium dendrite formation.

Creating SE composites is one method to reduce formation of Li dendrites. Porosity exists in inorganic SEs primarily due to the sintering step in the production process. Xu et al. have shown that by introducing additives porosity can be significantly reduced. By adding Li_3PO_4 powder to the electrolyte LLZT, it was possible to significantly decrease both number of defects and ionic resistance.[160] It is shown in figure 1.13a) that the glassy Li_3PO_4 is able to fill the porous gaps in the LLZT. During plating the Li_3PO_4 is transformed to Li_3P, an ionically conducting material, that fills the voids and suppresses Li dendrite growth.

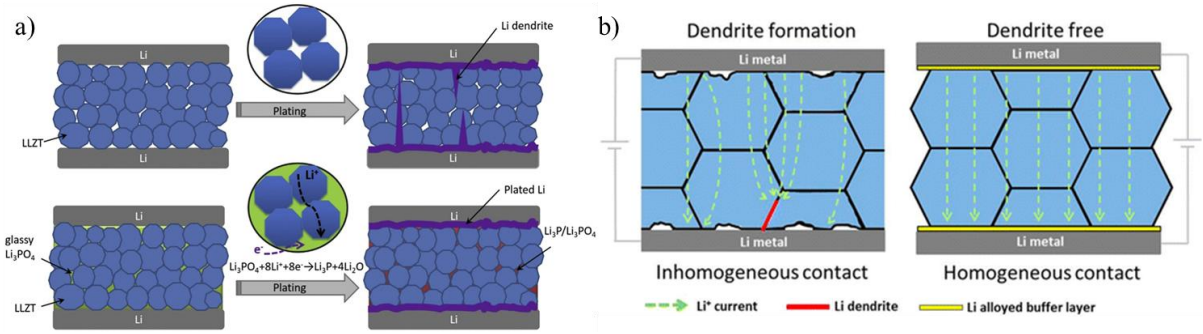

Figure 1.13: a) Schematic showing of the dendrite suppression mechanism of adding Li_3PO_4 to LLZT electrolyte.[160] *b) Demonstrating how a coating layer could improve interfacial contact in ASSBs, therefore improving lithium flux through SE and preventing dendrite formation..*[161]

Another method to supress Li dendrite growth is the use of coating layers on the SE at the interface with the lithium anode. The use of coating layers has been well reported on in the literature with PEO being the most popular for organic coatings;[162,163] for inorganic coatings use of Al_2O_3, ZnO, Ge and Au materials have been reported.[41,161,164,165] There are two primary functions of a coating layer, the first is to homogenise the flux of lithium ions by improving the interfacial contact, as can be seen in figure 1.13b). The second function is to reduce the interfacial resistance of the lithium ion flux by increasing the Li-ion wettability on the SE surface. Coatings allow ASSBs to exhibit better cycling stability and increase Li dendrite suppression.

1.5.4.3 Solid Electrolyte Fracture Mechanics

An alternative theory is that fracture of the solid electrolyte is caused by a stress build up within the SE itself rather than the lithium, resulting in internal crack initiation and subsequently propagation.[147] This internal stress build-up can have several different origins; one mechanism is the associated stress due to volume changes in the composite cathode as the primary cause for ASSB cracking. During cycling the active material particles found in the composite cathode expand and contract which results in volume variation, increasing the shear stress ultimately leading to cracking in cathode active material particles.[116,166] Formation of interphase layers between the anode and SE can lead to solid electrolyte interphase (SEI) induced cracks.[147] During early stages of cycling the SEI formation can help reduce interfacial resistance by filling any micro gaps formed between the anode and SE. However, continued growth of the interphase can trap Li-ions at the SEI, which are then reduced to form Li metal. This can result in a volume expansion at the SEI which generates a build-up of stress causing cracks in the SE.[167] Figure 1.14 is a schematic showing the stress build up at the SEI leading to cracking.

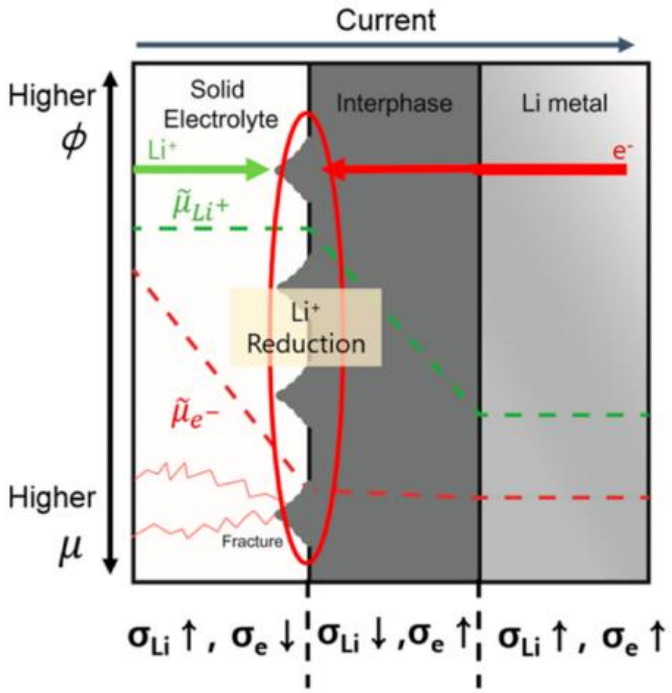

Figure 1.14: Schematic of the SE, the interphase, and Li metal illustrating the chemical potential change for Li ions and electrons during electrochemical reactions.[167]

An alternative mechanism is cracking caused by the thermal residual stresses that have been created during the fabrication process.[168] Volume or lattice changes caused during the fabrication process e.g. during sintering can then lead to stress build up high enough to generate cracks. Finally, environmental factors can also cause cracking. Kobi et al. showed that LLZO that had been stored in inert conditions had good mechanical stability when cycling, however if exposed to air spontaneous cracking occurred.[169]

1.5.4.4 Debonding Mechanics

Debonding refers to a break or physical separation between two phases and therefore failure occurs at the interface. This usually either occurs in the composite cathode if an active material particle becomes isolated,[111,170] or as layer delamination in planar layer ASSBs.[171–173] Debonding causes a decrease in conduction of Li-ions therefore increasing interfacial resistance and a reduction in capacity.[174,175] As mentioned previously during cycling of ASSBs there is a

volume change in the composite cathode, specifically the active material particles, which can result in debonding at the interface. Debonding at the cathode/SE interface can lead to a crack along the interface as well as through the electrolyte itself.[170] Sun et al. showed that in planar layer batteries if local stress exceeds the elastic modulus of the SE, then deformation to the SE is permanent and can initiate micro-voids at the interface.[171] During further cycling these micro-voids can grow and stretch to ultimately result in delamination and debonding. Work done by Su et al. showed that variation in chemical composition may alter the mechanical properties of the components which can then cause debonding to occur.[176] The growth of lithium dendrites can also cause debonding to occur.[147] Using *in-situ* SEM, Dollé et al. were able to show that Li dendrites formed during cycling were able to induce debonding.[154] Figure 1.15 shows that instead of penetrating the SE, if the dendrites grew along the interface this could cause delamination of the anode layer, resulting in loss of contact.

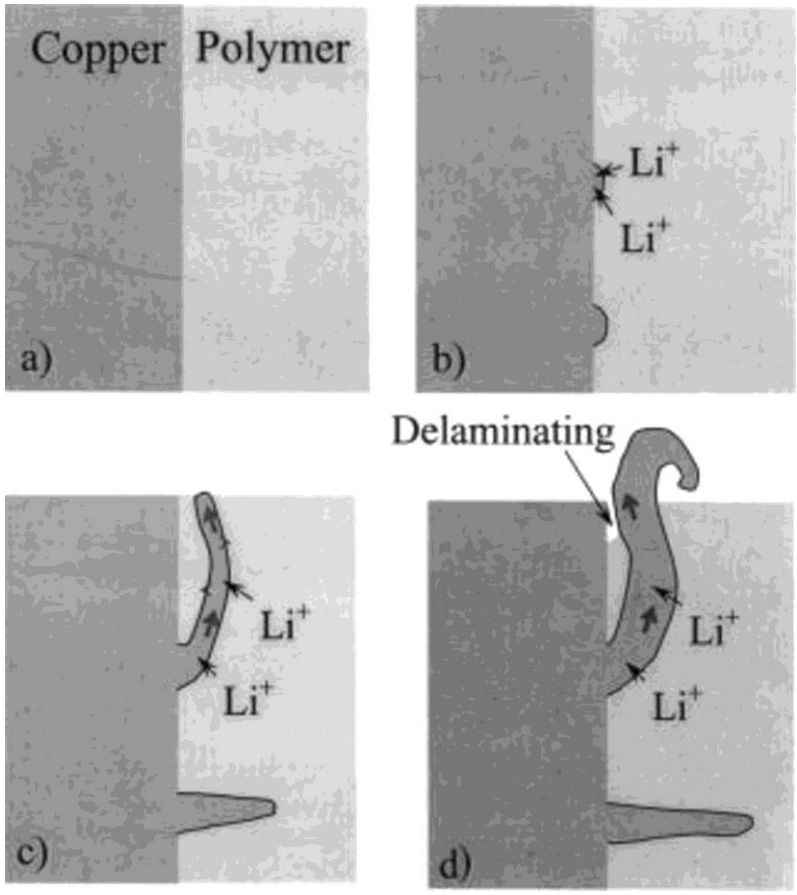

Figure 1.15: Schematic showing the possible mechanisms of debonding induced by dendritic growth.[154]

1.6 Thesis Aims

This chapter has detailed both the need and great potential of the all-solid-state-battery. The ASSB will enable the use of lithium metal anodes making the next generation of batteries both safer and far more energy dense. There are several current issues that hinder progress, with solid electrolyte the primary component linked to many of the difficulties the ASSB faces. One of the biggest problems is short circuit dendritic failure through the solid electrolyte, it is clear that the mechanical properties of the solid electrolyte are the key to solving this issue. The mechanism of how dendrites ingresses and then propagates is also still unknown; the mechanics focused approach demonstrated in this thesis provides a breakthrough answer allowing

significant progress and superior material design choices to be made. As little is known about the mechanical properties of battery materials and the challenges of their high air-sensitivity, this thesis demonstrates both novel testing methods that enable mechanical characterisation of these materials.

In the first experimental chapter the question posed is what techniques can we use to measure the mechanical properties of these highly air-sensitive materials and can they be improved? The chapter discusses the novel methods used to provide the mechanical characterisations of several popular solid electrolytes; it then goes on to suggest how creating composites, using existing low-cost processing routes, may be used to improve the mechanical properties of the solid electrolyte. The following experimental chapter demonstrates a pioneering mechanical testing method that provides the first mechanistic understanding of the dendrite mechanism for initiation and propagation in the solid electrolyte. This then asks the question how can the dendrite resistance of the ASSB be improved? Through mechanical testing carried out in this chapter a new understanding of the mechanical properties of the solid electrolyte was determined; which was used to further improve mechanical properties of the solid electrolyte through both different processing routes and introducing a composite material. The final experimental chapter investigates the issue of ASSB cycle lifetimes, in particular the cyclic fatigue of the solid electrolyte. The successful ASSB will be expected to undergo several 1000s of charge/discharge cycles which means repeated cyclic stresses on the solid electrolyte, for example, through the volume expansion of the SE during plating or through stress concentration build up at surface defects. With solid state literature often reporting the best case electrochemical performances, usually after only one cycle, it is important to consider the effect of several cycles. Using a novel testing procedure an experiment designed to apply cyclic stress

to the solid electrolyte was use to probe the fatigue properties of the material, to better inform the design choices when producing the next generation ASSB.

2. Experimental Techniques

2.1 Aim

This chapter introduces the various different sample preparation methodology, mechanical testing techniques and experimental material characterisation used throughout this thesis. The theory behind each procedure is explained, and consideration is given for how each technique is used or adapted for solid-state battery research.

2.2 Sample Preparation

2.2.1 Cold Pressing

The compaction of powders to manufacture metal and ceramic products is a widely used technique,[177] this is known as cold die compaction, or more commonly as cold pressing. Cold pressing is a room temperature procedure which uses applied pressure to shape material powder into a green compact. The process starts with a measured amount of powder, in this case ceramic powder, loaded into a specific mould cavity of a die set. Once assembled and sealed, the die set is then loaded into a hydraulic press which applies a specified uniaxial load to the die set, and therefore applying pressure to the powder particles. This pressure forces the particles together, reducing the volume occupied by gas between the particles, densifying the powder and forming a green compact. This green compact formed is then removed from the die set, retaining the shape of the die cavity.

The relative density of the green compact depends on several material factors such as particle shape, size,[178] elastic modulus and yield strength.[179] Other factors such as compaction pressure also determine the final density of the compact.[180] The theoretical limit for density of a green compact can be above 90% relative density; however due to the limiting factors described above green compacts typically have relative densities in the range of 60-80%.

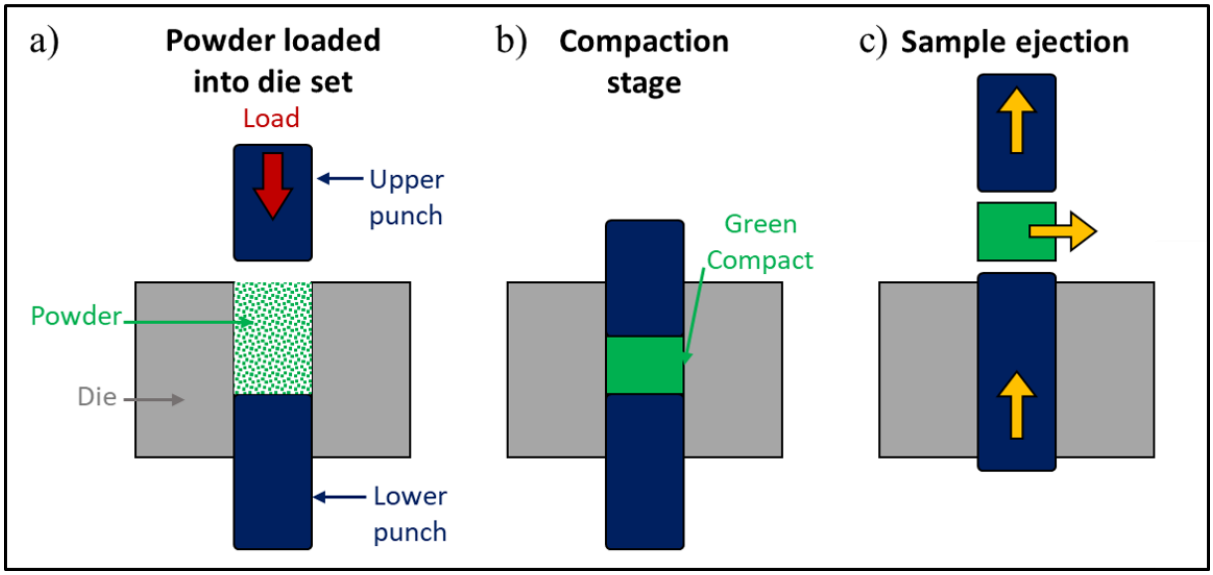

Figure 2.1: A diagram showing the three stages of forming a green compact by cold pressing.

2.2.2 Sintering

Sintering is a heat treatment process that can be used to consolidate powder particles, and is the most widely used method to produce ceramic bodies with higher densities.[181] The temperature of the heat treatment is required to be well below the melting point of the material powder. The process starts with a green compact of the ceramic powder, usually produced through cold pressing as described above in section 2.2.1. The green compact is then heated to a specific temperature, usually around 0.5-0.7 times the melting point of the material, transforming the compacted powder into a dense solid.

The driving force for this transformation stems from the fundamental thermodynamic principle, the reduction of total Gibbs free energy of the system, ΔG. The free energy of the green compact system is comprised of the free energy changes of particle boundaries, ΔG_b, surfaces, ΔG_s, and volume, ΔG_v, as shown in equation 2.1.

$$\Delta G = \Delta G_b + \Delta G_s + \Delta G_v \quad (eqn\ 2.1)$$

During sintering the reduction in overall free energy is dominated by the decrease in surface area of the particles. The individual powder particles have a greater surface energy than that of solidified material, therefore densifying the material will reduce the surface free energies, ΔG_s, thereby decreasing total Gibbs free energy.

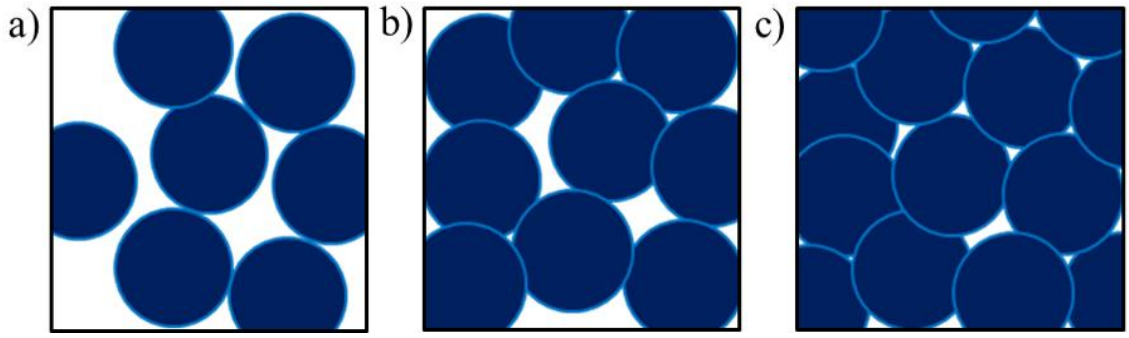

Figure 2.2: The densification of powder particles during sintering. a) Powder particles in a green compact, b) intermediate stage particle re-arrangement, c) final stage particles necking together.

Figure 2.2 shows the stages of sintering. During the heat treatment process solid-diffusion of the particles occurs, this re-arrangement of particles results in points of contact between the particles. Atoms diffuse across the interface between and form interatomic bonds, thereby reducing the interfacial area and decreasing surface energy.[182] At the points of contact between the particles, the material undergoes necking and increases in size due to diffusion. Necking refers to the increased contact area between adjacent powder particles, due to the growth of particles and the formation of bonds between them.[183] This reduces the number and size of pores and reduces surface area energies, shrinking the ceramic body.[181] The higher temperature increases the driving force for densification, however too high temperatures can cause grain

growth which can negatively affect the mechanical properties. Optimisation of the particle shape and size, as well as heating temperature, rates and times can increase the thermodynamic driving force for densification, and therefore producing a consolidated ceramic body for use in an ASSB. Cold pressing was used in this thesis to transform solid electrolyte Li_6PS_5Cl powder into green compacts that could be used for both electrochemical and mechanical testing. Conventional sintering is not used to densify the Li_6PS_5Cl solid electrolyte as it degrades at high temperatures[184];[185] however, there have been promising results for Li_6PS_5Cl densification using hot pressing.

2.2.3 Field Assisted Sintering

Field assisted sintering (FAST), also known as spark plasma sintering (SPS), is a consolidation technique, carried out under low atmospheric pressure, that uses a pioneering variation of hot pressing. Specifically utilising an applied pressure and an electric field to achieve densification of a ceramic body. Similar to hot pressing the heat treatment and uniaxial powder pressing are carried out simultaneously; the key difference being that the heat treatment is performed through electric current pulses, therefore allowing densification to occur at lower temperatures compared to traditional sintering (section 2.2.2).

In traditional sintering the densification mechanism of diffusion and bonding between powder particles is driven by thermal energy. The introduction of an electric field during field assisted sintering causes several different material interactions, therefore other densifications mechanisms:

- Joule heating, generated by the electric current passing through the electrically conductive die and ceramic body means that the powder is heated both internally and externally. This

enables rapid heating of the ceramic body and removes the requirement for external heating, lowering the temperature overall heat treatment process.[186]

- Enhanced diffusion, diffusion of atoms at the points of contact between particles is increased by the electric field, which accelerates the formation of interatomic bonds.[187]
- Plasma effects, at high temperatures the temporary formation of a low-pressure plasma has been observed; which could potentially influence powder particle interactions and further contribute to heating effects, however this specific mechanism is surrounded by controversy.

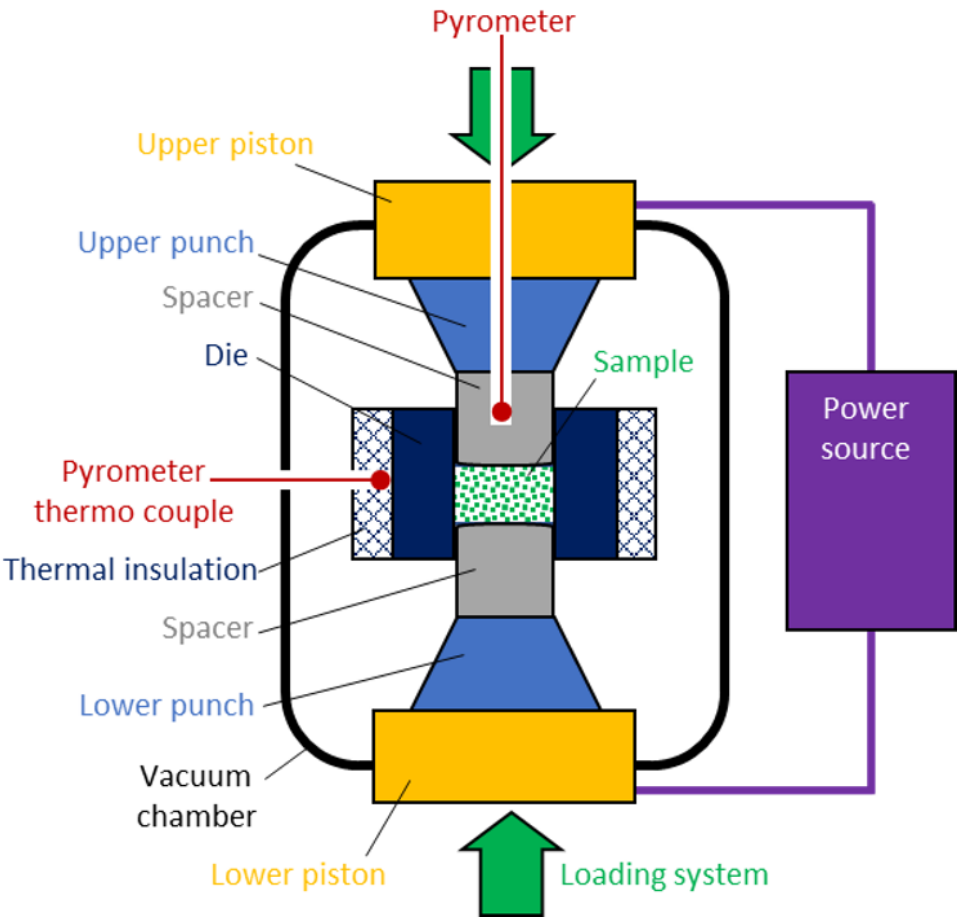

Figure 2.3:Schematic of a field assisted sintering arrangement.[188]

Figure 2.3 shows a schematic of a field assisted sintering arrangement. The material powder is loaded into the die set, graphite dies are typically used due to their good electrical and thermal conductivity as well as their low thermal expansion and being low cost. The die is loaded

between two pistons inside the chamber, the chamber is then placed under vacuum and pressure applied to the die set, through a load applied to the pistons. The power source applies electrical current pulses (100-1000 A) through the die to induce heating, which is monitored by the pyrometer or thermocouples. Field assisted sintering was used in this thesis to transform solid electrolyte powders into densified ceramic bodies at low temperatures to prevent significant degradation of the solid electrolyte materials that occur at high temperatures; for example, grain growth in ceramic electrolytes which can lead to decreases in ionic conductivity or thermal decomposition causing chemical breakdown into less stable components.

2.3 Air-Sensitive Materials Characterisation

The materials used for manufacture of the ASSB, especially those containing lithium are highly air-sensitive; undergoing chemical degradation with even the slightest exposure. As established in the previous chapter, the air-sensitivity of these materials as well as the previous use of a liquid phase LIB, has meant that there is little to no mechanical information on battery materials. Given the need for mechanical characterisation a novel set-up to enable this very difficult mechanical testing was required.

To accurately investigate their properties *in-situ* nanoindentation was carried out in an enclosed Argon system; avoiding the compromises seen in the literature where reported mechanical properties have been either investigated in air or theoretically estimated. An innovative system was developed to allow air-sensitive mechanical testing to be carried out, providing experimentally determined mechanical characterisation of these materials. The system comprises an Argon glovebox combined with a TESCAN Mira 3 SEM and mechanical testing was performed using the Bruker Hysitron PI 89 in-situ nanoindenter, a schematic is shown in

figure 2.4a). More detail on the workings of the SEM, nanoindenter and other necessary techniques is given later in this chapter.

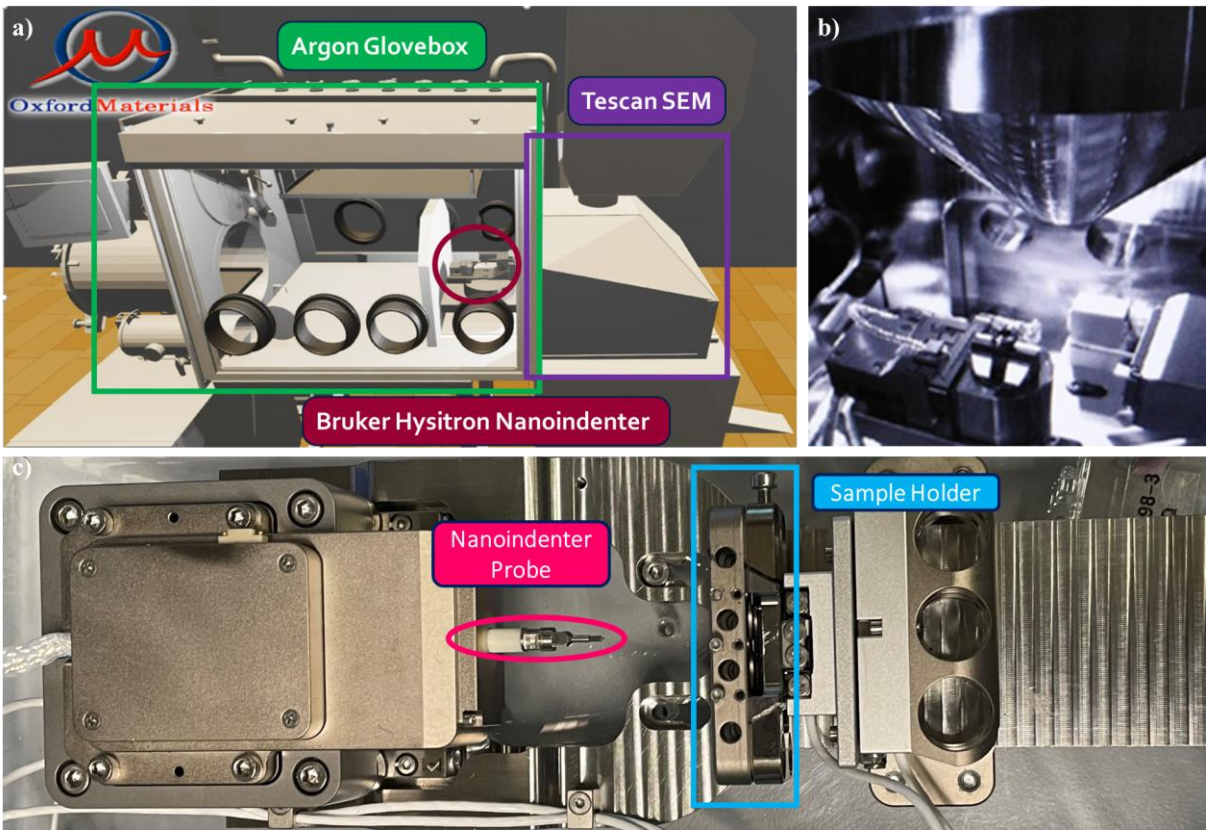

Figure 2.4:a) Schematic depicting the novel air-sensitive mechanical testing set-up, comprising an SEM directly attached to an Ar glovebox, with an in-situ *nanoindenter. b) Image showing the nanoindenter inside the SEM chamber, c) Image detailing the Bruker Hysitron PI 89* in-situ *nanoindenter.*

The Ar glovebox is the same standard as is used for processing and handling of ASSB materials by academia and the wider industry. An SEM is attached to the Ar glovebox, with the SEM chamber door opening directly into the glovebox, this allows the transfer of samples into the microscope to only be exposed to the argon atmosphere of the box and the vacuum of the SEM chamber. The ground-breaking step is the inclusion of an *in-situ* nanoindenter, this allows for samples to be loaded in an argon atmosphere and then indentation is carried out under vacuum inside the SEM chamber (figure 2.4b); therefore, preventing any exposure to air during testing or transfer. There are limitations to the capabilities of the *in-situ* nanoindenter such as load, tip

geometries and testing mechanisms, combined with the often poorly processed solid electrolytes that prevent some traditional nanoindentation techniques from being used. Novel testing procedures were developed in this thesis to investigate the necessary mechanical properties, further details of these methodologies are discussed later in section 2.6.

2.4 Fundamental Microscopy Techniques

2.4.1 Scanning Electron Microscopy

Scanning electron microscopy (SEM) is a microstructural characterisation technique that uses electrons to study the surface structure of bulk specimens. Electrons have very short wavelengths, therefore can enable higher resolving powers than the optical microscopy techniques which are constrained by the diffraction limit of visible light.[189] As a result, electron microscopy techniques are the preferred method to investigate the composition and topography of a material surface, providing high-magnification images.[190] During SEM an electron beam is scanned across a minimally prepared sample surface; the technique allows relatively large areas to be imaged, making it a versatile and popular choice for material characterisation.

Figure 2.5a) shows the schematic for an SEM column. The electron source contains an electron gun which produces electrons through thermionic emission, in the case of TESCAN Mira 3 it is a tungsten source. The generated electrons are then accelerated towards the specimen at voltage between 2–40 kV, under ultra-high vacuum conditions (~10^{10} mbar). A set of condenser lenses are initially used to converge the electrons into a fine beam, forming the initial spot size. Apertures are positioned after the condenser lenses to remove any aberration effects and to additionally control the spot size, so that as the beam hits the specimen the beam diameter is 2–10 nm. Scanning or deflector coils are used to scan the beam across the specimen.[191] The

objective lenses are used to perform the final focus of the beam on the sample surface. Multiple detectors are positioned inside the SEM chamber to record and analyse the different signal types generated. The highest resolution when performing SEM imaging is directly dependent on the set-up configuration used. Whilst using higher electron accelerating voltages and greater beam intensities can improve spatial resolution and increase the electron interaction volume, the higher energy electrons can cause beam damage to the sample, therefore not producing a well resolved image. Therefore, a balance between the greatest depth of field with an achievable final spot size must be reached.[192]

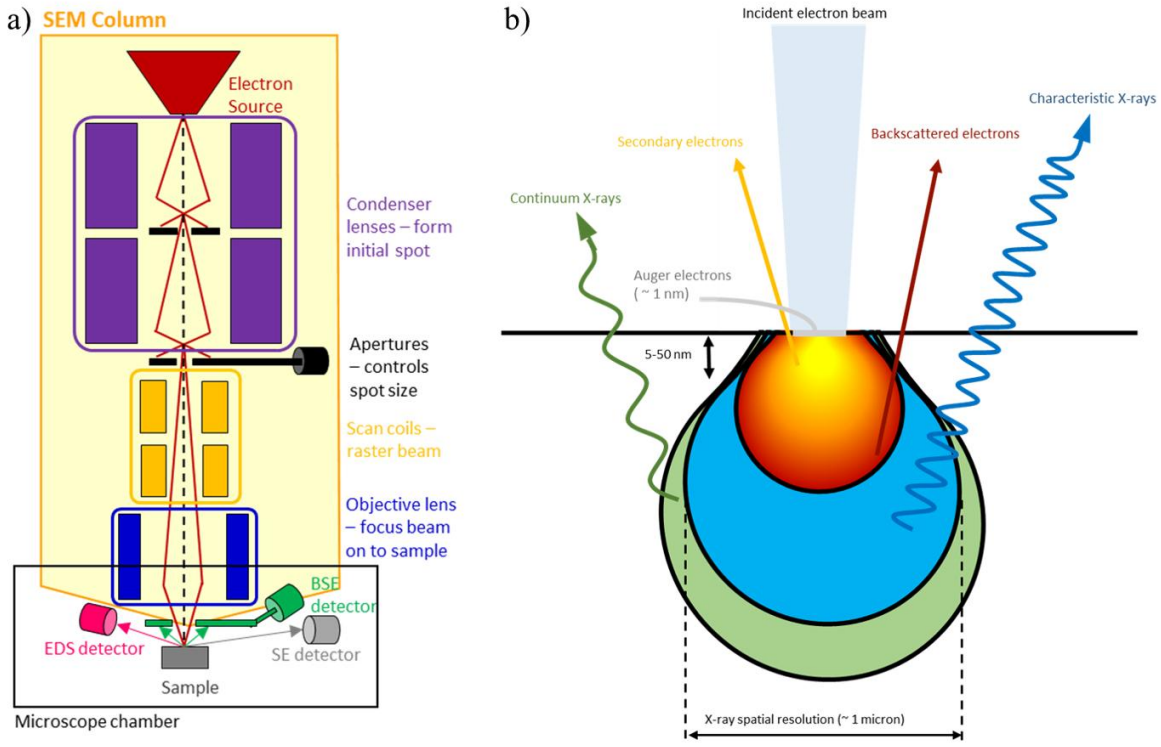

Figure 2.5:a) Schematic showing the key components and detectors of a typical scanning electron microscope. b) Schematic displaying the sample emissions caused by an incident electron beam.

There are various different interactions of the accelerated incident electrons with the sample surface, which generate several different types of signals, shown by the schematic in figure 2.5b). The most commonly emitted electrons are either backscattered electrons (BSE) or secondary electrons (SE), these are capture using their respective detectors (figure 2.5a).

Secondary electrons are low energy electrons, that typically originate within 5-50 nm of the atom surface. They are generated by the inelastic scattering interactions between the incident electron beam and the atom, which releases electrons from the inner atom core.[192] Due to the shallow origin of the secondary electrons, the sample surface orientation, morphology and presence of defects; has a strong effect on the efficiency to which secondary electrons are released. Sharp edges usually result in the highest efficiencies, as such secondary electron images reveal the most information about the surface topography. Backscattered electrons originate from deeper regions ~1-2 μm of the sample. They are incident beam electrons which have interacted with the nuclei of the atoms and as a result been scattered through high angles. The intensity of emitted backscattered electrons is correlated to the atomic number of the elements present, and therefore provide good compositional contrast. The higher the atomic number of the scattering nuclei, the more efficient the scatter of electrons, which are represented by brighter regions in BSE images, therefore providing compositional information.[192]

As discussed during SEM imaging a focused beam of electrons scans the sample surface, typically fewer electrons are released during the various signal emissions from the sample surface than are incident. In a conductive material these excess electrons easily flow through the material and escape through the electrically grounded SEM. For the case of an electronically insulating sample this is not possible, a local negative charge build-up can occur on the surface, leading to image distortion, image drift, and uneven bright spots. A requirement of solid electrolytes is that they are good electronic insulators, which increases the risk of charging during electron imaging. Several effective techniques to prevent the effects of charging include coating the sample with a conductive thin film (e.g., Au, Pt, C) or imaging using lower beam currents (beam intensity) and lower accelerating voltage (beam energy). In this thesis the use of a silver epoxy to affix the samples to SEM pin stubs in combination with low beam currents

and voltages were sufficient to prevent significant charging effects whilst still providing high resolution images. The SEM micrographs in this thesis were primarily produced by secondary electrons, selected as they are low energy electrons (<25 eV), emitted from near the specimen surface and provide high resolution and good topographic contrast.

2.4.2 Focussed Ion Beam

The focused ion beam (FIB) is a powerful microscopy tool that can be used as a precision sectioning tool whilst simultaneously provide high-resolution imaging. A FIB microscope functions according to the same principle as an SEM; a beam of charged particles is scanned across sample, the resultant interaction between incident particle and surface atom produces a signal which is used to form a magnified high-resolution image.[193] The key difference being that FIB typically uses positively charged ions, rather than electrons used in SEM. Typically FIB microscope set-ups will include both a FIB and SEM column that focus on the material, see figure 2.6a). Similarly to SEM, the entire FIB system operates under high vacuum conditions (~ 10^{-7} Pa) enabling a focused and clean interaction with the sample by minimising collisions between any present gas molecules and the ion beam.

The FIB technology typically utilises gallium ions (Ga^+), finely focused into a beam, fired at the sample where the ions interact with the surface atoms. The FIB column contains a Liquid Metal Ion Source (LMIS), which consists of a liquid metal (typically gallium) and an incredible fine needle tip emitter.[194] The suppressor applies a negative voltage relative to the LMIS tip, this forces any neutral Ga atoms or low energy electrons emitted back to the tip, ensuring that only a steady beam of Ga^+ ions are released to the extractor. The suppressor also helps to converge the Ga^+ ions, preventing any premature divergence and initially focuses the beam.

The extractor creates a strong electric field between the LMIS tip and the extractor, by applying positive voltage relative to the tip through a specifically designed electrode. This electric field ionises Ga atoms at the LMIS tip surface, the positively charged field then accelerates the Ga^+ ions towards the extractor.

Similar to an SEM electrostatic lenses, apertures and deflector/scanning coils are also found in the FIB column. The first electrostatic lens is located nearer the LMIS source and extractor, this lens converges the ions into a finely focussed beam. The apertures are located after the condenser lens and only permits the central higher intensity ions to pass through, thereby controlling the beam spot size and controlling the overall beam current. The deflector uses electric fields to manipulate the Ga^+ ion beam, which provides the ability for the raster scanning of the beam across the sample surface. The final electrostatic lens is the objective lens which is the final focussing lens, positioned closer to the sample it allows for the Ga^+ ion beam to be finely focussed onto the target region of the sample.[195]

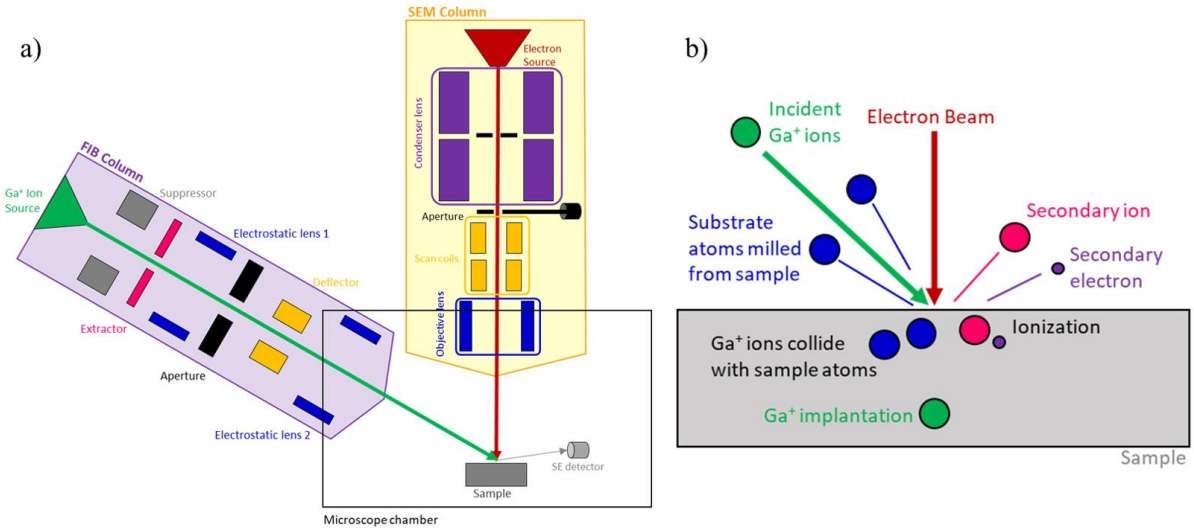

Figure 2.6:a) Schematic showing the workings of a FIB system, b) Diagram demonstrating the interaction between incident ions and sample surface atoms.[196]

The different interactions between the sample surface atoms and Ga^+ ion beam enable different functions of FIB, demonstrated in figure 2.6b). Imaging primarily occurs when the Ga^+ ions are incident on the sample surface they cause the ionisation of atoms.[196] The ejection of a secondary ion from the surface can also release a secondary electron, similar to SEM this secondary electron is collected by a detector and used to for a high-resolution image; images formed this way using FIB have very high depth of field resolution. FIB can also be used for precision sectioning, this is achieved through a process known as milling. Milling is achieved by increasing the Ga^+ ion beam energy and current to precisely sputter (eject) specific surface material. The removal of surface atoms can allow specific patterns to created, enabling the formation of specific microstructures; this technique is extensively used in this thesis to prepare microcantilevers for mechanical testing.

2.4.3 X-ray Computed Tomography

X-ray computed tomography (XCT) is powerful technique which enables non-destructive imaging of complex systems and can create a three-dimensional reconstruction of the internal structure of the material. X-rays enable high spatial resolutions ranging from 10 nm - 10 µm, making XCT an ideal method to image solid-state batteries with key mechanisms occurring at the micron length scale and often at buried interfaces.[197]

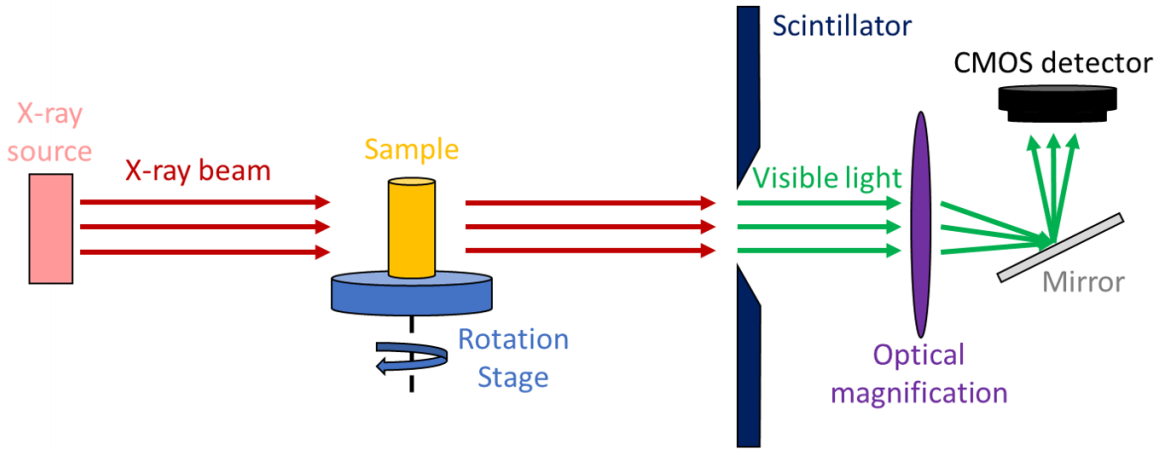

Figure 2.7: Schematic of an XCT system.[197]

An XCT system (figure 2.7) directs a collimated (and usually coherent) beam of X-rays, from an X-ray source, through a sample mounted onto a rotating stage. The X-rays are high energy photons that penetrate through the sample as it undergoes a controlled rotation, enabled by the rotating stage. The transmitted X-rays are collected by a scintillator, where they are converted into visible light. The visible light rays then pass through an optical magnifier, reflected off a mirror where they are collected by a CMOS detector. The XCT process enables a two-dimensional projection to be imaged; by rotating the sample through 180^{o} it is possible for multiple projection images to be collected at increasing incremental angles. Each projection image reveals the X-ray intensity that transmitted through the sample at that specific angle.

The two-dimensional projection images provide virtual sections through the sample, these are fed into a (Fourier-based) algorithm and used to reconstruct a tomogram. Based on the strength of transmitted X-ray signal within each voxel (volumetric pixel), the tomogram provides a three-dimensional representation of the reconstructed volume internal structure[198197]

2.5 Electrochemical Techniques

2.5.1 Potentiostatic Electrochemical Impedance Spectroscopy

Impedance spectroscopy is an electrochemical investigate technique which can explore the physical processes in an electrochemical system in a non-destructive manner. Potentiostatic Electrochemical Impedance Spectroscopy (PEIS) combines Electrochemical Impedance Spectroscopy (EIS) with Potentiostatic Control; which involves applying sinusoidal potentials and measuring the current response over a range of frequencies (figure 2.8a). EIS measures the impedance response of the system to the applied voltage perturbation. The resulting impedance spectrum is able to resolve the contributions of resistance to their respective individual components; a capacitive component (energy storage) and a resistive component (energy loss). Impedance measurements are able to provide valuable insights into processes occurring at the electrode/electrolyte interface (e.g. charge transfer resistance) and within the solid electrolyte itself (e.g. ion migration limitations).[199–201] The Potentiostatic Control simply means that the potential of the working electrode is held constant throughout the EIS measurement, and the current response is measured.

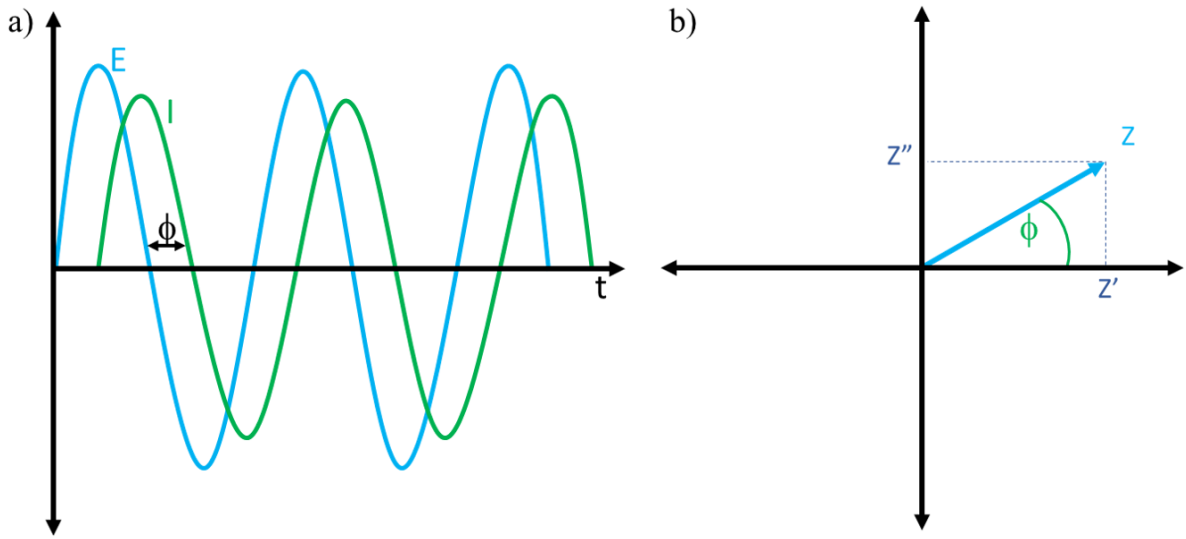

Figure 2.8: a) Relationship between applied voltage (blue curve) and current response (green curve) during an EIS experiment, b) A Nyquist plot showing total impedance, Z, and phase shift, ϕ.

Electrochemical systems can be modelled as a circuit; in all circuit components there is some resistance, *R*, to electrical current flow. Using Ohm's law (eqn 2.2), resistance can be defined in terms of potential, *E* and current, *I*.

$$E = I\,R \quad (eqn\ 2.2)$$

However, this relationship only applies to an ideal resistor, in a DC (direct current) system, most electrochemical systems contain circuit components that are much more complex. Impedance is a measure of a circuit's resistance to current that is not limited to the simplifying properties of Ohmic resistance; therefore, EIS allows for the electrochemical characterisation solid electrolyte interfaces beyond simple resistance.[201] Impedance is defined as the ratio between potential and current for AC (alternating current) systems. Impedance is a complex number defined by two parameters which incorporates both the total impedance (*Z)*, and the phase shift (*ϕ)*. The phase shift is defined as the constant time shift between the periodic waves of the applied potential and resultant current, shown in figure 2.8a). The total impedance is defined as the ratio between the amplitude peaks of the applied potential waveform and the

corresponding amplitude of the current response. Total impedance can also be expressed in terms of real impedance, *Z'* and imaginary impedance, *Z* (figure 2.8b)

For a given frequency, the applied potential can be represented as:

$$E_t = E_0 \sin(\omega t) \quad (eqn\ 2.3)$$

Where E_t is the potential at time *t*, E_0 is the amplitude of the potential, and ω is the radial frequency. The current response can be similarly expressed:

$$I_t = I_0 \sin(\omega t - \mathrm{f}) \quad (eqn\ 2.4)$$

Where I_t is the current at time *t*, I_0 is the amplitude of the current, and ϕ is the phase shift.

Total impedance, *Z*, is expressed below:

$$Z = \frac{E_t}{I_t} = \frac{E_0 \sin(\omega t)}{I_0 \sin(\omega t - f)} = Z_0 \frac{\sin(\omega t)}{\sin(\omega t - f)} \quad (eqn\ 2.5)$$

Using Euler's relation, *Z* can be expressed as:

$$Z = Z_0 \exp(if) = Z_0(\cos f + i \sin f) \quad (eqn\ 2.6)$$

Impedance is represented on a Nyquist Plot by polar coordinates *Z* and ϕ for a complex plane, where $|Z|$ is the magnitude of the vector and ϕ is the angle between the vector and X axis. Each point on a Nyquist Plot is the impedance at one specific frequency.[202] Total impedance can also be expressed in terms of real impedance, *Z'* and imaginary impedance, *Z''*.

A real circuit component will have both resistive and capacitive components, represented on a Nyquist Plot (figure 2.9) by a semicircle, because both responses occur in parallel. For comparison, a pure Ohmic resistor would give a flat line, i.e. no change in response with frequency. The plot contains all contributions to impedance, within the measured frequency range. The Nyquist plot can be resolved into semicircles corresponding to individual component (resistive and capacitive) contributions, by using the angular frequency response was measured

at as each one occurs on different timescales. The real (X-axis) intercept of the semicircles can be used to calculate the resistances. PEIS is used in this thesis to determine the ionic conductivity of the various solid electrolytes used.

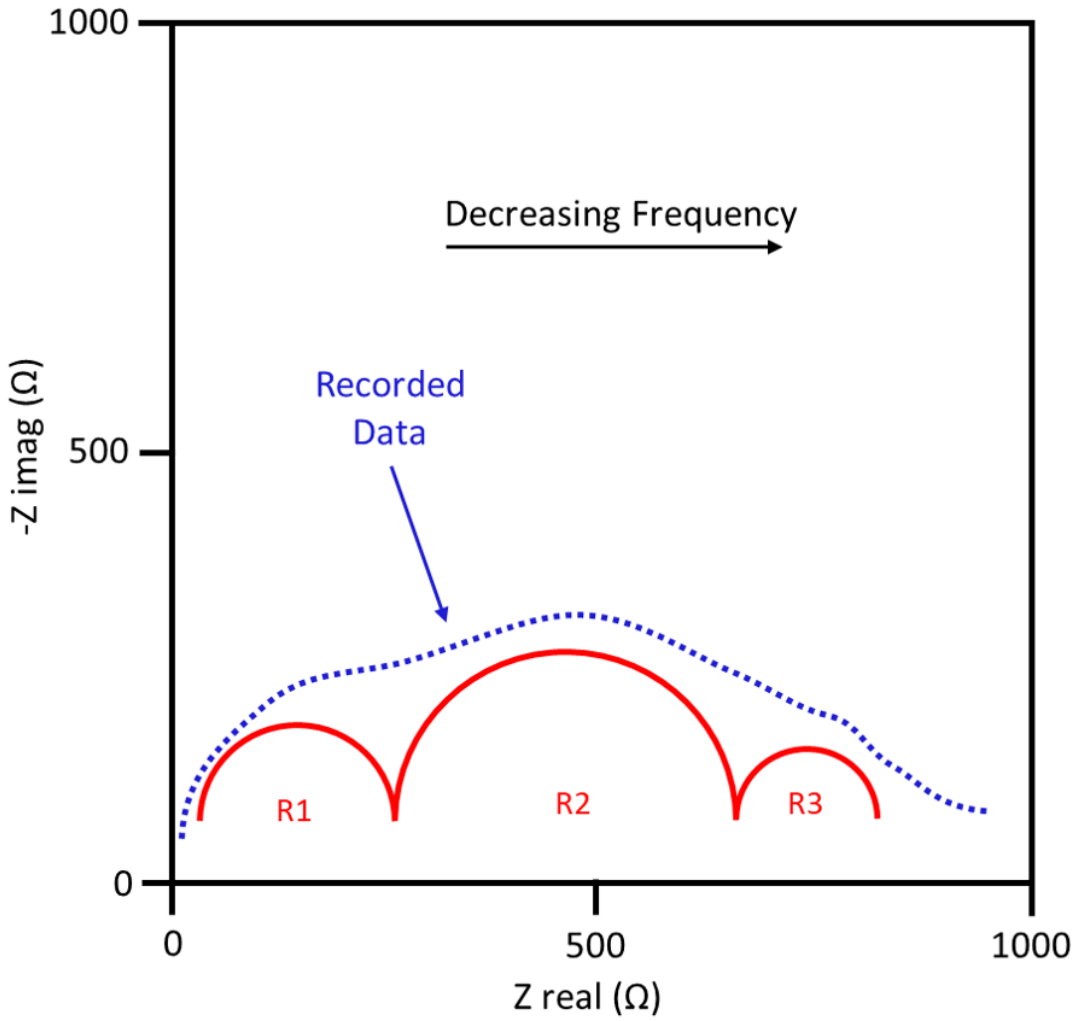

Figure 2.9: Nyquist plot showing resolved impedance semicircles for different components R1, R2, R3.

2.5.2 Galvanostatic Cycling

Galvanostatic cycling is a fundamental technique used to evaluate the electrochemical performance of solid-state cells. Galvanostatic cell testing involves passing a constant current (*I*) such that metal ions travel between the working electrode and counter electrode and

measuring the potential (*V*) relative to the reference electrode, to observe how cell performance and cycle-life changes over time.[198]

Different set-ups that can be used for galvanostatic cell tests, with the two-electrode configuration being the most common. A two-electrode configuration comprises a working electrode (WE) and a counter electrode (CE); the counter electrode also serves to act as the reference electrode (RE) during testing, see figure 2.10a). In all two-electrode cell testing experiments constant current was initially driven from the CE to the WE; during this process the WE is plated whilst the CE is simultaneously stripped. When the half-cycle flips, the current flow reverses direction and plating/stripping of metal swaps to the opposite electrode.[203] By applying a periodically alternating current it is possible to simulate charge and discharge cycles.[204] Using Ohm's law (eqn 2.2), any observed change in potential, provided applied current through the cell is constant, can be interpreted as a change in the internal resistance (*R*) within the cell. The resultant cell potential profiles can offer insight into any electrochemical processes (specifically degradation that occurs during cell cycling) and is used to indicate the cycle life of the cell.[205]

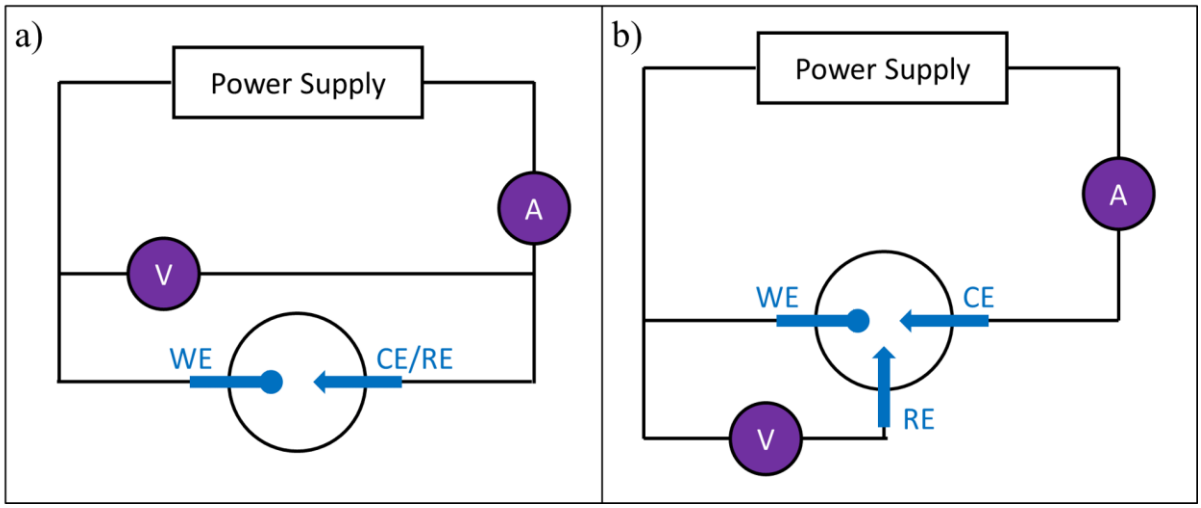

Figure 2.10: Diagrams of a) two-electrode, b) three-electrode configurations used in galvanostatic cell testing.

Throughout the research in this thesis symmetric cells were used in all electrochemical testing. A three-electrode configuration (figure 2.10b) was also used throughout this thesis; primarily for critical current density (CCD) measurements, carried out by galvanostatic rate-test experiments.[206] A three-electrode configuration involves a WE and CE as before, but with the addition of a third separate reference electrode (RE), which is also attached to the electrolyte, on the same side as the CE.[198] During two-electrode cycling the voltage response is recorded across both electrodes, therefore polarisation changes are difficult to isolate to one interface. As with the two-electrode configuration, the applied constant current flows between the WE and CE; with the key difference being the potential is measured between the WE and separate RE. There is no current flow between WE and RE, therefore no plating/stripping occurring at the RE. As a result, its interfacial composition/contact will not change and the RE potential is constant; this effectively allows any observed changes in potential to be isolated to the electrochemical effects occurring at one interface. As the potential response for three-electrode cycling is isolated to one interface, plating occurs as capacity increases (metal flux towards interface), and stripping occurs as capacity decreases (metal flux away). This three-electrode cycling data produces a profile of potential versus capacity for the cell, which can be used to draw conclusions about the electrochemical and mechanical changes at the electrode/solid electrolyte interface.

2.6 Mechanical Testing

There have been very few studies or reviews investigating the physical mechanisms and mechanics of batteries principally due to their highly air-sensitive nature, therefore the mechanical properties of the individual components remain relatively unknown.[207] In this thesis novel investigation techniques based on traditional testing methods are used to help characterise

various battery materials and for the first reveal insights into the failure mechanisms of the solid-state battery.

2.6.1 Four-Point Beam Bending

Macroscale mechanical testing involves evaluating the mechanical properties of materials at a scale visible to the naked eye, typical sample volumes tested are on the scale of 10s mm^3. It is particularly important to consider the mechanical properties of the SE material on the macroscale and these types tests are also key for understanding material behaviour under various loading conditions. Testing larger volumes of material may reveal changes in the mechanical properties that might not be seen at the nano/microscale, such as lower fracture stress caused by an increased number of defects/impurities (generated due to poor processing methods) included by the greater sampling volume.

One common macroscale mechanical test is the four-point bend test, it can be used to determine the flexural strength and elasticity modulus of a material. Four-point bending is a widely used mechanical testing technique, used to investigate the mechanical properties of a material under flexion. A four-point bend test involves a beam that is supported from below by two fixed supports and subjected to an applied load from above by two inner points, and the flexural response is recorded; it is often used to examine brittle ceramic materials susceptible to shear failure. Ceramics traditionally have excellent compressive strength but can suffer brittle fracture due to shear stress, four-point bending specifically probes this mechanical response. Given the use of inorganic ceramic solid electrolytes in this thesis that are inherently brittle in nature[208], and their failure mechanism of cracking; four-point bending is a technique that should yield relevant characterisation of the fracture properties of solid electrolytes. Using a four-point bend test will subject a larger area to maximum stress and therefore, will expose a greater

number and more accurate severity of flaws that which directly affects the flexural strength of the sample.[209]

The test specimens were all prismatic beam-shaped samples made by cold-pressing (section 2.2.1) the material or composite under investigation in a specific beam-shaped die. Figure 2.11a) shows a diagram representing the principle of a four-point bend test, with the actual setup used for testing shown by the figure 2.11b).

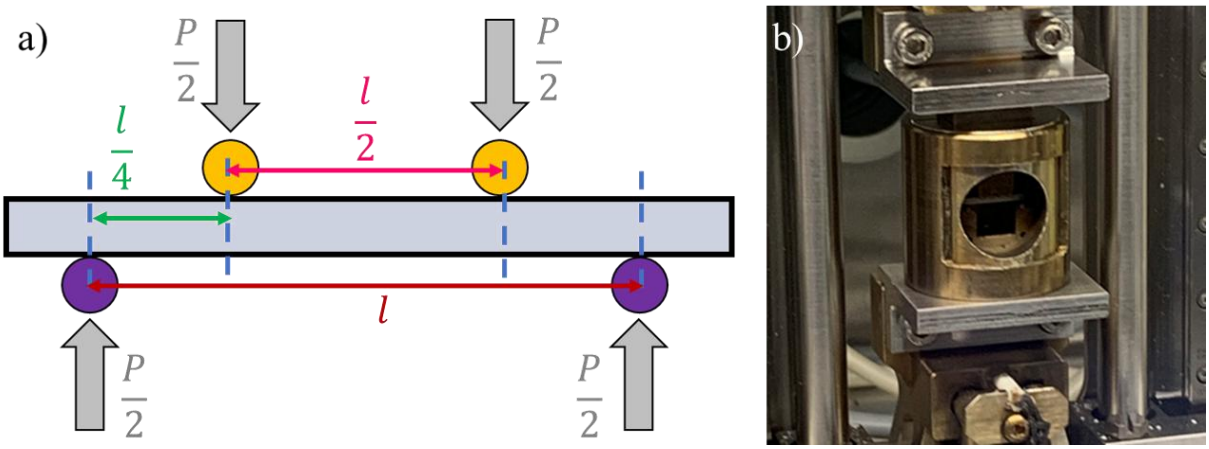

Figure 2.11: a) Diagram to show the principle of a four-point bend test, b) Actual four-point jig used for testing.

Two lower fixed support points (purple circles), are placed at a support span of l apart. The beam specimen is positioned on top of these supports, ensuring the prismatic rectangular cross section is constant across the support span. Two loading points (yellow circles) are position above the sample with a loading span of $l/2$ between them, each one-quarter of the support span ($l/4$) from their respective fixed support points. The loading and fixed support points are typically metal rollers and referred to as top and bottom rollers respectively.

Flexion is applied to the beam by the top and bottom rollers being brought together at a constant displacement rate and the resultant load experienced by the beam recorded. Beam bending theory can relate the applied load (P), bending moment (M), shear force (V), deflection (δ), to

the material properties of the beam. In this thesis the flexural stress applied was of interest, to determine the fracture stress at the point of failure. Failure in a beam bend test of the brittle ceramic solid electrolytes will be caused by fracture due to a crack initiating at the largest flaw present on surface, revealing the stress required for fracture to initiate. To calculate the stress distribution within the beam using equation 2.7; the bending moment (*M*) and beam geometry must known.

$$\sigma = \frac{My}{I} \quad (eqn\ 2.7)$$

Where

- σ is the beam stress
- M is the bending moment acting on the loading span region, between the two loading points. The bending moment for the four-point bend test set-up (figure 2.11a) is defined as applied load ($\frac{P}{2}$) times the length ($\frac{l}{4}$).
- y is distance between the neutral axis of the beam to the point where stress is being calculated, for the rectangular cross-section *y* is simple half the beam thickness ($\frac{d}{2}$).
- I is the moment of inertia of the beam. For a rectangular prism, I is defined as $\frac{bd^3}{12}$.

The four-point bend jig used had rollers positioned in the same ratio as specified in figure 2.11a), therefore the fracture stress of the test specimen could be expressed from the highest recorded load (taken to be the fracture load, *P*) and the known dimensions of the beam sample, using the following equation 2.8:

$$\sigma_f = \frac{3}{4}\frac{Pl}{bd^2} \quad (eqn\ 2.8)$$

Where

- P is the fracture load.
- l is the distance between the outer rollers.

- b is the width of the beam.
- d is the thickness of the beam.

In this thesis four-point bend tests were carried out on cold pressed electrolytes and the above laid out method was used to calculate the flexural fractures stress for each material, also known as flexural strength, to approximate the stress required for a crack to initiate in the as-manufactured solid electrolyte.

2.6.2 Nanoindentation

For a long time, indentation testing has been a fundamental materials science technique used to provide valuable insights into the physical and mechanical properties of materials.[210] Indentation methods such as Brinell, Rockwell, and Vickers hardness tests were developed to assess the macro-scale mechanical properties of bulk materials. Traditional indentation hardness measurements consist of an applied single static load with a quantified tip geometry and material, and a corresponding hold time. The resulting hardness impression is imaged and measured, typically with dimensions on the order of millimetres. Following multiple indentation tests a single indentation hardness value is calculated to represent a measure of the relative indentation tip sample penetration depth.[210] These methods are very effective for characterisation on the macro-scale, demand for testing methods with higher precision and micro/nano-scale measurements propelled the birth of nanoindentation.

Nanoindentation is a useful and commonplace tool used to evaluate the mechanical properties of small volumes of material[211], enabling the mechanical properties of materials to be probed at the nanoscale and without the need for supplementary imaging. It can be used to characterise elastic modulus, hardness, and fracture toughness, amongst other mechanical properties such

as: adhesion, friction, creep, plastic deformation etc. Nanoindentation follows the operating principle used by that of other indentation testing setups; a hard and sharp indenter tip (also known as a probe) that is typically made of diamond and has well-defined symmetric three-sided pyramidal geometry (much sharper than traditional indentation tips); is driven into the surface of the material under a controlled applied load, inducing both elastic and plastic deformation.

The example sequence of a nanoindentation test is depicted by figure 2.12d). Both the vertical displacement and applied load of the tip continuously measured during the indentation test. Through analysis of the load-displacement data it is possible to calculate various mechanical properties of the material.[211] This can be done either from discrete events or from a continuous measurement. As well as nanoscale resolution for mechanical properties characterisation, nanoindentation has several other key advantages such as versatility, it can be applied to a wide range of materials including metals, ceramics, polymers and biological samples, with minimal sample preparation, making it suitable for testing of small or delicate samples.[212] More recently the development of *in-situ* imaging combined with nanoindentation allows for characterisation of other mechanical properties such as fracture toughness, fracture strength; as well as enabling studies of materials under various environmental conditions.[213] These qualities of nanoindentation testing make it possible to conduct mechanical characterisation of air-sensitive samples, under vacuum conditions, enabling the possibility to mechanically test fragile, highly reactive, battery materials.

2.6.2.1 Quasi-Static (Discrete) Loading/Measurement

Quasi-static measurements are the standard technique for nanoindentation tests, typically multiple indentations are carried out at specified locations across the sample surface; when combined with *in-situ* testing it allows for specific areas of the material to be probed. Carrying

out multiple indentation tests at discrete points enables mapping of material properties, meaning it is possible to create characterisation maps of properties such as elastic modulus and hardness to investigate any changes in mechanical properties across the sample, particularly useful for heterogenous materials or composites.[214] Multiple indents provide a more statically significant dataset, producing both a more accurate assessment and reliable results of the material's properties. Fatigue analysis is another very useful technique that is carried out through repeated indentations at the same position on the sample, this can provide valuable insight to the life cycle of a material as it undergoes cyclic stresses throughout its operation.[215] Quasi-static nanoindentation is a load-controlled process, where a transducer applies, holds and removes a load, depicted by the curve in figure 2.12a). The tip displacement is continuously measured throughout the test and used to produce a load-displacement curve like the one depicted in figure 2.12b). In this thesis the Oliver and Pharr method is used to resolve the modulus and hardness of the investigated material, following nanoindentation with a tip of three-sided pyramid geometry.[216]

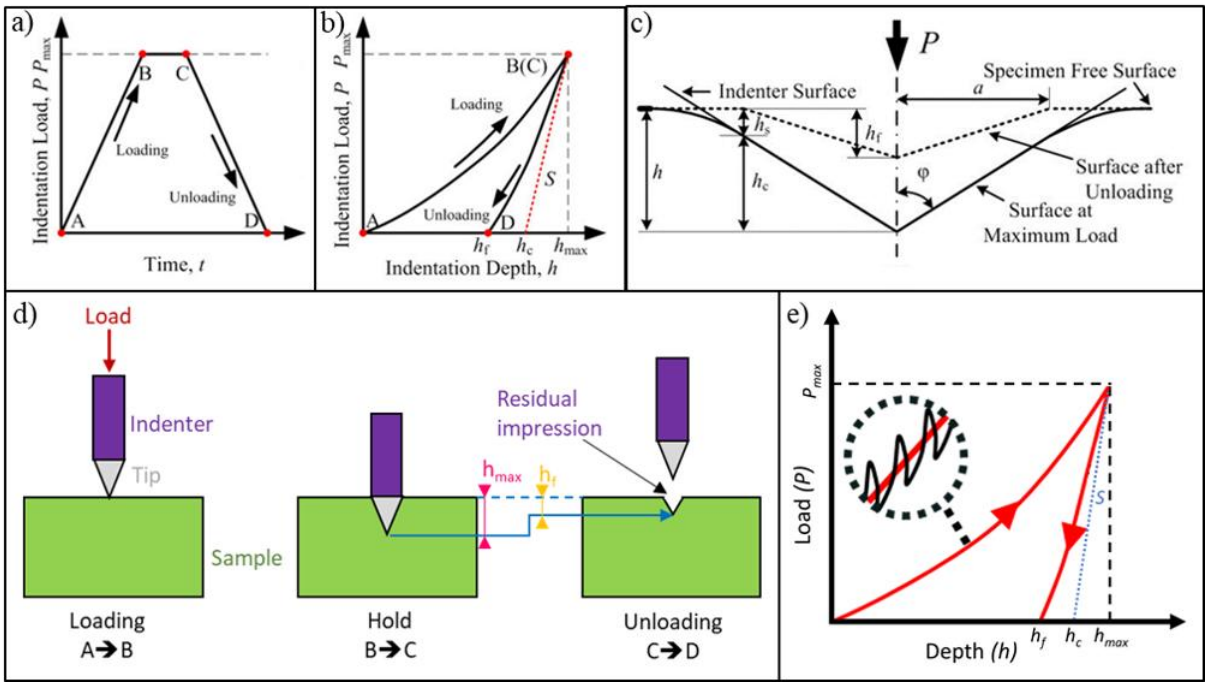

Figure 2.12: a) Typical load-time curve of quasi-static nanoindentation, showing the different load, hold and unload segments,[217] b) Typical load-displacement curve of quasi-static nanoindentation, showing what portions of the curve the different load, hold and unload segments correspond to,[217] c) Diagram to show the physical representation of the parameters used in the properties calculation process,[217] d) Schematic depicting an example of physical movement of the indenter tip during an indentation test, highlighting the elastic and plastic response, e) Typical load-displacement curve of CSM nanoindentation, highlighting the superimposed oscillating load (black curve).

The method of nanoindentation testing and analysis most widely in use today was published by Oliver and Pharr in 1992; establishing a method by which both hardness and elastic modulus could be calculated from the load-displacement data without the need for imaging the indent itself.[216] There are several key steps to the Oliver and Pharr method:

- **Load-displacement curve acquisition.** Achieved through a controlled and recorded nanoindentation test of the sample.
- **Maximum load and depth.** This data is also recorded from the nanoindentation test.
- **Contact depth calculation.** The contact depth (h_c) is determined by analysing the unloading portion of the load-displacement curve, it is the difference between the displacement (h) and the final displacement (h_f).

- **Projected contact area calculation.** The projected contact area (A) between the indenter and the material is calculated using the contact depth (h_c) and the area function of the indenter tip (eqn 2.10).
- **Hardness calculation.** Hardness (H) is calculated as the maximum load (P_{max}) divided by the projected contact area (A) (eqn 2.11).
- **Reduced modulus calculation.** The reduced modulus (E_r) is calculated using the unloading stiffness (S), a geometric constcomant (β) and the contact area (A) (eqn 2.12).
- **Elastic Modulus Calculation:** The material elastic modulus (E) is determined by considering the relationship between the reduced modulus (E_r) and the indenter tip (E_i) (eqn 2.13).[216]

The Oliver and Pharr method assumes the recovery during unloading is only elastic deformation and there are no plastic deformation effects. Therefore, by using the gradient of the initial segment of the unload curve the unloading stiffness could be experimentally measured for the peak indentation load. Then using the depth calculated projected contact area, combined with measured load and stiffness, both elastic modulus and hardness could be calculated. The validity of this method depends on a precisely determined projected contact area, factors such as pile-up or sink could severely affect the accuracy of measured material property. Driven by advancements in the understanding of original model's limitations, in 2002 Oliver and Pharr published an improvement to this method of nanoindentation, also published with better empirical constants.[218] In this improved method the unload curve is initially fitted as a power law curve using equation 2.9:

$$P = \alpha(h - h_f)^m \ (eqn\ 2.9)$$

Where P is load, h is displacement, h_f is final displacement after unloading, α and m are power law fitting constants. Figure 2.12c) shows the surface geometry at maximum indentation loading and after unloading and highlights the parameters of the appropriate contact geometry.

The contact area (A) of the indenter must be known in order to calculate the mechanical properties of the material. For a Berkovich tip, the contact area (A) can be calculated for a known indentation depth by the following geometrical relationship, equation 2.10:[218]

$$A = 3\sqrt{3}{h_c}^2 sin^2\phi = (for\ Berkovich)\ 24.56{h_c}^2 \quad (eqn\ 2.10)$$

Whereby, h_c is defined as the contact depth between the specimen surface and indenter surface (figure 2.12c) and ϕ is the angle of the indenter face. For a Berkovich tip ϕ is specified to be 65.27°.[218]

The indentation hardness (H) of a material can be determined from the load-displacement curve using the following relationship, equation 2.11:[218]

$$H = \frac{P_{max}}{A}\ (eqn\ 2.11)$$

Whereby, P_{max} is defined as the maximum applied load and A is the contact area between the tip and the material surface. For modulus and hardness measurements made throughout this thesis a Berkovich tip, which is of three-sided pyramid geometry, was used.

The elastic modulus (E) can be of a material can be determined from the load-displacement curve using the relationship between the measured unloading stiffness (S) and the contact area (A) set out in the following equation 2.12:[218]

$$S = \beta \frac{2}{\sqrt{\pi}} E_r \sqrt{A}\ (eqn\ 2.12)$$

The elastic unloading stiffness, S (also known as contact stiffness), is the key parameter in calculating elastic modulus. It is defined as the gradient of the from the initial portion of the unloading curve $\left(\frac{\delta P}{\delta h}\right)$, demonstrated by the red dashed line in figure 2.12b), and can be calculated by taking the derivative of the power law curve fitting above (equation 2.9). β is a numerical constant that is typically unity. E_r is the reduced elastic modulus, which is represented by the following relationship, equation 2.13:[218]

$$\frac{1}{E_r} = \frac{1-\nu^2}{E} + \frac{1-\nu_i}{E_i} \ (eqn\ 2.13)$$

Despite the diamond indenter tip being very hard, some elastic displacement may occur in the indenter. The reduced elastic modulus (E_r) effectively takes any indenter elastic displacement into account and allows the material elastic modulus (E) to be resolved using equation 2.13. Whereby, ν is the Poisson's ratio of the tested material and the known indenter properties are represented by E_i and ν_i, the indenter modulus and Poisson's ratio respectively.

In this thesis indents were performed in several distinct locations within each sample, using a varying range of applied loads (1 – 400 mN), this ensured that inherent material properties of the sample were measured, and statistical error due to limitations in surface preparation was reduced. To calculate the unload stiffness the unload segment of the load-displacement curve was initially fit to a power law curve. The gradient was calculated from the upper most points of the fitted power law curve and was taken to be the unload stiffness. The upper portion of the unloading curve is used as this typically represents the linear elastic response of the material.[216] Modulus and hardness results for each test were then calculated using the equations above. All the measured modulus results from a tested sample were then fitted to a normal distribution curve, the mode of this normal distribution was taken (this returns the most expected result and avoids skew from anomalous outliers) as the modulus value for the tested material. The

expected margin of error on the modulus value was calculated using the normal distribution fitting parameters to provide upper and lower bounds for a 95% confidence interval (calculated using a t-distribution of the input data). The hardness value of the material (and expected margin of error) was calculated using this same normal distribution fitting procedure with the measured harness results from all the indentation tests carried out on the sample.

2.6.2.2 Continuous Stiffness Measurement

The traditional technique of nanoindentation, as demonstrated by the Oliver and Pharr method, primarily focuses utilising the upper portion of the unloading section from the load-displacement curve, to extract the mechanical properties of the material. However, during the entire indentation test, valuable information and data can be collected from both the loading and unloading processes. A recent development in nanoindentation techniques is Continuous Stiffness Measurement (CSM), which enables the collection of this valuable information by continuously monitoring the material stiffness throughout the indentation test.

As described in the previous section hardness and elastic modulus can be calculated if the stiffness is known. Through continuous stiffness measurement (CSM), hardness and elastic modulus can be calculated at each point along the load-displacement curve, which allows for continuous profile of mechanical properties as a function of depth.[219] To carry out CSM a small load, oscillating sinusoidally, is applied to the primary load signal. An example load-displacement curve of a CSM test is depicted in figure 2.12e). During a CSM nanoindentation test, as the continuously increasing load is applied to the tip (red curve), a small oscillating load is superimposed on top of the tip (black oscillating curve, superimposed on red curve). The phase and amplitude of the displacement generated by the oscillation is measured at the same frequency. The ratio between displacement amplitude and load amplitude can be used to

calculate the stiffness of any given data point; as with quasi-static tests, the displacement of tip into the material surface is continuously measured. As shown in figure 2.12e), the oscillating load creates a profile with numerous mini unload curves at constant intervals during the overall loading segment. Using equation 2.12, stiffness measurements can be calculated for all the mini unload curves, thereby providing a continuous stiffness profile of the material across the whole load-displacement curve.

Using the Oliver and Pharr method to calculated projected contact area, for continuous measurement of material mechanical properties is possible during the loading cycle for each elastic contact.[216,218–220] This enables modulus and hardness to be calculated as a function of indentation depth, revealing any variations of material mechanical properties with depth of the material. CSM has several advantages with advanced material characterisation the main one, a continuous stiffness profile can provide insights into material microstructure, phase transitions and other material mechanical properties. Other advantages include early detection of plastic deformation, identification of pop-in events, and investigation into strain rate effects.[221] Due to instrument capability limitation, CSM nanoindentation tests in thesis were performed up to a maximum load of 8 mN.

2.6.3 Fracture Toughness by Nanoindentation

Traditionally fracture toughness is often calculated using an initial controlled flaw, however it is possible to calculate fracture toughness by means of inducing controlled cracking through nanoindentation. Indentation is a commonly used technique to investigate the fracture toughness of a material, one such method is a Vickers indentation test,[222] however, traditional

Vickers indentation typically requires large samples and the testing set-up itself is relatively large and therefore not able to be performed under airless conditions.

Nanoindentation fracture toughness testing is a technique used to measure the ability of a material to resist crack propagation, and can be performed by our novel testing system. By driving the indenter tip into the surface of the material, the surface undergoes plastic deformation leaving a residual indent (figure 2.12d). When brittle materials are indented by a sharp indenter, the radial cracks are observed to emanate from the corners of the residual indent. By measurement of the radial crack lengths, in combination with the known applied load and other known material mechanical properties, the fracture toughness of the material can be calculated. There are several key steps involved in this testing technique:

- **Indentation.** A sharp indenter, typically made of diamond, is pressed into the surface of a material under a controlled applied load.
- **Initiation of a crack.** Through specific loading conditions (especially in brittle materials), radial cracks can initiate from the corners of the residual indentation impression.
- **Measurement of the crack length:** High-resolution microscopy techniques, such as scanning electron microscopy (SEM), are used to measure the length of the generated cracks.
- **Calculation of fracture toughness.** Using the measured crack length combined with the applied load and known indenter geometry, fracture toughness can be calculated using empirical relationships.[223–227]

Nanoindentation with a cube corner tip can be performed on smaller samples, under airless conditions using the same principles as traditional indentation fracture toughness. Using a

quasi-static nanoindentation test (section 2.6.2.1) the tip is driven into the sample surface and the resultant radial cracks emanating from the residual indent are measured. A cube corner tip is used as it has a smaller indenter face angle (ϕ), 35.26°, than a Berkovich tip and therefore is a much sharper tip.[226] The sharper cube corner tip allows the indenter to probe a greater displacement for an applied load, this results in a greater displaced volume of material for the same contact area. This increases the likelihood of fracture of the material and induces radial cracks.

A simple relationship derived by Lawn, Evans and Marshall between the radial crack lengths and applied load was used to calculate the fracture toughness of each indent, equation 2.14:[228]

$$K_{1c} = \alpha \left(\frac{E}{H}\right)^{1/2} \left(\frac{P}{c^{3/2}}\right) \ (eqn\ 2.14)$$

Where

- E is the elastic modulus.
- H is the hardness.
- P is the applied load.
- c is the total radial crack length (figure 2.13).
- α is a geometric constant, for a cube corner tip this is determined to be 0.038.[226,228]

The Lawn, Evans and Marshall equation assumes a near-half-penny subsurface crack geometry and is only valid if radial cracking is the primary method of fracture, indents with other fracture mechanisms e.g. chipping, were not used in fracture toughness analysis; however images of these indents were used in qualitative analysis to compare fracture mechanisms and properties of tested materials.[228] Multiple indents were performed on the sample surface, in several distinct regions and over a range of applied loads, to produce as many indents with radial cracking as possible. To further increase the likelihood of inducing radial cracks, higher applied loads were

used (100-400 mN). Post nanoindentation testing, SEM was used to image each indentation site. For those indents that displayed primarily radial cracking, each indent diagonal and each resultant radial crack was measured. These measurements were then used to calculate the average total radial crack length for each indent (see figure 2.13), which in turn was used to calculate a fracture toughness result for that indent according to Lawn, Evans and Marshall relation (equation 2.14).

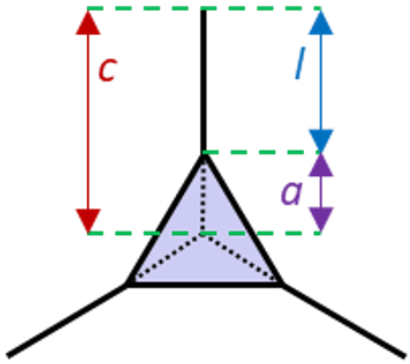

Figure 2.13: Diagram of a residual cube corner indent, the dashed black lines represent the indent diagonals, the emanating solid black lines represent the radial crack, the total radial crack length (c) is the combination of both lengths.

The Lawn, Evans and Marshall relationship was originally developed when using Vickers indentation tests where the loads are of the order 1 N if not higher and are easily high enough to generate radial cracks. To overcome this issue with the typically significantly lower loads use in nanoindentation, a different tip shape is often used. As mentioned a cube-corner tip has three-sided pyramidal geometry, like the commonly used Berkovich, but is much sharper and with a higher aspect ratio. The use of the cube-corner indenter allows the load threshold for cracking to be reduced by 1-2 orders of magnitude.[229] The constant α needs to then be adjusted when using a cube-corner tip and takes a value between 0.032-0.040 for a brittle material.[230]

All the measured fracture toughness results from a tested sample were then fitted to a normal distribution curve, the mode of this distribution was taken as the expected fracture toughness

values modulus value for the tested material. The expected margin of error on the fracture toughness value was calculated using the normal distribution fitting parameters to provide upper and lower bounds for a 90% confidence interval.

2.6.4 Microcantilevers

2.6.4.1 Overview

Microcantilever testing typically involves the use of microscale, flexible beams to measure forces or detect changes in surface properties.[231,232] Microcantilevers are typically manufactured using microfabrication techniques such as focused ion beam (FIB) milling. The use of microcantilevers for mechanical testing was first demonstrated over 30 years ago by Johansson et al. with the mechanical deflection of silicon microcantilevers and by Weihs et al. for testing Au and SiO_2 thin films.[233,234] The procedure involved preparing a very small beam (microcantilever) that was fixed at one end and free standing at the other. These microcantilevers were then mechanically deflected at the free-standing end using a nanoindenter and the load-displacement data was recorded. Using simple beam theory, it is possible to calculate the stress-strain relationship of the material. The deflection procedure and technique has remained the same, however the microcantilevers are now manufactured using FIB milling. As such it is now preferential to use pentagonal microcantilevers for ease of FIB preparation as described by Di Maio and Roberts.[235] Using microcantilevers allows for specific areas/features of the material to be selected from the bulk and mechanically tested.[236] Figure 2.14 shows an example of a pentagonal microcantilever and how beam bending may be achieved by using a nanoindenter to apply the force.

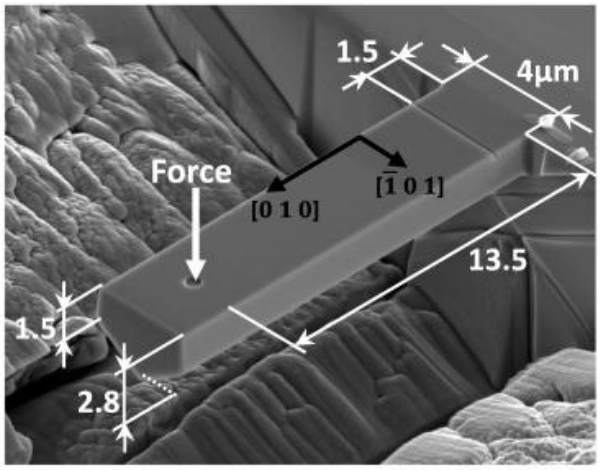

Figure 2.14: Image of a pentagonal microcantilever before testing.[237]

2.6.4.2 Preparation

Microcantilevers are an instrumental feature of various scientific investigative techniques, typically a microcantilever is a microscopic beam with one fixed end. There are several different methods by which they can be manufactured, in this thesis focused ion beam (FIB) milling was used to directly mill the cantilever shape onto the material. For all microcantilever bending experiments, prismatic pentagonal cantilevers with an upper rectangular cross-section were produced, example geometry is shown in figure 2.15. Each cantilever was prepared using the following FIB procedure:

- A high ion beam current of 16 nA was used to mill a U-shaped trench, creating a cantilever large than the desired dimensions (l and w) and a surrounding trench sufficiently wide and deep to permit bending of the cantilever.
- A lower ion beam current of 2 nA was used to cut the cantilever precisely to the desired dimensions (l and w), using a U-shaped trench.
- The sample was then tilted such that the FIB beam would be incident on the sample surface at 45^{o}, a rectangular trench was milled to create an undercut at the desired depth, creating a rectangular cross-section of height, b.

- The sample was then rotated 180°, and another rectangular trench milled at the desired depth (*b*), producing the complementary 45° undercut to form a pentagonal microcantilever with geometry specified by figure 2.15, where *y* is the distance to the neutral plane of the cantilever.

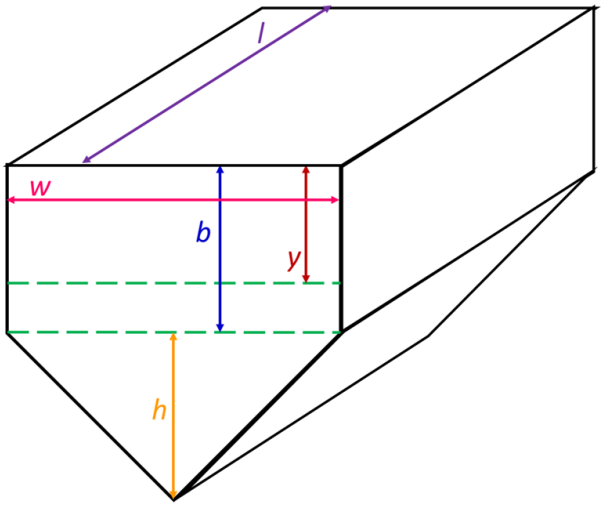

Figure 2.15: A diagram showing the example geometry of a pentagonal micro cantilever.

2.6.4.3 Microcantilever Bending

The milled microcantilevers were then subject to bending tests, a nanoindenter with a cube corner tip was used to perform displacement controlled tests. Two different types of testing were performed on the manufactured micro cantilevers: fracture strength and fatigue. The local fracture strength of a material was investigated using single bend tests on multiple cantilevers; a constantly increasing displacement (rate of 2 nm per second) was applied to the cantilever to induce fracture and mechanical failure, with the necessary applied load continuously measured. The fracture stress results from each cantilever was calculated using equation 2.15, then the mean of all the results was taken to be the value of local fracture strength of the tested solid electrolyte material; the standard deviation was taken to represent the expected error in each fracture strength value.

In fatigue testing the cantilever was subject to cyclic loading, in which the displacement was repeatedly increased and decreased with an R-ratio of 0.5, whilst the necessary applied load was continuously measured. This cycling was repeated until either failure had occurred by fracture, or 1000 cycles had passed without any significant change in the applied load. The fracture point was identified by a significant decrease in measured stiffness of the cantilever, the stiffness was calculated from the measured load-displacement data, specifically upper portion of the unload cycle using the method set out in 2.6.2.1. The measured load and known dimensions of the cantilever were used to calculate the stress on each cantilever using the relationship for stress laid out below.

A relationship for the stress (σ) of a pentagonal microcantilever is given by the following equation, 2.15.[238]

$$\sigma = \frac{PL_c y}{I} \ (eqn\ 2.15)$$

Where

- P is the applied load.
- L_c is the length between the fixed end and position of the indenter tip.
- y is the vertical distance between the upper surface and neutral plane (figure 2.15, red line).
- I is the second moment of area.

The vertical distance between the upper surface and neutral plane (y) for a pentagonal cantilever is determined using equation 2.16.[236]

$$y = \frac{6b^2 + 3bh + h^2}{12b + 3h} \ (eqn\ 2.16)$$

The second moment of area (I) for a pentagonal cantilever is determined using equation 2.17.[236]

$$I = \frac{wb^3}{12} + \left(y - \frac{b}{2}\right) bw + \frac{wh^3}{36} + \left(\frac{h}{3} + b - y\right)^2 \frac{wh}{2} \quad (eqn\ 2.17)$$

SEM images were taken of the cantilever before, during and after testing, and used to measure the actual dimensions of each microcantilever.

3. Mechanical Characterisation of Cold Pressed Solid Electrolyte

3.1 Aim

The success of the ASSB battery is determined by its electrochemical properties which in turn are linked to its mechanical properties. This chapter experimentally characterises the mechanical properties of highly air-sensitive solid electrolytes and suggests how through specific design considerations, better mechanical properties might be achieved; therefore improving the electrochemical properties of the solid electrolyte.

3.2 Introduction

Choosing a solid electrolyte for use in an ASSB thus far has been purely driven by electrochemical performance; this is partly because it is an important characteristic but also because, due to their highly air-sensitive nature, there is very little experimentally measured mechanical properties of solid electrolytes. As a result, there is very little research or agreement in how important the mechanical properties are on the failure mechanisms of ASSBs. Investigating and characterising the mechanical properties of these solid electrolytes will better inform material selection when choosing the best performing solid electrolyte. To achieve this novel testing methods were designed which enabled investigation and experimentation to be conducted without any air exposure and without the need for other buffering materials, e.g. submersed in oil. This allowed for the true, experimentally measured, mechanical properties of air-sensitive solid electrolytes to be reported.

Three different classes of solid electrolytes were investigated to compare their mechanical properties. All the solid electrolytes initially started as powders and were formed into solid discs by cold pressing. Cold pressing is a popular way to prepare solid electrolyte discs from their starting powders because it is easy and cheap method of manufacture that can be easily scaled up.[239,240] Another factor is that many of the highly air-sensitive solid electrolytes investigated also chemically degrade at high temperatures (e.g. above 550 °C for LPSCl),[241] therefore high temperature sintering was not possible. The characterisation of the mechanical properties, combined with knowledge of their electrochemical properties will inform material selection when choosing the best solid electrolyte.

This chapter investigates how the mechanical properties of solid electrolytes are linked to their electrochemical properties, specifically their failure; it has long been thought these are linked but not previously experimentally determined. Electrochemical failures of the solid electrolyte during cycling are often due to a short circuit caused by lithium dendrite penetration, which is preceded by the fracture of the solid electrolyte. Mechanical testing was used to reproduce the fracture seen during electrochemical cycling to investigate the mechanisms behind the observed mechanical effects during failure. This led to an exploration into whether the fracture properties of the solid electrolyte could be improved whilst still using cold pressing as a manufacturing method.

3.3 Experimental

3.3.1 Manufacture of powders for Cold Pressed Samples

All the samples tested were prepared with the help of Bingkun Hu. The starting materials for all samples were prepared as follows:

- Li_6PS_5Cl (LPSCl or Argyrodite) samples were made using Li_6PS_5Cl solid electrolyte powder that was purchased from *MSE Supplies*.
- LGPS samples were made using $Li_{10}GeP_2S_{12}$ solid electrolyte powder that was purchased from *MSE Supplies*.
- LSC samples were made from Li_3ScCl_6 solid electrolyte powder. The powder was made by mixing LiCl and $ScCl_3$, purchased from Sigma-Aldrich, in a 3:1 molar ratio using pestle and mortar. The mixture was then sintered, under vacuum ($<10^{-5}$ mbar), for 12 hours at 650 °C with a heating/cooling rate of 2 °C min^{-1}. Post sintering the powder mixture was ground, inside an Ar-filled glovebox, using pestle and mortar to achieve a fine particle size (~1 μm).
- β-LPS samples were made from Li_3PS_4 solid electrolyte powder. The powder was made by mixing Li_2S and P_2S_5, purchased from Sigma-Aldrich, in a 3:1 molar ratio using planetary ball milling at 550 rpm for 7 hours. Inside an Ar-filled glovebox, the mixed powders were pressed into discs under 400 MPa, then heated at 400 °C for 15 min (with a heating rate of 10 °C min^{-1}), followed by quenching in the glovebox atmosphere. Post sintering the discs were ground using pestle and mortar to achieve a fine particle size (~1 μm).
- LAC samples were made from $LiAlCl_4$ solid electrolyte powder. The powder was made by mixing LiCl and $AlCl_3$, purchased from Sigma-Aldrich, in a 1:1 molar ratio using

pestle and mortar. The powder mixture was then ground by mechanical ball milling for 24 hours, inside an Ar-filled glovebox, to achieve a fine particle size (~1 μm).[242]

- LIC samples were made from Li_3InCl_6 solid electrolyte powder. The powder was made by mixing LiCl and $ScCl_3$, purchased from Sigma-Aldrich, in a 3:1 molar ratio using pestle and mortar. The mixture was then sintered, under vacuum ($<10^{-5}$ mbar), for 5 hours at 260 °C with a heating/cooling rate of 2 °C min^{-1}. Post sintering the powder mixture was ground, inside an Ar-filled glovebox, using mechanical ball milling to achieve a fine particle size (~1 μm).[243,244]

3.3.2 Pressing of Cold Pressed samples

All preparation and pressing procedures were performed inside an Ar-filled glovebox (O_2 and H_2O levels < 1 ppm). To prepare the monolithic samples for indentation testing, 40 mg of each respective solid electrolyte powder (Li_6PS_5Cl, LGPS, β-LPS, LAC, LIC, LSC), was loaded into a stainless-steel die set, 5 mm in diameter, and pressed into a disc under a uniaxial pressure of 400 MPa.

To prepare the monolithic beam samples for 4-point bend testing, 40 mg of each respective solid electrolyte powder (Li_6PS_5Cl, LGPS, β-LPS, LSC), was loaded into a custom designed beam shaped stainless-steel die set, with a rectangular testing cross-section of dimensions 11 x 2 mm, and pressed into a beam under a uniaxial pressure of 400 MPa.

To prepare the bi-layer beam samples for 4-point bend testing, a 30 mg base layer of each respective solid electrolyte powder (LGPS, β-LPS, LSC), was loaded into a custom designed beam shaped stainless-steel die set, with a rectangular testing cross-section of dimensions 11 x

2 mm, and pressed by hand (low compaction pressure). Then 10 mg of Li_6PS_5Cl was loaded into the die set on top of the base layer, and then pressed into a bi-layer beam under a uniaxial pressure of 400 MPa. The specific 1:3 loading ratio was used to ensure that the interface between the two solid electrolytes was away from the neutral axis of the beam and tested under compression, in the top half of the beam sample.

To prepare the 3-layer beam samples for 4-point bend testing, a 13.3 mg base layer of Li_6PS_5Cl, was loaded into a custom designed beam shaped stainless-steel die set, with a rectangular testing cross-section of dimensions 11 x 2 mm, and pressed by hand (low compaction pressure). Then 13.3 mg inner layer of LGPS was loaded into the die set on top of the base layer, and pressed by hand. A 13.3 mg top layer of Li_6PS_5Cl was loaded into the die set, and all three layers then pressed into a tri-layer beam under a uniaxial pressure of 400 MPa.

To prepare the 5-layer beam samples for 4-point bend testing, a 10 mg base layer of Li_6PS_5Cl, was loaded into a custom designed beam shaped stainless-steel die set, with a rectangular testing cross-section of dimensions 11 x 2 mm, and pressed by hand (low compaction pressure). A 10 mg inner layer of LGPS was then loaded into the die set on top of the base layer, and pressed by hand. Followed by a 10 mg inner layer of Li_6PS_5Cl, loaded into the die, and pressed by hand. Followed by another 10 mg inner layer of LGPS, loaded into the die, and pressed by hand. Finally, a 10 mg top layer of Li_6PS_5Cl was loaded into the die set, and all five layers then pressed into a pent-layer beam under a uniaxial pressure of 400 MPa.

3.3.3 Preparation of Cold Pressed Samples for Indentation

All the cold pressed monolithic samples were prepared using the following method. All the different samples were approximately disc-shaped measuring approximately 5 mm in diameter and approximately 1 mm in thickness. The samples were kept inside an Ar-filled glovebox (O_2 and H_2O concentrations < 1 ppm), samples were polished using 2500 and 4000 grit SiC paper. When typically preparing a flat surface for nanoindentation testing there are several other subsequent steps that follow to achieve a completely smooth surface,[245] however, due to the air-sensitive and moisture-sensitive nature of the samples none of these further polishing steps were possible. Each sample was then mounted onto a custom aluminium pin stub 6 mm in diameter, with a pin length of 3.5 mm. An electrically conductive two-part silver epoxy was used to affix the sample to the pin stub. As the temperature of the glovebox was usually around 15 ^oC, the epoxy was left to cure for at least 12 hours. Each sample was then transferred to the custom glovebox, SEM and indenter set up, where the SEM opens up directly into the glovebox enabling airless transfer. In this glovebox a final polishing step, again with 4000 SiC grit paper (approx. 3-5 μm) was performed, to achieve the best surface finish possible. After this final polishing step the sample surface was smooth and somewhat reflective to light.

3.3.4 Berkovich Nanoindentation of all Samples

Indentation was performed using a Bruker-Hysitron PI89 in situ nanoindenter; with the nanoindenter mounted to the five-axis stage of the SEM. The indentation testing axis was aligned at 80^o to the electron beam, and all tests carried out under vacuum condition. Using the Bruker-Hysitron PI89 in situ nanoindenter, indentation was performed using the highload testing mode of the indenter. Indents were carried out in three distinct regions of the sample with at least 80 μm spacing, using an electrically conductive diamond Berkovich

instrumentation tip (Bruker-Hysitron). A fused silica reference sample was used to carry out the machine compliance calibration and calculate the tip area function, using the Hysitron software, according to the procedure by Oliver and Pharr.[216] The machine compliance was measured to be 3.627 nm/mN. Before each indent, the thermal drift rate was measured when in contact with the sample, over 40 s using a preload of 80 μN, and corrected for. Indentation tests were carried out using the Hysitron load controlled open-loop mode, at least 50 single highload indents were performed on each sample. The applied load was increased linearly over a 10 s period, to the target loads between 10 to 400 mN. The indentation was then held at the target load for 2 s before it was then unloaded linearly to 0 mN over a 10 s period. From the initial gradient of the measured load-displacement unload curve the sample stiffness was calculated. From the calculated stiffness the indentation modulus and hardness were obtained as discussed in section 2.6.2.

3.3.5 Indentation Fracture Toughness

Fracture toughness indentation measurements were performed using a Bruker-Hysitron PI89 in situ nanoindenter, with an electrically conductive diamond cube corner instrumentation tip (Bruker-Hysitron). The samples were prepared, polished, and mounted inside an Ar filled glovebox, using the steps outlined in section 3.3.3. Indentation tests were carried out using the Hysitron load controlled open-loop mode, at least 50 single highload indents were performed on each sample. Before each indent, the thermal drift rate was measured when in contact with the sample, over 40 s using a preload of 100 μN, and corrected for. The applied load was increased linearly over a 10 s period, to the target loads of 100, 200 and 400 mN. The indentation was then held at the target load for 2 s before it was then unloaded linearly to 0 mN over a 10 s period. The cube corner tip was used instead of the Berkovich tip as it has a much

smaller angle, 35.3°, between the axis of symmetry and a face than for the Berkovich, 65.3°, and thus is a much sharper tip. This means that for the same contact area, the cube corner tip geometrically displaces 3 times more volume of material than a Berkovich tip, therefore the applied loading threshold for cracking can be reduced substantially. The sharper cube corner tip promotes radial cracking and as such the Lawn, Evans and Marshall (LEM) equation can be used.[225,228] Post indentation images of the indentation site were taken using the SEM; from these images the indentation diagonal and the radial crack length were measured. Using the dimensions of the indent, crack length and the applied load the fracture toughness was calculated using the LEM equation.

3.3.6 Four-point bend tests of cantilevers

All four-point bend tests were carried out using a DEBEN Microtest dual leadscrew in situ tensile stage, with 1 kN loadcell and a custom designed four-point bend jig, all inside an Ar-filled glovebox. Each beam sample was placed onto the bottom outside rollers, 10 mm spacing, of the four-point bend jig. The top inner rollers, 5 mm spacing, were then placed on top of the beam sample completing the four-point bend jig set up. The jig was then placed in the DEBEN Microtest stage, which was operated in compression, closing the jaws (1 mm min^{-1}) until a 1 mN compressive force on the beam was measured. Then the compression was applied to the four-point bend jig with a loading rate of 0.1 mm min^{-1}) until fracture of the beam occurred, force-extensions readings were taken at a recording rate of 10 s^{-1}.

3.3.7 SEM

A TESCAN Mira-3 SEM was used to take magnified images of the fracture surfaces of the beam samples post-fracture during the 4-point bend test. The SEM opened directly into Ar-

filled glovebox which enabled airless transfer of the sample, discussed in further detail in section 2.3.

3.4 Results and Discussion

3.4.1 Nanoindentation

Indentation was carried out in total across a range of loads from 10-400 mN, the highload testing regime. For highload indentation single indents were performed and the stiffness (S) calculated from the gradient of the initial linear upper portion of the unload curve as shown in Figure 2.12. Analysis of the raw load-displacement data was carried out as described in section 2.6.2. Due to the polishing limitations the sample surface was not completely flat, only measurements with maximum displacement greater than 1000 nm were included in the results, more detail and reasoning can be found in chapter 4, section 4.4.1.

As discussed in section 1.5 there has been no previous measurements of the mechanical properties of these highly air-sensitive solid electrolytes. Six different cold pressed samples, produced following the methods in sections 3.3.1 and 3.3.3, were tested using highload Berkovich indentation, according to the procedure in section 3.3.4. The figures below show both the modulus and hardness data for each respective solid electrolyte sample, calculated using the method set out in previously in section 2.6.2. All curves in figure 3.1 show a general horizontal trend for both modulus and hardness results that is invariant with depth; which indicates a single value for the intrinsic material properties of modulus and hardness respectively.

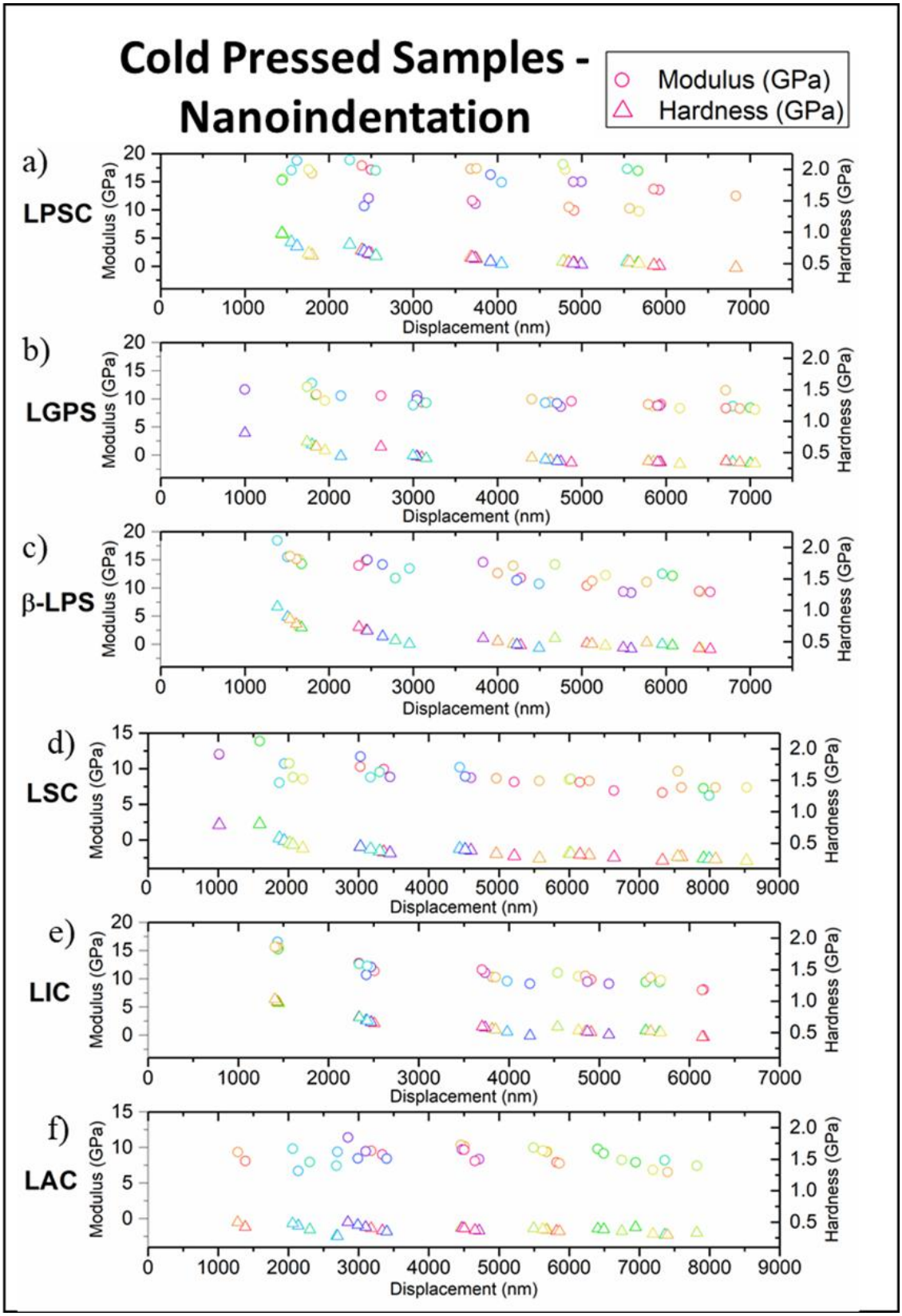

Figure 3.1: Modulus-displacement and hardness-displacement values for a) LPSC/argyrodite (Li_6PS_5Cl), b) LGPS ($Li_{10}GeP_2S_{12}$), c) β-LPS (Li_3PS_4), d) LSC (Li_3ScCl_6), e) LIC (Li_3InCl_6), f) LAC ($LiAlCl_4$).

To calculate the intrinsic value for the modulus of each respective material, all the individual moduli results were fit to a log-normal distribution. From this distribution the mode of the data was taken to be the true material property, as the expected value of the distribution. This process was followed to calculate the modulus of each material, and then repeated with the hardness results to find the intrinsic hardness value of each material. Figure 3.2 shows a summary comparing both the intrinsic modulus and hardness values for each different density sample. The error bars displayed on figure 3.2 represent a 95% confidence interval for the upper and lower bounds for the range of each material property. Table 3.1 below compares the sample relative density with its measured modulus and hardness.

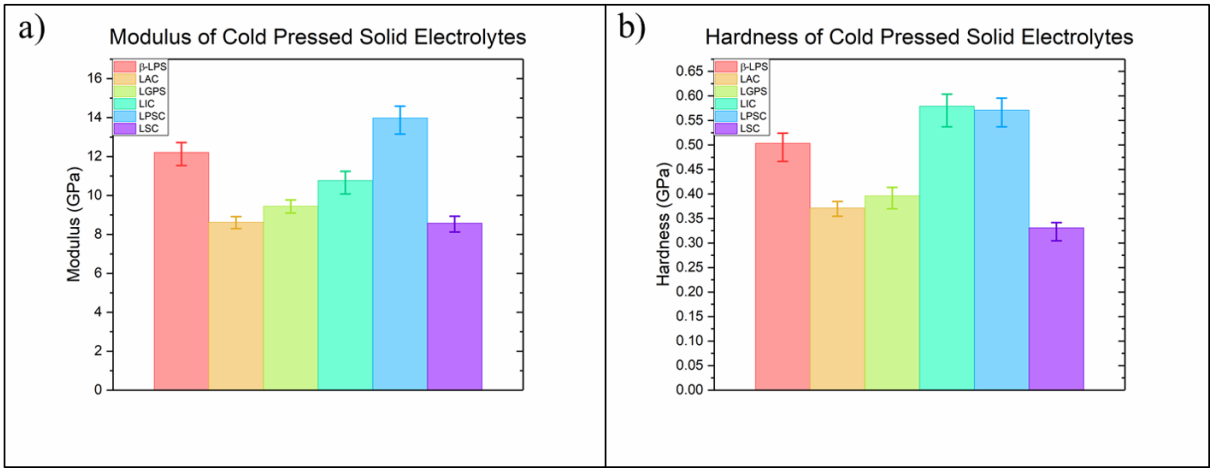

Figure 3.2: Graph showing a summary of a) modulus, b) hardness values for different cold pressed solid electrolytes.

These results provide the first experimentally determined values for modulus and hardness for these classes of air-sensitive solid electrolytes. These mechanical properties can be used to help influence material selection decisions. Figure 3.2 shows that both the modulus and hardness of the selected high ionic conductivity materials are all relatively low, indicating relatively poor mechanical properties and strength. This is likely due to the method of manufacture, cold pressing, as the green body formed will not be fully dense (typically 80-85% relative density) as shown in table 3.1.

Sample	Relative Density	Modulus (GPa)	Hardness (MPa)
Li_6PS_5Cl (LPSC)	83.8%	14.0	571
$Li_{10}GeP_2S_{12}$ (LGPS)	83.2%	9.5	396
Li_3ScCl_6 (LSC)	84.5%	8.6	331
Li_3PS_4 (β-LPS)	84.1%	12.2	504
$LiAlCl_4$ (LAC)	84%	8.6	371
Li_3InCl_6 (LIC)	84%	10.8	579

Table 3.1: Table showing the relative density of each cold pressed sample and compared with the measured mechanical properties of modulus and hardness.

There is evidence that better densified SEs have better mechanical properties and one way to achieve higher densification is through sintering. For example, oxide SEs can withstand high temperatures without any chemical degradation and as a result very high density (>95% relative density) solid electrolytes can be produced; their measured (with air-exposure) mechanical properties are displayed in table 3.2.

Oxide SE Material	Relative Density	Modulus (GPa)	Hardness (GPa)
$Li_{6.19}Al_{0.28}La_3Zr_2O_{12}$ (LLZO)[246]	99%	150 ± 2.2	9.1 ± 0,53
$Li_{0.33}La_{0.57}TiO_3$ (LLTO)[247]	99%	200 ± 3	9.5 ± 0.63
$Li_{1.3}Al_{0.3}Ti_{1.7}(PO_4)_3$ (LATP)[248]	97%	115	7.1

Table 3.2: Table showing the mechanical properties of sintered oxide SEs with very high relative density.

The modulus can be used to identify how much a material will deform the least under an applied stress that is less than the material yield stress. Glasses and other oxides have relatively high moduli, as a result the particles do not deform large amounts under pressure and therefore, cold pressing the material does not form well compacted green bodies, which has been shown to be associated with lower ionic conductivities and easier dendrite penetration.[71] Through sintering higher relative densities can be achieved, and it appears that the oxide SEs have better mechanical properties compared to their cold pressed counterparts and therefore should be a

better choice SE. Work by Monroe and Newman initially suggested that if the shear modulus of a solid electrolyte was two times greater than the shear modulus of Li, then lithium dendrite formation could be avoided.[86] However, recent work has shown that even with 99% dense ceramic oxide electrolytes that failure due to short circuits still occurs.[36,110,249] For example, the shear stress of Li is ~5 GPa, therefore the criterion to avoid dendritic failure should be >10 GPa.[250] Lithium dendrite formation is still observed in LLZO, which has a predicted shear modulus of ~60 GPa, again demonstrating that the dendrite formation mechanism is not well understood and this criterion does not hold for current solid electrolytes.

During material selection for a desired SE, as discussed in section 1.3.2, the ionic conductivity is the most important property to consider as it determines the efficiency of ions moving through the material. The mechanical properties are the next most important to consider, as the solid electrolyte needs to be able to withstand applied stresses such as general handling of the battery or the stress caused by volume expansion during cycling; which the mechanical characterisation performed in this thesis gives the first experimentally determined values for these highly air-sensitive classes of SEs.[251] There is a general consensus that materials with better mechanical properties will have better overall performance as solid electrolytes, even if it does not necessarily aid dendrite prevention.[52] Also important to consider when designing a solid electrolyte, is that a middle ground, intermediate modulus, must be found, to strike a compromise between high mechanical strength and the ability to accommodate volume change during cycling.[71] Due to prioritising ionic conductivity the chosen solid electrolytes for mechanical characterisation are all initially relatively soft materials; therefore, for these solid electrolytes it will be beneficial to consider materials with the highest moduli.

Hardness is a measure of a material's ability to resist permanent plastic deformation on the surface, demonstrated and measured through techniques like indentation. When considering solid electrolyte selection, resistance to plastic deformation is beneficial as it will help dendrite penetration prevention in a material; therefore, a higher hardness is preferred. Of these materials, Li_6PS_5Cl has the highest measured modulus and second highest hardness making it the most promising material to be selected for use as a solid electrolyte.

3.4.2 Indentation Fracture Toughness Results

The main failure of solid electrolytes is via dendrite penetration, which occurs due to the fracture of the material. Due to the air-sensitive nature of the solid electrolytes conventional methods of facture measurement were not possible. Work done by Lawn, Evans and Marshall outlines a method by which cracking caused by indentation, specifically radial cracks, can be measured and used to calculate the fracture toughness of a material.[228] Highload indentation with a cube corner tip was used to induce fracture by radial cracking,

Indentation was carried out as described in section 3.3.5 and images of the post indentation sites taken using a TESCAN Mira-3 SEM. Examples of several cube corner indents are shown in figure 3.3. Figures 3.3a-c) show cube corner indents at various loads, from the images cracking of various geometries can be seen surrounding the indent. The cracks appear to be following the direction of the particle boundaries, showing that there is poor bonding (adhesion) between the particles when formed by cold pressing, and is an easier fracture route than through the particles themselves. For the LEM model to be valid radial cracking must be the dominant mode of fracture, given the observed cracks it was not possible to determine the fracture toughness of cold pressed Li_6PS_5Cl by this method. Figure 3.3d) shows an example cube corner indent for

LGPS, again showing various crack geometries, meaning fracture toughness determination was not possible. Similar crack geometries were observed for all the cold pressed samples. The mode of fracture is dominated by the densification of the sample, leading to a complex stress state and then complex cracking; therefore, the calculation of fracture toughness by the LEM model was not possible. The cracks were curved in nature and approximately followed the edges of the indentation site; similar shaped patterns are seen as a result of pile-up surrounding indents.[252] Pile-up occurs when the material is compliant or soft, and the material is displacement by the indenter volume and pushed to the side. However, despite all the cold pressed samples being soft, significant pile-up (i.e. > 2 μm) was not observed on the surface, (evidence of this can be seen in figure 4.9 in chapter 4). As the density of the cold pressed samples is so low, it is likely that the sharp indenter geometry caused the surrounding plastic zone of the indent to become further densified. The displacement of the material followed the same movement path as that occurs in pile-up, hence the various crack geometries formed in similar shaped patterns.

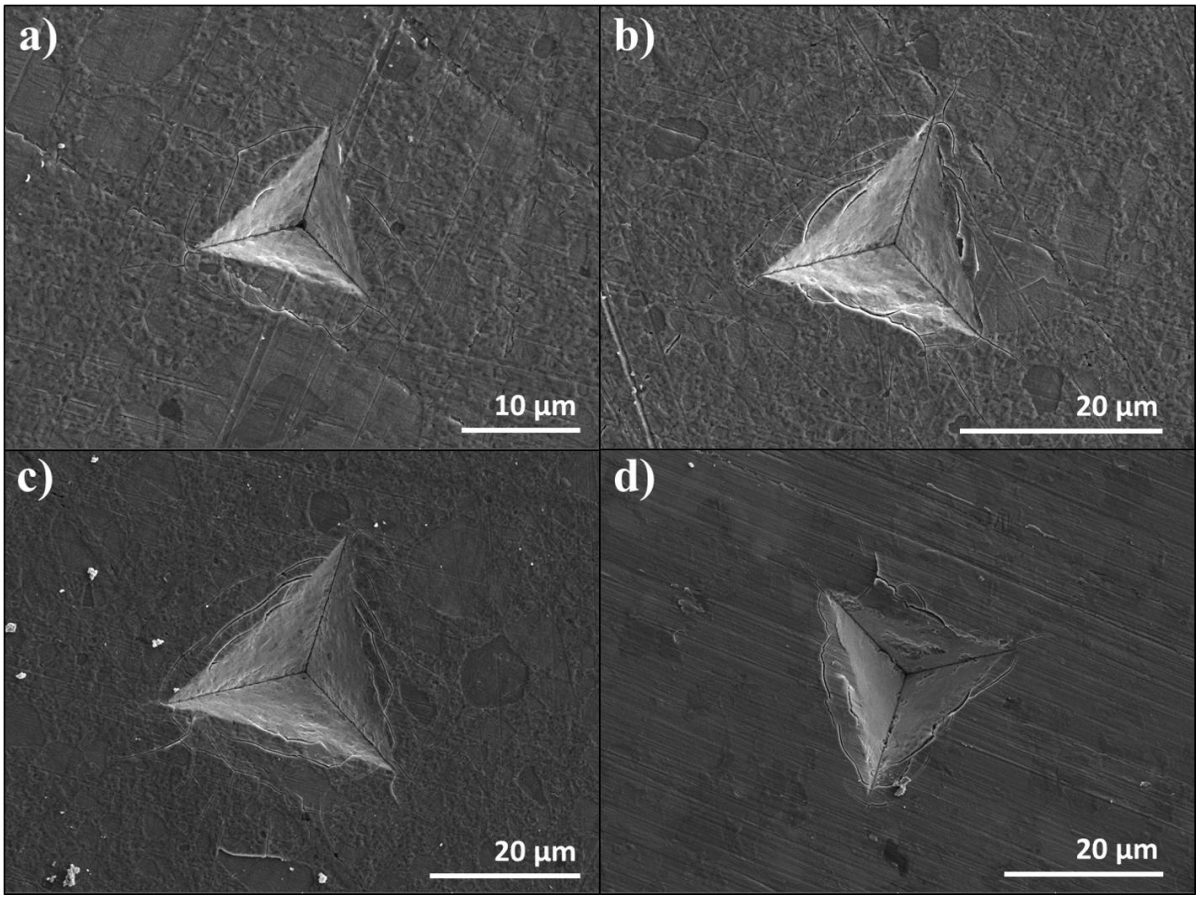

Figure 3.3:Cube corner indentation sites of a) Li_6PS_5Cl with 100 mN load, b) Li_6PS_5Cl with 200 mN load, c) Li_6PS_5Cl with 400 mN load, d) LGPS with 200 mN load.

3.4.3 Four-point Beam Bending Results

3.4.3.1 Pure Beams

As previously discussed dendrite penetration is a major source of failure for the ASSB; dendrite formation is preceded by (or leads to) a crack penetrating the solid electrolyte. Knowing the fracture properties of the material can help to inform the ease at which dendrites can penetrate the solid electrolyte. As discussed in section 3.4.2 fracture toughness experiments were very difficult to perform and as a result a simpler testing method had to be developed to understand fracture of the cold pressed electrolytes.

A method for determining flexural fracture strength was developed and is laid out in section 3.3.6. To test the selected solid electrolytes, cold pressed beams were produced using a custom-built die set as described in section 3.3.2. By testing beams using a bend test, failure by fracture will be caused by a crack initiating at the largest flaw on the surface. The point of fracture occurred under the highest applied load, this value was taken to be the fracture load, *P*. Using the known geometries of the 4-point bend jig, as laid out in section 3.3.6, and the measured dimensions of the beam, the flexural fracture strength, σ_f, for each beam was calculated using equation 3.1, which describes the moment created by a 4-point bend test.

$$\sigma_f = \frac{3}{4}\frac{Pl}{bd^2} \ (eqn\ 3.1)$$

Where

- P is the fracture load.
- l is the distance between the outer rollers.
- b is the width of the beam.
- d is the thickness of the beam.

At least 10 beams were tested for each material, the mean of the flexural fracture strength values for each solid electrolyte are shown in figure 3.4a). The figure shows pure β-LPS and LSC to have a similar flexural fracture strength that is measurably higher than the strength of LGPS and Li_6PS_5Cl, which themselves have similar flexural fracture strength. The differences in measured strength values is due to difference in critical flaw size presence. From comparison with figure 3.2 the trend for modulus and hardness values do not align with the flexural fracture strength values. This suggests that the processability of the material, specifically how well the material densifies under cold press to form a green body, will determine the size and dispersion of pores in the material and as a result the ease at which a crack initiates at a critical flaw. When considering material selection, the flexural fracture strength of all these materials are relatively

low values, indicating poor resistance to cracking, and are within the same order of magnitude - range of 13.3 MPa for LGPS to 18.0 MPa β-LPS. Therefore, when selecting a suitable solid electrolyte ionic conductivity should still be prioritised, meaning Li_6PS_5Cl is still the preferred choice for solid electrolyte.

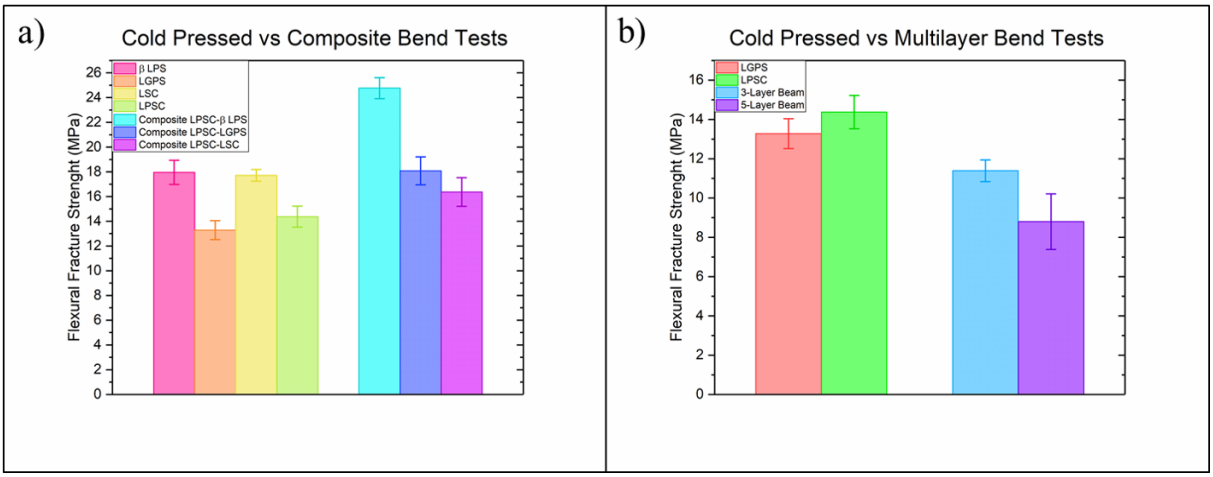

Figure 3.4: a) The measured flexural fracture strength of the pure cold pressed beam samples and the composite cold pressed beam samples, b) The measured flexural fracture strength of the multilayer cold pressed samples compared with the component pure cold pressed samples.

3.4.3.2 Composite Beams

Composite beams were manufactured, using the method described in section 3.3.2, to investigate effect of creating a layered composite solid electrolyte on the measured flexural fracture strength. From the indentation experiment carried out in section 3.4.1, it was evident that Li_6PS_5Cl had the best mechanical properties. When considering the promising electrochemical properties of Li_6PS_5Cl, it became the choice material for a solid electrolyte; therefore all composites were made using Li_6PS_5Cl and a second different solid electrolyte.

As stated in section 3.3.2 the composite beam was manufactured such that the interface between the two composite layers was placed under compression away from the neutral axis, this would closely replicate the conditions under which crack deflection was observed during the

electrochemical tests. 4-point bend tests of the composite beam samples were carried using the same method as for the pure cold pressed samples, set out in section 3.3.6. Multiple beams were tested for each composite and the mean of the flexural fracture strength values for each solid electrolyte are shown in figure 3.4b), Comparing the cold pressed pure beams with composite beams revealed a difference in the flexural fracture strength. To consider whether the difference in these measured values was statistically significant, Welch's T-Test was used.[253]

Using the method set out by Welch, the T-Test value and Degrees of Freedom was calculated and shown in table 3.3 below. By comparing these results with the Two Tails T-Distribution Table,[254] with a 0.05 significance level, it was possible to determine whether there was a statistically significant difference between each pure cold pressed sample and the composite sample. Figure 3.4b) showed that the flexural fracture strengths of the composite cold pressed beams were greater than that of the measured values for the pure cold pressed beams. The Li_6PS_5Cl/β-LPS composite had the highest flexural fracture strength and showed the greatest increase compared to its component materials, with Welch's T-Test confirming a statistically significant difference to both component materials. The Li_6PS_5Cl/LGPS composite also showed a higher flexural fracture strength than its component materials, with Welch's T-Test confirming a statistically significant difference to both component materials. The Li_6PS_5Cl/LSC composite showed a slight increase flexural fracture strength compared to Li_6PS_5Cl but a decreased when compared to LSC. Welch's T-Test showed a statistically significant difference only comparing the Li_6PS_5Cl/LSC composite to Li_6PS_5Cl; when comparing the composite to LSC the flexural fracture strength values were very similar.

Composite	Pure Sample	T-Test	Degrees of Freedom	Statistically Significant
Argyrodite/β-LPS	β-LPS	5.3	13.0	Pass
Argyrodite/LGPS	LGPS	4.6	13.6	Pass
Argyrodite/LSC	LSC	0.8	7.9	Fail
Argyrodite/β-LPS	Argyrodite	8.7	12.0	Pass
Argyrodite/LGPS	Argyrodite	3.6	12.9	Pass
Argyrodite/LSC	Argyrodite	3.0	10.8	Pass

Table 3.3: Shows a T-Test analysis of the fracture strength of the composite solid electrolyte beams compared to their pure counterparts, to demonstrate whether the fracture properties can be improved through forming a composite.

A critical current density (CCD) electrochemical test (carried out by Bingkun Hu) of pure Li_6PS_5Cl was performed; figure 3.5b) shows a short circuit occurred at 2.75 $mAcm^{-2}$. Figure 3.5a) shows that in pure Li_6PS_5Cl, a monolithic SE that a straight dendritic crack forms, with no deflection. The aim of the composite solid electrolyte is that some crack deflection will occur, increasing resistance to crack propagation and therefore increase the CCD.

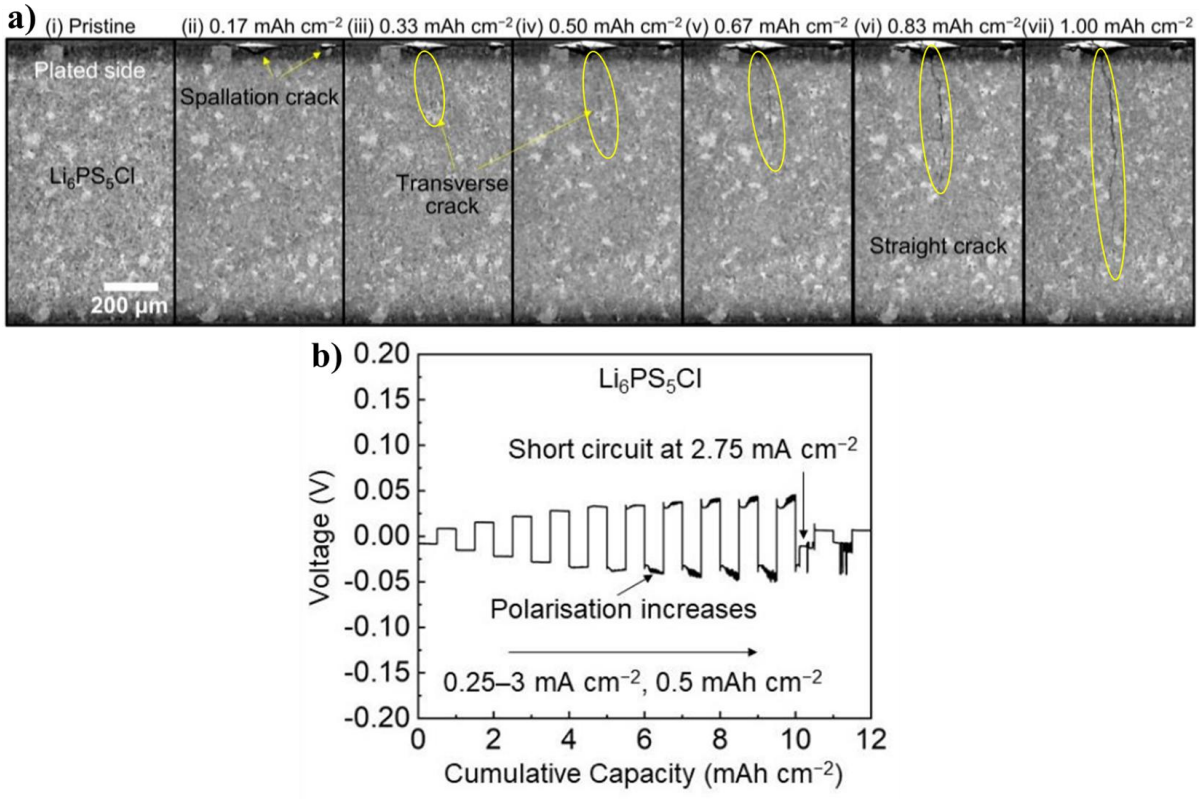

Figure 3.5: a) XCT images for pure Li_6PS_5Cl showing a transverse crack propagating through the sample without deflection. b) The voltage profile of a Li/Li_6PS_5Cl/Li cell showing a short circuit at 2.75 mAcm^{-2}.[255]

Subsequent electrochemical CCD tests on symmetric samples of these composites were carried and results shown in figure 3.6. Figure 3.6a) and 3.6b) show that for the Li_6PS_5Cl/LSC and Li_6PS_5Cl/LGPS composites there was an increase in the CCD of the composite materials when compared to their pure components. Figure 3.6c) shows no significant improvement in the CCD for the Li_6PS_5Cl/β-LPS composite. These results show that show that a greater improved flexural fracture strength of the composite solid electrolytes does not correlate with improved electrochemical properties. X-ray Computed Tomography (XCT) was also performed during the electrochemical CCD tests and the images shown in figure 3.6. Figures 3.6d-f) all show an initial crack that grows transversely across the Li_6PS_5Cl layer, eventually reaching the interface between the composite materials. In both the Li_6PS_5Cl/LSC and Li_6PS_5Cl/LGPS composites (figures 3.6d,e) respectively) the crack then appears deflect and propagate along the interface,

this phenomenon is known as crack deflection. In comparison, during the CCD test for the Li_6PS_5Cl/β-LPS composite the crack penetrates through without any sign of deflection (figures 3.6f) respectively). The XCT images in figure 3.6 propose that crack deflection at the interface is the mechanism responsible for improved CCD performance.

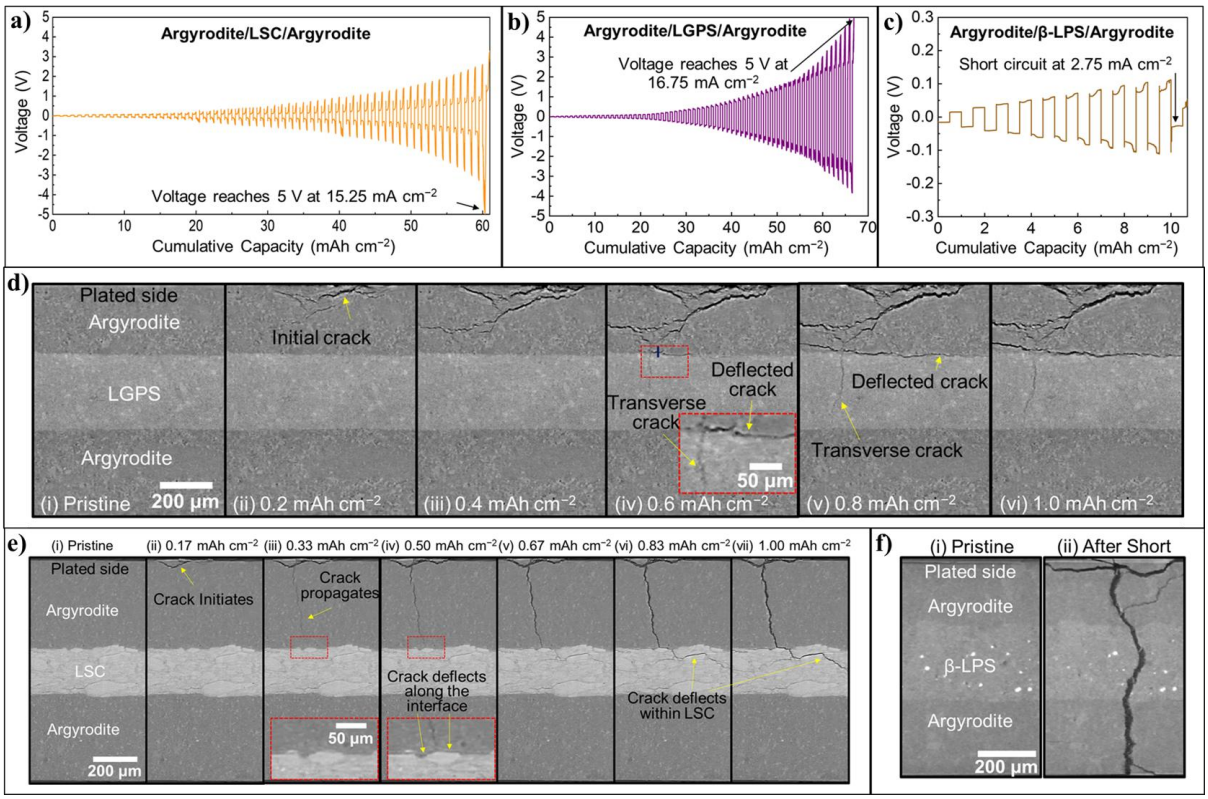

Figure 3.6:CCD test for a) Li_6PS_5Cl/LSC/Li_6PS_5Cl composite, b) Li_6PS_5Cl/LGPS/Li_6PS_5Cl composite, c) Li_6PS_5Cl/β-LPS/Li_6PS_5Cl composite. XCT images for d) Li_6PS_5Cl/LSC/Li_6PS_5Cl composite showing crack deflection along interface, e) Li_6PS_5Cl/LGPS/Li_6PS_5Cl composite showing crack deflection along interface, c) Li_6PS_5Cl/β-LPS/Li_6PS_5Cl composite with no observed crack deflection. Figure was made with the help of Bingkun Hu.[255]

The 4-point bend test results in figure 3.4a) suggest Li_6PS_5Cl/LSC and Li_6PS_5Cl/LGPS composites had a weaker interface which facilitated the crack deflection, therefore improving the overall solid electrolyte electrochemical properties. Figure 3.7 is a diagram to show the loading direction and orientation during the 4-point bend tests of the composite beams. To investigate the crack deflection mechanism further post-fracture SEM images were taken of the composite samples used in the 4-point bend tests.

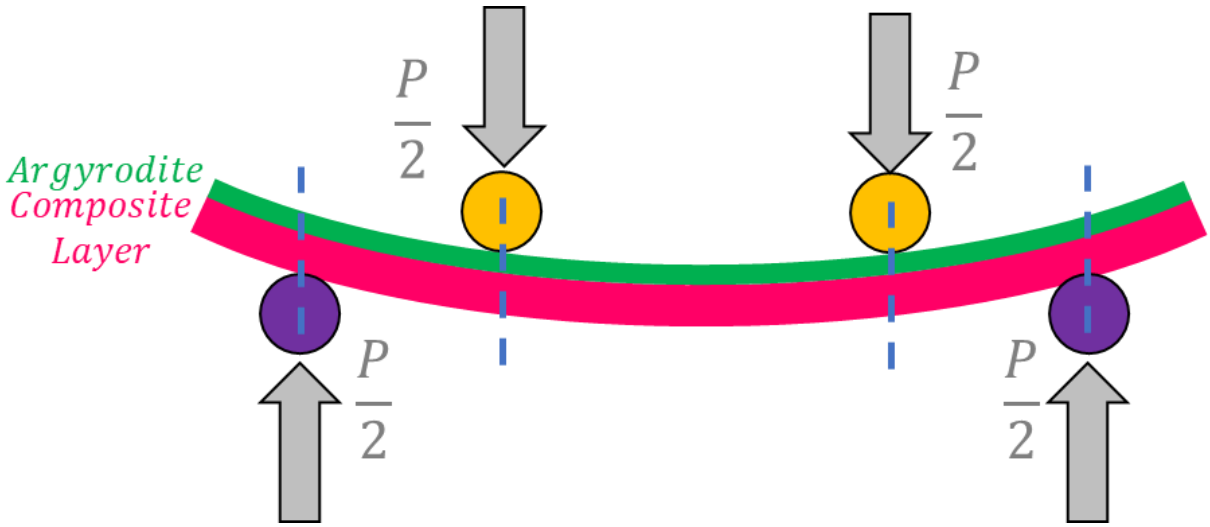

Figure 3.7 Schematic of the composite beam under flexion, showing the loading direction and the interface tested within the compressive bending regime.

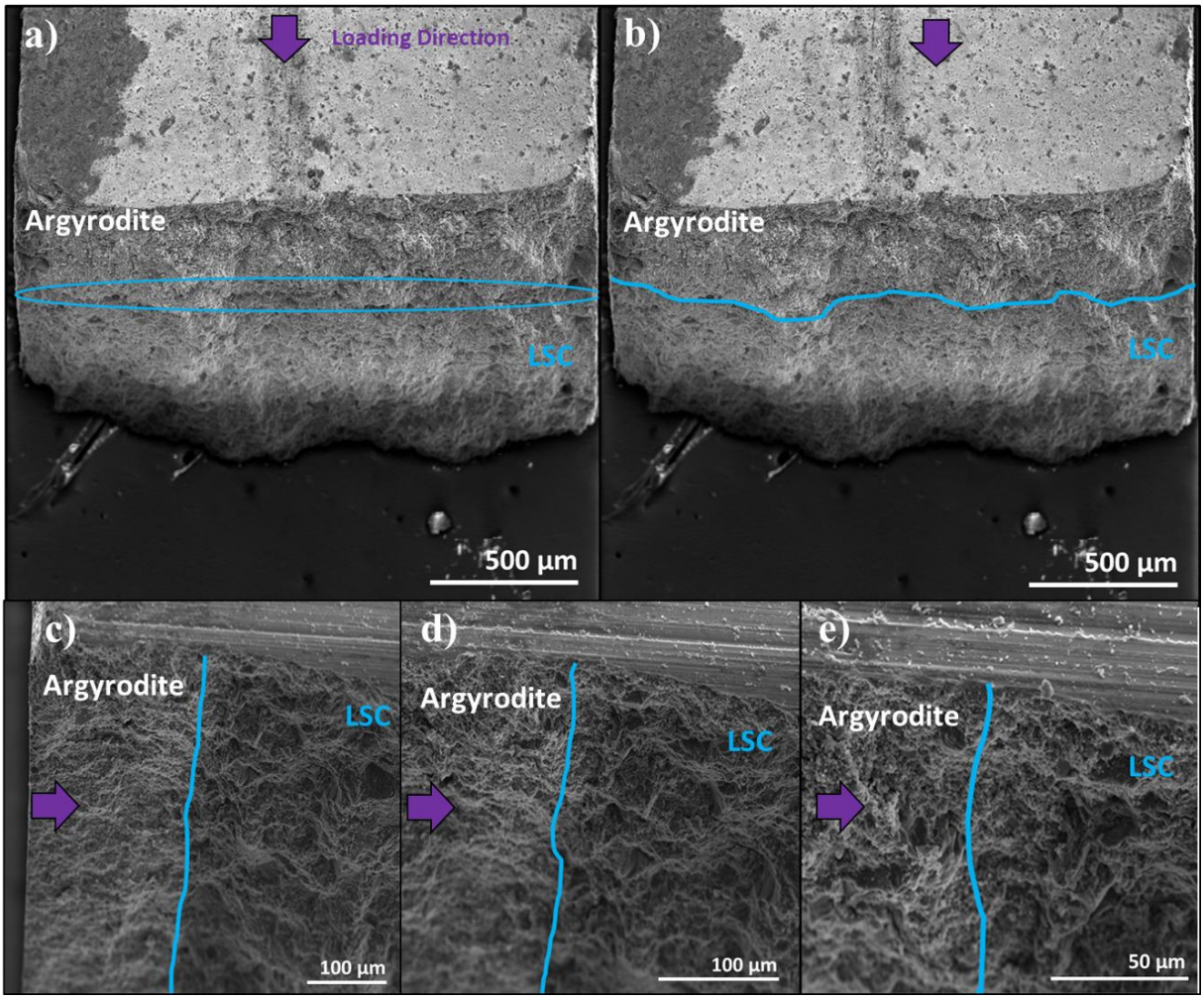

Figure 3.8:a-b) a top down image of a composite beam highlighting a crack at the interface between Li_6PS_5Cl and LSC, c-e) successively magnified sideways cross-section image showing the Li_6PS_5Cl/LSC interface.

Figures 3.8a-b) show evidence of a crack that has formed at the composite interface, supporting the weak interface argument. Figures 3.8c-e) show a sideways cross section of the composite beam fracture surface.

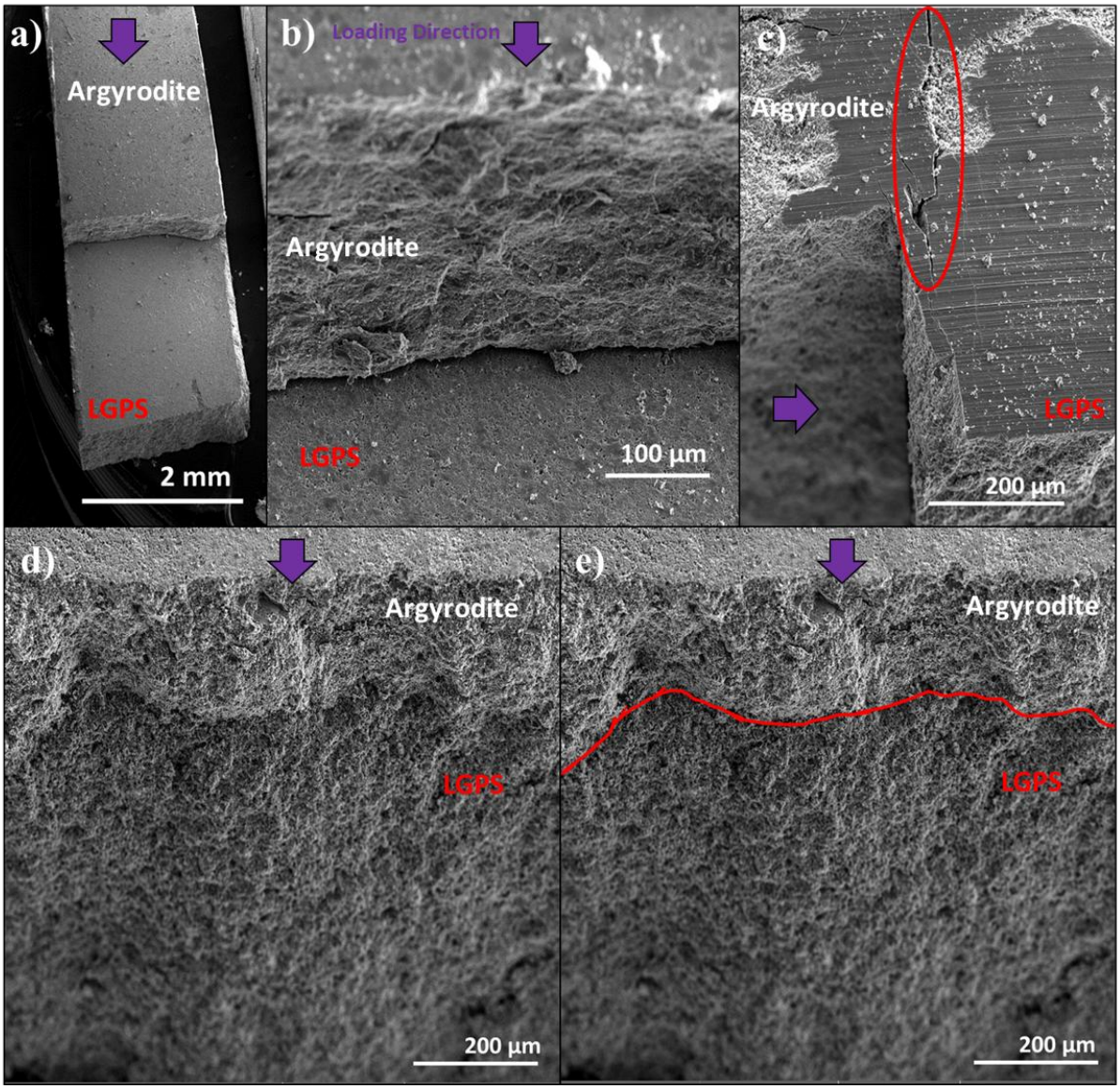

Figure 3.9: a-b) a top down image showing two different fracture surfaces in Li_6PS_5Cl and LGPS, indicating crack deflection at the interface, c) a side-on image showing a crack deflecting both ways across the interface, d-e) sideways cross-section image showing the Li_6PS_5Cl/LGPS interface.

Figures 3.9a) and b) show an Li_6PS_5Cl/LGPS composite beam with two different fracture surfaces, showing where the crack has traversed the Li_6PS_5Cl layer before deflecting along the interface approximately 3 mm, before then traversing the LGPS layer resulting in the Li_6PS_5Cl cleaving off the top; very clear evidence for crack deflection. Evidence of the crack deflection across the whole interface can be seen by a side-on image of a composite beam in figure 3.9c). Figures 3.9d-e) show a front on cross section of the composite beam fracture surface.

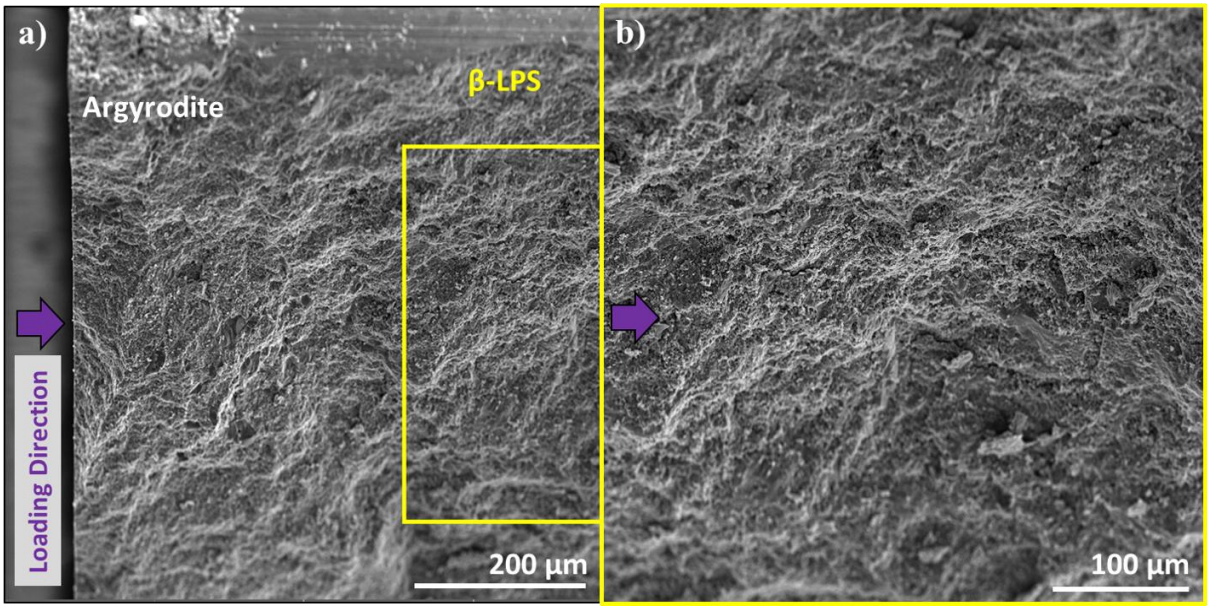

Figure 3.10:a) sideways cross-section image showing the Li_6PS_5Cl/β-LPS composite, b) a magnified image of where the interface is suspected to be.

In post-fracture SEM images of the Li_6PS_5Cl/β-LPS there was no evidence of crack deflection in any samples. Figure 3.10a) shows a sideways cross section of the composite beam and unlike previous composites it was not possible to clearly identify the interface between Li_6PS_5Cl and the β-LPS layers, figure 3.10b) shows a magnified image of where the interface is likely to be, but no clear identification of the layers was possible.

Crack deflection in layered ceramics is a toughening mechanism which can occur due to a weak interface between the layers. Once a crack has initiated in the first layer it propagates through the layer arriving at the interface, in the case of these composites the crack initiates in the Li_6PS_5Cl layer and propagates along the grain/particle boundaries. When the crack arrives at the interface it encounters a change in material properties. In the case of Li_6PS_5Cl/LSC and Li_6PS_5Cl/LGPS composites, the crack encounters a weak interface formed by cold-pressing, as evidenced by the 4-point bend test results. For the crack to propagate further it must overcome a new energetic barrier, either:[256]

- the surface fracture energy of the new layer, in this case LSC or LGPS.
- the interfacial energy of the bonds that exist between the layers.

A weak interface provides the path of least resistance, as the interfacial energy is lower than the surface fracture energy of the secondary layer; thereby encouraging crack deflection as demonstrated in figures 3.6d-e), 3.8 and 3.9. This deflection along the interface therefore increases the resistance to crack propagation in the solid electrolyte,[257] thereby allowing greater cycling performance (figure 3.5a-b). In the case of Li_6PS_5Cl/β-LPS the 4-point bend test flexural fracture strength of the composite increased significantly, suggesting that a comparatively strong interface was formed. Therefore, once the crack has reached the interface, the path of least resistance for crack propagation would be through the second layer rather than deflecting along the interface, as shown in figures 3.6f) and 3.10. This results in no significant improvement in cycling performance (figure 3.6c). In summary, the post-fracture SEM images of the 4-point bend tests provides evidence supporting the argument that for the cold pressed solid electrolytes, creating a composite with a weak interface will introduce a crack deflection toughening mechanism, thereby improving its electrochemical properties.

3.4.3.3 Layer Beams

As discussed in the previous section the presence of a weak interface encourages crack deflection to occur. The next step taken was to investigate the effect of introducing more layers into the composite. As the Li_6PS_5Cl/LGPS composite showed the highest CCD and best evidence for crack deflection, multilayer beams were created from these two materials as described in section 3.3.2. The 3-layer beam comprised Li_6PS_5Cl/LGPS/Li_6PS_5Cl and the 5-layer beam comprised Li_6PS_5Cl/LGPS/Li_6PS_5Cl/LGPS/Li_6PS_5Cl. Figure 3.4b) shows that for the 3-layer beam there was a significant decrease in flexural fracture strength and shows an even greater decrease for the 5-layer beam. These results from 4-point bend testing could

suggest the presence of weak interfaces between the layers. To confirm whether crack deflection had occurred along the interface, post-fracture SEM images were taken.

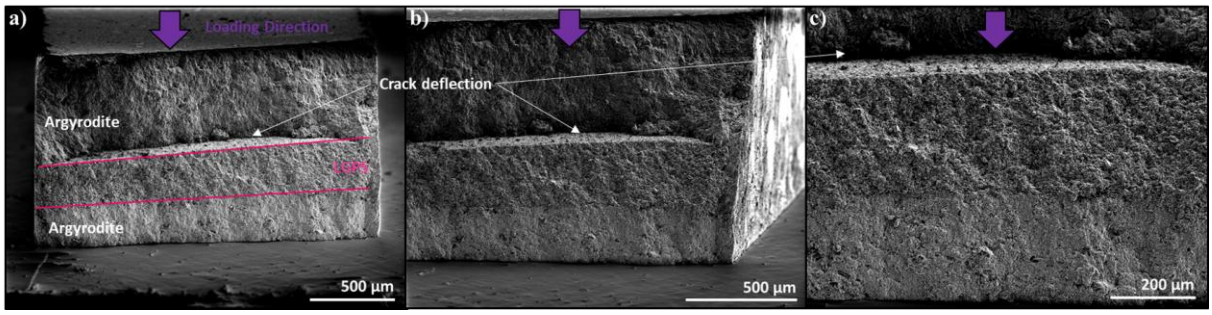

Figure 3.11: successively magnified images of fracture surface of a 3-layered beam, with observed crack deflection

Examining the fracture surface of the 3-layer beam in figure 3.11a) revealed three distinct layers and the respective interfaces (pink lines). At the top interface between Li_6PS_5Cl/LGPS there is clear evidence that there is a weak interface and that crack deflection has occurred (figure 3.11). However, at the bottom interface the interface between the LGPS/Li_6PS_5Cl can be clearly seen but no crack deflection is evident.

When investigating the 5-layer beam there was clear evidence of the individual layers, shown by the green lines in figure 3.12c). Figure 3.12a) shows some evidence of crack deflection at the first interface from the top, and significant crack deflection along the third interface from the top. It is interesting to note that in both these deflection cases the crack would have propagated through Li_6PS_5Cl to reach the interface with LGPS. For the other two interfaces, LGPS/Li_6PS_5Cl, no significant crack deflection is observed, similar to that of the 3-layer beam.

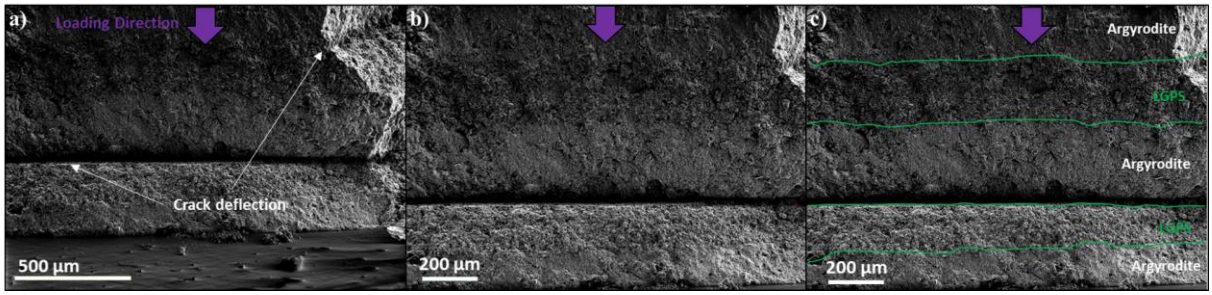

Figure 3.12:fracture cross-sections of a 5-layer beam showing a) crack deflection sites, b) the five individual layers, c) highlighting the four interfaces.

In summary the 3-layer beam only appears to have crack deflection along one interface, meaning there is no added crack resistance benefit from introducing the second interface. In the 5-layer beam there is evidence of crack deflection at two of the interfaces but not in the other two. This is accompanied by a significant decrease in flexural fracture strength as shown by figure 3.4b) but also evidenced in the very poor handleability of these samples during the production process, especially during cold pressing, meaning the overall mechanical properties of the solid electrolyte composite have worsened.

3.5 Conclusion

This chapter has demonstrated novel testing methods which enable experimentally measured mechanical properties, such as modulus, hardness and fracture strength, of the highly-air sensitive solid electrolytes to be reported. The nanoindentation experiments revealed that Li_6PS_5Cl exhibited the best mechanical properties of all the cold pressed solid electrolytes, combined with its promising electrochemical properties made it the preferred solid electrolyte for testing. However, for all the cold pressed samples the mechanical properties were all quite poor, specifically exhibiting low density and large porosity. This was evidenced by the fracture toughness testing where the powder was so poorly bonded, it appeared to be pushed by the indenter rather than any breaking of bonds. This suggests that better processing to improve both

the density and microstructure is required to enable the starting powders to form viable solid electrolytes.

The 4-point beam testing revealed that by creating a composite solid electrolyte it was possible to increase the overall CCD. The increases CCD occurred in composite samples that a weak interface, thereby enabling crack deflection at the interface. The weak interface was created by cold pressing layers of different solid electrolyte powders on top of each other. Despite the increase in crack resistance, this method of processing the composite solid electrolytes even further decreased their already poor mechanical properties. The trade-off for higher CCD but worse mechanical properties, especially handleability, is ultimately not viable for a solid electrolyte candidate. However, the principles of introducing a composite to promote crack deflection, thereby increasing the toughness, is worth further investigation.

4. Development of the Mechanical Properties of Solid Electrolytes

4.1 Aim

In the previous chapter the experimentally gathered data was used to characterise the mechanical properties of several leading cold pressed solid electrolytes. The research showed these solid electrolytes, despite their excellent electrochemical properties, had relatively poor mechanical properties; this led to the exploration of methods to improve the mechanical properties of these solid electrolytes, which may be one possible method by which to improve their electrochemical performance. Li_6PS_5Cl was the cold pressed SE that showed the best electrochemical performance and the most promising mechanical properties; this chapter aims to further improve its mechanical properties. The crack deflection mechanism discussed in the previous chapter suggests SEs with better mechanical properties, such as improved fracture resistance, will improve electrochemical performance. One method to improve the mechanical properties of the cold pressed SEs is to increase the relative density of the SE, through methods such as sintering. Another method is to create composites of the solid electrolytes by introducing a stronger material into the SE matrix, with the aim to improve the overall mechanical properties. Novel investigative methods are used and demonstrated in this chapter to measure the results.

4.2 Introduction

Lithium penetration through the solid electrolyte is a problem that has prevented the realisation of a functioning Li ASSB. In previous literature many different theories have been put forward, with no consensus as to the exact method by which lithium dendrites form. More recent research has shown issues such as cracking, cycling stress state and contact mechanics to be contributing factors to poor electrochemical performance and cell failure.[147] Therefore, necessitating investigation into whether it may be an underlying mechanical problem rather than electrochemical hindering progress of the ASSB.[159,258–260] However, there is very little existing literature that accurately measures the mechanical properties of solid electrolytes, due to their highly air-sensitive nature. The research carried out in this chapter provides some of the first experimentally determined mechanical characterisation of these materials, enabled through the development of novel air-sensitive testing techniques.

In combination with this research, a dendrite initiation model was put forward by Dominic Melvin et al. stating that if the hydrodynamic pressure build-up of the lithium dendrite exceeds the fracture criterion for the solid electrolyte then a crack will initiate.[261] The research carried out in this chapter was used to validate this model and for the first time provided an accepted dendrite initiation model. The investigation was carried with Li_6PS_5Cl the choice solid electrolyte, as demonstrated in the previous chapter, it had the most promising electrochemical properties. From this model it is evident that to resist crack initiation, the local fracture strength of the solid electrolyte should be increased. Through a field-assisted sintering manufacturing process, Li_6PS_5Cl samples with increasing density were produced. Once produced the challenge became examining the mechanical properties of the various solid electrolytes, due to their air-sensitive nature. Using the fully enclosed Ar-glovebox, SEM and nano-indenter setup,

combined with novel testing procedures, the mechanical characterisation of Li_6PS_5Cl was made possible and experimentally measured values of modulus, hardness and local fracture strength discovered for the first time.

Crack propagation is another problem that plagues solid electrolytes which the literature again comments very little about, due to the increased difficulty of air-sensitive mechanical characterisation. Another model put forward in collaboration with this research, by Dominic Melvin, shows that the plating of lithium can generate enough crack tip driving force to exceed the solid electrolyte fracture toughness, allowing a dry crack to propagate and create a path for a lithium dendrite; the research carried out in this chapter was used to validate the model. Therefore increasing the fracture toughness of the solid electrolyte will resist crack propagation, thereby enabling higher critical current densities and greater cycle lifetimes. One method to improve the mechanical properties of a ceramic is to create a composite by introducing another material with better mechanical properties. Ceria-Stabilised-Zirconia (CSZ) was used to create different Li_6PS_5Cl-CSZ composites with the aim of improving the fracture toughness of the composite solid electrolyte, specifically through transformation toughening.[262,263] Air-sensitive mechanical characterisation was carried out to investigate whether producing a Li_6PS_5Cl composite would improve the mechanical properties of a solid electrolyte, and in turn its electrochemical properties.

4.3 Experimental

4.3.1 Manufacture of various Li_6PS_5Cl Samples

All samples tested were prepared with the help of Dominic Melvin. All procedures, including pressing and sintering, were performed inside an Ar-filled glovebox (O_2 and H_2O

levels < 1 ppm). All Li_6PS_5Cl samples were made using Li_6PS_5Cl solid electrolyte powder that was purchased from *MSE Supplies – Ampcera*. The purity of the powder was >99.9%, the average particle size was ~1 µm, and the powder distribution was D50.[76]

To prepare the cold pressed Li_6PS_5Cl sample, Li_6PS_5Cl solid electrolyte powder was loaded into a stainless-steel die set, 5 mm in diameter, and pressed into a disc under a uniaxial pressure of 400 MPa. To prepare field assisted sintering samples with varying density, the following method was used. Li_6PS_5Cl solid electrolyte powder was loaded into a 20 mm diameter graphite die set, which was then placed into a spark plasma sintering system (FCT Systeme GmbH). Field assisted sintering was then carried out at either 300, 350, or 400 °C for 5 minutes, under uniaxial pressure of 50 MPa whilst under vacuum, by passing an electrical current through the die set. Using micro-XCT the volume of the discs was measured and using the measured weight of each disc, the relative density was calculated. Potentiometric electrochemical impedance spectroscopy was carried out to calculate the ionic conductivity and 3-electrode cells using a single plating protocol to calculate the critical current density, more detail given in section 2.5.[50,264] The results of density and electrochemical characterisation are shown in table 4.1.

Li_6PS_5Cl SPS Sintering Temperature (°C)	**Relative Density**	**Ionic Conductivity (mS cm^{-1})**	**Critical Current Density (mA cm^{-2})**
Cold Pressed	83%	1.3	1
300	86%	2.2	2
350	95%	5.3	5
400	98%	6.1	10

Table 4.1: For each different sintering temperature of Li_6PS_5Cl, the table shows the relative density of the produced material and its electrochemical properties.

To prepare the composite Li_6PS_5Cl-CSZ samples the following method was used. 12 mol% CeO_2-ZrO_2 (CSZ) powder was purchased from *TOSOH*. To ensure the CSZ contained sufficient

amount of metastable tetragonal phase, the CSZ was calcined in air for 1 hour at 900 °C, with a heating/cooling rate of 5 °C/min. To make each sample at the corresponding ratio, both Li_6PS_5Cl and calcined CSZ powders were mixed and initially ground for 30 minutes using pestle and mortar. Next the mixture of powders was sieved (100 µm mesh) to further mix the powder and break up any agglomerates, this process was repeated three times. The mixed powders were loaded into a graphite die set, which was then placed into a spark plasma sintering system (FCT Systeme GmbH). Field assisted sintering was then carried out at 400 ^oC for 5 minutes, under uniaxial pressure of 50 MPa whilst under vacuum, by passing an electrical current through the die set.

CSZ was used to gain the benefit of transformation toughening in the Li_6PS_5Cl -CSZ composite. To investigate as to whether this effect occurred a sample using ZrO_2 (zirconia), purchased from *Sigma Aldrich*, in its monoclinic phase was produced; specifically a 20% Li_6PS_5Cl - zirconia composite. To make the sample an 80-20 ratio, both Li_6PS_5Cl and zirconia powders were mixed and initially ground for 30 minutes using pestle and mortar. Next the mixture of powders was sieved (100 µm mesh) to further mix the powder and break up any agglomerates, this process was repeated three times. The mixed powders were loaded into a graphite die set, which was then placed into a spark plasma sintering system (FCT Systeme GmbH). Field assisted sintering was then carried out at 400 ^oC for 5 minutes, under uniaxial pressure of 50 MPa whilst under vacuum, by passing an electrical current through the die set.

4.3.2 Preparation of the Li_6PS_5Cl Samples

All sintered Li_6PS_5Cl samples made using field assisted sintering, were prepared using the following method. All the samples were approximately disc-shaped measuring approximately

5 mm in diameter and approximately 1 mm in thickness. The samples were kept in an Ar filled glovebox (O_2 and H_2O concentrations < 1 ppm), samples were polished using successively finer SiC paper, using grits of 400, 600, 800, 1200, 2500 and finally 4000. When typically preparing a flat surface for nanoindentation testing there are several other subsequent steps that follow to achieve a completely smooth surface,[245] due to the air-sensitive and moisture-sensitive nature of the samples none of these further polishing steps were possible. Each sample was then mounted onto a custom aluminium pin stub 6 mm in diameter, with a pin length of 3.5 mm. An electrically conductive two-part silver epoxy from Agar Scientific was used to affix the sample to the pin stub. As the temperature of the glovebox was usually around 20 °C, the epoxy was left to cure for at least 12 hours. Each sample was then transferred to the custom glovebox, SEM and indenter set up, where the SEM opens up directly into the glovebox enabling airless transfer. In this glovebox a final polishing step, again with 4000 SiC grit paper was performed, to achieve the best surface finish possible. After this final polishing step the sample surface was smooth and somewhat reflective to light.

The cold pressed Li_6PS_5Cl sample, once manufactured, was prepared using the above method, with the following change. Once the sample had been pressed, the surface was already relatively smooth and as a result the only initial polishing step was using 4000 grit SiC paper, more detail can be found in section 3.3.3. The remainder of the above procedure was carried out to mount the cold pressed sample to the pin stub prior to indentation.

4.3.3 Berkovich Nanoindentation of all Samples

Indentation was performed using a Bruker-Hysitron PI89 in-situ nanoindenter; the nanoindenter mounted to the five-axis stage of the SEM. The indentation testing axis was aligned at 80^o to

the electron beam, and all tests carried out under vacuum condition. Using the lowload testing mode of the indenter, indents were carried out in three distinct regions of the sample. All indents were spaced at least 30 μm apart, carried out with a continuous stiffness measurement frequency of 120 Hz and using an electrically conductive diamond Berkovich instrumentation tip (Bruker-Hysitron). A fused silica reference sample was used to carry out the machine compliance calibration and calculate the tip area function, using the Hysitron software, according to the procedure by Oliver and Pharr.[216] The machine compliance was measured to be 3.627 nm/mN. Before each indent, the thermal drift rate was measured when in contact with the sample, over 40 s using a preload of 20 μN, and corrected for. Indentation tests were carried out using the Hysitron load controlled open-loop nanoDynamic mode, enabling continuous stiff measurement (linear CMX). The applied load was increased linearly over 10 s, to each target load of 1000, 2000, 4000, 8000 μN. From the continuous stiffness measurement indentation, the reduced modulus and hardness were obtained; using the known indenter modulus and hardness, the sample indentation modulus and hardness were calculated.

Using the Bruker-Hysitron PI89 in situ nanoindenter, indentation was performed using the highload testing mode of the indenter. Indents were carried out in three distinct regions of the sample with at least 60 μm spacing, using an electrically conductive diamond Berkovich instrumentation tip (Bruker-Hysitron). Before each indent, the thermal drift rate was measured when in contact with the sample, over 40 s using a preload of 80 μN, and corrected for. Indentation tests were carried out using the Hysitron load controlled open-loop mode, at least 60 single highload indents were performed on each sample. The applied load was increased linearly over a 10 s period, to the target loads between 10 to 500 mN. The indentation was then held at the target load for 2 s before it was then unloaded linearly to 0 mN over a 10 s period. From the initial gradient of the measured load-displacement unload curve the sample stiffness

was calculated. From the calculated stiffness the indentation modulus and hardness were obtained.

4.3.4 Fracture Toughness testing of Li_6PS_5Cl-Zirconia Composites

Fracture toughness indentation measurements were performed using a Bruker-Hysitron PI89 in-situ nanoindenter, with an electrically conductive diamond cube corner instrumentation tip (Bruker-Hysitron). The samples were prepared, polished and mounted inside an Ar filled glovebox, using the steps outlined in section 4.3.2. Indentation tests were carried out using the Hysitron load controlled open-loop mode, at least 50 single highload indents were performed on each sample. Before each indent, the thermal drift rate was measured when in contact with the sample, over 40 s using a preload of 80 μN, and corrected for. The applied load was increased linearly over a 10 s period, to the target loads of 100, 200 and 400 mN. The indentation was then held at the target load for 2 s before it was then unloaded linearly to 0 mN over a 10 s period. The cube corner tip was used instead of the Berkovich tip as it has a much smaller angle, 35.3°, between the axis of symmetry and a face than for the Berkovich, 65.3°, and thus is a much sharper tip. This means that for the same contact area, the cube corner tip geometrically displaces 3 times more volume of material than a Berkovich tip, therefore the applied loading threshold for cracking can be reduced substantially. The sharper cube corner tip promotes radial cracking and as such the Lawn, Evans and Marshall (LEM) equation can be used.[225,228] Post indentation images of the indentation site were taken using the SEM; from these images the indentation diagonal and the radial crack length were measured. Using the dimensions of the indent, crack length and the applied load, the fracture toughness was

calculated using the LEM equation. Example images of post-indentation sites are displayed in figure 4.9, in section 4.4.2.

4.3.5 FIB of Cantilevers

Pentagonal micro-cantilever beams were milled using a ZEISS Auriga FIB-SEM system with a gallium ion (Ga^+) source.[235,265–267] The sample was prepared, polished and mounted inside an Ar filled glovebox, using the steps outlined in section 4.3.2. The mounted sample was loaded into a Semi Labs Transfer Shuttle, whilst still inside an Ar filled glovebox, to allow for an airless transfer into the FIB-SEM. Using the gallium FIB, three overlapping rectangular trenches 10 μm deep were milled using a beam current of 16 nA to create a cantilever top surface approximately 32 x 7 μm. Using a large beam current allowed faster milling but did not produce vertical sides due to the lower precision associated with a large beam tail. Using a beam current of 2 nA and three overlapping trenches of 8 μm depth, produced a cantilever of dimensions 30 x 5 μm with vertical sides. To form the underside of the cantilever, the sample was tilted 45° (about the long axis of the cantilever), and using a beam current of 2 nA the base was milled away approximately 5 μm. The cantilever was then rotated and this same milling procedure was carried out on the other side, produce a cantilever that had a symmetrical pentagonal cross section. The target dimensions are shown in figure 4.1. The SEM was used to capture images after the milling of the cantilever was complete to measure and record the dimensions of the cantilever.

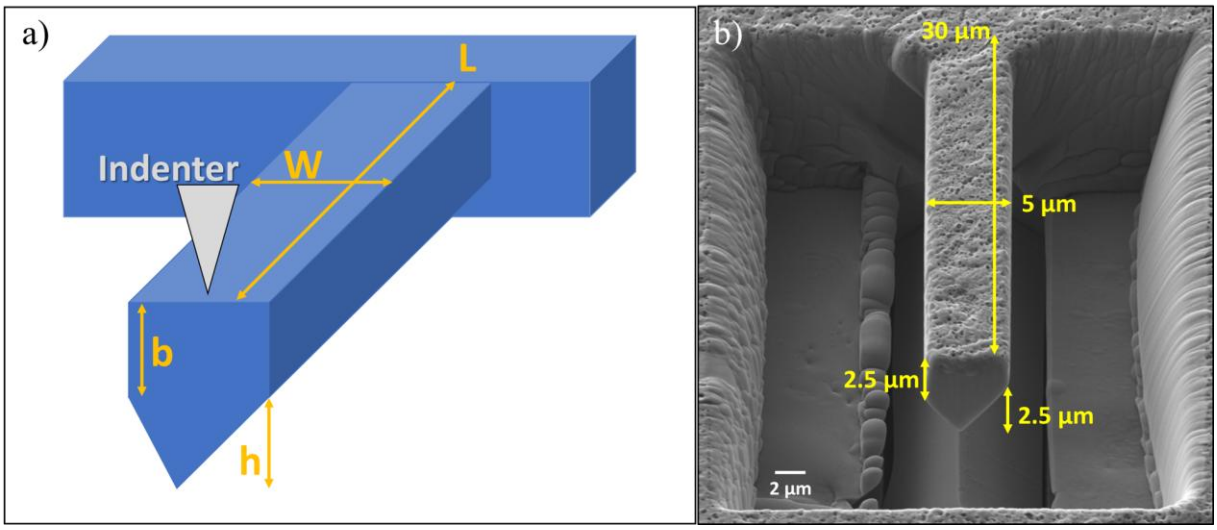

Figure 4.1: a) Schematic to demonstrate the shape of pentagonal cantilever to be milled and positioning of indenter tip, b) SEM image showing microcantilever of Li_6PS_5Cl with the ideal target dimensions.

4.3.6 Testing of Cantilevers

Testing of the prepared microcantilevers was carried out using the Bruker-Hysitron PI89 in-situ nanoindenter. The Semi Labs Transfer Shuttle was used to ensure an airless transfer into the glovebox connected SEM and in-situ indenter. The indenter was used in the lowload mode configuration and with an electrically conductive diamond cube corner instrumentation tip (Bruker-Hysitron). By using the sharper cube corner tip this allowed for greater visibility when positioning the indenter so that indenter tip could be accurately placed at a known distance from the fixed end and in the center-line of the cantilever. Before each indent, the thermal drift rate was measured when in contact with the sample, over 40 s using a preload of 5 µN, and corrected for. The cantilever was then loaded to failure by fracture using the Hysitron displacement controlled closed-loop feedback mode, with a displacement rate of 2 nms^{-1}, an example of the load-displacement curve of a tested microcantilever is shown in figure 4.12, in section 4.4.3. The fracture point was identified by a significant decrease in measured load, the peak load was

measured and recorded as the fracture load. The fracture load and measured dimensions of the cantilever was used to calculate the fracture stress of the cantilever.

4.4 Results and Discussion

4.4.1 Nanoindentation

Similarly to the previous chapter, nanoindentation was used to characterise the different Li_6PS_5Cl solid electrolytes produced in accordance with section 4.3.1. In this chapter lowload nanoindentation to provide continuous stiffness measurement (CSM) was also used.

4.4.1.1 Lowload and Highload Testing

As stated in 4.3.3 the lowload indentation was performed using continuous stiffness measurement mode and it was possible to measure modulus and hardness as a function of depth. For highload indentation single indents were performed and the stiffness (S) calculated from the gradient of the initial linear upper portion of the unload curve as shown in Figure 4.2. A step-by-step guide as to how the stiffness was calculated is shown in section 2.6.2.

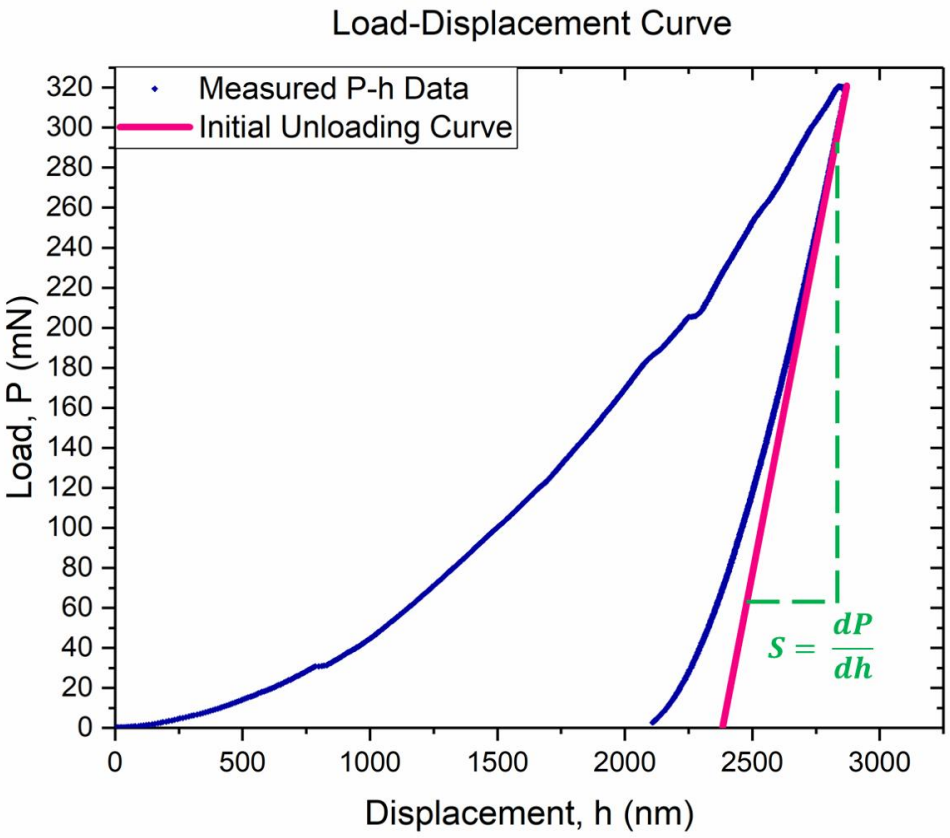

Figure 4.2: A load-displacement curve form a pure Arygrodite sample with and applied maximum load of 320 μN represented by the blue dots. A linear extrapolation of the initial portion is shown by the pink solid line. The calculated Stiffness (S) take from the gradient of the unload curve is shown by the green dashed line.

Indentation was carried out in total across a range of loads from 1-500 mN, using both lowload and highload testing modes. Analysis of the raw data sets was carried out as described in section 2.6.2, the results of modulus and hardness for both testing regimes are shown in figure 4.3. As both testing modes characterise the fundamental mechanical properties of the Li_6PS_5Cl a combined plot of both testing regimes is possible, as shown in figure 4.4.

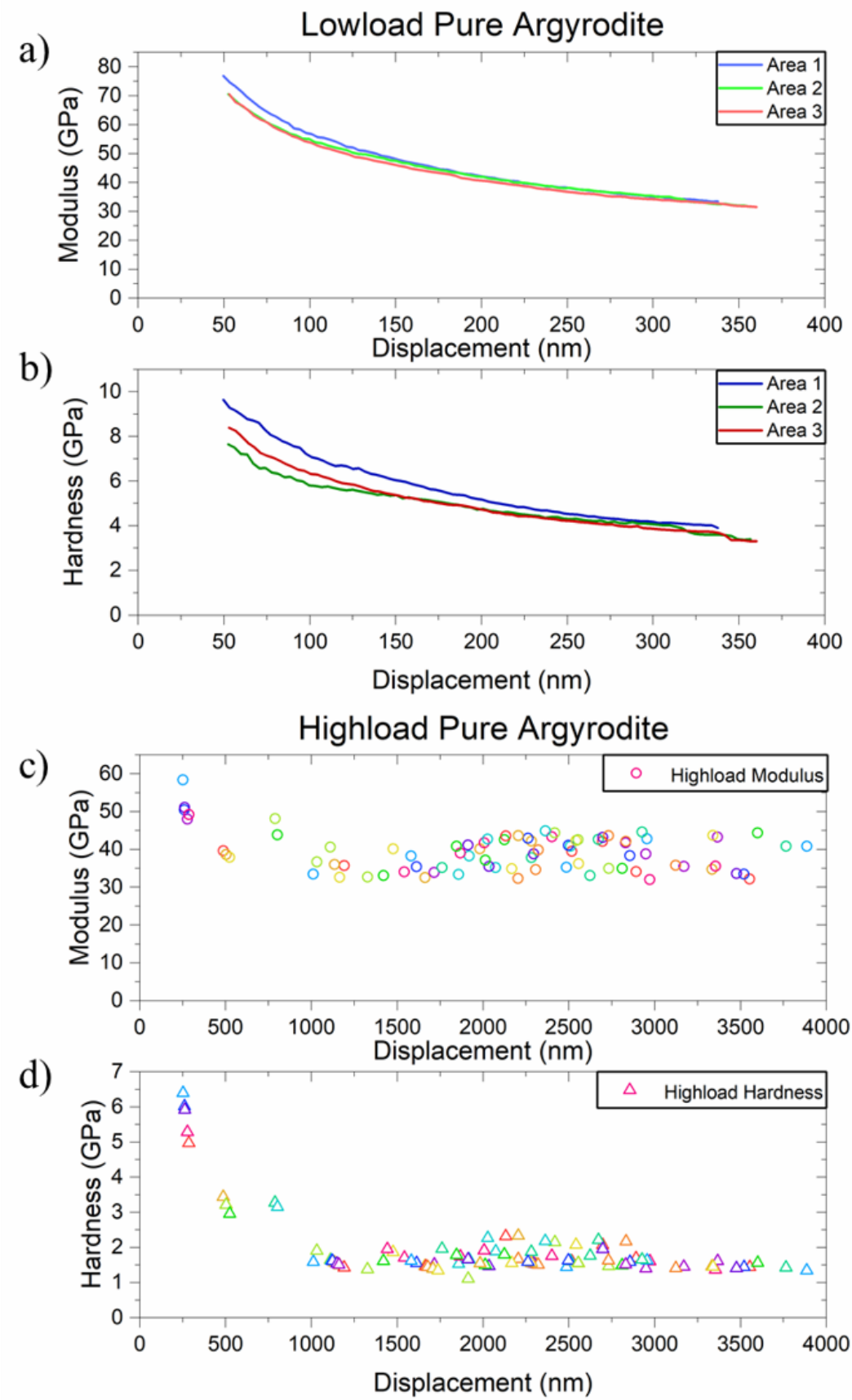

Figure 4.3: a) Modulus-displacement data, lowload testing mode. B) Hardness-displacement data, lowload testing mode. C) Modulus-displacement data, highload testing mode. D) Hardness-displacement data, lowload testing mode.

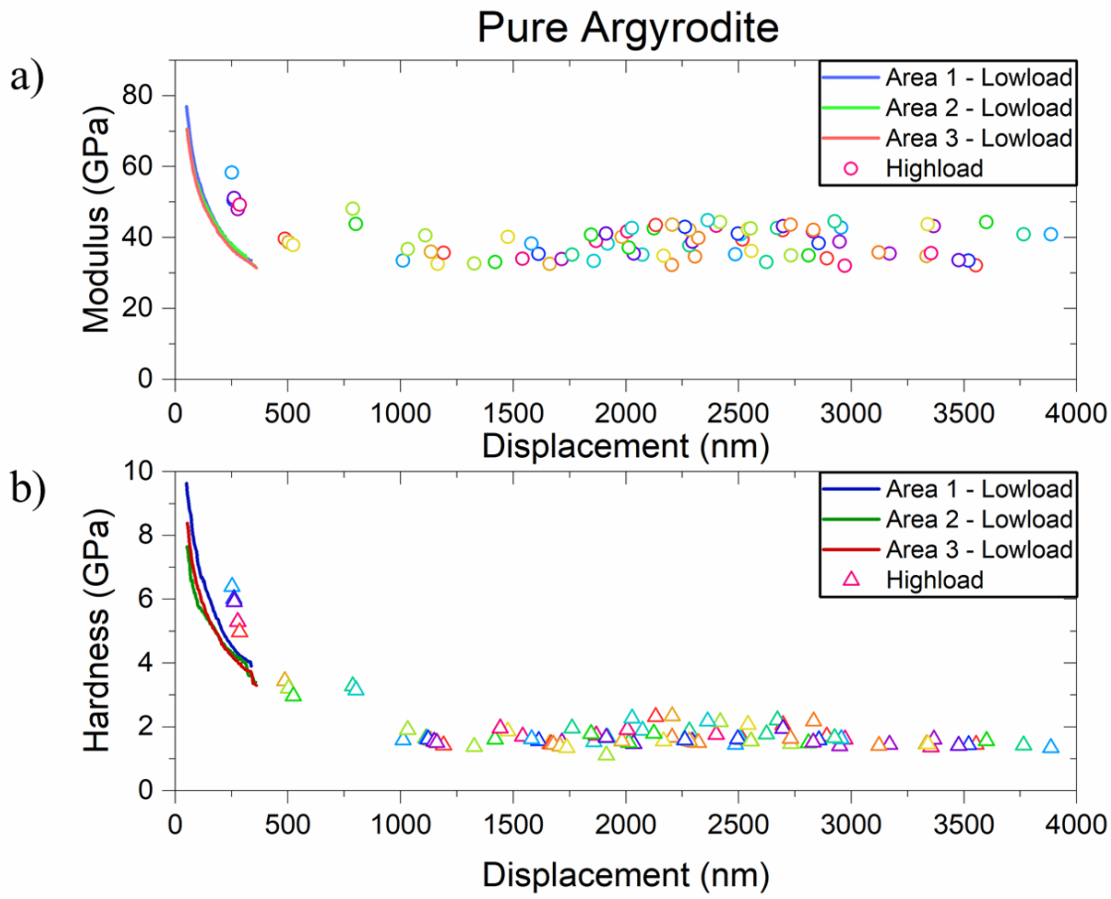

Figure 4.4: Graphs for both lowload and highload testing data combined showing a) modulus-displacement curve b) hardbesss-displacement curve.

In the modulus plot of figure 4.4a) there is initially a downward sloping curve, showing modulus decreasing with displacement; this trend is represented by data from both the lowload and highload testing modes. This trend continues until approximately a displacement of 1000 nm at which the curve asymptotically levels out and becomes horizontal, represented by the highload data. In the hardness plot of figure 4.4b) again there is initially a downward sloping curve, showing hardness decreasing with displacement; the trend represented by data from both lowload and highload testing modes. Similarly, to the modulus, this trend continues until approximately a displacement of 1000 nm at which the curve asymptotically levels out and becomes horizontal, represented by the highload data.

In previous indentation studies, initially decreasing trends in hardness with displacement can be attributed to the indentation size effect (ISE).[268] The ISE describes a phenomenon observed in indentation experiments; as the indentation depth decreases, the hardness of the material appears to increase.[269] The Nix and Gao model is the most popular and widely used model to explain these experimental observations known as the ISE.[268,270] The model states that geometrically necessary dislocations (GND) are required to accommodate strain caused by the volume of material displaced by the indenter tip. The relationship between hardness (H) at any given depth (h) and the intrinsic material property of hardness (H_0) is described by equation 4.1, where h^* is a constant that depends on the shape of the indenter tip used.

$$H = H_0 \sqrt{1 + \frac{h^*}{h}} \quad (eqn\ 4.1)$$

The ISE is readily seen in metals due to their ability to deform plastically, more easily creating GNDs as they are more ductile. Ceramics being generally more brittle will have other mechanisms to accommodate during indentation; Li_6PS_5Cl being a particularly soft ceramic will again have other mechanisms allowing it to deform more easily.

The ISE could explain the decrease in hardness with increase in depth, but it would not be able to explain the same change seen in modulus. Further investigation into the sample preparation showed that sample preparation, specifically the surface finish, could be an affecting factor. The final grinding stage used 4000 SiC grit paper, which had a particle size of ~ 1 μm. This resulting in the sample surface not being perfectly flat and at depths of less than 1 μm the actual surface contact area is likely to be greater than the calculated projected contact area. This would result in an overestimate for both modulus and hardness as evidenced by the trend in figure 4.4. At greater depths both curves asymptotically converge towards a horizontal line; this indicate a single true value for the intrinsic material properties of both modulus and hardness. As a

result, going forwards in subsequent indentation tests, only the highload testing mode was used and any data recorded at depths <1000 nm removed as it was deemed to be unreliable due to sample surface preparation issues.

4.4.1.2 Porosity/Density Results

The improved density of the Li_6PS_5Cl solid electrolyte is expected to be accompanied by an improvement in the mechanical properties of the material. Four samples with different densities, produced following the methods in sections 4.3.1 and 4.3.2, were tested using highload Berkovich indentation, according to the procedure in section 4.3.3. The figures below show both the modulus and hardness results for the different density samples, calculated using the method set out in previously in section 2.6.2, displayed on double Y-axis graphs. All curves in figure 4.5 show a horizontal trend modulus and hardness results that is invariant with depth; which indicates a single value for the intrinsic material properties of modulus and hardness respectively.

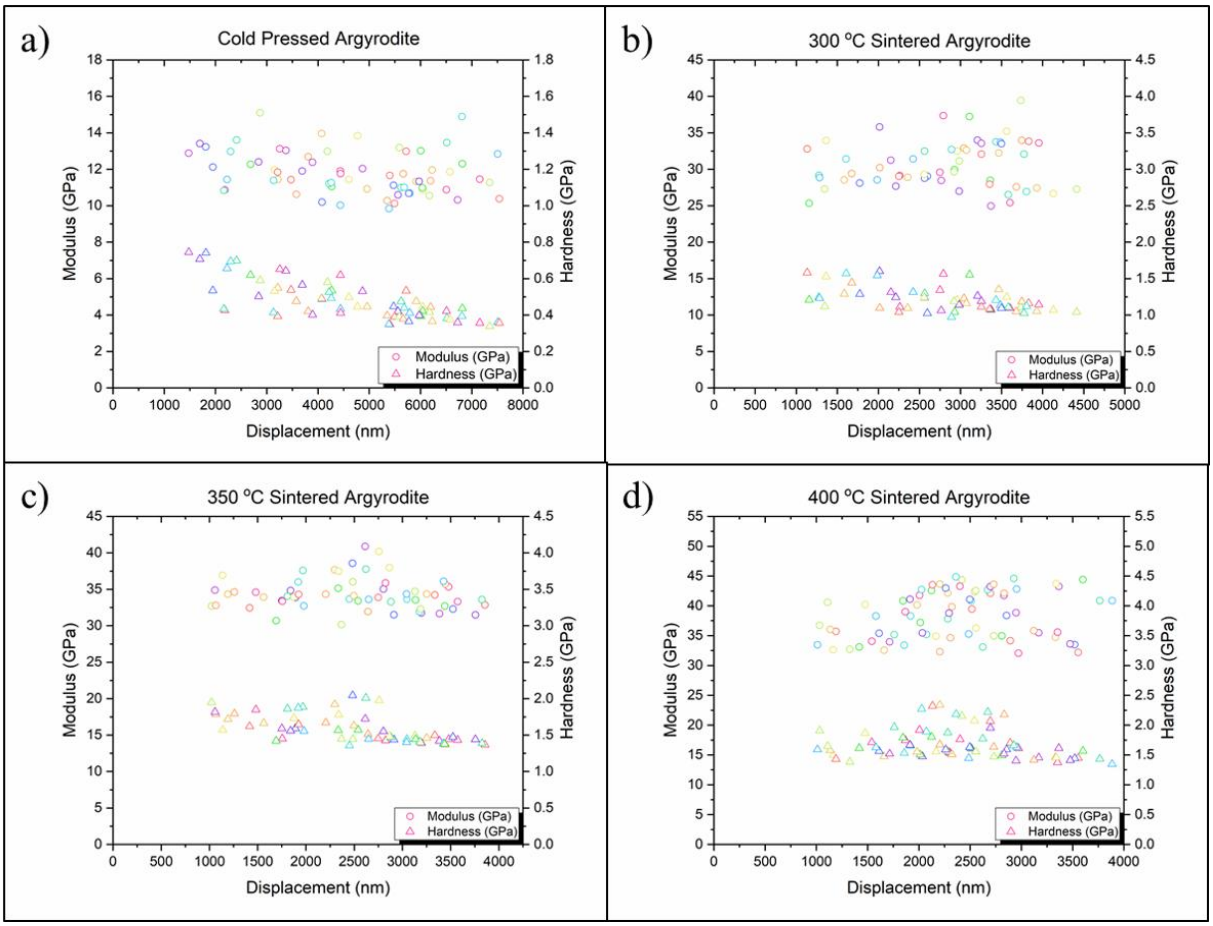

Figure 4.5: Modulus-displacement and hardness-displacement values for a) Cold pressed samples, b) field assisted sintered at 300 °C sample, c) field assisted sintered at 350 °C sample, d) field assisted sintered at 400 °C sample.

To calculate the intrinsic value for the modulus of each respective material, all the individual moduli results were fit to a log-normal distribution. From this distribution the mode of the data was taken to be the true material property, as the expected value of the distribution. This process was followed to calculate the modulus of each material, and then repeated with the hardness results to find the intrinsic hardness value of each material. Figure 4.6 shows a summary comparing both the intrinsic modulus and hardness values for each different density sample. The error bars displayed on figure 4.6 represent a 95% confidence interval for the upper and lower bounds for the range of each material property.

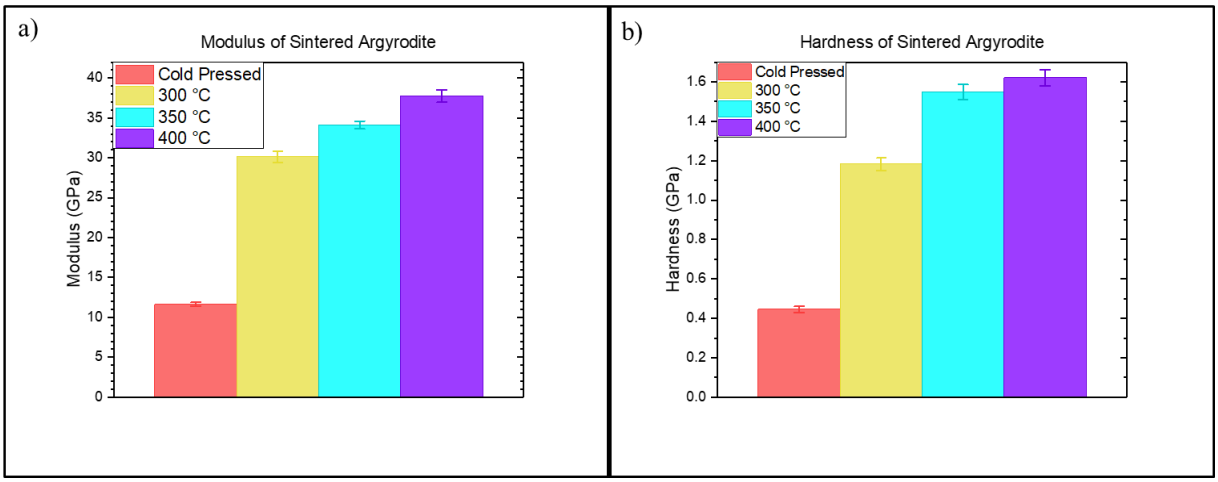

Figure 4.6: Graph showing a summary of a) modulus, b) hardness values for Li_6PS_5Cl of different densities.

Figure 4.6a) shows a significant increase in modulus from the lowest density cold pressed sample to the field assisted sintered samples. Figure 4.6b) also shows a significant increase in hardness from the cold pressed sample to the field assisted sintered samples. Both of these trends show that the sintering of Li_6PS_5Cl is accompanied by an improvement in mechanical properties.

The field assisted sintered samples display an increase in density with increasing sintering temperature. As sintering temperature increases an increase in both the modulus and hardness values is observed for all the samples. Therefore, as the density increases the mechanical properties of modulus and hardness are improved in Li_6PS_5Cl, which accompanies an improvement in electrochemical properties as listed in section 4.2.

It should also be noted the difference in 95% confidence interval between the cold pressed and sintered samples. As mentioned in section 4.3.2 surface preparation, in particular obtaining a flat surface was very difficult due to the air-sensitive nature of the samples. The smaller confidence interval seen in the cold pressed sample can be attributed to its method of production and resulting surface finish. The cold pressed sample was made by pressing in a stainless steel

dieset between two mirror-finish spacers, in accordance with the method set out in section 4.3.1. This would have created a relatively flat surface, therefore fewer incidents where the calculated projected contact area differed to the actual contact area, resulting in less variance in indentation test result and therefore a smaller confidence interval. The sintered samples were formed using field assisted sintering in a graphite dieset, as described in section 4.3.1, as a result a series of grinding steps, as described in section 4.3.2, were required to remove any graphite and achieve the best possible surface finish. These grinding steps produced a less smooth surface finish than that produced by the cold pressing method. This meant that the sintered sample had a higher variance in modulus and hardness results, and therefore a comparatively larger confidence interval. Overall, the confidence intervals for all values are relatively small, meaning that the measured values of modulus and hardness values can be taken as true.

4.4.1.3 Li_6PS_5Cl-CSZ Results

The aim of producing a Li_6PS_5Cl-CSZ composite is to improve the mechanical properties of the solid electrolyte, in particular the fracture toughness properties. Adding CSZ to Li_6PS_5Cl not only will affect fracture toughness but other intrinsic material mechanical properties such as modulus and hardness. The highload indentation tests were carried out following the procedure in section 4.3.3, and the expected value for both modulus and hardness was calculated using the method described in section 2.6.2.

An estimation of modulus for each respective Li_6PS_5Cl-CSZ composite was made using the rules of mixtures, with the Voigt model to define the upper bound and the Reuss model to define the lower bound.[271] The Voigt model is based on an equal strain assumption, with the two components deforming in series under stress. The following equation 4.2 represents the Voigt model and was used to calculate the upper bound of the composite modulus, E_c.[272]

$$E_c = fE_p + (1-f)E_m \ (eqn\ 4.2)$$

Where

- E_p is the modulus of the introduced particles, CSZ.[273]
- E_m is the modulus of the original matrix, Li_6PS_5Cl.
- f is the volume fraction of the particles.

The Reuss model is based on an equal stress assumption, with the two components deforming in parallel under stress. The following equation 4.3 represents the Reuss model and was used to calculate the lower bound of the composite modulus, E_c.[274]

$$E_c = \left(\frac{f}{E_p} + \frac{(1-f)}{E_m}\right)^{-1} \ (eqn\ 4.3)$$

The upper and lower bounds for the modulus of the Li_6PS_5Cl-CSZ composite are shown in figure 4.7a) below, alongside the experimentally measured modulus values. Figure 4.7a) shows that the measured values are within the calculated upper and lower bounds values for modulus.

The rule of mixtures can also be applied to calculate upper and lower bound estimates for the hardness.[271] Using the same Voigt and Reuss models, with the same respective strain and stress assumptions, the following equations can be used to define upper and lower bounds. Equation 4.4 defines the Voigt model for hardness, H_c.

$$H_c = fH_p + (1-f)H_m \ (eqn\ 4.4)$$

Where

- H_p is the hardness of the introduced particles, CSZ.[273]
- H_m is the hardness of the original matrix, Li_6PS_5Cl.
- f is the volume fraction of the particles.

Equation 4.5 defines the Reuss model for hardness, H_c.

$$H_c = \left(\frac{f}{H_p} + \frac{(1-f)}{H_m}\right)^{-1} \quad (eqn\ 4.5)$$

The upper and lower bounds for the hardness of the Li_6PS_5Cl-CSZ composite are shown in figure 4.7b) below, alongside the experimentally measured hardness values. Figure 4.7b) shows that when considering the error bars for the measured values of hardness, they fall within the calculated upper and lower bounds values for hardness.

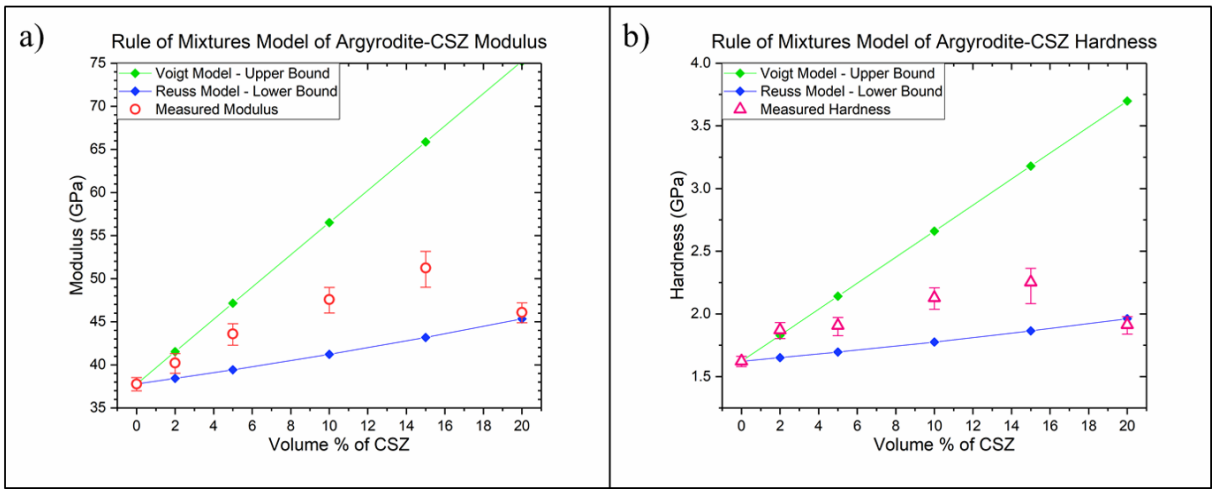

Figure 4.7:The rule of mixtures prediction for a) modulus, b) hardness, using Voigt and Reuss models to define the upper and lower bounds.

Figure 4.8 below shows a summary comparing both the intrinsic modulus and hardness values for each different composition of Li_6PS_5Cl-CSZ sample. The error bars displayed on figure 4.8 represent a 95% confidence interval for the upper and lower bounds for the range of each material property.

The trend displayed by figure 4.8a) shows initially as the volume percent of added CSZ increases so does the modulus of the Li_6PS_5Cl-CSZ composite. This trend is observed from pure Li_6PS_5Cl with a modulus of 37.8 ± 0.8 GPa, up to a maximum modulus value of 51.2 ± 2.0 GPa for Li_6PS_5Cl with 15% added CSZ. This trend can be explained by the strengthening mechanism of load sharing.[275] As the modulus of CSZ, ~ 225 GPa,[273] is significantly higher

than that of pure Li_6PS_5Cl, 37.8 GPa, it will resist elastic deformation more than Li_6PS_5Cl. During the application of stress there will be a redistribution of load within the composite, with more load carried by the CSZ with a smaller amount of strain. This means that the overall composite material will deform less; hence the stiffness, and therefore the modulus, will increase. However, for greater amounts of CSZ added, 20%, the modulus value falls off, 46.1 ± 1.1 GPa. Examining images of the sample surface shows that at this higher composition the added CSZ nanoparticles have agglomerated, meaning they are no longer evenly distributed throughout the sample. This uneven distribution means that under an applied stress, the load is not effectively shared throughout the sample, therefore the overall resistance to deformation will not be as great resulting in the observed decrease in modulus.

Figure 4.8b) shows that this trend in modulus is also be observed in the measured hardness values, with hardness increasing from 1.62 ± 0.04 GPa for pure Li_6PS_5Cl, up to 2.25 ± 0.14 GPa for 15% CSZ, and then as further CSZ is added hardness decreases to 1.91 ± 0.07 GPa, for 20% CSZ. One mechanism to explain the increase in hardness is again the concept of load sharing.[275] The CSZ has a higher inherent hardness ~12 GPa,[273] therefore it will have a greater resistance to plastic deformation than Li_6PS_5Cl. For up to 15% CSZ the particles appear well distributed and will carry a significant portion of the applied load, therefore reducing the overall stress on the Li_6PS_5Cl matrix. This reduces the amount of plastic deformation in the total composite, leading to an increased hardness value. As mentioned previously the 20% CSZ was not well distributed and formed agglomerates, meaning that the load was not well shared between CSZ particles and Li_6PS_5Cl matrix, resulting in a decrease in hardness for increase in volume percent CSZ.

Another strengthening mechanism that aids to resist plastic deformation is transformation toughening.[276,277] As discussed in section 4.3.1 CSZ was used as the zirconia is in its metastable tetragonal phase, which under applied stress can undergo a martensitic transformation to monoclinic phase zirconia particles; this phase change is known as transformation toughening. The phase transformation is accompanied by a volume increase in the zirconia of ~3-5%, this volume expansion generates a compressive stress around the transforming material and acts to resist any plastic deformation. However, simply by introducing the CSZ particles does not guarantee that transformation toughening will occur and the increase in modulus maybe simply be from introducing a stronger composite material as explained above. To investigate whether transformation toughening is occurring, a composite Li_6PS_5Cl sample with 20% zirconia (in its monoclinic phase) was produced using the field-assisted-sintering process previously described and tested using highload indentation. The aim being to compare the two 20% samples, one with the CSZ and zirconia particles initially in the tetragonal phase and the other zirconia particles in its monoclinic phase so no transformation (and therefore no toughening) would occur.

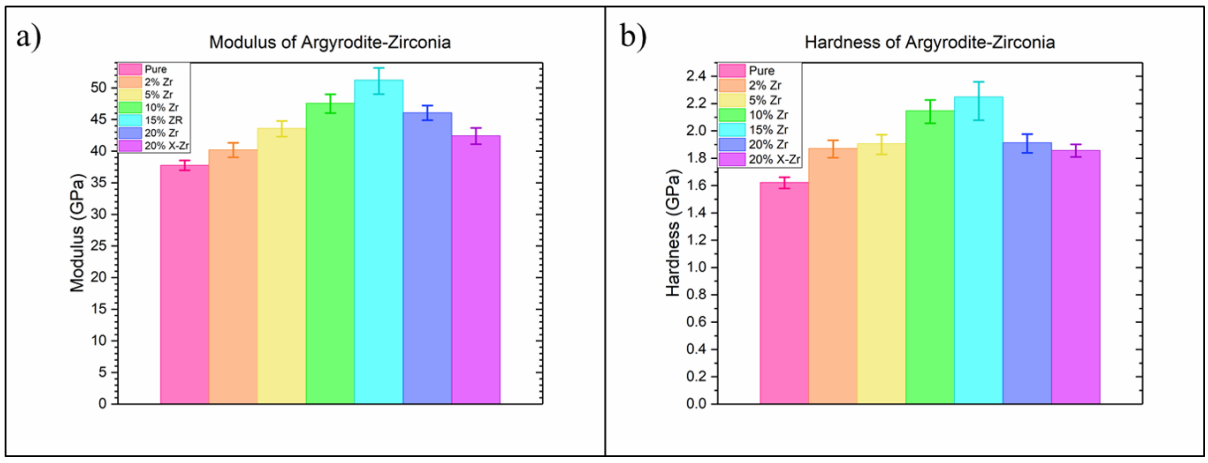

Figure 4.8: Graph showing a summary of a) modulus, b) hardness values for different Li_6PS_5Cl-CSZ composites.

The modulus and hardness values for the Li_6PS_5Cl-20% zirconia sample, were calculated from the indentation data following the same procedure as described a 2.6.2. Figure 4.8a) shows a

lower modulus, 42.5 ± 1.3 GPa, when compared to the Li_6PS_5Cl-20% CSZ sample, 46.1 ± 1.2 GPa. This comparatively higher modulus for the Li_6PS_5Cl-20% CSZ sample could be evidence that the sample is undergoing transformation toughening, and the compressive stress generated by the transformation effect is enhancing the stiffness. However, this difference in indentation modulus between the samples could also be caused by the initial difference in the elastic modulus of the compositing particles, CSZ and zirconia respectively. The zirconia particles have a lower elastic modulus (~205 GPa) than CSZ,[278] suggesting that less load sharing would occur; therefore it would be expected that the Li_6PS_5Cl-zirconia composite will have a lower modulus than the composite. Using the rule of mixtures model, the ~9% decrease in the pure zirconia modulus compared to the CSZ modulus, should only lead to ~1-2% difference in modulus when comparing 20% composite samples of Li_6PS_5Cl-zirconia and Li_6PS_5Cl-CSZ. However, the results when comparing the two composites is a ~8% difference in modulus, which is greater than the difference expected if purely caused by the inherent material properties of each respective compositing material; suggesting that some additional stiffness maybe be occurring in the Li_6PS_5Cl-CSZ due to transformation toughening.

In figure 4.8b), the hardness for 20% Li_6PS_5Cl-CSZ, 1.91 ± 0.07 GPa, is slightly higher than that of the Li_6PS_5Cl-zirconia composite, 1.86 ± 0.05 GPa. This increase in hardness can be explained by the compressive stresses caused by the phase transformation leading to an improved resistance to plastic deformation, and therefore could evidence transformation toughening. An alternative explanation is that the lower hardness of zirconia (~11 GPa) resulted in less of the load being able to be shared in the Li_6PS_5Cl-zirconia sample. There is a ~2.6% in the hardness measurements of the 20% composites, using the rule of mixtures the ~9% difference between the inherent hardness of CSZ and zirconia respectively, could be responsible for up to a ~5% difference in the hardness between the 20% composites, therefore accounting

for the difference in hardness seen. However, the difference in the values is small and the confidence intervals of both measured hardness values overlap, meaning that it cannot be said with confidence that the difference in these values is significant.

Transformation toughening mainly aids with resisting plastic deformation, in particular the generated compressive stresses work to hinder crack propagation. In section 4.4.2 fracture toughness of the samples is measured to investigate further as to whether transformation toughening is occurring.

4.4.2 Indentation Fracture Toughness Results

Once a lithium dendrite has initiated a crack, failure by short-circuit can occur if the crack penetrates throughout the whole thickness of the solid electrolyte, allowing the lithium dendrite to transverse from anode to cathode. The driving mechanism for crack propagation is the hydrodynamic pressure build up caused by the lithium plating into the crack, creating a resultant stress field at the dry crack tip. By modelling the stress field, the strain energy release rate (energy available to drive the crack) can be calculated.[261] For the crack to propagate the strain energy release rate must exceed the fracture criterion of the solid electrolyte which is an intrinsic material property dependent on the modulus, hardness and fracture toughness. Due to the air-sensitive nature of Li_6PS_5Cl and sulphides more generally, no experimental measurements of fracture toughness exist in the literature. As conventional toughness testing methods were not possible, a pioneering testing method using highload indentation using a cube corner tip was used to conduct the experiments; providing the first experimentally measured value of fracture toughness of Li_6PS_5Cl. A summary of solid electrolyte fracture toughness values produced by Kalnaus et al. with values sourced from both experimental and theoretical

measurements, is shown in figure 4.11b). The fracture toughness value for Li_6PS_5Cl, represented by a green square, is overlaid on this graphic, showing that the experimentally measured value fits in well amongst other values.[279]

If propagation of the crack can be restricted, then the lithium dendrite will be unable to traverse the solid electrolyte therefore preventing failure by short circuit. By increasing the fracture toughness of the solid electrolyte, resistance of crack propagation will also increase. As described in section 4.3.1 Li_6PS_5Cl-CSZ composites were manufactured, with the aim to improve the mechanical properties; especially the fracture toughness.

Indentation was carried out as described in section 4.3.4 and images of the post indentation sites are shown in figure 4.9. An example of a cube corner indent is shown figure 4.9a), the radial cracks were measured using the software ImageJ and fracture toughness calculated using the LEM equation.[228] Due to the sharp geometry of the cube corner tip, at higher loads fracture also occurred via other crack systems, such as chipping. Figure 4.9b) shows a 400 mN indent with chipping being the dominant crack system by which fracture occurred. For the LEM equation to be valid fracture must occur by radial cracking only,[225,226] therefore any indents that showed chipping were not used for this investigation; this resulted in mostly the 100 and 200 mN indents being used.

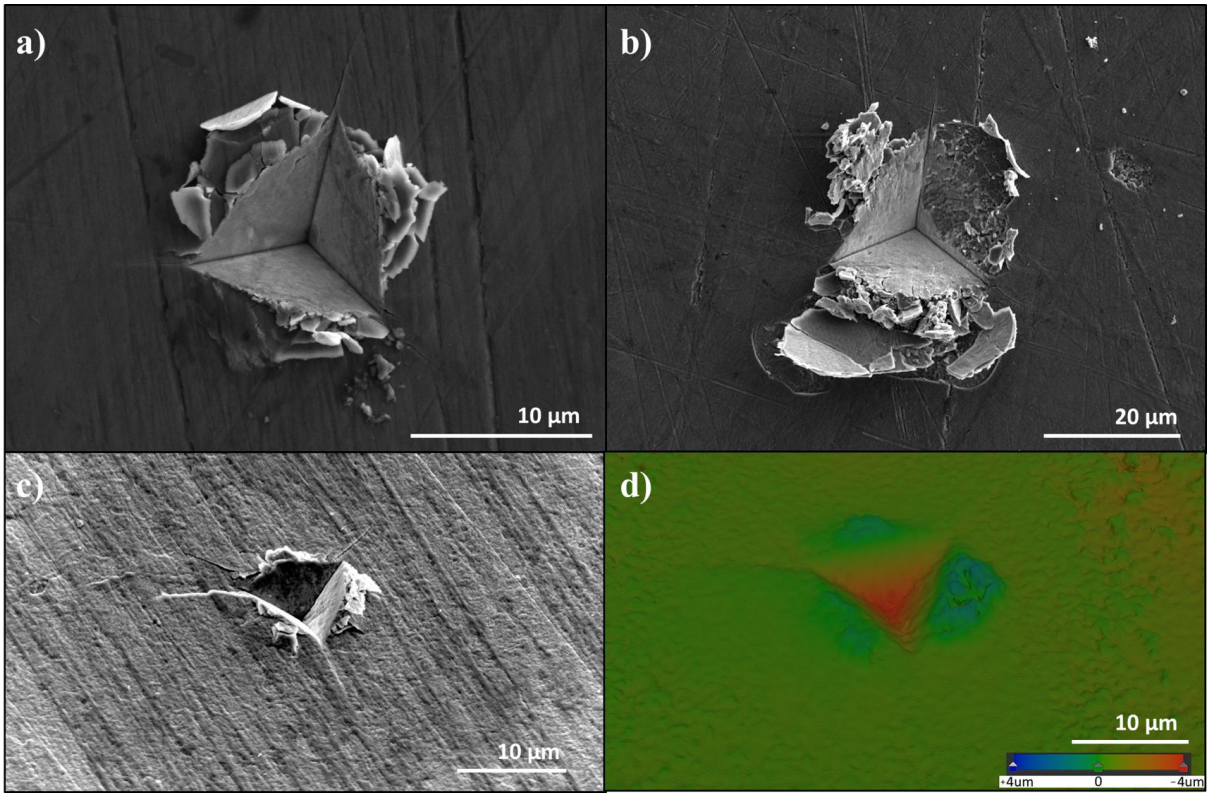

Figure 4.9: Post indentation images of 99% dense Li_6PS_5Cl a) 100 mN cube corner indent, showing radial cracks emanating from the corners, b) 400 mN cube corner indent, showing significant chipping, demonstrating presence of an alternate fracture mechanism, c) a digitally constructed 3D image to demonstrate minimal pileup is observed surrounding a 100 mN cube corner indent, d) a colour map which shows the degree to which pileup occurred surrounding a 100 mN cube corner indent.

Using this method of cube corner indentation and LEM model, the fracture toughness of all the Li_6PS_5Cl-CSZ composites was investigated. Figure 4.10 shows example indentation sites post a 200 mN cube corner indent for each Li_6PS_5Cl-CSZ composite. The figure shows a change in the microstructure as the volume of CSZ increases; with increasingly lighter regions seen on the SEM images of the surface corresponding to an increased presence of CSZ particles. Figure 4.10 also shows that as the volume of CSZ increases (up to 15% CSZ) the residual indent impressions and the length of radial cracks decrease in size and length respectively.

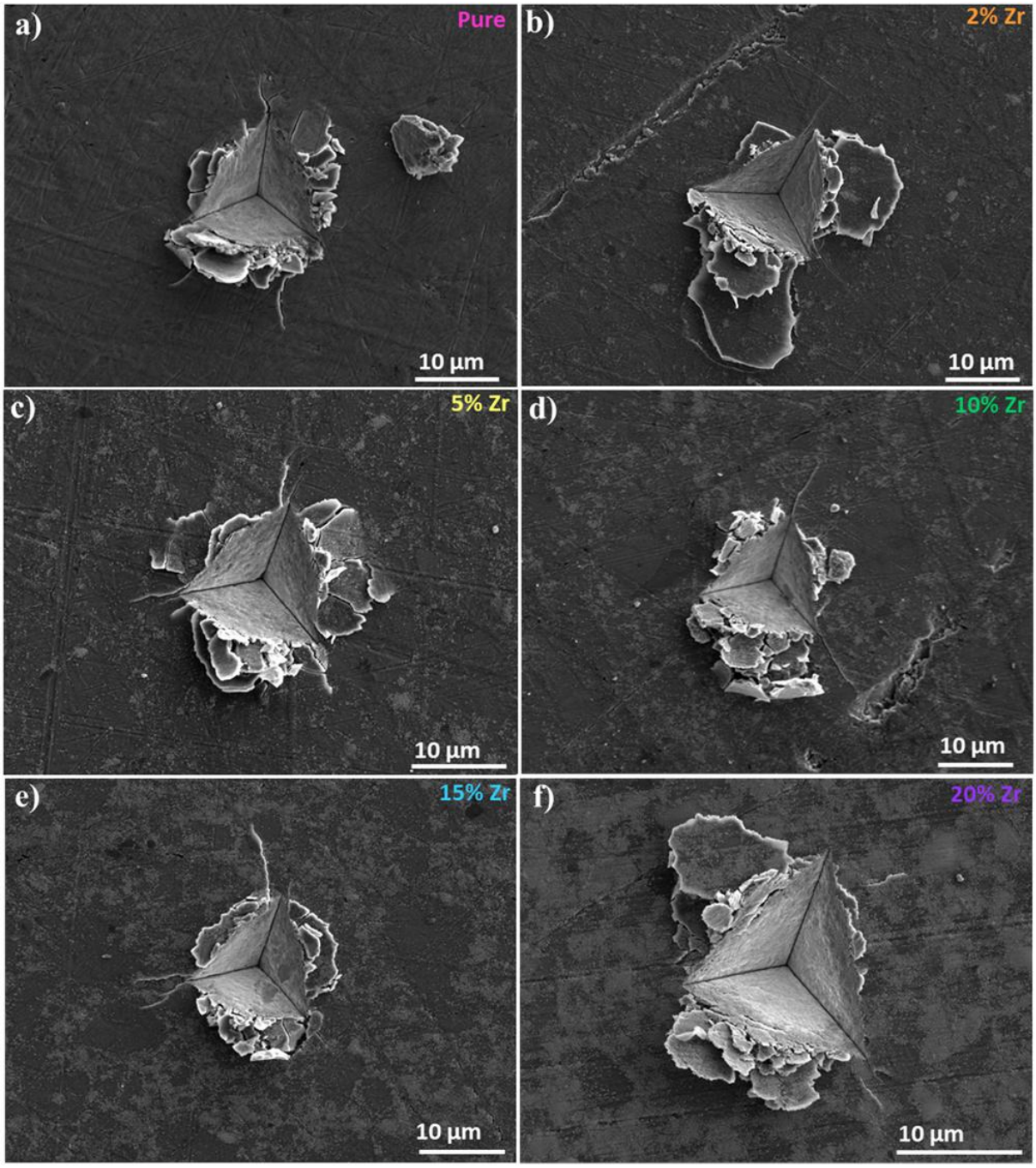

Figure 4.10: SEM images of the Li_6PS_5Cl-CSZ composite microstructures and the residual indentation impression following a 200 mN cube corner indent for a) pure Li_6PS_5Cl, b) 2% CSZ, c) 5% CSZ, d) 10% CSZ, e) 15% CSZ, f) 20% CSZ.

CSZ has a higher fracture toughness (~13 MPa.m$^{0.5}$) than pure Li_6PS_5Cl, measured to be 0.669 ± 0.033 MPa.m$^{0.5}$, which means that it is a significantly tougher material. Adding the tougher CSZ particles to the existing Li_6PS_5Cl matrix can significantly increase the fracture toughness as shown in figure 4.11a), through mechanisms such as crack deflection or transformation

toughening. The figure shows an increasing trend in fracture toughness as the volume percent of CSZ increases, up to 0.834 ± 0.027 MPa.m$^{0.5}$ for 15% Li_6PS_5Cl-CSZ. For this section of data, a linear fit (demonstrated by the pink line of figure 4.11a) can be used to draw a proportional relationship between the volume percent of CSZ added and the measured fracture toughness. The goodness-of-fit was measured to be 0.94 using the adjusted R-square method, this is a high value indicating that this proportional relationship can be drawn with a degree of confidence.

One toughening mechanism that could explain this observed increase in fracture toughness is crack deflection. As a crack propagates through the Li_6PS_5Cl, if it encounters a tougher CSZ particle the crack will likely deflect to go around the particle; this increases the overall crack length, therefore more energy is needed for the crack to propagate.[280] Another toughening mechanism is crack bridging, where the tougher CSZ particles can act to bridge the crack faces; therefore, increasing the energy required for the separation of the crack faces, slowing down the crack growth.[281] Both of these toughening mechanisms require small and evenly disturbed CSZ particles, as this increases the possible interaction area of the crack with the tougher particles. For the 20% Li_6PS_5Cl-CSZ composite the fracture toughness falls off slightly to 0.818 ± 0.028 MPa.m$^{0.5}$. Despite the decrease only being small in value, it quite significantly falls off the proportional trend, pink line in figure 4.11a), observed for 0-15% added CSZ. An explanation for this could be the poor distribution of CSZ particles, as stated in section 4.4.1.3 for the 20% Li_6PS_5Cl-CSZ the particles appear to have agglomerated, forming bigger particles and not uniformly distributed. This would reduce the effect of the toughening mechanisms such as crack deflection and crack bridging, resulting in the observed decrease in fracture toughness.

The observed increase in fracture toughness of the Li_6PS_5Cl-CSZ below 20% could also be explained by transformation toughening. As discussed previously in 4.4.1.3, CSZ contains stabilised zirconia which exists in a metastable tetragonal phase. Following crack propagation through the Li_6PS_5Cl-CSZ composite, the stress field around the crack tip can instigate a phase transformation of the metastable zirconia from the tetragonal phase to monoclinic phase, which is more stable. This phase transformation is accompanied by a volume expansion of ~3-5%, creating a compressive stress around the crack tip (transforming region); this stress acts to close the crack tip, therefore restricting further crack propagation.

As mentioned in section 4.4.1.3, the presence of CSZ particles does not guarantee the phase transformation, and resultant toughening effect, will occur. To investigate as to whether the transformation toughening effect is present fracture toughness of Li_6PS_5Cl-20% CSZ and Li_6PS_5Cl-20% zirconia samples were compared. As figure 4.11a) shows the fracture toughness for the Li_6PS_5Cl-20% zirconia sample is lower, 0.786 ± 0.028 $MPa.m^{0.5}$. This comparative decrease could be taken as evidence that transformation toughening is occurring in the sample with CSZ to produce a higher fracture toughness for the same volume of particles. The addition of either CSZ or zirconia particles will cause toughening to occur via mechanisms such as crack deflection and crack bridging. Therefore, the increased fracture toughness for the Li_6PS_5Cl-20% CSZ could be due to transformation phase change of the CSZ particles. Overall there is insufficient evidence to say with that transformation toughening is either occurring or not occurring with any degree of confidence, further investigation such as the use of high resolution TEM is needed to able to draw a conclusion on the presence of transformation toughening.

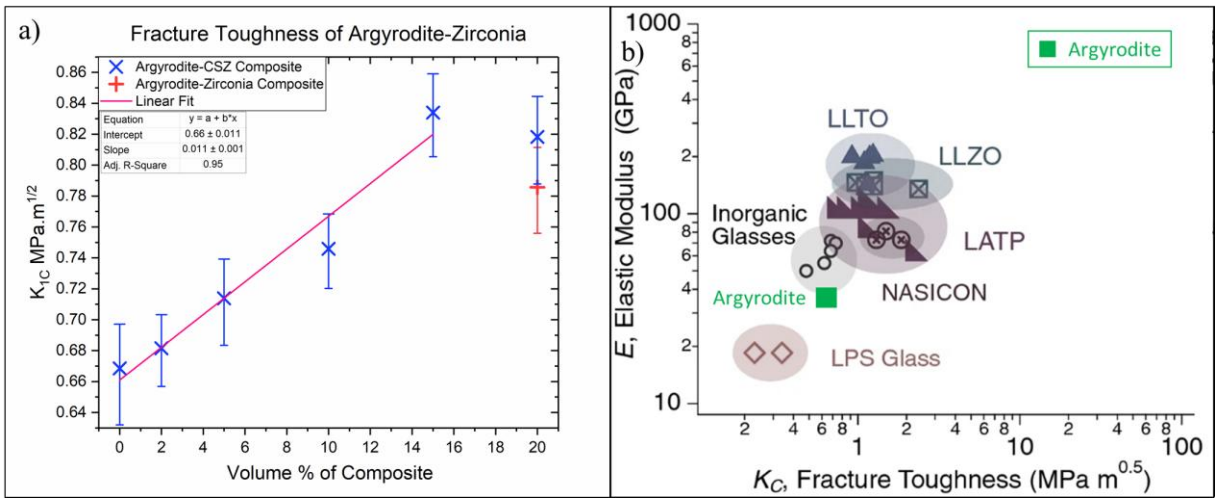

Figure 4.11: a) Fracture toughness-volume of added composite material graph, derived proportional relationship is represented by the pink line, b) Experimentally measured fracture toughness value of Li_6PS_5Cl, green square, overlaid on solid electrolyte fracture toughness summary figure produced by Kalnaus et al.[279]

4.4.3 Cantilever Bending Results

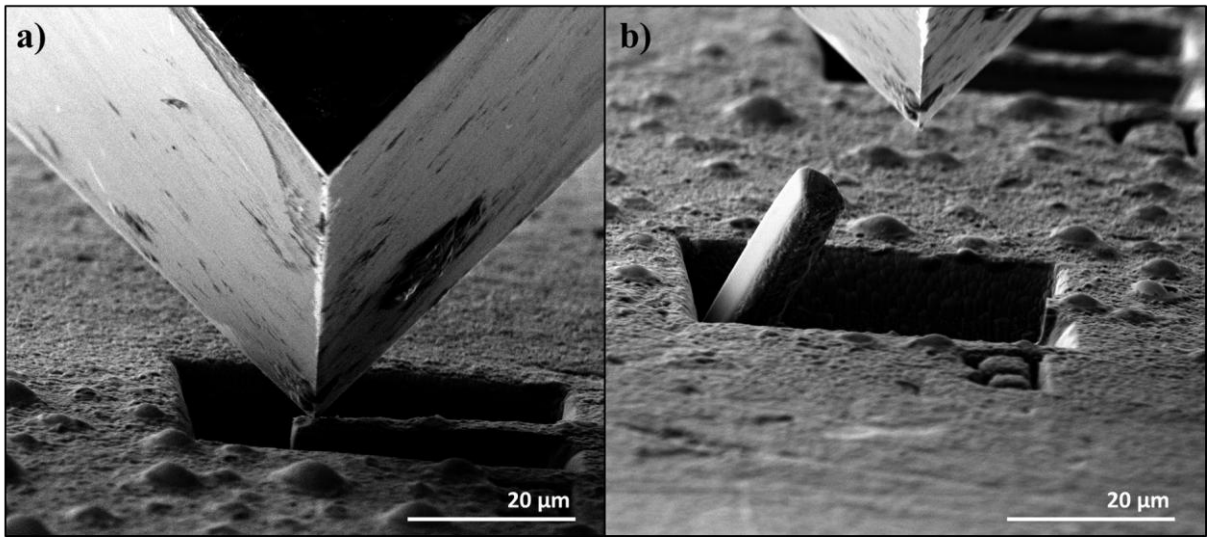

Figure 4.12: a) shows image of indenter applying load to cantilever, b) shows image of cantilever after fracture

The model of crack inhiation requires the fracture criterion of the solid electrolyte to be exceeded by the hydrodynamic pressure build-up of the lithium dendrite.[261] Due to the air-sensitive nature of Li_6PS_5Cl conventional fracture measurements were not possible, therefore a novel testing procedure of microcantilever bending was used to determine the local fracture

stress of the solid electrolyte. An example of the testing procedure is shown in above figure 4.12 and an example load displacement curve shown below in figure 4.13a).

The cantilever testing was carried out on four samples with different densities, produced by sintering at different temperatures as described in section 4.3.1. The microcantilevers were created by using FIB milling (ZEISS Auriga FIB-SEM) using the procedure described in section 4.3.5, and the bend tests themselves following the method in section 4.3.6.

The load-displacement curve of an example microcantilever bend test is shown by figure 4.13a). The curve is approximately a straight line, showing that cantilever was deforming elastically as the load was applied until the point of fracture. The fracture point is identified by the sharp decrease in load as the displacement continues to increase. The load value at this point is taken to be the load required for fracture, P_f. Using equation 4.6 the fracture stress, σ_f, for each cantilever was calculated.

$$\sigma_f = \frac{P_f L_c y}{I} \ (eqn\ 4.6)$$

Where

- L_c is the distance between loading point and crack.
- y is the vertical distance between the upper surface and neutral plane.
- I is the second moment of area.

The values of y and I were calculated for a pentagonal cantilever as shown by Chen et al.[236] More details can be found in section 2.6.4.3.

Multiple cantilevers were tested for each sample and the mean of the calculated fracture stress values for each sample are displayed on figure 4.13b). The figure shows a trend of increasing

fracture stress as the relative density increases. The increase in fracture stress appears to increase by a greater amount at higher densities, leading to deduction that there could be an exponential relationship between density and fracture stress. Figure 4.13c) show a possible exponential trend, with a goodness-of-fit reduced chi-square result of 0.61. This would usually be considered a good fit and mean the exponential trend accepted, however, as the sample size is quite small the goodness-of-fit should be viewed with caution. More fracture stress measurements at different densities are need to draw a strong conclusion about the exact nature of the fracture stress-density relationship. In summary, it can only be observed with confidence that increasing the density will increase the fracture stress. Therefore, to reduce the likelihood of crack initiation, solid electrolytes with higher relative densities should be manufactured.

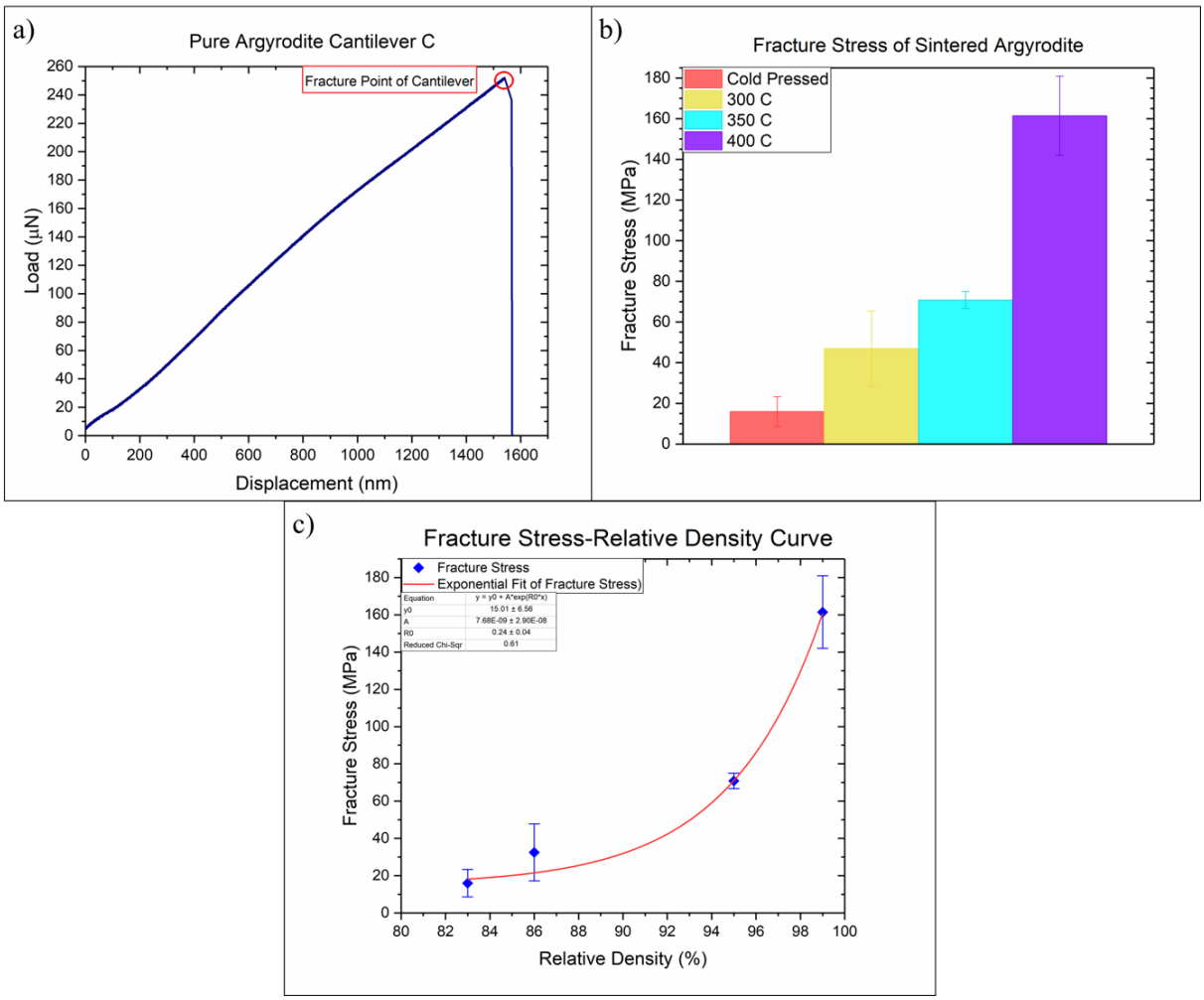

Figure 4.13: a) Load-displacement curve for cantilever C of pure Li_6PS_5Cl, field assisted sintered at 400 °C, b) Histogram comparing the calculated values of fracture stress for different density Li_6PS_5Cl, c) a graph showing the exponential relationship between fracture stress and relative density.

4.5 Conclusion

The highly air-sensitive nature of Li_6PS_5Cl necessitated the development of innovative testing techniques to investigate the mechanical properties of the solid electrolyte. The research shows that the method of field assisted sintering can be used to densify the Li_6PS_5Cl powder into solid electrolyte discs with relative density 99%. This increase in density was accompanied by a significant improvement in the measured modulus and hardness mechanical properties, which

resulted in an increase in electrochemical performance. The investigation into local fracture stress using a pioneering micro-cantilever testing procedure provided the experimental evidence required for a model explaining dendrite initiation to be established. Further experimentation led to the conclusion that a higher density solid electrolyte, therefore containing lower porosity and fewer flaws, would increase resistance to dendrite penetration, thereby improving its resistance to short circuit failure.

The fracture toughness of the highly air-sensitive Li_6PS_5Cl is characterised for the first time using an original experimental approach. This result was able to provide experimentally measured mechanical properties that evidence a model for crack propagation within the solid electrolyte. To hinder crack propagation the fracture toughness of the solid electrolyte must be improved, this chapter demonstrates how introducing secondary phase nanoparticles with greater mechanical properties can produce a well bonded composite material that improves the fracture toughness of the solid electrolyte; with the results show that a 15% Li_6PS_5Cl-CSZ composite had the highest fracture toughness. Also investigated was the presence of transformation toughening using when using CSZ as the secondary phase. The results suggest that there may be some transformation toughening present but no definitive conclusion can be drawn from the existing data. Further mechanical investigation of other CSZ and Zirconia composite samples, via high resolution TEM, is required to confirm whether this effect is due to a transformation toughening mechanism from the CSZ introduced to the matrix.

5. Chapter 5 Fatigue

5.1 Aim

Throughout this thesis the overarching theme has been how identifying and then improving the mechanical properties of the solid electrolyte can help progress the development of the ASSB. In the literature there are many SEs that show very promising electrochemical performance, including Li_6PS_5Cl. However, the values cited are determined from tests that are not representative of the environments and conditions that an actually functioning ASSB will undergo.[206] One aspect in particular is cycle lifetimes, with ASSBs expect to complete 1000s of cycles and critical current density tests often performed for a single charge/discharge cycle. Thus far all mechanical testing in this thesis has been single event, i.e. an indent or the maximum fracture stress, and the repeated nature of charging/discharging cycles not yet considered.

This cyclical nature brings the effect of material fatigue into consideration. As discussed in previous chapters the dendritic failure of an SE occurs by crack initiation and crack propagation mechanisms; with the mechanical properties of the SE dictating the ease at which dendrites can form. Having demonstrated the mechanical nature of the dendritic failure issue, it necessitates investigation into the issue of cyclical mechanical loading of the SE, to explore the effects of fatigue on the SE ceramic. An innovative mechanical testing regime was designed using an *in-situ* nanoindenter and microcantilevers to simulate the mechanical stress experienced within an SE during electrochemical cycling. The results of this research hope to inform and influence new mechanical requirements and considerations when designing an SE for the ASSB.

5.2 Introduction

The electrochemical cycling of the ASSB causes the evolution of stress and strain to occur within the solid electrolyte (SE), due to a volume change caused by the lithium plating/stripping process that occurs during charging/discharging respectively.[282,283] In single event mechanical characterisation testing this evolution of stress is not an issue. However, the successful ASSB is expected to undergo several 1000s of charge/discharge cycles; these cyclic stresses applied to the SE will affect the mechanical longevity of the ASSB and could cause failure through a fatigue crack. A fatigue crack refers to the fracture of a material subjected to repeated or cyclical applied stress that is below its fracture stress.[284]

As established in the previous chapter, a dendrite will only grow once a crack has been initiated at a surface defect, and for the crack to initiation the local fracture stress criterion must be exceed. The fatigue behaviour caused by the cyclic charging/discharging stresses within the SE, leads to plastic deformation occurring around the surface defects and weakens the material. This lowers the localised stress criterion for fracture to occur in the material, meaning that a crack can initiate at a lower stress, known as a fatigue crack.[285] Previously CCDs for SEs have been calculated and recognised as the limit for which failure due to the lithium dendrite penetration occurs. The stress applied to the SE during cycling is proportional to the current density charging/discharging rate. Therefore, if the ASSB charging/discharging occurs below the CCD, then respective mechanical stress criterions required for dendrite initiation and propagation will not be exceeded. However, if the SE undergoes fatigue during the ASSB cycling and the material becomes weaker, then the initiation and propagation stress criterions will decrease meaning that it will be possible for dendritic failure to occur at current densities

lower than the CCD. Therefore, it is imperative to understand the fatigue effects of repeated cell cycling on SE materials. Two different SEs were used to investigate the fatigue properties of the ASSB, $Li_{6.4}La_3Zr_{1.4}Ta_{0.6}O_{12}$ and Li_6PS_5Cl. Using the fully enclosed Ar-glovebox, SEM and nanoindenter setup, combined with novel testing procedures it was possible to replicate the applied cyclic stress, in an air-sensitive environment, and investigate the fatigue crack properties in a localised area of both materials.

5.3 Experimental

5.3.1 Manufacture of the $Li_{6.4}La_3Zr_{1.4}Ta_{0.6}O_{12}$ Sample

The sample was prepared with the help of Marco Siniscalchi. All procedures, including pressing and sintering, were performed inside an Ar-filled glovebox (O_2 and H_2O levels < 1 ppm). The $Li_{6.4}La_3Zr_{1.4}Ta_{0.6}O_{12}$ sample was made using $Li_{6.4}La_3Zr_{1.4}Ta_{0.6}O_{12}$ solid electrolyte powder that was purchased from *MSE Supplies – Ampcera*. The purity of the powder was >99.9%, the average particle size was ~1 μm, and the powder distribution was D50.[286]

Field assisted sintering was used to prepare the $Li_{6.4}La_3Zr_{1.4}Ta_{0.6}O_{12}$ sample, the $Li_{6.4}La_3Zr_{1.4}Ta_{0.6}O_{12}$ solid electrolyte powder was loaded into a graphite die set, cold pressed and then placed into a spark plasma sintering system (FCT Systeme GmbH). Field assisted sintering was then carried out at 1200 °C for 5 minutes, under a uniaxial pressure of 50 MPa whilst under vacuum, by passing an electrical current through the die set.

5.3.2 Preparation of the $Li_{6.4}La_3Zr_{1.4}Ta_{0.6}O_{12}$ Sample

The $Li_{6.4}La_3Zr_{1.4}Ta_{0.6}O_{12}$ sample was approximately disc-shaped, measuring approximately 5 mm in diameter and approximately 1 mm in thickness. The sample was kept in an Ar filled glovebox (O_2 and H_2O concentrations < 1 ppm), the sample was polished using successively finer SiC paper, using grits of 400, 600, 800, 1200, 2500 and 4000. The final polishing step involved using a diamond lapping film to polish the surface down to 1 µm. When typically preparing a flat surface for nanoindentation testing there are several other subsequent steps that follow to achieve a completely smooth surface,[245] due to the air-sensitive and moisture-sensitive nature of the samples none of these further polishing steps were possible. The sample was then mounted onto a custom aluminium pin stub 6 mm in diameter, with a pin length of 3.5 mm. An electrically conductive two-part silver epoxy was used to fix the sample to the pin stub. As the temperature of the glovebox was usually around 15 °C, the epoxy was left to cure for at least 12 hours. The sample was then transferred to the custom glovebox, SEM and indenter set up, where the SEM opens up directly into the glovebox enabling airless transfer. In this glovebox a final polishing step, again with diamond lapper paper was performed, to achieve the best surface finish possible. After this final polishing step the sample surface was smooth and somewhat reflective to light.

5.3.3 Manufacture of the Li_6PS_5Cl Sample

The sample was prepared with the help of Dominic Melvin. All procedures, including pressing and sintering, were performed inside an Ar-filled glovebox (O_2 and H_2O levels < 1 ppm). All Li_6PS_5Cl samples were made using Li_6PS_5Cl solid electrolyte powder that was purchased from *MSE Supplies – Ampcera*. The purity of the powder was >99.9%, the average particle size was ~1 µm, and the powder distribution was D50.[76]

To prepare the sample field assisted sintered sample, the following method was used. Li_6PS_5Cl solid electrolyte powder was loaded into a graphite die set, which was then placed into a spark plasma sintering system (FCT Systeme GmbH). Field assisted sintering was then carried out at 400 °C for 5 minutes, under uniaxial pressure of 50 MPa whilst under vacuum, by passing an electrical current through the die set.

5.3.4 Preparation of the Li_6PS_5Cl Sample

The Li_6PS_5Cl sample was approximately disc-shaped, measuring approximately 5 mm in diameter and approximately 1 mm in thickness. The sample was kept in an Ar filled glovebox (O_2 and H_2O concentrations < 1 ppm), the sample was polished using successively finer SiC paper, using grits of 400, 600, 800, 1200, 2500 and finally 4000. When typically preparing a flat surface for nanoindentation testing there are several other subsequent steps that follow to achieve a completely smooth surface,[245] due to the air-sensitive and moisture-sensitive nature of the samples none of these further polishing steps were possible. The sample was then mounted onto a custom aluminium pin stub 6 mm in diameter, with a pin length of 3.5 mm. An electrically conductive two-part silver epoxy was used to affix the sample to the pin stub. As the temperature of the glovebox was usually around 15 °C, the epoxy was left to cure for at least 12 hours. Each sample was then transferred to the custom glovebox, SEM and indenter set up, where the SEM opens up directly into the glovebox enabling airless transfer. In this glovebox a final polishing step, again with 4000 SiC grit paper was performed, to achieve the best surface finish possible. After this final polishing step the sample surface was smooth and somewhat reflective to light.

5.3.5 FIB of Cantilevers

Pentagonal micro-cantilever beams were milled using a ZEISS Auriga FIB-SEM system with a gallium ion (Ga^+) source.[235,265–267] Each sample was prepared, polished and mounted inside an Ar filled glovebox, using the steps outlined in section 5.3.2 and 5.3.4 respectively. Each mounted sample was loaded into a Semi Labs Transfer Shuttle, whilst still inside an Ar filled glovebox, to allow for an airless transfer into the FIB-SEM. Using the gallium FIB, three overlapping rectangular trenches 10 μm deep were milled using a beam current of 16 nA to create a cantilever approximately 32 x 7 μm. Using a large beam current allowed faster milling but did not produce vertical sides due to the lower precision associated with a large beam tail. Using a beam current of 2 nA and three overlapping trenches of 8 μm depth, produced a cantilever of dimensions 30 x 5 μm with vertical sides. To achieve the desired depth in each sample a different number of doses (passes) by the beam current was used, with an approximate ratio of 3:2 for $Li_{6.4}La_3Zr_{1.4}Ta_{0.6}O_{12}$:$Li_6PS_5Cl$. To form the base of the cantilever, the sample was tilted 45^o (about the long axis of the cantilever), and using a beam current of 2 nA an approximately 5 μm deep trench was milled away. The cantilever was then rotated and this same milling procedure was carried out on the other side, to produce a cantilever that had a symmetrical pentagonal cross section. The target dimensions are shown in figure 5.1. The SEM was used to capture images after the milling of the cantilever was complete, to measure and record the dimensions of the cantilever.

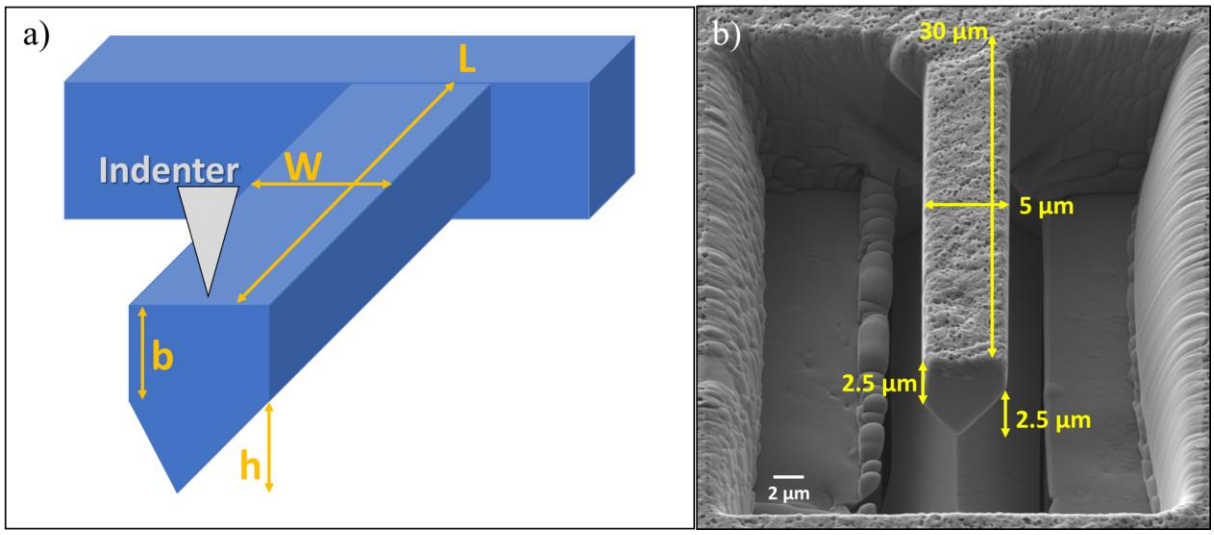

Figure 5.1: a) Schematic to demonstrate the shape of pentagonal cantilever to be milled and positioning of indenter tip, b) SEM image showing microcantilever of Li_6PS_5Cl with the ideal target dimensions.

5.3.6 Testing of Cantilevers

Testing of the prepared microcantilevers was carried out using the Bruker-Hysitron PI89 in situ nanoindenter; the nanoindenter mounted to the five-axis stage of the SEM. The Semi Labs Transfer Shuttle was used to ensure an airless transfer into the glovebox connected SEM and in situ indenter. The indenter was used in the lowload mode configuration and with an electrically conductive diamond cube corner instrumentation tip (Bruker-Hysitron). By using the sharper cube corner tip this allowed for greater visibility when positioning the indenter so that indenter tip could be accurately placed at a known distance from the fixed end and in the center-line of the cantilever. Before each indent, the thermal drift rate was measured when in contact with the sample, over 40 s using a preload of 5 µN, and corrected for. Using the Hysitron displacement controlled close-loop feedback mode, the cantilever was loaded to an initial set maximum displacement over a time duration of 4 s, held at this set maximum displacement for 1 sec, unloaded to half of the set maximum displacement over a time duration of 2 s, and held at the half of the set displacement for 1 second. This loading cycling was then repeated until either failure had occurred by fracture, or 1000 cycles had passed without any significant change in

applied load. An example of the cycling load-displacement curve of a tested microcantilever is shown in figure 5.2 with an R-ratio of 0.5 used for testing. The R-ratio in fatigue testing is defined as the ratio between the maximum and minimum applied stress or strain in a loading cycle. The fracture initiation point was identified by a significant decrease (>0.1%) in measured stiffness of the cantilever, the stiffness was calculated from the measured load-displacement data, specifically upper portion of the unload cycle using the method set out in 2.6.2.1. The measured load and known dimensions of the cantilever were used to calculate the stress on each cantilever.

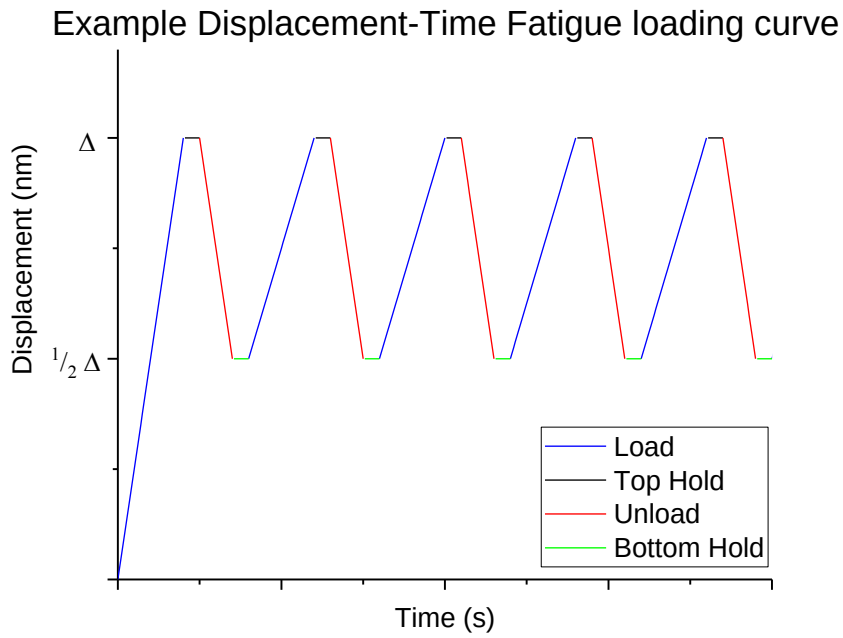

Figure 5.2:Example displacement-time graph showing the cyclical loading of the sample micro-cantilever.

5.4 Results and Discussion

5.4.1 Cycling of the $Li_{6.4}La_3Zr_{1.4}Ta_{0.6}O_{12}$ Cantilevers

Following method set out in section 5.3.6 and similarly to the cantilever testing in the previous chapter, 24 $Li_{6.4}La_3Zr_{1.4}Ta_{0.6}O_{12}$ cantilevers were made using FIB and then subjected to cyclic fatigue testing using nanoindentation. $Li_{6.4}La_3Zr_{1.4}Ta_{0.6}O_{12}$ was initially used for fatigue testing to help develop this novel air sensitive cyclic microcantilever testing as it has a reasonable stability should any air exposure occur and it is mechanically relatively stiff (modulus ~ 220 GPa); both these qualities made for easier navigation of this new and challenging testing procedure. Initially four single event (one loading half cycle) tests to were carried out to find the maximum fracture stress of a $Li_{6.4}La_3Zr_{1.4}Ta_{0.6}O_{12}$, and then used to determine a suitable displacement testing range. From the single event tests the average maximum fracture stress of a $Li_{6.4}La_3Zr_{1.4}Ta_{0.6}O_{12}$ was calculated, using the method in section 2.6.4.3, to be 1090 ± 160 MPa, and a minimum displacement depth of 1703 nm for the weakest cantilever. Directed by this initial information cyclic testing was then carried out on the remaining 20 cantilevers with different set maximum displacements ranging from 400 to 1000 nm.

5.4.1.1 Demonstrate Loading and cracking of a Cantilever

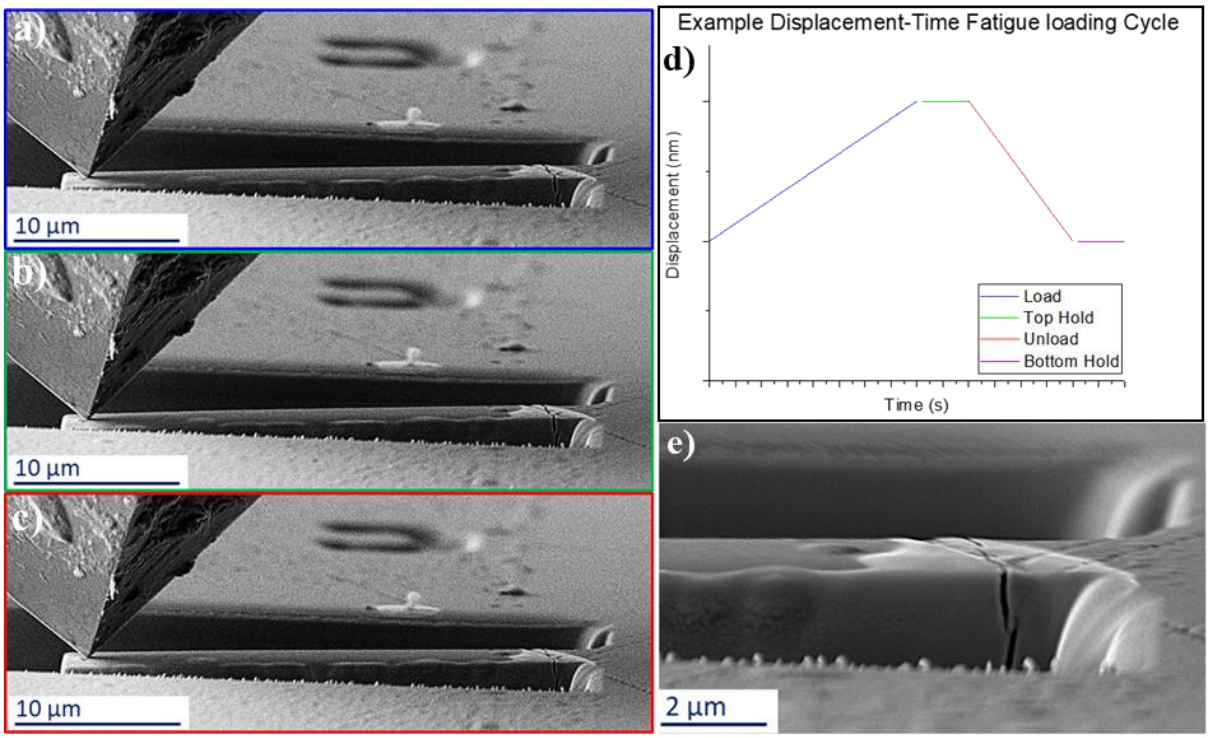

Figure 5.3: Shows an $Li_{6.4}La_3Zr_{1.4}Ta_{0.6}O_{12}$ cantilever in various stages of the fatigue testing cycle, a) loading, b) hold at the top of the cycle, c) unloading. d) Figure to show the corresponding sections of the nanoindenter applied fatigue testing cycle. e) show a crack that has grown at the fixed end of this tested cantilever after repeated physical cycling.

Figure 5.3 above gives a visual *in-situ* demonstration of how the different stages of the testing cycle physically correspond to the bending of the cantilever. This cantilever was subjected to a maximum displacement of 800 nm and cycled with an R-ratio of 0.5. The maximum stress experienced at the top of the fixed end of the cantilever was calculated to be 350 MPa, which is approximately three times lower than the average fracture stress required for a single loading test of a $Li_{6.4}La_3Zr_{1.4}Ta_{0.6}O_{12}$ cantilever, yet figure 5.3e) demonstrates that at even significantly lower applied stresses it is still possible for a crack to form near the fixed end of the cantilever, which in an ASSB could lead to dendritic failure as described in chapter 4.

5.4.1.2 Cyclic Fatigue Testing and Slow Crack Growth

This asks the question as to how a crack can form and grow despite the applied stress not exceeding the respective criterions for crack initiation and propagation. One mechanism which could enable the observed cracking is cyclic fatigue; specifically fatigue cracking and fatigue crack growth. Cyclic fatigue is a mechanism by which a material that is subjected to recurring cycles of applied stress can lead to failure. Even though the applied stress is relatively low, the repeated nature over a long period of time can cause cracks to form and develop with in the material. Under cyclic loading the typical toughening mechanisms introduced, such as composites and transformation toughening, are themselves subject to fracture and wear resulting in increased loading at the crack tip and subcritical crack growth.[287]

The process by which cyclic fatigue can lead to crack growth starts with the initiation of the crack. In the prepared $Li_{6.4}La_3Zr_{1.4}Ta_{0.6}O_{12}$ solid electrolyte the relative density very high and was greater than 99%, however this still leaves some porosity within the material. Given the added challenges of surface preparation for the highly air-sensitive SEs it is highly likely that some form of existing defect may be found on the surface e.g. a pore or a surface scratch. At the site of this pre-existing material defect, the repeated cyclic stress can result in the nucleation of a crack. The cycle number at which the relative stiffness of the cantilever had decreased by more than 0.1% of its initial value was used to determine the point of crack initiation during analysis of the cantilever.[288] Following initiation, each subsequent applied stress cycle causes incremental growth in the crack, known as slow crack growth. The rate of this slow crack growth is determined by factors such as the stress intensity factor, the environmental conditions and the fundamental material properties itself. Finally, complete fracture occurs when the crack has grown to a critical size and the remaining material cannot withstand the applied cyclic stress. This leads to catastrophic failure of the material, complete propagation of the crack tip,

and ultimately to fracture of the cantilever. The cycle number at which the relative stiffness of the cantilever had decreased by more than 1% of its initial starting value was used to determine the point of final fracture failure (complete crack propagation) during analysis of the cantilever.[288]

5.4.1.3 Fracture Analysis of the $Li_{6.4}La_3Zr_{1.4}Ta_{0.6}O_{12}$ cantilevers

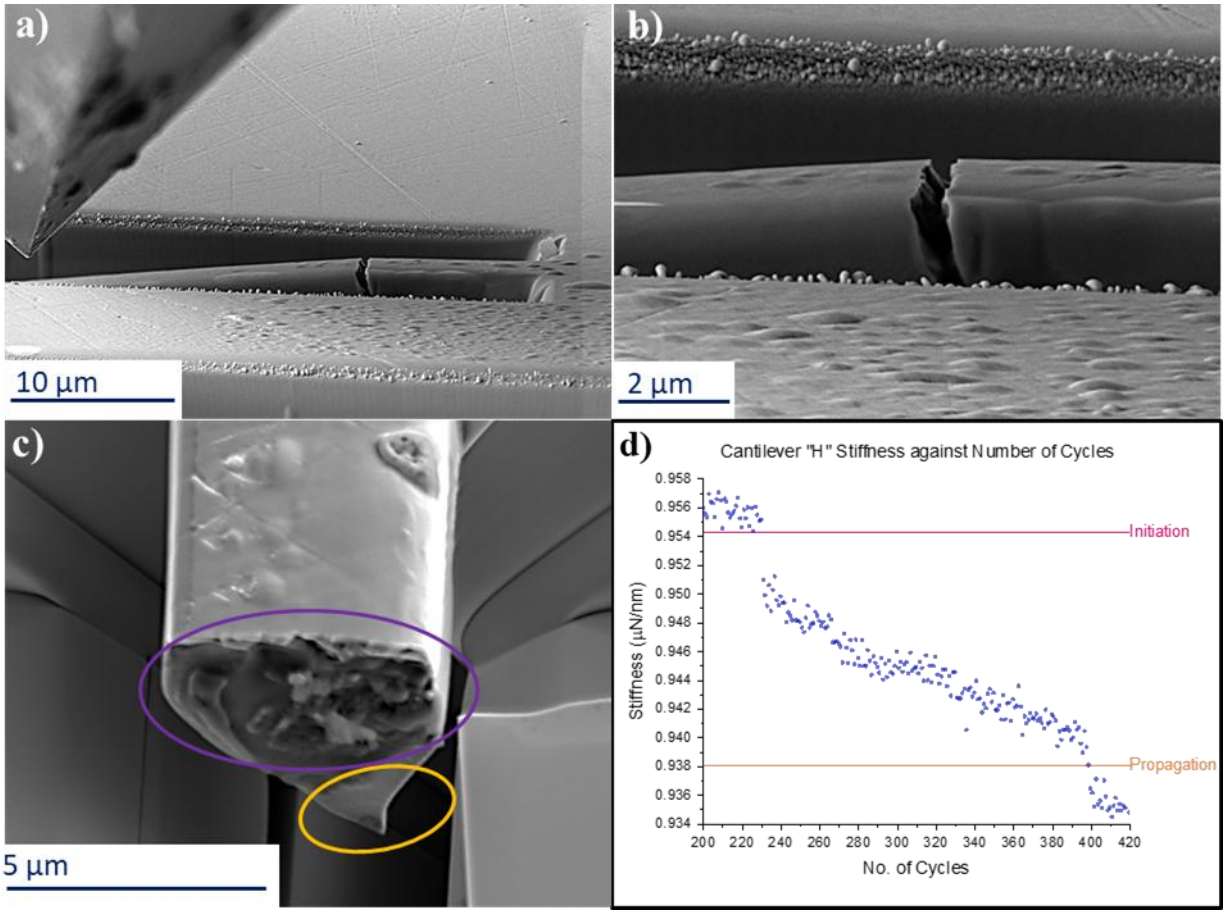

Figure 5.4: a) shows crack growth of the failed $Li_{6.4}La_3Zr_{1.4}Ta_{0.6}O_{12}$ cantilever 'H' post cycling, b) magnified image showing the crack in the cantilever, c) two different fracture surfaces can be observed at the fixed end of the failed cantilever, d) the measured stiffness values calculated from each unload cycle of the cantilever and the criteria for crack initiation and complete propagation.

As described in section 5.4.1.2, a cyclically applied low stress can cause fatigue crack growth and failure. Cantilever 'H' is depicted in figure 5.4 and the initial cyclical applied stress was

410 MPa; as shown in figure 5.4a) & b) a crack has formed despite the significantly lower cycling stress. Figure 5.4d) shows the trend in stiffness decreases as the number of cycles increases, and the points of crack initiation (cycle 228) and complete crack propagation (cycle 396). The graph shows that once the crack has initiated there is a steady decrease in stiffness, this suggests that the conditions are suitable for slow incremental crack growth. Towards the end of the graph, the stiffness of the cantilever rapidly decreases suggesting that the crack is now propagating much faster. This is also evidenced by the two different fracture surfaces seen in figure 5.4c) and highlighted by the purple and yellow circles respectively, this is explained in further detail below.

Figure 5.5 below again shows that cantilever 'C' cycled at a much lower stress (340 MPa) than the initially determined fracture stress for a $Li_{6.4}La_3Zr_{1.4}Ta_{0.6}O_{12}$ cantilever. Figure 5.5d) again shows the trend in stiffness decreases as the number of cycles increases; it also shows a significant decrease in stiffness near the point of complete crack propagation. Figure 5.5a) shows the fracture surface of the failed cantilever and figure 5.5b) shows the fracture surface of the corresponding fixed end. Similarly to figure 5.4c), two different fracture surfaces appear to be present in figure 5.5a) & b), highlighted by purple and yellow circles in 5.5a).

The areas highlighted by the purple circles have a rough surface finish, with material protruding different amounts at different depths. This surface texture indicates that there has been slow crack growth through this portion of the cantilever and that the crack has propagated incrementally with each cycle. In particular figure 5.5b) has some evidence of lateral crack geometries, showing a tortuous crack path, further indicating slow crack growth. The areas highlighted by the purple circles likely correspond to the portion of the stiffness graphs between the "initiation" and "propagation" lines on figures 5.4d) and 5.5d) respectively. The areas

highlighted by the yellow circles in both figures, by contrast appear relatively smooth and much flatter. This is indicative of a much faster crack propagation and a relatively brittle fracture where the crack tip has traversed the rest of the cantilever in a very few cycles. The areas highlighted by the yellow circles likely correspond to the portion of the stiffness graphs after the "propagation" line on figures 5.4d) and 5.5d) respectively, representing the areas at which complete crack propagation has occurred.

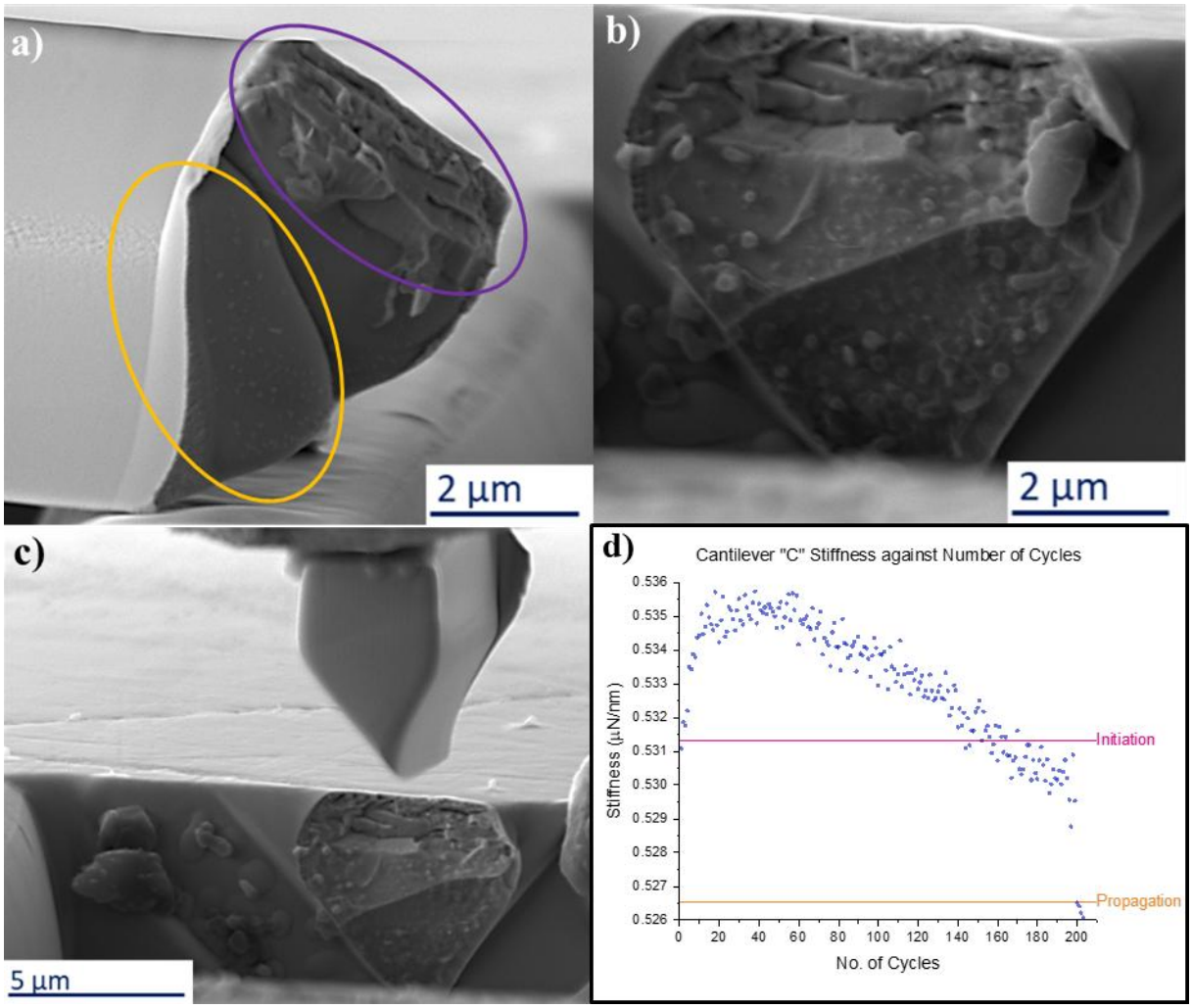

Figure 5.5: a) shows fracture surface of failed $Li_{6.4}La_3Zr_{1.4}Ta_{0.6}O_{12}$ cantilever 'C' post cycling, b) magnified image showing fracture surface of cantilever fixed end, c) fracture surface of the fixed and the failed cantilever stuck to the indenter tip, d) the measured stiffness values calculated from each unload cycle of the cantilever and the criteria for crack initiation and complete propagation.

In both cantilevers ‘H’ & ‘C’ the rough surface demonstrates a tortuous crack path and is evidence of slow crack growth. Slow crack growth refers to the time dependent process by which a crack propagates slowly over time under cyclically applied stress.[289] The interaction between the crack tip and the surrounding material/environment affects the rate of crack growth, particularly prevalent in oxide ceramics. The presence of porosity and other defects in the material can act as stress concentrators, which can accelerate crack propagation. The inherent material toughness and strength of a ceramic also affects the resistance to crack propagation; with increased toughness and higher strength acting to delay crack initiation and propagation.[290] The $Li_{6.4}La_3Zr_{1.4}Ta_{0.6}O_{12}$ cantilevers have relatively low porosity (< 1%), relatively high mechanical properties (modulus > 220 GPa), and the highly reactive nature of oxide ceramics all suggest that slow crack growth due to fatigue behaviour can be seen in both figures 5.4 and 5.5.[290]

The two examples above both demonstrate how cycling at significantly lower relative stresses can give the right fatigue conditions for slow crack growth. The following two examples again show failure due to cyclically applied relative low stress however, there is not apparent evidence of slow crack growth. Figures 5.6b) & c) show magnified images of the post fracture surface of the fixed end of cantilever ‘E’. The fracture surface appears to be relatively smooth and flat across the entire face with no surface roughness that would indicate slow crack growth. Cantilever ‘E’ was cycled at an initial stress of 500 MPa, which is still significantly lower than the calculated cantilever fracture stress but is ~ 20% greater than applied stress in the cantilevers ‘H & C’ that demonstrated slow crack growth. Figure 5.6d) again shows the decrease in stiffness as number of cycles increases, however it shows a comparatively greater rate of stiffness decrease than cantilevers ‘H & C’ as well as a fewer overall cycles before failure. This indicates that, once the crack had been initiated, the increased applied cyclic stress causes the

crack growth (propagation) to occur faster through and as a result the cantilever failed after a lower number of cycles. The faster crack propagation has led to a smoother fracture surface being produced post cantilever failure as shown in figures 5.6b) & c).

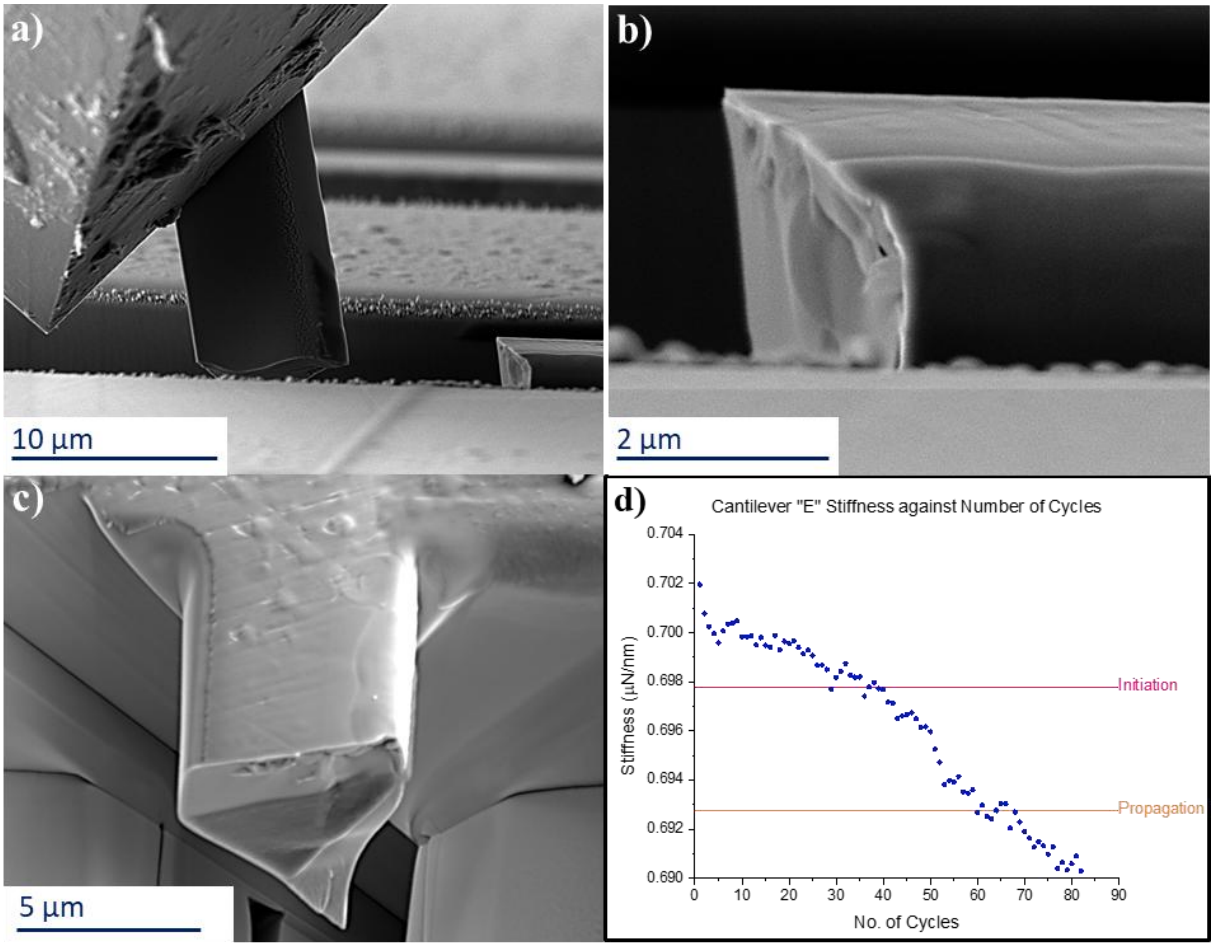

Figure 5.6: a) the fractured fixed end and the remaining failed $Li_{6.4}La_3Zr_{1.4}Ta_{0.6}O_{12}$ cantilever 'E', b) magnified side-on image of the fracture surface of the fixed end, c) magnified front-on image of the fracture surface of the fixed end, d) the measured stiffness values calculated from each unload cycle of the cantilever and the criteria for crack initiation and complete propagation.

Figure 5.7a) also shows the very smooth and flat post fracture surface of the fixed end of cantilever 'I'. Cantilever 'I' was cycled with an initially applied stress of 520 MPa and figure 5.7b) shows that cantilever 'I' failed in a relatively few number of cycles, with a steep drop in stiffness through both the "initiation" and "propagation" criteria. This severe drop in stiffness when considered with the very smooth fracture surface, suggests that the initiation and complete

crack propagation happened possibly even within the same cycle. Similarly to cantilever 'E', this again demonstrates that cyclical fatigue can cause failure to occur below the critical fracture stress; and that it can occur quickly in a brittle fracture manner without any observed slow crack growth.

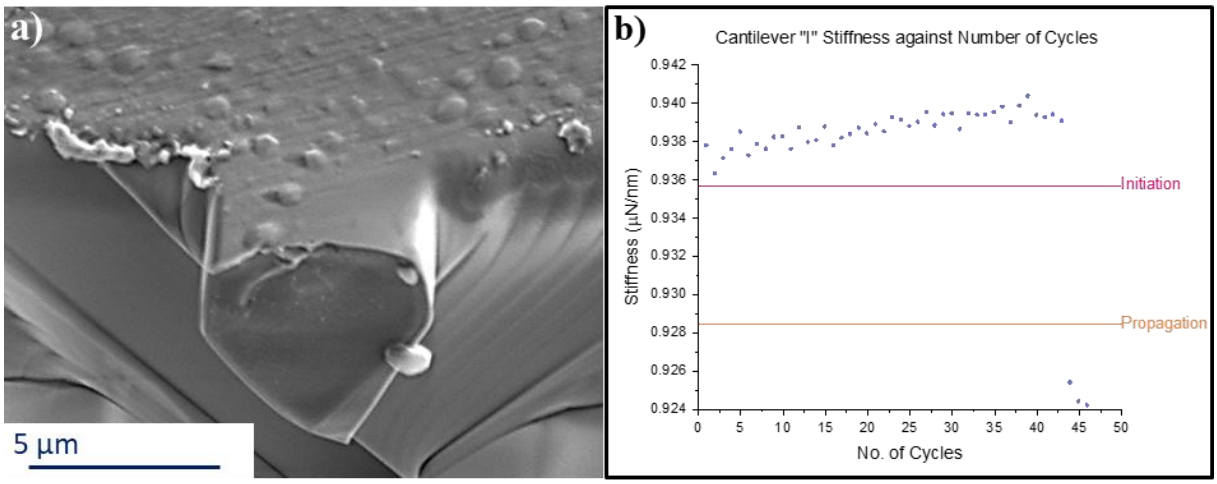

Figure 5.7: a) magnified front-on image of the fracture surface of the fixed end, b) the measured stiffness values calculated from each unload cycle of $Li_{6.4}La_3Zr_{1.4}Ta_{0.6}O_{12}$ cantilever 'I' and the criteria for crack initiation and complete propagation.

5.4.1.4 Cyclic Fatigue Results

Due to the difficult nature of performing air-sensitive *in-situ* microcantilever testing of the 24 prepared cantilevers, 19 were successfully tested and the results for each cantilever shown in figure 5.8 below. Given the tests were carried out in displacement control, the strain amplitude for each test was calculated using the equation put forward by Yamaguchi et al. (2020) for pentagonal microcantilevers.[291] Figure 5.8a) shows the number of cycles at which a crack was deemed to have initiated and figure 5.8b) the number of cycles at which complete crack propagation had occurred, both determined by the previously laid out criteria. Figure 5.8c) shows both trends of strain amplitude vs number of cycles on the same graph, which allows for comparison of the number of cycles between crack initiation and propagation. As the test was

displacement controlled the strain remains constant between the point of initiation and the point of complete crack propagation.

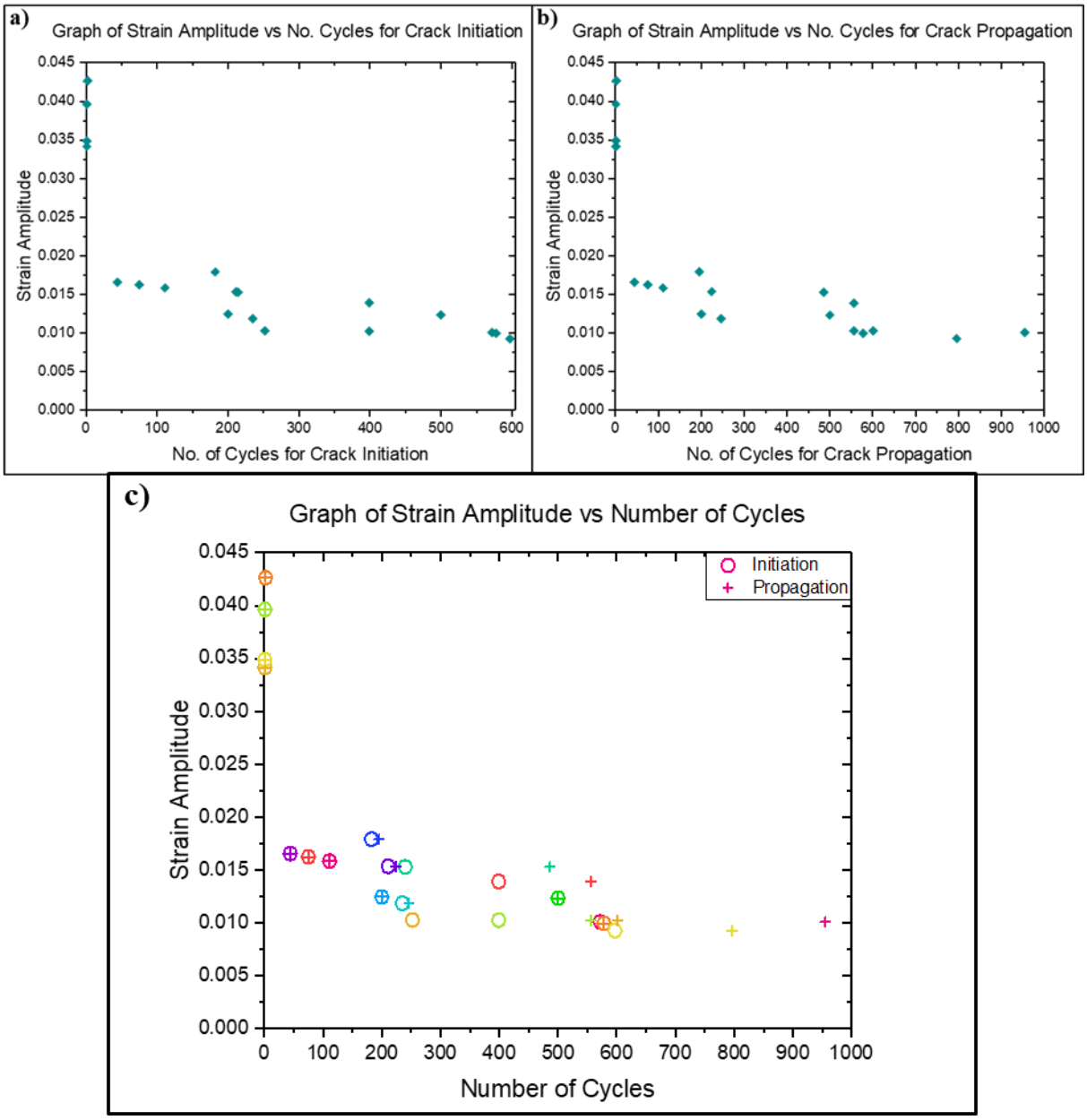

Figure 5.8: Graph of strain amplitude against a) number of cycles for crack initiation, b) number of cycles for complete crack propagation in $Li_{6.4}La_3Zr_{1.4}Ta_{0.6}O_{12}$ cantilevers, c) Both trends are displayed on the same axes to compare the number of cycles between initiation and propagation.

The curves in figure 5.8 show the same trend, as the strain amplitude on each cantilever decreases, the number of cycles to respective crack initiation and full crack propagation increase. In particular figure 5.8c) shows that at lower strain amplitude the number of cycles

between crack initiation and complete crack propagation also increases. This is in agreement with the fatigue crack growth mechanism, where the rate of crack propagation is determined by the size of the stress concentration driving the crack tip, which in of itself is linked back to the strain amplitude.

Given the stress concentration is a key driver for crack tip propagation it is important to consider the relationship between stress and the number of cycles at points of crack initiation and complete crack propagation, both are shown in figure 5.9. Figure 5.9a) shows the trend that the cantilevers with the initially lower cyclical stress required more cycles for a crack to initiate, supporting the previous trends displayed above and the fatigue failure mechanism. Figure 5.9b) also shows a similar trend in the applied stress at the point of complete crack propagation suggesting that the number of cycles to failure increases as the applied cyclical stress decreases. However, there are some outliers, as for some samples as the number of cycles increased the measured applied stress of the samples also increased. Figure 5.9c) displays both trends and the change in required applied stress (effectively the stiffness change of the cantilever) between the point of crack initiation and crack propagation can be compared.

This is likely due to some kind of strengthening mechanism that is occurring at the fixed end cantilever improving the resistance of the material to crack growth. One possible mechanism that could cause the observed increase in stress is induced residual stress. The cyclic nature of the applied displacement to the cantilever can induce residual stresses to be trapped inside the ceramic lattice, if the stresses are compressive in nature they can act to counter the crack tip driving force and as a result increase the stress required for complete crack propagation. Another mechanism could be some kind of chemical reaction at the interface, $Li_{6.4}La_3Zr_{1.4}Ta_{0.6}O_{12}$ is highly air sensitive and very readily forms a very thin reactive layer (~

several nm's) even when exposed to incredibly low amounts of air. This could lead to the slow crack growth seen in section 5.4.1.3 as even the slightest moisture in the testing environment can interact with the atomic bonds, especially with oxide ceramics.[290] It is possible that during the transfer stages between FIB and SEM that minute traces of contaminant gasses may have been present which then enabled a reactive layer to grow around, near, or even in the initiated crack which could increase the resistance to crack propagation and therefore lead to an increased applied stress at the point of complete crack propagation. Further investigation is required to accurately determine which of these mechanisms is causing the observed increase in applied stress.

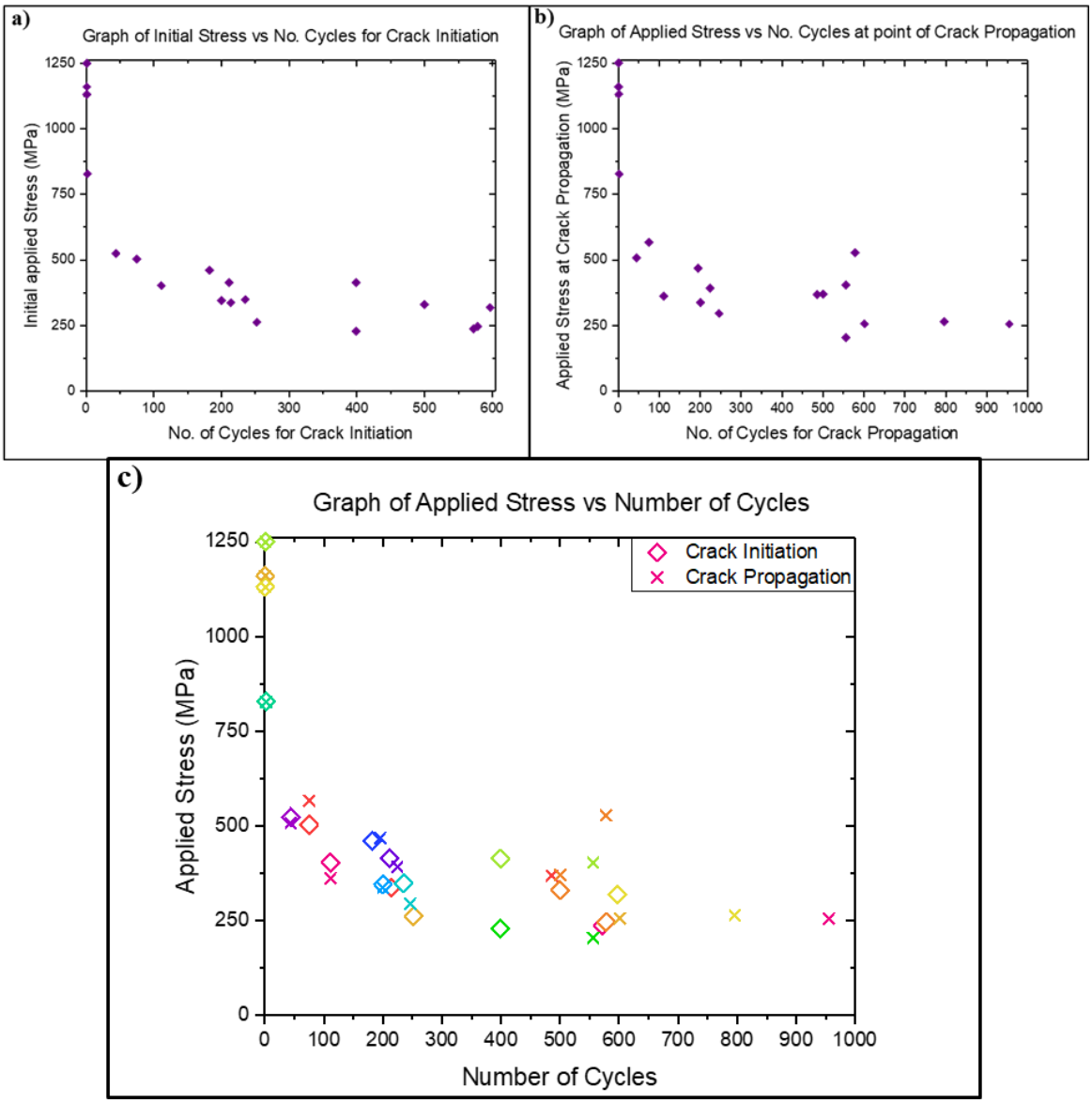

Figure 5.9: a) Graph of the initial stress against the number of cycles for crack initiation, b) Graph of the applied stress against the number of cycles for complete crack propagation in $Li_{6.4}La_3Zr_{1.4}Ta_{0.6}O_{12}$ cantilevers. c) Both trends displayed on the same axes to compare the difference in applied stress between crack initiation and crack propagation.

5.4.2 Cycling of the Li_6PS_5Cl Cantilevers

As discussed previously Li_6PS_5Cl is the solid electrolyte of choice to be used in the next generation ASSB. Once the cyclic fatigue testing technique had been developed on $Li_{6.4}La_3Zr_{1.4}Ta_{0.6}O_{12}$ the same technique was used to investigate the fatigue properties of

Li_6PS_5Cl. Following the method described in section 5.3 16 Li_6PS_5Cl cantilevers were made using FIB and then subject to cyclic fatigue testing using nanoindentation. Initially four single event (one loading half cycle) tests to were carried out to find the maximum fracture stress of a Li_6PS_5Cl, and then used to determine a suitable displacement testing range. From the single event tests the average maximum fracture stress of a Li_6PS_5Cl was calculated, using the method in section 2.6.4.3, to be 160 ± 117 MPa, significantly lower than that of $Li_{6.4}La_3Zr_{1.4}Ta_{0.6}O_{12}$ by approximately an order of magnitude. The minimum displacement depth for fracture of the weakest cantilever was 1491 nm. Directed by this initial information cyclic testing was then carried out on the remaining 12 cantilevers with different set maximum displacements ranging from 400 to 800 nm.

5.4.2.1 Cyclic Fatigue Testing

The mechanism for cyclic fatigue in Li_6PS_5Cl is very similar as that described in section 5.4.1.2. In the prepared Li_6PS_5Cl solid electrolyte the relative density was high, greater than 97%, however this still leaves some porosity within the material; and, as with all highly air-sensitive SEs, there are again challenges of surface preparation. As with the $Li_{6.4}La_3Zr_{1.4}Ta_{0.6}O_{12}$ SE, there are highly likely to be surface defects found in the Li_6PS_5Cl solid electrolyte, given the higher level of porosity and even great surface preparation challenges due to Li_6PS_5Cl even more reactive nature. At the site of a pre-existing material defect, the repeated cyclic stress can result in the initiation of a crack which can lead to cyclic fatigue crack growth.

The cycle number at which the point of crack initiation was deemed to have occurred was when relative stiffness of the cantilever had decreased by more than 0.1% of its initial value.[288] As before each subsequent applied stress cycle causes incremental growth in the crack, known as slow crack growth. If the relative stiffness of the cantilever had decreased by more than 1% of

its initial value complete crack propagation throughout was deemed to have occurred leading to catastrophic failure through brittle fracture of the ceramic SE.[288]

5.4.2.1 Fracture Analysis of the Li_6PS_5Cl cantilevers

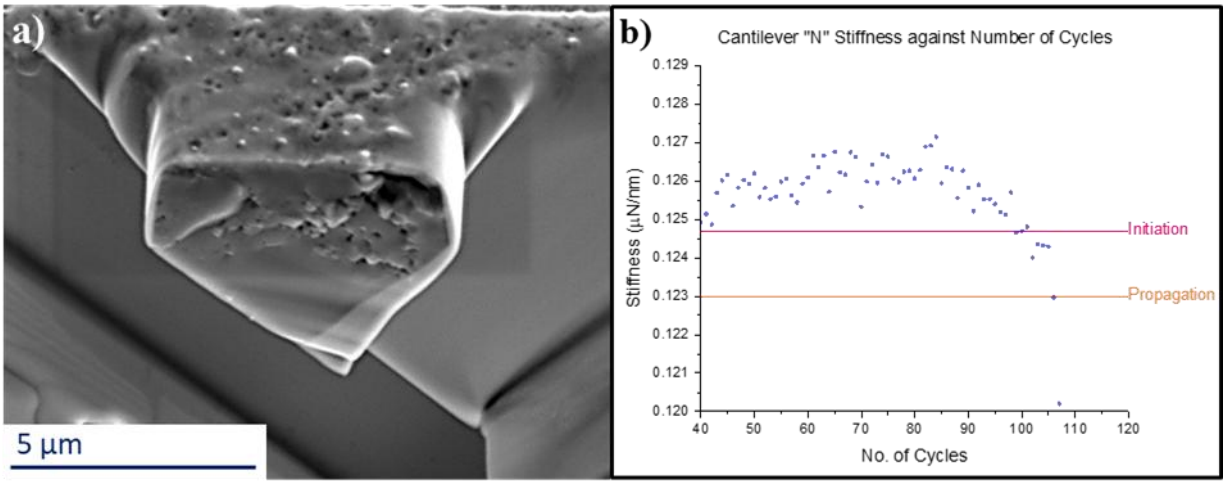

Figure 5.10: a) magnified front-on image of the fracture surface of the fixed end, b) the measured stiffness values calculated from each unload cycle of Li_6PS_5Cl cantilever 'N' and the criteria for crack initiation and complete propagation.

Figure 5.10 shows cantilever 'N' that was initially at a relatively low stress of 43 MPa, suggesting that any failure would be due to the effects of cyclic fatigue. The graph in figure 5.10b) shows that after ~90 cycles there is an increased rate in the decrease in stiffness as the crack initiation criterion is approached. This is evidence that there is some slow crack behaviour occurring and that there is an incremental weakening in the cantilever as the number of cycles increases. There is an even greater change in stiffness as the complete crack propagation criterion is approached, which occurs over a very few (~5) cycles. This suggests that the crack propagates through the cantilever at a fast rate, much more representative of brittle fracture and little evidence of any toughening mechanism due to the cyclical loading. This is further evidenced by figure 5.10a) as the fracture face is relatively smooth with little protruding material suggesting that the crack tip propragated quickly through the material.

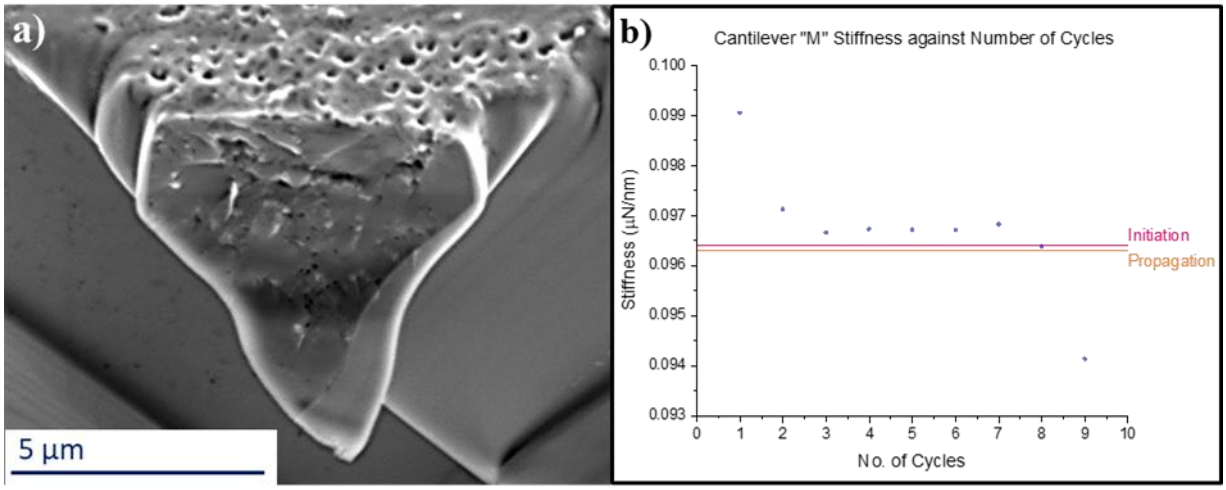

Figure 5.11: a) magnified front-on image of the fracture surface of the fixed end, b) the measured stiffness values calculated from each unload cycle of Li_6PS_5Cl cantilever 'M' and the criteria for crack initiation and complete propagation.

Figure 5.11 shows cantilever 'M' that was initially at an intermediate stress of 80 MPa. The graph in figure 5.11b) shows that cantilever fails very quickly after only 9 cycles. After the first cycle there is an initial decrease in stiffness that appears to stabilise before the criteria for crack initiation and propagation are exceeded within a very low number of cycles. The initial decreases in stiffness could be explained by some plastic deformation in the cantilever occurring after the first loading. The applied stress was significantly lower than the measured fracture stress for an Li_6PS_5Cl cantilever therefore the failure, even though quick, is still due to the effects of cyclic fatigue. However, the low number of cycles to failure combined with the relatively flat fracture surface observed in figure 5.11a) suggests that again brittle fracture of the ceramic has occurred and that that the crack tip propragated very quickly through the material. It should be noted that the number of cycles during testing of Li_6PS_5Cl are far fewer than those recorded during testing of $Li_{6.4}La_3Zr_{1.4}Ta_{0.6}O_{12}$ SE, which suggests that crack resistance in the Li_6PS_5Cl material is comparatively lower; this evidenced by the smoother fracture surfaces in figures 5.10 and 5.11. This is evidence that slow crack growth is not occurring in the Li_6PS_5Cl cantilevers; this is to be expected give the increased number of pores and defects (~ 3%) and lower material strength (modulus ~ 45 MPa) which means resistance to

crack initiation and propagation is lower, therefore crack growth is faster. The faster fracture process is also representative of greater plastic deformation occurring in the Li_6PS_5Cl material.

5.4.2.2 Cyclic Fatigue Results

Cyclic fatigue testing of the Li_6PS_5Cl was again difficult due to their highly air-sensitive nature, of the 16 prepared cantilevers, 15 were successfully tested and the results for each cantilever shown in figure 5.12 below. Tests were carried out in displacement control and the strain amplitude for each test was calculated using the equation put forward by Yamaguchi et al. (2020) for pentagonal microcantilevers.[291] Figure 5.12a) shows the number of cycles at which a crack was deemed to have initiated and figure 5.12b) the number of cycles at which complete crack propagation had occurred, both determined by the previously laid out criteria. Figure 5.12c) shows both trends of strain amplitude vs number of cycles on the same graph, which allows for comparison of the number of cycles between crack initiation and propagation. As the test was displacement controlled the strain remains constant between the point of initiation and the point of complete crack propagation.

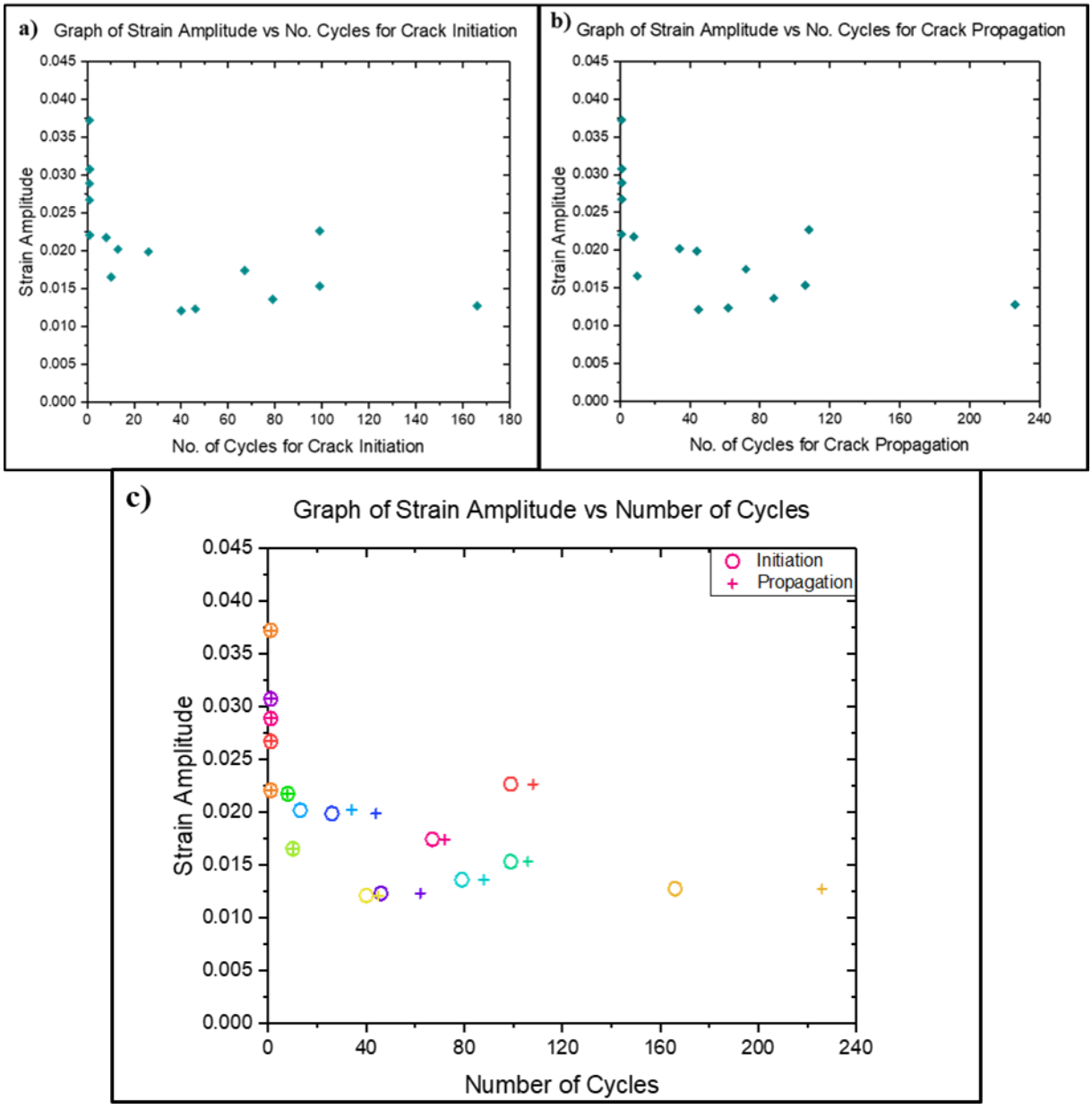

Figure 5.12: Graph of strain amplitude against a) number of cycles for crack initiation, b) number of cycles for complete crack propagation in Li_6PS_5Cl cantilevers, c) Both trends are displayed on the same axes to compare the number of cycles between initiation and propagation.

There is a weak trend in figure 5.12c) that suggests as strain amplitude on each cantilever decreases, the number of cycles to respective crack initiation and full crack propagation increase. This is supporting evidence of the fatigue crack growth mechanism, showing that failure by fracture can still occur below the critical fracture stress. It also confirms that the rate

of crack propagation is determined by the size of the stress concentration driving the crack tip, which in of itself is linked back to the strain amplitude.

Figure 5.13 considers the relationship between stress and the number of cycles at points of crack initiation and complete crack propagation. Similarly to the previous trends seen for $Li_{6.4}La_3Zr_{1.4}Ta_{0.6}O_{12}$, figure 5.13a) shows that for Li_6PS_5Cl the cantilevers with a lower initial cycle stress required more cycles for a crack to initiate, supporting the fatigue failure mechanism. Figure 5.13b) shows an ambiguous trend in the applied stress at the point of complete crack propagation, with some samples following the trend suggesting that the number of cycles to failure increases as the applied cyclical stress decreases. However, figure 5.13c) shows that for several samples the applied stress had to increase in order to achieve the desired strain; resulting in increased measured applied stress at the point of complete crack propagation.

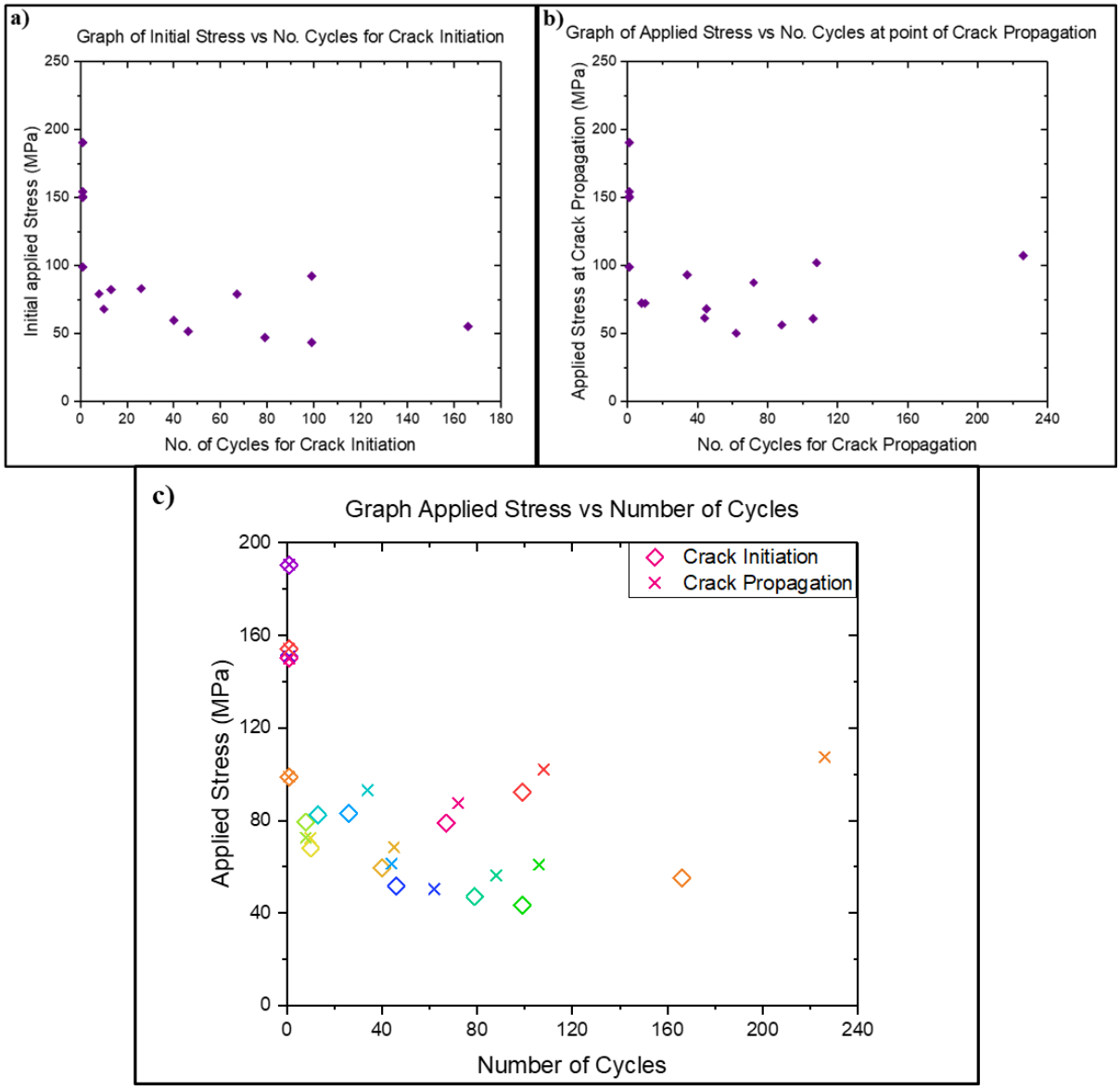

Figure 5.13: a) Graph of the initial stress against the number of cycles for crack initiation, b) Graph of the applied stress against the number of cycles for complete crack propagation in Li_6PS_5Cl cantilevers, c) Both trends displayed on the same axes to compare the difference in applied stress between crack initiation and crack propagation.

This suggests that there is some kind of strengthening mechanism that is occurring at the fixed end cantilever, similar to the $Li_{6.4}La_3Zr_{1.4}Ta_{0.6}O_{12}$ cantilevers. The same mechanisms as discussed in section 5.4.1.2, namely induced residual stress and chemical reaction at the freshly exposed surface, are the expected cause of the improved resistance of the material to crack growth. When comparing the $Li_{6.4}La_3Zr_{1.4}Ta_{0.6}O_{12}$ cantilevers to the Li_6PS_5Cl cantilevers, there is a greater number of cycles between crack initiation and propagation for the

$Li_{6.4}La_3Zr_{1.4}Ta_{0.6}O_{12}$ cantilevers (figure 5.8c) suggesting the presence of slow crack growth and that the strengthening mechanism is more prevalent in $Li_{6.4}La_3Zr_{1.4}Ta_{0.6}O_{12}$ cantilevers. There are differences in the mechanical properties between Li_6PS_5Cl and $Li_{6.4}La_3Zr_{1.4}Ta_{0.6}O_{12}$, principally that Li_6PS_5Cl is generally mechanically weaker; with lower modulus, hardness, and fracture toughness. However, the highly reactive nature of the oxide layer in the $Li_{6.4}La_3Zr_{1.4}Ta_{0.6}O_{12}$ material suggests that the reaction layer could provide some strengthening in some $Li_{6.4}La_3Zr_{1.4}Ta_{0.6}O_{12}$ cantilevers. As discussed previously further investigation is required to determine was is the mechanism by which a cyclically fatigue tested SE cantilever increases in strength as the number of cycles increases.

5.5 Conclusion

The novel testing methodology developed in this chapter provided a first look into the challenges facing solid electrolyte cycle lifetimes; this setup can be used for further investigation into the mechanical challenges facing highly air-sensitive SEs. The research in this chapter demonstrates that mechanical failure due to crack initiation and crack propagation, ultimately leading to material fracture, is possible even at significantly lower applied stresses (less than half) than the material fracture stress. As the electrochemical cycling can lead to internal cyclic stresses within the SE, that can lead to a fatigue crack initiation at relatively low stress. This means that operation of an ASSB below its critical current density, to prevent dendrite initiation (and penetration), can still lead to failure over a number of cycles. Incremental slow crack growth with each subsequent electrochemical cycle can lead to complete crack propagation and brittle fracture. In the context of an operational ASSB, fatigue crack growth can lead to formation of dendrites at low operational currents and eventually to dendritic failure below the critical current density.

The results also suggest that for both SEs tested, but in particular Li_6PS_5Cl, there appears to be some kind of strengthening mechanism as the number of cycles increases before complete crack propagation occurs. Further investigation is required to determine the driving factor behind this strengthening mechanism. Given the cyclical nature of the use of ASSBs, the issue of mechanical material fatigue is a significant problem. More research is needed to investigate methods by which the fatigue crack resistance can be improved, in particular finite element modelling could be used to specifically further investigate the link between repeated cyclical stress and crack initiation. Techniques such as microstructural toughening could be used to hinder crack propagation, for example the introduction of zirconia could introduce a toughening phase similar to that explored in chapter 4.

6. Conclusion

The successful all-solid-state-battery will enable the use of lithium metal anodes and make the next generation of batteries both safer and far more energy dense. Despite significant research into this area, the issues surrounding the solid electrolyte still hinders the progress of fully achieving the potential of lithium metal anodes. There is a lack of understanding of the mechanical properties of solid electrolytes in the existing literature. This thesis highlights how an improved mechanistic understanding could help solve the challenges facing the ASSB; even those appearing electrochemical in nature. One of the biggest issues is short circuit failure due to the ingress of a lithium dendrite, this thesis uses a mechanics focused approach to help solve this problem.

Chapter 3 starts with the first look at the mechanical properties of solid electrolytes; given their highly air-sensitive nature novel testing methods are developed in this chapter to enable experimentally measured mechanical properties, such as modulus, hardness and fracture strength to be determined. By providing a first look at the mechanical properties of SEs, this chapter showed that the mechanical fracture of the SE was the method by which dendritic failure occurred in ASSBs due to electrochemical cycling. Mechanical characterisation revealed that Li_6PS_5Cl exhibited the best mechanical properties of all the cold pressed solid electrolytes tested. However, fracture testing demonstrated that the mechanical properties of all cold pressed samples tested were all quite poor, due to low density and large porosity. It was also observed that by creating composite solid electrolytes a crack deflection mechanism was activated, improving the electrochemical performance, specifically increasing the overall CCD. The idea of increasing solid electrolyte fracture toughness by introducing a composite to

promote crack deflection, merited further investigation; however, better processing is required to improve both the density and microstructure of viable solid electrolytes.

Chapter 4 uses these first look mechanical discoveries to improve the mechanical properties of the Li_6PS_5Cl solid electrolyte. By improving the density of the solid electrolyte both the electrochemical performance and mechanical properties were improved. The method of field assisted sintering was used to produced Li_6PS_5Cl solid electrolyte with a relative density of 99%. An investigation into SE local fracture strength, using a pioneering micro-cantilever testing procedure, provided the first mechanistic understanding and experimental evidence required to establish a model for dendrite initiation.[261] Using an original experimental approach, the fracture toughness of the highly air-sensitive Li_6PS_5Cl was characterised aiding the development of a model for dendrite propagation.[261] The evidence shows that ease of dendrite propagation, therefore ease of short circuit, is directly linked to the fracture toughness of the solid electrolyte. Building on chapter 3 a densified Li_6PS_5Cl composite was made by introducing secondary phase ceria-stabilised-zirconia nanoparticles; the 15% Li_6PS_5Cl-CSZ composite showed significant improvement in fracture toughness and as a result the cycling performance. Further investigation, via high resolution TEM or alike, is required to confirm whether this effect is due to a transformation toughening mechanism from the CSZ introduced to the matrix.

Chapter 5 considers the issue of ASSB cycle lifetimes, in particular the cyclic fatigue of the solid electrolyte. The existing research thus far and the work done in chapters 3 and 4, only considers the static fracture of the solid electrolyte; such as the single cycle CCD tests. A successful ASSB will undergo repeated cyclic stresses due to solid electrolyte volume changes caused by plating during the several 1000s of charge/discharge cycles. The research in chapter

5 demonstrates that even at significantly lower stresses (less than half than the material fracture stress), the cyclical nature of the applied stresses can cause crack initiation and crack propagation ultimately leading to material fracture and mechanical failure. Therefore, even operation of an ASSB below its critical current density can still lead to failure during repeated electrochemical cycling. Once a crack has initiated, each subsequent electrochemical cycle causes incremental slow crack growth which can lead to complete crack propagation and brittle fracture. In the context of an operational ASSB, fatigue crack growth can lead to formation of dendrites at low operational currents and eventually to dendritic failure below the critical current density. The expected operation of an ASSB is cyclical in nature and therefore the issue of mechanical material fatigue is a significant problem.

The work done in this thesis has provided a better mechanistic understanding of the issues surrounding the ASSB and suggested some solutions. The effect of SE density was investigated, and this research has shown that a well densified SE ceramic improves both electrochemical and mechanical performance, however this did not significantly improved plating/stripping currents. The creation of composite SEs had a positive effect on the mechanical properties of the SE. Further investigation is required into the strengthening mechanisms occurring within the composites (specifically transformation toughening) and into the effect on the electrochemical properties, to expand the understanding of SE composites. The critical issue of failure due to mechanical fatigue has been highlighted by this research and is of paramount importance when designing an SE for use in an ASSB. Further work to model the stresses experienced within the SE, in combination with electrochemical cycling data for dendritic failure, will help provide solutions to preventing fatigue failure during cycling of an ASSB.

References

1. Sudduth, W. M. The Voltaic Pile and Electro-Chemical Theory in 1800. *Ambix* **27**, 26–35 (1980).
2. Bullock, K. R. Lead/acid batteries. *J. Power Sources* **51**, 1–17 (1994).
3. Hauel, A. P. The Cadmium-Nickel Storage Battery. *Trans. Electrochem. Soc.* **76**, 435 (1939).
4. Tarascon, J.-M. & Armand, M. *Issues and challenges facing rechargeable lithium batteries*. www.nature.com (2001).
5. Larcher, D. & Tarascon, J.-M. Towards greener and more sustainable batteries for electrical energy storage. *Nat. Chem.* **7**, 19–29 (2014).
6. Crabtree, G. The coming electric vehicle transformation: A future electric transportation market will depend on battery innovation. *Science (80-.).* **366**, 422–424 (2019).
7. Li, M., Lu, J., Chen, Z. & Amine, K. 30 Years of Lithium-Ion Batteries. *Adv. Mater.* **30**, (2018).
8. Manthiram, A. An Outlook on Lithium Ion Battery Technology. **3**, 18 (2017).
9. Lu, L., Han, X., Li, J., Hua, J. & Ouyang, M. A review on the key issues for lithium-ion battery management in electric vehicles. (2012) doi:10.1016/j.jpowsour.2012.10.060.
10. Warner, J. *The handbook of lithium-ion battery pack design: chemistry, components, types and terminology*. (2015).
11. Winter, M. & Brodd, R. J. What are batteries, fuel cells, and supercapacitors? *Chem. Rev.* **104**, 4245–4269 (2004).
12. Sideris, P. & Greenbaum, S. *Lithium Ion Batteries, Electrochemical Reactions in. In: Brodd R. (eds) Batteries for Sustainability. Springer, New York, NY*. (2013).

13. Goodenough, J. B. & Kim, Y. Challenges for Rechargeable Li Batteries. *Chem. Mater* 587–603 (2010).

14. Goodenough, J. B. & Park, K.-S. The Li-Ion Rechargeable Battery: A Perspective. *J. Am. Chem. Soc* **13**, 2020 (2013).

15. Goodenough, J. B. reverse engineering How we made the Li-ion rechargeable battery. *Nat. Electron.* (1928) doi:10.1038/s41928-018-0048-6.

16. Zhang, J., Zhang, L., Sun, F. & Wang, Z. An Overview on Thermal Safety Issues of Lithium-ion Batteries for Electric Vehicle Application. *IEEE Access* **6**, 23848–23863 (2018).

17. Edström, K., Herstedt, M. & Abraham, D. P. A new look at the solid electrolyte interphase on graphite anodes in Li-ion batteries. *J. Power Sources* **153**, 380–384 (2006).

18. Verma, P., Maire, P. & Novák, P. A review of the features and analyses of the solid electrolyte interphase in Li-ion batteries. *Electrochim. Acta* **55**, 6332–6341 (2010).

19. Broussely, M. *et al.* Main aging mechanisms in Li ion batteries. *J. Power Sources* **146**, 90–96 (2005).

20. Booth, S., Nedoma, A., Anthonisamy, N., Materials, P. B.-A. & 2021, undefined. Perspectives for next generation lithium-ion battery cathode materials. *pubs.aip.org*.

21. Li, T. *et al.* Degradation Mechanisms and Mitigation Strategies of Nickel-Rich NMC-Based Lithium-Ion Batteries. *Electrochem. Energy Rev.* **3**, 43–80 (2020).

22. Liu, X. *et al.* In situ observation of thermal-driven degradation and safety concerns of lithiated graphite anode. *nature.comX Liu, L Yin, D Ren, L Wang, Y Ren, W Xu, S Lapidus, H Wang, X He, Z Chen, GL XuNature Commun. 2021•nature.com*.

23. Liu, K., Liu, Y., Lin, D., Pei, A. & Cui, Y. *Materials for lithium-ion battery safety*. http://advances.sciencemag.org/ (2018).

24. Wang, Q. *et al.* Thermal runaway caused fire and explosion of lithium ion battery. *J.*

Power Sources **208**, 210–224 (2012).

25. Janek, J. & Zeier, W. G. A solid future for battery development. *Nat. Publ. Gr.* **1**, (2016).
26. Park, M. S. *et al.* A Highly Reversible Lithium Metal Anode. (2014) doi:10.1038/srep03815.
27. Korthauer, R. Areas of activity on the fringe of lithium-ion battery development, production, and recycling. in *Lithium-Ion Batteries: Basics and Applications* 249–251 (Springer Berlin Heidelberg, 2018). doi:10.1007/978-3-662-53071-9_20.
28. Tarascon, J. M. Is lithium the new gold? *Nat. Chem. 2010 26* **2**, 510–510 (2010).
29. Ionics, K. B.-S. S. & 1994, undefined. Historical development of secondary lithium batteries. *Elsevier*.
30. Sources, D. A.-J. of P. & 2000, undefined. Review of selected electrode–solution interactions which determine the performance of Li and Li ion batteries. *ElsevierD AurbachJournal of Power Sources, 2000•Elsevier.*
31. Xu, W. *et al.* Lithium metal anodes for rechargeable batteries. *pubs.rsc.orgW Xu, J Wang, F Ding, X Chen, E Nasybulin, Y Zhang, JG ZhangEnergy Environ. Sci. 2014•pubs.rsc.org*.
32. Chen, J. Recent progress in advanced materials for lithium ion batteries. *Materials* vol. 6 156–183 (2013).
33. Lu, Y., Tu, Z. & Archer, L. A. Stable lithium electrodeposition in liquid and nanoporous solid electrolytes. (2014) doi:10.1038/NMAT4041.
34. Zhao, Y. *et al.* A new solid polymer electrolyte incorporating Li10GeP2S12 into a polyethylene oxide matrix for all-solid-state lithium batteries. *J. Power Sources* **301**, 47–53 (2016).
35. Khurana, R., Schaefer, J. L., Archer, L. A. & Coates, G. W. Suppression of Lithium Dendrite Growth Using Cross-Linked Polyethylene/Poly(ethylene oxide) Electrolytes:

A New Approach for Practical Lithium-Metal Polymer Batteries. *J. Am. Chem. Soc* **136**, 31 (2014).

36. Porz, L. *et al.* Mechanism of Lithium Metal Penetration through Inorganic Solid Electrolytes. *Adv. Energy Mater.* **7**, 1701003 (2017).

37. Famprikis, T., Canepa, P., Dawson, J. A., Saiful Islam, M. & Masquelier, C. Fundamentals of inorganic solid-state electrolytes for batteries. doi:10.1038/s41563-019-0431-3.

38. Banerjee, A., Wang, X., Fang, C., Wu, E. A. & Meng, Y. S. Interfaces and Interphases in All-Solid-State Batteries with Inorganic Solid Electrolytes. (2020) doi:10.1021/acs.chemrev.0c00101.

39. Wang, Y. *et al.* Design principles for solid-state lithium superionic conductors. (2015) doi:10.1038/NMAT4369.

40. McGrogan, F. P. *et al.* Compliant Yet Brittle Mechanical Behavior of Li2S–P2S5 Lithium-Ion-Conducting Solid Electrolyte. *Adv. Energy Mater.* **7**, 1602011 (2017).

41. Han, X. *et al.* Negating interfacial impedance in garnet-based solid-state Li metal batteries. *Nat. Mater.* **16**, 572–579 (2017).

42. Experimental researches in electricity. by Michael Faraday | Open Library. https://openlibrary.org/books/OL6925439M/Experimental_researches_in_electricity.

43. Goodenough, J., Hong, H., Bulletin, J. K.-M. R. & 1976, undefined. Fast Na+-ion transport in skeleton structures. *ElsevierJB Goodenough, HYP Hong, JA KafalasMaterials Res. Bull. 1976•Elsevier*.

44. Solid State Electrochemistry. (1994) doi:10.1017/CBO9780511524790.

45. sources, B. O.-J. of power & 2000, undefined. Solid state electrolytes: overview of materials and applications during the last third of the Twentieth Century. *ElsevierBB OwensJournal of power sources, 2000•Elsevier*.

46. Dahbi, M., Ghamouss, F., Tran-Van, F., … D. L.-J. of P. & 2011, undefined. Comparative study of EC/DMC LiTFSI and LiPF6 electrolytes for electrochemical storage. *ElsevierM Dahbi, F Ghamouss, F Tran-Van, D Lemordant, M AnoutiJournal Power Sources, 2011•Elsevier*.

47. Ohno, S., Banik, A., Dewald, G., … M. K.-P. in & 2020, undefined. Materials design of ionic conductors for solid state batteries. *iopscience.iop.orgS Ohno, A Ban. GF Dewald, MA Kraft, T Krauskopf, N Minafra, P Till, M Weiss, WG ZeierProgress Energy, 2020•iopscience.iop.org*.

48. Han, F. *et al.* High electronic conductivity as the origin of lithium dendrite formation within solid electrolytes. *Nat. Energy 2019 43* **4**, 187–196 (2019).

49. Xiao, Y. *et al.* Understanding interface stability in solid-state batteries. *Nature Reviews Materials* vol. 5 105–126 (2020).

50. Kasemchainan, J. *et al.* Critical stripping current leads to dendrite formation on plating in lithium anode solid electrolyte cells. *Nat. Mater.* **18**, 1105–1111 (2019).

51. Tikekar, M. D., Choudhury, S., Tu, Z. & Archer, L. A. Design principles for electrolytes and interfaces for stable lithium-metal batteries. *Nat. Energy* **1**, (2016).

52. Wang, M. J., Kazyak, E., Dasgupta, N. P. & Sakamoto, J. Transitioning solid-state batteries from lab to market: Linking electro-chemo-mechanics with practical considerations. *Joule* **5**, 1371–1390 (2021).

53. Manthiram, A., Yu, X. & Wang, S. Lithium battery chemistries enabled by solid-state electrolytes. (2017) doi:10.1038/natrevmats.2016.103.

54. Ning, Z. *et al.* Visualizing plating-induced cracking in lithium-anode solid-electrolyte cells. *Nat. Mater.* (2021) doi:10.1038/s41563-021-00967-8.

55. Wenzel, S. *et al.* Interphase formation on lithium solid electrolytes—An in situ approach to study interfacial reactions by photoelectron spectroscopy. *Elsevier*.

56. Connell, J. G. *et al.* Kinetic versus Thermodynamic Stability of LLZO in Contact with Lithium Metal. *Chem. Mater.* **32**, 10207–10215 (2020).

57. Murugan, R., Thangadurai, V., ENGLISH-, W. W.-E. I. & 2007, undefined. Fast lithium ion conduction in garnet-type Li7La3Zr2O12. *Acad. Murugan, V Thangadurai, W WeppnerANGEWANDTE CHEMIE-INTERNATIONAL Ed. ENGLISH-, 2007•academia.edu*.

58. Sharafi, A. *et al.* Impact of air exposure and surface chemistry on Li–Li 7 La 3 Zr 2 O 12 interfacial resistance. *pubs.rsc.orgA Sharafi, S Yu, M Naguib, M Lee, C Ma, HM Meyer, J Nanda, M Chi, DJ Siegel, J SakamotoJournal Mater. Chem. A, 2017•pubs.rsc.org*.

59. Brugge, R. H. *et al.* Garnet Electrolytes for Solid State Batteries: Visualization of Moisture-Induced Chemical Degradation and Revealing Its Impact on the Li-Ion Dynamics. *Chem. Mater.* **30**, 3704–3713 (2018).

60. Brugge, R., Pesci, F., Cavallaro, A., … C. S.-J. of M. & 2020, undefined. The origin of chemical inhomogeneity in garnet electrolytes and its impact on the electrochemical performance. *pubs.rsc.orgRH Brugge, FM Pesci, A Cavallaro, C Sole, MA Isaacs, G Kerherve, RS Weather. Mater. Chem. A, 2020•pubs.rsc.org*.

61. Schmaltz, T. *et al.* A Roadmap for Solid-State Batteries. *Adv. Energy Mater.* **13**, (2023).

62. Wang, S. *et al.* Lithium Chlorides and Bromides as Promising Solid-State Chemistries for Fast Ion Conductors with Good Electrochemical Stability. *Angew. Chemie - Int. Ed.* **58**, 8039–8043 (2019).

63. Li, X. *et al.* Water-Mediated Synthesis of a Superionic Halide Solid Electrolyte. *Angew. Chemie - Int. Ed.* **58**, 16427–16432 (2019).

64. Zhang, H., Zeng, Z., Shi, X., Wang, C. H. & Du, Y. Doping engineering of scandium-based solid-state electrolytes toward superior ionic conductivity. *EcoMat* **5**, (2023).

65. Bahmani, F., Rodmyre, C. & Smirnova, A. Li 3 InCl 6 Electrolyte with High Voltage Compatibility for All-Solid-State Batteries . *ECS Meet. Abstr.* **MA2023-01**, 1017–1017 (2023).

66. Riegger, L. M., Schlem, R., Sann, J., Zeier, W. G. & Janek, J. Lithium-Metal Anode Instability of the Superionic Halide Solid Electrolytes and the Implications for Solid-State Batteries. *Angew. Chemie - Int. Ed.* **60**, 6718–6723 (2021).

67. Li, X. *et al.* Origin of Superionic Li3Y1- xInxCl6Halide Solid Electrolytes with High Humidity Tolerance. *Nano Lett.* **20**, 4384–4392 (2020).

68. Mizno, F., Hayashi, A., Tadanaga, K., & Tatsumisago, M. New, Highly Ion-Conductive Crystals Precipitated from Li2S-P2S5 Glasses. *Adv Mater* 918–921 (2005).

69. Ong, S. *et al.* Phase stability, electrochemical stability and ionic conductivity of the Li 10±1 MP 2 X 12 (M= Ge, Si, Sn, Al or P, and X= O, S or Se) family of superionic conductors. *pubs.rsc.orgSP Ong, Y Mo, WD Richards, L Miara, HS Lee, G CederEnergy Environ. Sci. 2013•pubs.rsc.org*.

70. Deiseroth, H.-J. *et al.* Li6PS5X: A Class of Crystalline Li-Rich Solids With an Unusually High Li+ Mobility. *Angew. Chemie Int. Ed.* **47**, 755–758 (2008).

71. Sakuda, A., Hayashi, A., reports, M. T.-S. & 2013, undefined. Sulfide solid electrolyte with favorable mechanical property for all-solid-state lithium battery. *nature.comA Sakuda, A Hayashi, M TatsumisagoScientific reports, 2013•nature.com*.

72. Chen, Y., Marple, M., Tan, D., … S. H.-J. of M. & 2022, undefined. Investigating dry room compatibility of sulfide solid-state electrolytes for scalable manufacturing. *pubs.rsc.org*.

73. Wenzel, S. *et al.* Interfacial reactivity and interphase growth of argyrodite solid electrolytes at lithium metal electrodes. *Elsevier*.

74. Winkler, C. Germanium, Ge, ein neues, nichtmetallisches Element. *Berichte der Dtsch.*

Chem. Gesellschaft **19**, 210–211 (1886).

75. Zhou, L., Minafra, N., Zeier, W. G. & Nazar, L. F. Innovative Approaches to Li-Argyrodite Solid Electrolytes for All-Solid-State Lithium Batteries. *Acc. Chem. Res.* **54**, 2717–2728 (2021).

76. Boulineau, S., Courty, M., Tarascon, J.-M. & Viallet, V. Mechanochemical synthesis of Li-argyrodite Li6PS5X(X=Cl, Br, I) as sulfur-basedsolid electrolytes for all solid state batteries application. *Solid State Ionics* **221**, 1–5 (2012).

77. Zheng, F., Kotobuk, M., Song, S., Lai, M. O. & Lu, L. Review on solid electrolytes for all-solid-state lithium-ion batteries. *J. Power Sources* **196**, 13–24 (2011).

78. Zhou, L. *et al.* Solvent-Engineered Design of Argyrodite Li 6 PS 5 X (X = Cl, Br, I) Solid Electrolytes with High Ionic Conductivity. *ACS Energy Lett.* **4**, 265–270 (2019).

79. Schwietert, T. K. *et al.* Clarifying the relationship between redox activity and electrochemical stability in solid electrolytes. *Nat. Mater.* **19**, 428–435 (2020).

80. Zhou, Y. *et al.* Observation of Interfacial Degradation of Li6PS5Cl against Lithium Metal and LiCoO2 via In Situ Electrochemical Raman Microscopy. *Batter. Supercaps* batt.201900218 (2020) doi:10.1002/batt.201900218.

81. Deng, Z., Wang, Z., Chu, L.-H., Luo, J. & Ong, S. P. Elastic Properties of Alkali Superionic Conductor Electrolytes from First Principles Calculations. *J. Electrochem. Soc* **163**, (2016).

82. Ulvestad, A. A Brief Review of Current Lithium Ion Battery Technology and Potential Solid State Battery Technologies. (2018).

83. Krauskopf, T., Richter, F. H., Zeier, W. G. & Rgen Janek, J. Physicochemical Concepts of the Lithium Metal Anode in Solid-State Batteries. (2020) doi:10.1021/acs.chemrev.0c00431.

84. Cao, D. *et al.* Lithium Dendrite in All-Solid-State Batteries: Growth Mechanisms,

Suppression Strategies, and Characterizations. *Matter* **3**, 57–94 (2020).

85. Monroe, C. & Newman, J. The Impact of Elastic Deformation on Deposition Kinetics at Lithium/Polymer Interfaces. *J. Electrochem. Soc* **152**, 396–404 (2005).

86. Monroe, C. & Newman, J. The Impact of Elastic Deformation on Deposition Kinetics at Lithium/Polymer Interfaces. *J. Electrochem. Soc.* **152**, A396 (2005).

87. Swamy, T. *et al.* Lithium Metal Penetration Induced by Electrodeposition through Solid Electrolytes: Example in Single-Crystal Li 6 La 3 ZrTaO 12 Garnet . *J. Electrochem. Soc.* **165**, A3648–A3655 (2018).

88. Kerman, K., Luntz, A., Viswanathan, V., Chiang, Y.-M. & Chen, Z. Review-Practical Challenges Hindering the Development of Solid State Li Ion Batteries. *J. Electrochem. Soc* 164 (2017) doi:10.1149/2.1571707jes.

89. Zhou, W. *et al.* Polymer lithium-garnet interphase for an all-solid-state rechargeable battery. *Nano Energy* **53**, 926–931 (2018).

90. Pang, Q., Liang, X., Shyamsunder, A. & Nazar, L. F. An In Vivo Formed Solid Electrolyte Surface Layer Enables Stable Plating of Li Metal. *Joule* **1**, 871–886 (2017).

91. Nagao, M. *et al.* In situ SEM study of a lithium deposition and dissolution mechanism in a bulk-type solid-state cell with a Li2S-P2S5 solid electrolyte. *Phys. Chem. Chem. Phys.* **15**, 18600–18606 (2013).

92. Lotsch, B. V. & Maier, J. Relevance of solid electrolytes for lithium-based batteries: A realistic view. *J. Electroceramics* **38**, 128–141 (2017).

93. Porz, L. *et al.* Mechanism of Lithium Metal Penetration through Inorganic Solid Electrolytes. *Adv. Energy Mater.* **7**, 1701003 (2017).

94. Yu, S. *et al.* Elastic Properties of the Solid Electrolyte Li 7 La 3 Zr 2 O 12 (LLZO). (2015) doi:10.1021/acs.chemmater.5b03854.

95. Cheng, E. J., Sharafi, A. & Sakamoto, J. Intergranular Li metal propagation through

polycrystalline Li 6.25 Al 0.25 La 3 Zr 2 O 12 ceramic electrolyte. (2016) doi:10.1016/j.electacta.2016.12.018.

96. Ishiguro, K. *et al.* Stability of Nb-Doped Cubic Li7La3Zr2O12 with Lithium Metal. *J. Electrochem. Soc.* **160**, A1690 (2013).

97. Ishiguro, K. *et al.* Ta-Doped Li7La3Zr2O12 for Water-Stable Lithium Electrode of Lithium-Air Batteries. *J. Electrochem. Soc.* **161**, A668 (2014).

98. Tsai, C. L. *et al.* Li7La3Zr2O12 Interface Modification for Li Dendrite Prevention. *ACS Appl. Mater. Interfaces* **8**, 10617–10626 (2016).

99. Cheng, X.-B. *et al.* Dual-Phase Lithium Metal Anode Containing a Polysulfide-Induced Solid Electrolyte Interphase and Nanostructured Graphene Framework for Lithium–Sulfur Batteries. *ACS Nano* **9**, 6373–6382 (2015).

100. Wang, C., Bai, G., Yang, Y., Liu, X. & Shao, H. Dendrite-free all-solid-state lithium batteries with lithium phosphorous oxynitride-modified lithium metal anode and composite solid electrolytes. *Nano Res.* **12**, 217–223 (2019).

101. Barroso-Luque, L., Tu, Q. & Ceder, G. An Analysis of Solid-State Electrodeposition-Induced Metal Plastic Flow and Predictions of Stress States in Solid Ionic Conductor Defects. *J. Electrochem. Soc.* **167**, 020534 (2020).

102. Armstrong, R., Dickinson, T., Acta, J. T.-E. & 1974, undefined. The breakdown of β-alumina ceramic electrolyte. *ElsevierRD Armstrong, T Dickinson, J TurnerElectrochimica Acta, 1974•Elsevier*.

103. Klinsmann, M., Hildebrand, F. E., Ganser, M. & McMeeking, R. M. Dendritic cracking in solid electrolytes driven by lithium insertion. *J. Power Sources* **442**, (2019).

104. Ren, Y., Shen, Y., Lin, Y. & Nan, C. W. Direct observation of lithium dendrites inside garnet-type lithium-ion solid electrolyte. *Electrochem. commun.* **57**, 27–30 (2015).

105. Shen, F., Dixit, M. B., Xiao, X. & Hatzell, K. B. Effect of Pore Connectivity on Li

Dendrite Propagation within LLZO Electrolytes Observed with Synchrotron X-ray Tomography. *ACS Energy Lett* **3**, 12 (2018).

106. Mancktelow, N. S., Grujic, D. & Johnson, E. L. *An SEM study of porosity and grain boundary microstructure in quartz mylonites, Simplon Fault Zone, Central Alps*.

107. Cheng, E. J., Sharafi, A. & Sakamoto, J. Intergranular Li metal propagation through polycrystalline Li6.25Al0.25La3Zr2O12 ceramic electrolyte. *Electrochem. Acta* 85–91 (2017).

108. Liu, X. *et al.* Local electronic structure variation resulting in Li 'filament' formation within solid electrolytes. *Nat. Mater. 2021* 1–6 (2021) doi:10.1038/s41563-021-01019-x.

109. Yonemoto, F. *et al.* Temperature effects on cycling stability of Li plating/stripping on Ta-doped Li7La3Zr2O12. *J. Power Sources* **343**, 207–215 (2017).

110. Manalastas, W. *et al.* Mechanical failure of garnet electrolytes during Li electrodeposition observed by in-operando microscopy. *J. Power Sources* **412**, 287–293 (2019).

111. Koerver, R. *et al.* Capacity Fade in Solid-State Batteries: Interphase Formation and Chemomechanical Processes in Nickel-Rich Layered Oxide Cathodes and Lithium Thiophosphate Solid Electrolytes. *Chem. Mater.* **29**, 5574–5582 (2017).

112. Koerver, R. *et al.* Chemo-mechanical expansion of lithium electrode materials-on the route to mechanically optimized all-solid-state batteries. *Energy Environ. Sci.* **11**, 2142–2158 (2018).

113. Koshikawa, H. *et al.* Dynamic changes in charge-transfer resistance at Li metal/Li7La3Zr2O12 interfaces during electrochemical Li dissolution/deposition cycles. *J. Power Sources* **376**, 147–151 (2018).

114. Botros, M., Djenadic, R., Clemens, O., Möller, M. & Hahn, H. Field assisted sintering

of fine-grained Li7-3xLa3Zr2AlxO12 solid electrolyte and the influence of the microstructure on the electrochemical performance. *J. Power Sources* **309**, 108–115 (2016).

115. Mukhopadhyay, A. & Sheldon, B. W. Deformation and stress in electrode materialsfor Li-ion batteries. *Prog. Mater. Sci.* **63**, 58–116 (2014).
116. Zhang, W. *et al.* Degradation Mechanisms at the Li 10 GeP 2 S 12 /LiCoO 2 Cathode Interface in an All-Solid-State Lithium-Ion Battery. (2018) doi:10.1021/acsami.8b05132.
117. Lord, J. & Morrell, R. Elastic modulus measurement. (2007).
118. Glossary of Materials Testing Terms - Instron. https://www.instron.us/en-us/our-company/library/glossary.
119. Chen, R., Qu, W., Guo, X., Li, L. & Wu, F. The pursuit of solid-state electrolytes for lithium batteries: From comprehensive insight to emerging horizons. *Materials Horizons* vol. 3 487–516 (2016).
120. Smith, S. *et al.* Electrical, mechanical and chemical behavior of Li1.2Zr1.9Sr0.1(PO4)3. *Solid State Ionics* **300**, 38–45 (2017).
121. Ramesh, S., Winie, T. & Arof, A. K. Investigation of mechanical properties of polyvinyl chloride-polyethylene oxide (PVC-PEO) based polymer electrolytes for lithium polymer cells. *Eur. Polym. J.* **43**, 1963–1968 (2007).
122. Kato, A., Yamamoto, M., Sakuda, A., Hayashi, A. & Tatsumisago, M. Mechanical Properties of Li2S-P2S5 Glasses with Lithium Halides and Application in All-Solid-State Batteries. *ACS Appl. Energy Mater.* **1**, 1002–1007 (2018).
123. Lei, D. *et al.* Progress and Perspective of Solid-State Lithium–Sulfur Batteries. *Advanced Functional Materials* vol. 28 1707570 (2018).
124. Wang, J. J., Meng, F. Y., Ma, X. Q., Xu, M. X. & Chen, L. Q. Lattice, elastic,

polarization, and electrostrictive properties of BaTiO3 from first-principles. *J. Appl. Phys.* **108**, 034107 (2010).

125. Nonemacher, J. F. *et al.* Microstructure and properties investigation of garnet structured Li7La3Zr2O12 as electrolyte for all-solid-state batteries. *Solid State Ionics* **321**, 126–134 (2018).

126. Sharafi, A., Haslam, C. G., Kerns, R. D., Wolfenstine, J. & Sakamoto, J. Controlling and correlating the effect of grain size with the mechanical and electrochemical properties of Li7La3Zr2O12 solid-state electrolyte. *J. Mater. Chem. A* **5**, 21491–21504 (2017).

127. Huang, X. *et al.* A Li-Garnet composite ceramic electrolyte and its solid-state Li-S battery. *J. Power Sources* **382**, 190–197 (2018).

128. Singh, D., Henss, A., Mogwitz, B., … A. G.-C. reports physical & 2022, undefined. Li6PS5Cl microstructure and influence on dendrite growth in solid-state batteries with lithium metal anode. *cell.comDK Singh, A Henss, B Mogwitz, A Gautam, J Horn, T Krauskopf, S Burkhardt, J SannCell reports Phys. Sci. 2022•cell.com*.

129. Diallo, M. S. *et al.* Effect of solid-electrolyte pellet density on failure of solid-state batteries. *Nat. Commun. 2024 151* **15**, 1–9 (2024).

130. Garcia-Mendez, R., Smith, J. G., Neuefeind, J. C., Siegel, D. J. & Sakamoto, J. Correlating Macro and Atomic Structure with Elastic Properties and Ionic Transport of Glassy Li $_2$ S-P $_2$ S $_5$ (LPS) Solid Electrolyte for Solid-State Li Metal Batteries. *Adv. Energy Mater.* 2000335 (2020) doi:10.1002/aenm.202000335.

131. Yersak, T. A., Salvador, J. R., Pieczonka, N. P. W. & Cai, M. Dense, Melt Cast Sulfide Glass Electrolyte Separators for Li Metal Batteries. *J. Electrochem. Soc.* **166**, A1535–A1542 (2019).

132. Cho, Y. H. *et al.* Mechanical properties of the solid Li-ion conducting electrolyte: Li 0.33 La 0.57 TiO 3. *J. Mater. Sci.* **47**, 5970–5977 (2012).

133. Athanasiou, C. E., Jin, M. Y., Ramirez, C., Padture, N. P. & Sheldon, B. W. High-Toughness Inorganic Solid Electrolytes via the Use of Reduced Graphene Oxide. *Matter* **3**, 212–229 (2020).

134. El-Shinawi, H. *et al.* Liquid-Phase Approach to Glass-Microfiber-Reinforced Sulfide Solid Electrolytes for All-Solid-State Batteries. *ACS Appl. Mater. Interfaces* **15**, 36512–36518 (2023).

135. Yersak, T., Salvador, J. R., Schmidt, R. D. & Cai, M. Hot Pressed, Fiber-Reinforced (Li2S)70(P2S5)30 Solid-State Electrolyte Separators for Li Metal Batteries. *ACS Appl. Energy Mater.* **2**, 3523–3531 (2019).

136. Croce, F. *et al.* Physical and Chemical Properties of Nanocomposite Polymer Electrolytes. (1999) doi:10.1021/jp992307u.

137. Krawiec, W. *et al.* Polymer nanocomposites: a new strategy for synthesizing solid electrolytes for rechargeable lithium batteries. *J. Power Sources* **54**, 310–315 (1995).

138. Choi, J. H., Lee, C. H., Yu, J. H., Doh, C. H. & Lee, S. M. Enhancement of ionic conductivity of composite membranes for all-solid-state lithium rechargeable batteries incorporating tetragonal Li7La3Zr2O12 into a polyethylene oxide matrix. *J. Power Sources* **274**, 458–463 (2015).

139. Heavens, S. N. Strength improvement in beta″ alumina by incorporation of zirconia. *J. Mater. Sci.* **23**, 3515–3518 (1988).

140. Green, D. J. Transformation toughening and grain size control in β″-Al2O3/ZrO2 composites. *J. Mater. Sci.* **20**, 2639–2646 (1985).

141. Viswanathan, L., Ikuma, Y. & Virkar, A. V. Transfomation toughening of β″-alumina by incorporation of zirconia. *J. Mater. Sci.* **18**, 109–113 (1983).

142. Binner, J. G. P. & Stevens, R. Improvement in the mechanical properties of polycrystalline beta-alumina via the use of zirconia particles containing stabilizing oxide

additions. *J. Mater. Sci.* **20**, 3119–3124 (1985).

143. Olson, D. & De Jonghe, L. C. Zirconia-toughened sodium beta″-alumina solid electrolyte. *J. Mater. Sci.* **21**, 4221–4226 (1986).

144. Sheng, Y., Sarkar, P. & Nicholson, P. S. The mechanical and electrical properties of ZrO2-Na β″-Al2O3 composites. *J. Mater. Sci.* **23**, 958–967 (1988).

145. Samad, Y. A., Asghar, A. & Hashaikeh, R. Electrospun cellulose/PEO fiber mats as a solid polymer electrolytes for Li ion batteries. *Renew. Energy* **56**, 90–95 (2013).

146. Li, D., Chen, L., Wang, T. & Fan, L.-Z. 3D Fiber-Network-Reinforced Bicontinuous Composite Solid Electrolyte for Dendrite-free Lithium Metal Batteries. *ACS Appl. Mater. Interfaces* **10**, 7069–7078 (2018).

147. Zhang, F. *et al.* A review of mechanics-related material damages in all-solid-state batteries: Mechanisms, performance impacts and mitigation strategies. *Nano Energy* vol. 70 104545 (2020).

148. LePage, W. S. *et al.* Lithium Mechanics: Roles of Strain Rate and Temperature and Implications for Lithium Metal Batteries. *J. Electrochem. Soc.* **166**, A89 (2019).

149. Masias, A., Felten, N., Garcia-Mendez, R., Wolfenstine, J. & Sakamoto, J. Elastic, plastic, and creep mechanical properties of lithium metal. *J. Mater. Sci. 2018 543* **54**, 2585–2600 (2018).

150. Zeng, H. *et al.* Enhanced cycling performance for all-solid-state lithium ion battery with LiFePO4 composite cathode encapsulated by poly (ethylene glycol) (PEG) based polymer electrolyte. *Solid State Ionics* **320**, 92–99 (2018).

151. Strauss, F. *et al.* Impact of Cathode Material Particle Size on the Capacity of Bulk-Type All-Solid-State Batteries. *ACS Energy Lett* **3**, 47 (2018).

152. Wen, J., Yu, Y. & Chen, C. A review on lithium-ion batteries safety issues: Existing problems and possible solutions. *Materials Express* vol. 2 197–212 (2012).

153. Pang, Q. *et al.* Tuning the electrolyte network structure to invoke quasi-solid state sulfur conversion and suppress lithium dendrite formation in Li–S batteries. *Nat. Energy* **3**, 783–791 (2018).

154. Dollé, M., Sannier, L., Beaudoin, B., Trentin, M. & Tarascon, J. M. Live scanning electron microscope observations of dendritic growth in lithium/polymer cells. *Electrochem. Solid-State Lett.* **5**, A286 (2002).

155. Voss, R. F. & Tomkiewicz, M. Computer Simulation of Dendritic Electrodeposition. *J. Electrochem. Soc.* **132**, 371–375 (1985).

156. The electrolytic growth of dendrites from ionic solutions. *Proc. R. Soc. London. Ser. A. Math. Phys. Sci.* **268**, 485–505 (1962).

157. Monroe, C. & Newman, J. The Impact of Elastic Deformation on Deposition Kinetics at Lithium/Polymer Interfaces. *J. Electrochem. Soc.* **152**, A396 (2005).

158. Natsiavas, P. P., Weinberg, K., Rosato, D. & Ortiz, M. Effect of prestress on the stability of electrode-electrolyte interfaces during charging in lithium batteries. *J. Mech. Phys. Solids* **95**, 92–111 (2016).

159. Bucci, G. & Christensen, J. Modeling of lithium electrodeposition at the lithium/ceramic electrolyte interface: The role of interfacial resistance and surface defects. *J. Power Sources* **441**, 227186 (2019).

160. Xu, B. *et al.* Li3PO4-added garnet-type Li6.5La3Zr1.5Ta0.5O12 for Li-dendrite suppression. *J. Power Sources* **354**, 68–73 (2017).

161. Tsai, C.-L. *et al.* Li 7 La 3 Zr 2 O 12 Interface Modification for Li Dendrite Prevention. (2016) doi:10.1021/acsami.6b00831.

162. Li, Y. *et al.* Hybrid Polymer/Garnet Electrolyte with a Small Interfacial Resistance for Lithium-Ion Batteries. *Angew. Chemie* **129**, 771–774 (2017).

163. Zhou, D. *et al.* SiO2 Hollow Nanosphere-Based Composite Solid Electrolyte for Lithium

Metal Batteries to Suppress Lithium Dendrite Growth and Enhance Cycle Life. *Adv. Energy Mater.* **6**, 1502214 (2016).

164. Wang, C. *et al.* Conformal, Nanoscale ZnO Surface Modification of Garnet-Based Solid-State Electrolyte for Lithium Metal Anodes. *Nano Lett.* **17**, 565–571 (2017).

165. Luo, W. *et al.* Reducing Interfacial Resistance between Garnet-Structured Solid-State Electrolyte and Li-Metal Anode by a Germanium Layer. *Adv. Mater.* **29**, 1606042 (2017).

166. Yao, X. *et al.* High-Performance All-Solid-State Lithium–Sulfur Batteries Enabled by Amorphous Sulfur-Coated Reduced Graphene Oxide Cathodes. *Adv. Energy Mater.* **7**, (2017).

167. Chung, H. & Kang, B. Mechanical and Thermal Failure Induced by Contact between a Li1.5Al0.5Ge1.5(PO4)3 Solid Electrolyte and Li Metal in an All Solid-State Li Cell. *Chem. Mater.* **29**, 8611–8619 (2017).

168. Waetzig, K., Rost, A., Langklotz, U., Matthey, B. & Schilm, J. An explanation of the microcrack formation in Li1.3Al0.3Ti1.7(PO4)3 ceramics. *J. Eur. Ceram. Soc.* **36**, 1995–2001 (2016).

169. Kobi, S. & Mukhopadhyay, A. Structural (in)stability and spontaneous cracking of Li-La-zirconate cubic garnet upon exposure to ambient atmosphere. *J. Eur. Ceram. Soc.* **38**, 4707–4718 (2018).

170. Liu, T. *et al.* Non-successive degradation in bulk-type all-solid-state lithium battery with rigid interfacial contact. *Electrochem. commun.* **79**, 1–4 (2017).

171. Sun, F. *et al.* Visualizing the morphological and compositional evolution of the interface of InLi-anode thio-LISION electrolyte in an all-solid-state Li-S cell by: In operando synchrotron X-ray tomography and energy dispersive diffraction. *J. Mater. Chem. A* **6**, 22489–22496 (2018).

172. Devaux, D. *et al.* Lithium Metal-Copper Vanadium Oxide Battery with a Block Copolymer Electrolyte. *J. Electrochem. Soc.* **163**, A2447–A2455 (2016).

173. Devaux, D. *et al.* Failure Mode of Lithium Metal Batteries with a Block Copolymer Electrolyte Analyzed by X-Ray Microtomography. *J. Electrochem. Soc.* **162**, A1301–A1309 (2015).

174. Jiang, G. *et al.* All solid-state lithium-polymer battery using poly(urethane acrylate)/nano-SiO2 composite electrolytes. *J. Power Sources* **141**, 143–148 (2005).

175. Yu, C. *et al.* Accessing the bottleneck in all-solid state batteries, lithium-ion transport over the solid-electrolyte-electrode interface. *Nat. Commun.* **8**, 1–9 (2017).

176. Su, X. *et al.* Deformation and Chemomechanical Degradation at Solid Electrolyte-Electrode Interfaces. *ACS Energy Lett.* **2**, 1729–1733 (2017).

177. Montes, J. M., Cuevas, F. G., Cintas, J. & Torres, Y. Powder compaction law for cold die pressing. *Granul. Matter* **12**, 617–627 (2010).

178. Fruhstorfer, J., International, C. A.-C. & 2017, undefined. Influence of particle size distributions on the density and density gradients in uniaxial compacts. *ElsevierJ Fruhstorfer, CG AnezirisCeramics Int. 2017•Elsevier*.

179. Angelo, P., Subramanian, R. & Ravisankar, B. *Powder metallurgy: science, technology and applications*. (2022).

180. Akisanya, A. R., Cocks, A. C. F. & Fleck, N. A. The yield behaviour of metal powders. *Int. J. Mech. Sci.* **39**, 1315–1324 (1997).

181. Carter, C. B. & Norton, M. G. Ceramic materials: Science and engineering. *Ceram. Mater. Sci. Eng.* 1–766 (2013) doi:10.1007/978-1-4614-3523-5.

182. Lee, W. & Rainforth, M. *Ceramic microstructures: property control by processing*. (1994).

183. Mazlan, M., Jamadon, N., Rajabi, A., … A. S. of materials & 2023, undefined. Necking

mechanism under various sintering process parameters–a review. *ElsevierMR Maz. NH Jamadon, A Rajabi, AB Sulong, IF Mohamed, F Yusof, NA Jamaljournal Mater. Res. Technol. 2023•Elsevier*.

184. Wang, Y. *et al.* Chemical and Electrochemical Characterization of Hot-Pressed Li6PS5Cl Solid State Electrolyte: Operating Pressure-Invariant High Ionic Conductivity. *ChemSusChem* (2024) doi:10.1002/CSSC.202400718.

185. Ando, K., Matsuda, T., Miwa, T., Kawai, M. & Imamura, D. Degradation mechanism of all-solid-state lithium-ion batteries with argyrodite Li7−xPS6−xClx sulfide through high-temperature cycling test. *Batter. Energy* **2**, (2023).

186. Guillon, O. *et al.* Field-assisted sintering technology/spark plasma sintering: Mechanisms, materials, and technology developments. *Adv. Eng. Mater.* **16**, 830–849 (2014).

187. Li, R., Yuan, T., Liu, X., materialia, K. Z.-S. & 2016, undefined. Enhanced atomic diffusion of Fe–Al diffusion couple during spark plasma sintering. *ElsevierR Li, T Yuan, X Liu, K ZhouScripta Mater. 2016•Elsevier*.

188. Hulbert, D. M. *et al.* The absence of plasma in 'spark plasma sintering'. *J. Appl. Phys.* **104**, (2008).

189. Köhler, H. On Abbe's theory of image formation in the microscope. *Opt. Acta (Lond).* **28**, 1691–1701 (1981).

190. Flegler, S. L., Heckman, J. W. & Klomparens, K. L. *Scanning and Transmission Electron Microscopy: An Introduction*. (1994).

191. Nellist, P. Microstructural characterization of materials: Lecture 6 – Scanning Electron Microscopy (SEM). 1–10 (2017).

192. Egerton, R. F. Physical principles of electron microscopy: An introduction to TEM, SEM, and AEM, second edition. *Phys. Princ. Electron Microsc. An Introd. to TEM,*

SEM, AEM, Second Ed. 1–196 (2016) doi:10.1007/978-3-319-39877-8.

193. Micron, M. P.- & 1999, undefined. Applications of focused ion beam microscopy to materials science specimens. *Elsevier*.

194. Zhao, L. *et al.* The 3D Controllable Fabrication of Nanomaterials with FIB-SEM Synchronization Technology. *Nanomaterials* **13**, (2023).

195. Volkert, C., bulletin, A. M.-M. & 2007, undefined. Focused ion beam microscopy and micromachining. *cambridge.org*.

196. 2: Schematic drawing of ion-solid interactions in FIB [FEI 04] | Download Scientific Diagram. https://www.researchgate.net/figure/Schematic-drawing-of-ion-solid-interactions-in-FIB-FEI-04_fig18_216713121.

197. Pietsch, P. & Wood, V. X-Ray Tomography for Lithium Ion Battery Research: A Practical Guide. *Annu. Rev. Mater. Res.* **47**, 451–479 (2017).

198. Browne, W. *Electrochemsitry*. (2018).

199. Irvine, J. T. S., Sinclair, D. C. & West, A. R. Electroceramics: Characterization by Impedance Spectroscopy. *Adv. Mater.* **2**, 132–138 (1990).

200. Macdonald, J. R. Impedance spectroscopy: Models, data fitting, and analysis. *Solid State Ionics* **176**, 1961–1969 (2005).

201. Basics of Electrochemical Impedance Spectroscopy. *Gamry Instruments Appl. Note* (2009).

202. Wang, S. *et al.* Electrochemical impedance spectroscopy. *nature.comS Wang, J Zhang, O Gharbi, V Vivier, M Gao, ME OrazemNature Rev. Methods Prim. 2021•nature.com*.

203. Ye, L., Nature, X. L.- & 2021, undefined. A dynamic stability design strategy for lithium metal solid state batteries. *nature.comL Ye, X LiNature, 2021•nature.com*.

204. Lee, Y.-G. *et al.* High-energy long-cycling all-solid-state lithium metal batteries enabled by silver–carbon composite anodes. *Nat. Energy 2020 54* **5**, 299–308 (2020).

205. Olson, J. Z., López, C. M. & Dickinson, E. J. F. Differential Analysis of Galvanostatic Cycle Data from Li-Ion Batteries: Interpretative Insights and Graphical Heuristics. *Chem. Mater.* **35**, 1487–1513 (2023).

206. Fuchs, T., Haslam, C. G., Richter, F. H., Sakamoto, J. & Janek, J. Evaluating the Use of Critical Current Density Tests of Symmetric Lithium Transference Cells with Solid Electrolytes. *Adv. Energy Mater.* **13**, (2023).

207. McBrayer, J., Apblett, C., … K. H.- & 2021, undefined. Mechanical studies of the solid electrolyte interphase on anodes in lithium and lithium ion batteries. *iopscience.iop.orgJD McBrayer, CA Apblett, KL Harrison, KR Fenton, SD MinteerNanotechnology, 2021•iopscience.iop.org*.

208. Bending flexural test - tec-science. https://www.tec-science.com/material-science/material-testing/bending-flexural-test/.

209. Four Point Bending. *Four Point Bend.* (2012) doi:10.1201/B12767.

210. VanLandingham, M. R. Review of instrumented indentation. *J. Res. Natl. Inst. Stand. Technol.* **108**, 249–265 (2003).

211. Schuh, C. A. Nanoindentation studies of materials. *Mater. Today* **9**, 32–40 (2006).

212. Wheeler, J. M., Armstrong, D. E. J., Heinz, W. & Schwaiger, R. High temperature nanoindentation: The state of the art and future challenges. *Curr. Opin. Solid State Mater. Sci.* **19**, 354–366 (2015).

213. Nili, H., Kalantar-zadeh, K., … M. B.-P. in M. & 2013, undefined. In situ nanoindentation: Probing nanoscale multifunctionality. *ElsevierH Nili, K Kalantar-zadeh, M Bhaskaran, S SriramProgress Mater. Sci. 2013•Elsevier*.

214. Oyen, M., biomedical, R. C.-J. of the mechanical behavior of & 2009, undefined. A practical guide for analysis of nanoindentation data. *ElsevierML Oyen, RF CookJournal Mech. Behav. Biomed. Mater. 2009•Elsevier*.

215. Islam, M., Shakil, S., Shaheen, N., Micron, P. B.- & 2021, undefined. An overview of microscale indentation fatigue: Composites, thin films, coatings, and ceramics. *Elsevier*.

216. Oliver, W. C. & Pharr, G. M. An improved technique for determining hardness and elastic modulus using load and displacement sensing indentation experiments. *J. Mater. Res.* **7**, 1564–1583 (1992).

217. Wang, S., Micromachines, H. Z.- & 2020, undefined. Low temperature nanoindentation: Development and applications. *mdpi.comS Wang, H ZhaoMicromachines, 2020•mdpi.com*.

218. Oliver, W. C. & Pharr, G. M. Measurement of hardness and elastic modulus by instrumented indentation: Advances in understanding and refinements to methodology. *J. Mater. Res.* **19**, 3–20 (2004).

219. Pharr, G. M., Strader, J. H. & Oliver, W. C. Critical issues in making small-depth mechanical property measurements by nanoindentation with continuous stiffness measurement. *J. Mater. Res.* **24**, 653–666 (2009).

220. Pharr, G. M. & Bolshakov, A. Understanding nanoindentation unloading curves. *J. Mater. Res.* **17**, 2660–2671 (2002).

221. Li, X., characterization, B. B.-M. & 2002, undefined. A review of nanoindentation continuous stiffness measurement technique and its applications. *ElsevierX Li, B BhushanMaterials Charact. 2002•Elsevier*.

222. Quinn, G. D. & Bradt, R. C. On the Vickers Indentation Fracture Toughness Test. *J. Am. Ceram. Soc.* **90**, 673–680 (2007).

223. Pharr, G. M. Measurement of mechanical properties by ultra-low load indentation. *Mater. Sci. Eng. A* **253**, 151–159 (1998).

224. Sebastiani, M., Johanns, K. E., Herbert, E. G. & Pharr, G. M. Measurement of fracture toughness by nanoindentation methods: Recent advances and future challenges. *Current*

Opinion in Solid State and Materials Science vol. 19 324–333 (2015).

225. Bruns, S., Petho, L., Minnert, C., Michler, J. & Durst, K. Fracture toughness determination of fused silica by cube corner indentation cracking and pillar splitting. *Mater. Des.* **186**, 108311 (2020).

226. Cuadrado, N., Casellas, D., Anglada, M. & Jiménez-Piqué, E. Evaluation of fracture toughness of small volumes by means of cube-corner nanoindentation. *Scr. Mater.* **66**, 670–673 (2012).

227. Cuadrado, N., Seuba, J., Casellas, D., Anglada, M. & Jiménez-Piqué, E. Geometry of nanoindentation cube-corner cracks observed by FIB tomography: Implication for fracture resistance estimation. *J. Eur. Ceram. Soc.* **35**, 2949–2955 (2015).

228. LAWN, B. R., EVANS, A. G. & MARSHALL, D. B. Elastic/Plastic Indentation Damage in Ceramics: The Median/Radial Crack System. *J. Am. Ceram. Soc.* **63**, 574–581 (1980).

229. Harding, D. S., Oliver, W. C. & Pharr, G. M. Cracking During Nanoindentation and its Use in the Measurement of Fracture Toughness. *MRS Online Proc. Libr.* **356**, 663–668 (1994).

230. Zhang, T., Feng, Y., Yang, R. & Jiang, P. A method to determine fracture toughness using cube-corner indentation. *Scr. Mater.* **62**, 199–201 (2010).

231. Nanotechnology, S. V.-J. of & 2007, undefined. A review of microcantilevers for sensing applications. *Res. VashistJ. Nanotechnology, 2007•researchgate.net*.

232. Thundat, T., Oden, P. I. & Warmack, R. J. Microcantilever sensors. *Microscale Thermophys. Eng.* **1**, 185–199 (1997).

233. Johansson, S., Schweitz, J., Tenerz, L. & Tirén, J. Fracture testing of silicon microelements in situ in a scanning electron microscope. *J. Appl. Phys.* **63**, 4799 (1998).

234. Weihs, T. P., Hong, S., Bravman, J. C. & Nix, W. D. Mechanical deflection of cantilever microbeams: A new technique for testing the mechanical properties of thin films. *J.*

Mater. Res. **3**, 931–942 (1988).

235. Maio, D. Di & Roberts, S. G. Measuring fracture toughness of coatings using focused-ion-beam-machined microbeams. *J. Mater. Res.* **20**, 299–302 (2005).

236. Chen, Y. *et al.* Measurements of elastic modulus and fracture toughness of an air plasma sprayed thermal barrier coating using micro-cantilever bending. *Surf. Coatings Technol.* **374**, 12–20 (2019).

237. Hajilou, T., Deng, Y., Rogne, B. R., Kheradmand, N. & Barnoush, A. In situ electrochemical microcantilever bending test: A new insight into hydrogen enhanced cracking. *Scr. Mater.* **132**, 17–21 (2017).

238. Chen, Y., Zhang, X., Zhao, X., … N. M.-S. and C. & 2019, undefined. Measurements of elastic modulus and fracture toughness of an air plasma sprayed thermal barrier coating using micro-cantilever bending. *ElsevierY Chen, X Zhang, X Zhao, N Markocsan, P Nylén, P XiaoSurface Coatings Technol. 2019•Elsevier*.

239. Dixit, M. *et al.* The Role of Isostatic Pressing in Large-Scale Production of Solid-State Batteries. *ACS Energy Lett.* **7**, 3936–3946 (2022).

240. Wang, Y., Hoang, B., Hoerauf, J., … C. L.-J. of T. & 2021, undefined. Hot and cold pressed LGPS solid electrolytes. *iopscience.iop.orgY Wang, B Hoang, J Hoerauf, C Lee, CF Lin, GW Rubloff, SB Lee, AC KozenJournal Electrochem. Soc. 2021•iopscience.iop.org*.

241. Wang, S. *et al.* High-Conductivity Argyrodite Li 6 PS 5 Cl Solid Electrolytes Prepared via Optimized Sintering Processes for All-Solid-State Lithium-Sulfur Batteries. *ACS Appl. Mater. Interfaces* **10**, 42279–42285 (2018).

242. Tanibata, N. *et al.* Metastable Chloride Solid Electrolyte with High Formability for Rechargeable All-Solid-State Lithium Metal Batteries. *ACS Mater. Lett.* **2**, 880–886 (2020).

243. Gao, X. *et al.* Solid-state lithium battery cathodes operating at low pressures. *Joule* **6**, 636–646 (2022).

244. Li, X. *et al.* Air-stable Li 3 InCl 6 electrolyte with high voltage compatibility for all-solid-state batteries †. *Energy Environ. Sci* **12**, 2665 (2019).

245. Ebnesajjad, S. Material Surface Preparation Techniques. *Handb. Adhes. Surf. Prep. Technol. Appl. Manuf.* 49–81 (2011) doi:10.1016/B978-1-4377-4461-3.10005-7.

246. Kim, Y. *et al.* The Effect of Relative Density on the Mechanical Properties of Hot-Pressed Cubic Li 7 la 3 Zr 2 O 12. *J. Am. Ceram. Soc.* **99**, 1367–1374 (2016).

247. Schell, K. G., Lemke, F., Bucharsky, E. C., Hintennach, A. & Hoffmann, M. J. Microstructure and mechanical properties of Li0.33La0.567TiO3. *J. Mater. Sci.* **52**, 2232–2240 (2017).

248. Jackman, S. D. & Cutler, R. A. Effect of microcracking on ionic conductivity in LATP. *J. Power Sources* **218**, 65–72 (2012).

249. Aguesse, F. *et al.* Investigating the Dendritic Growth during Full Cell Cycling of Garnet Electrolyte in Direct Contact with Li Metal. (2017) doi:10.1021/acsami.6b13925.

250. Wolfenstine, J., Allen, J. L., Sakamoto, J., Siegel, D. J. & Choe, H. Mechanical behavior of Li-ion-conducting crystalline oxide-based solid electrolytes: a brief review. *Ionics (Kiel).* **24**, 1271–1276 (2018).

251. Papakyriakou, M. *et al.* Mechanical behavior of inorganic lithium-conducting solid electrolytes. *ElsevierM Papakyriakou, M Lu, Y Liu, Z Liu, H Chen, MT McDowell, S XiaJournal Power Sources, 2021•Elsevier*.

252. Sullivan, M., Research, B. P.-J. of M. & 2015, undefined. Evaluating indent pile-up with metallic films on ceramic-like substrates. *cambridge.org*.

253. Welch, B. L. *The generalization of 'STUDENT'S'problem when several different populatio*. (1947).

254. T-Distribution Table (One Tail and Two-Tails) - Statistics How To. https://www.statisticshowto.com/tables/t-distribution-table/#two.

255. Hu, B. *et al.* Deflecting lithium dendritic cracks in multi-layered solid electrolytes. *Joule* **8**, 2623–2638 (2024).

256. Gee, I. A. *et al.* Enhanced fracture toughness by ceramic laminate design. *Adv. Appl. Ceram.* **104**, 103–109 (2005).

257. Clegg, W., Kendall, K., Alford, N., Nature, T. B.- & 1990, undefined. A simple way to make tough ceramics. *nature.com*.

258. Kalnaus, S., Dudney, N. J., Westover, A. S., Herbert, E. & Hackney, S. Solid-state batteries: The critical role of mechanics. *Science (80-.).* **381**, (2023).

259. Fitzhugh, W., Ye, L., A, X. L.-J. of M. C. & 2019, undefined. The effects of mechanical constriction on the operation of sulfide based solid-state batteries. *pubs.rsc.orgW Fitzhugh, L Ye, X LiJournal Mater. Chem. A, 2019•pubs.rsc.org*.

260. Bistri, D., Afshar, A. & Di Leo, C. V. Modeling the chemo-mechanical behavior of all-solid-state batteries: a review. *Meccanica* **56**, 1523–1554 (2021).

261. Ning, Z. *et al.* Dendrite initiation and propagation in lithium metal solid-state batteries. *Nat.* | **618**, (2023).

262. Rauchs, G., Fett, T., Munz, D., Ceramic, R. O.-J. of the E. & 2001, undefined. Tetragonal-to-monoclinic phase transformation in CeO2-stabilised zirconia under uniaxial loading. *Elsevier*.

263. Henshall, J., Ceramics, S. T.-E. & 2024, undefined. Compaction and sintering of toughened zirconia ceramics. *taylorfrancis.comJL Henshall, ST ThuraisinghamEngineering Ceram. 2024•taylorfrancis.com*.

264. Jolly, D. S. *et al.* Sodium/Na β″ Alumina Interface: Effect of Pressure on Voids. (2019) doi:10.1021/acsami.9b17786.

265. Armstrong, D., Haseeb, A., Roberts, S., Films, A. W.-T. S. & 2012, undefined. Nanoindentation and micro-mechanical fracture toughness of electrodeposited nanocrystalline Ni–W alloy films. *Elsevier*.

266. Armstrong, D. E. J. & Tarleton, E. Bend Testing of Silicon Microcantilevers from 21°C to 770°C. *JOM* **67**, 2914–2920 (2015).

267. Herbert, F. W. & Roberts, S. G. Micromechanical testing of stress corrosion cracking. *Int. Heat Treat. Surf. Eng.* **4**, 70–73 (2010).

268. Pharr, G. M., Herbert, E. G. & Gao, Y. The indentation size effect: A critical examination of experimental observations and mechanistic interpretations. *Annu. Rev. Mater. Res.* **40**, 271–292 (2010).

269. Rodrıguez, R., A, I. G.-M. S. and E. & 2003, undefined. Correlation between nanoindentation and tensile properties: influence of the indentation size effect. *ElsevierR Rodrıguez, I GutierrezMaterials Sci. Eng. A, 2003•Elsevier*.

270. Nix, W. D. & Gao, H. Indentation size effects in crystalline materials: A law for strain gradient plasticity. *J. Mech. Phys. Solids* **46**, 411–425 (1998).

271. Kim, H., Hong, S., Technology, S. K.-J. of M. P. & 2001, undefined. On the rule of mixtures for predicting the mechanical properties of composites with homogeneously distributed soft and hard particles. *ElsevierHS Kim, SI Hong, SJ KimJournal Mater. Process. Technol. 2001•Elsevier*.

272. Clyne, T. & Withers, P. *An introduction to metal matrix composites*. (1993).

273. Turon-Vinas, M., Roa, J., Marro, F., International, M. A.-C. & 2015, undefined. Mechanical properties of 12Ce–ZrO2/3Y–ZrO2 composites. *ElsevierM Turon-Vinas, JJ Roa, FG Marro, M AngladaCeramics Int. 2015•Elsevier*.

274. Barrett, C. R. . N. W. D. . T. A. S. The principles of engineering materials. *(No Title)*.

275. Zong, B. Y., Zhang, F., Wang, G. & Zuo, L. Strengthening mechanism of load sharing

of particulate reinforcements in a metal matrix composite. *J. Mater. Sci.* **42**, 4215–4226 (2007).

276. Porter, D. L., Evans, A. G. & Heuer, A. H. Transformation-toughening in partially-stabilized zirconia (PSZ). *Acta Metall.* **27**, 1649–1654 (1979).

277. Hannink, R. H. J., Kelly, P. M. & Muddle, B. C. Transformation Toughening in Zirconia-Containing Ceramics. *J. Am. Ceram. Soc.* **83**, 461–487 (2000).

278. Maithani, Y., Khan, J., Mehta, B., International, J. S.-C. & 2023, undefined. Cubic phase optimization and influence of post-annealing on microstructure, optical, wetting, and nanomechanical properties of zirconia thin films. *ElsevierY Maithani, JA Khan, BR Mehta, JP SinghCeramics Int. 2023•Elsevier*.

279. Kalnaus, S., Westover, A. S., Kornbluth, M., Herbert, E. & Dudney, N. J. Resistance to fracture in the glassy solid electrolyte Lipon. *J. Mater. Res.* (2021) doi:10.1557/s43578-020-00098-x.

280. Ritchie, R. O. Toughening materials: Enhancing resistance to fracture. *Philos. Trans. R. Soc. A Math. Phys. Eng. Sci.* **379**, (2021).

281. Rödel, J. Interaction between crack deflection and crack bridging. *J. Eur. Ceram. Soc.* **10**, 143–150 (1992).

282. Han, S. *et al.* Stress evolution during cycling of alloy-anode solid-state batteries. *cell.comSY Han, C Lee, JA Lewis, D Yeh, Y Liu, HW Lee, MT McDowellJoule, 2021•cell.com*.

283. Deng, Q., Hu, R., Xu, C., Chen, B. & Zhou, J. Modeling fracture of solid electrolyte interphase in lithium-ion batteries during cycling. *J. Solid State Electrochem.* **23**, 2999–3008 (2019).

284. A, R. R.-M. S. and E. & 1988, undefined. Mechanisms of fatigue crack propagation in metals, ceramics and composites: role of crack tip shielding. *Elsevier*.

285. Balan, K. *Metallurgical failure analysis: techniques and case studies*. (2018).

286. Kato, Y. *et al.* High-power all-solid-state batteries using sulfide superionic conductors. *Nat. Energy* **1**, (2016).

287. Härtelt, M. *et al.* Deducing the fatigue crack growth rates of natural flaws in silicon nitride ceramics: Role of R-curves. *J. Am. Ceram. Soc.* **96**, 2593–2597 (2013).

288. Straub, T., Berwind, M. F., Kennerknecht, T., Lapusta, Y. & Eberl, C. Small-Scale Multiaxial Setup for Damage Detection Into the Very High Cycle Fatigue Regime. *Exp. Mech.* **55**, 1285–1299 (2015).

289. Evans, A. G. Slow crack growth in brittle materials under dynamic loading conditions. *Int. J. Fract.* **10**, 251–259 (1974).

290. Jiang, J. *et al.* Microcantilever investigation of slow crack growth and crack healing in aluminium oxide. *ElsevierJ Jiang, S Falco, S Wang, F Giuliani, RI ToddActa Mater. 2024•Elsevier*.

291. Yamaguchi, H. *et al.* Dislocation-controlled microscopic mechanical phenomena in single crystal silicon under bending stress at room temperature. *J. Mater. Sci.* **55**, 7359–7372 (2020).